“Study of the Interactions of Gold, Silver and Molybdenum disulfide Nanostructures with Organic and Inorganic compounds towards the Development of Various Sensing and Biological Applications via Spectrofluorometric Method”

THESIS SUBMITTED TO THE

JADAVPUR UNIVERSITY

FOR THE DEGREE OF

DOCTOR OF PHILOSOPHY (SCIENCE)

By

Pradip Maiti

DEPARTMENT OF PHYSICS

JADAVPUR UNIVERSITY

JADAVPUR, KOLKATA 700032, INDIA

2023

Ref. No. PhD/05/2023

Date: 24/05/2023

CERTIFICATE FROM THE SUPERVISORS

This is to certify that the thesis entitled **"Study of the Interactions of Gold, Silver and Molybdenum disulfide Nanostructures with Organic and Inorganic compounds towards the Development of Various Sensing and Biological Applications via Spectrofluorometric Method"** submitted by **Sri Pradip Maiti** (Reference No. D-7/SC/1109/19, Index No. 123/19/Phys./26), who got his name registered on 08th November, 2019 for the award of Ph.D. (Science) degree of Jadavpur University, is absolutely based upon his own work under the supervision of **Prof. Pabitra Kumar Paul,** Department of Physics, Jadavpur University, Kolkata 700032 and co-supervision of **Dr. Sharmistha Paul,** Senior Scientist, West Bengal State Council of Science and Technology, Vigyan Chetana Bhavan, 26/B, DD Block, Sector 1, Saltlake, Kolkata 700064, and that neither this thesis nor any part of it has been submitted for either any degree/diploma or any other academic award anywhere before.

24/05/2023

(Dr. Sharmistha Paul)
Signature of Co-Supervisor
Senior Scientist
West Bengal State Council of
Science and Technology,
Vigyan Chetana Bhavan, 26/B,
DD Block, Sector 1, Saltlake,
Kolkata 700064

Dr. Sharmistha Paul
Senior Scientist
West Bengal State Council of Science & Technology
Vigyan Chetana Bhavan, 4th Floor
26/B, DD Block, Sector-I, Salt Lake, Kolkata-700064

Pabitra Kumar Paul 24/5/2023

(Prof. Pabitra Kumar Paul)
Signature of Supervisor
Professor
Department of Physics
Jadavpur University, Jadavpur
Kolkata 700032

Prof. (Dr.) Pabitra Kumar Paul
Professor
Department of Physics
Jadavpur University
Kolkata - 700032

Dedicated to my beloved father

Late Gostha Behari Maiti

Along with all respected Teachers

Declaration

I hereby declare that the work reported in this thesis is entirely original and carried out by me under the supervision of Prof. Pabitra Kumar Paul, Department of Physics, Jadavpur University, Jadavpur, Kolkata 700032 and co-supervision of Dr. Sharmistha Paul, Senior Scientist, West Bengal State Council of Science and Technology, Vigyan Chetana Bhavan, 26/B, DD Block, Sector 1, Saltlake, Kolkata 700064. I further declare that this thesis has not been submitted previously for any other degree/diploma or any other professional qualification.

Pradip Maiti

Date: 24.05.2023

Place: Jadavpur, Kolkata

(Pradip Maiti)
Research Scholar
Department of Physics
Jadavpur University

ACKNOWLEDGEMENTS

It is my great pleasure and privilege to express my sincere thanks to all whose constant support and cooperation make the journey of my doctoral research possible and to overcome many difficult circumstances. Words are not enough to express my feelings for them yet these lines are not exaggerations but feelings, which come straight from the heart.

First and foremost, I would likre to acknowledge my indebtedness and my sceincer gratitude to my supervisor Prof. Pabitra Kumar Paul and co-superviser Dr. Sharmistha Paul for giving me the opportunity to work under their guidance. Their arduous enlightement, prudent suggestions and never-ending cooperation have been invaluable throughout all stages of the work.

I am very grateful to our collaborators Prof. Parimal Karmakar, Dr. Arunima Sengupta and research scholar Shreya Das of Department of Life Science and Biotechnology, Jadavpur University, Kolkata for their nice support and co-operation in some experimental work whenever required.

I would also wish to express my sincere thanks to the Head of Department and other faculty members of the Department, Jadavpur University. I am also very much grateful to Physics Department of Jadavpur University for providing excellent infrastructural support and cooperation during my research work. I am thankful to the staff of this department for their constant help.

I bow my head and offer flowers of reverence to Jadavpur University, a great temple of learning for the course of millions of students like me.

I am also immensely thankful to all of my labmates, namely, Chaitali di, Utsav da, Tanmoy da, Ujjal, Alapan and Indrajit for their meticulous support, indelible inspiration, persistent encouragement, ingenious suggestions and best companion in during my research work.

This work would have been rather incomplete without the moral support and constant inspiration from all of my close friends, namely, Arijit, Biswajit, Kuntal, Dibyendu, Sukdev, Saikat, Somnath, Tamal, Tarak da, Saibal da.

Thanks are also due to all of my teachers and friends for their insprration and kind hearted support to reach this level of my journey.

Last but not the least, I would like to express my respect and regards to my family, my late father, my beloved wife Shampa Manna Maiti for their unconditional love, support and encouragement. I must extent my deepest respect to Dr. Parthasarithi Das of Midnapore College and Dr. Tapas Misra of Sabang Sajanikanta Mahavidyalaya for making everything possible for me.

Date: 24.05.2023

Place: Jadavpur, Kolkata

Pradip Maiti

(PRADIP MAITI)

List of Publications

List of research publications related to my Ph.D. thesis

[1] Comparative and Selective Interaction of Amino Acid D-Cysteine with Colloidal Gold Nanoparticles in the Presence of a Fluorescent Probe in Aqueous Medium.

Pradip Maiti, Ujjal Saren, Utsav Chakraborty, Tanmoy Singha, Sharmistha Paul, Pabitra Kumar Paul

ACS Omega, 7 (2022) 29013−29026 (American Chemical Society)

[2] Selective and sensitive detection of L-Cysteine via fluorometric assay using gold nanoparticles and Rhodamine B in aqueous medium.

Pradip Maiti, Tanmoy Singha, Utsav Chakraborty, Sannak Dutta Roy, Parimal Karmakar, Bapi Dey, Syed Arshad Hussain, Sharmistha Paul, Pabitra Kumar Paul

Materials Chemistry and Physics, 234 (2019) 158–167 (Elsevier)

Paper communicated to journal for publication

[1] Hydrothermal Synthesis of Bio-Inspired MoS_2 Nanoflakes for Highly Sensitive Fluorescence-based Detection of Mercury Ion in Aqueous Solution and Cellular Milieu.

Pradip Maiti, Shreya Das, Jnanranjan Panda, Devdas Karmakar, Alapan Pal, Samit Guha, Arunima Sengupta, Sharmistha Paul, Pabitra Kumar Paul

Paper communicated to Journal for publication.

List of publications where I have substantial contribution

[1] Interaction of hectorite clay with a phospholipid monolayer at air-saline interface in presence of a fluorescent dye

Tanmoy Singha, Ujjal Saren, **Pradip Maiti**, Utsav Chakraborty, Alapan Pal, Pabitra Kumar Paul

Molecular Crystals and Liquid Crystals, 738 (1) (2021). (Taylor & Francis)

[2] Effect of montmorillonite clay on the fluorescence resonance energy transfer between two cationic dyes Acridine Orange and Rhodamine B in solution.

Utsav Chakraborty, **Pradip Maiti**, Tanmoy Singha, Ujjal Saren, Alapan Pal, Pabitra Kumar Paul

Materials Today: Proceedings, 46 (2021) 6275–6285. (Elsevier)

[3] Development of a Schottky barrier diode using molecular network of 1-alkyl-2-(arylazo) imidazole prepared by Langmuir-Blodgett technique.
Tanmoy Singha, Debashis Mallick, Utsav Chakraborty, **Pradip Maiti**, Rajkumar Jana, chittranjan sinha, Partha Ray, Pabitra Kumar Paul
Journal of Physics and Chemistry of solids, 149 (2021) 109778. (Elsevier)

[4] Exfoliated Molybdenum Disulfide-Wrapped CdS Nanoparticles as a Nano-Heterojunction for Photo-Electrochemical Water Splitting.
Sukdev Dolai, **Pradip Maiti**, Arup Ghorai, Ritamay Bhunia, Pabitra Kumar Paul, Dibyendu Ghosh
ACS Applied Materials & Interfaces, 13 (2020) 438−448. (American Chemical Society)

[5] Photophysical study of the interaction between ZnO nanoparticles and globular protein bovine serum albumin in solution and in a layer-by-layer self-assembled film.
Chaitali Hansda, **Pradip Maiti**, Tanmoy Singha, Manisha Pal, Syed Arshad Hussain, Sharmistha Paul, Pabitra Kumar Paul
Journal of Physics and Chemistry of Solids, 121 (2018), 110–120. (Elsevier)

[6] Fabrication and characterization of next generation nano-structured organo-lead halide-based perovskite solar cell.
Abhishek Dhar, Argha Dey, **Pradip Maiti**, Pabitra Kumar Paul, Subhasis Roy, Sharmistha Paul, Rohit L. Vekariya
Ionics, 24 (2018) 1227–1233. (Springer)

Paper presented/attended in National/International seminar/conferences/Symposia

[1] 5th India International Science Festival (IISF-2019), 5th–8th November 2019, Kolkata, West Bengal.

[2] National Seminar on Physics at Surfaces and Interfaces of Soft Materials (PSISM-2019), 26th–27th September, 2019. Condensed matter Physics Research centre, Department of Physics, Jadavpur University, Kolkata-700032. Title of the poster presented: "***Detection of L-Cysteine using Gold nanoparticles and Rhodamine B via spectrofluorometric method***".

[3] Recent Trend in Frontier Research in Physics, 6th March 2018, Department of Physics, Jadavpur University, Kolkata.

[4] Twist and Turns in Physics Research: Special Emphasis on Condensed Matter and Biophysics (TTPR-2017), 21st–22nd February 2017, Department of Physics, Jadavpur University, Kolkata.

[5] 1st Regional Science & Technology Congress-2016, Presidency Division, West Bengal, 13th–14th November, 2016, Department of Science and Technology, Government of West Bengal, In collaboration with National Institute of Technical Teachers' Training and Research, Kolkata. Title of the poster presented: ***"Synthesis and potential use of ZnO nanorods in dye degradation".***

[6] One Day Workshop on Celebration of International Year of Light 25th July, 2016, West Bengal State Council of Science and technology, Department of Science & Technology, Govt. of West Bengal.

Synopsis

Metal and metal-based nanostructures such as gold nanoparticles (Au NPs), silver nanoparticles (Ag NPs) etc. and 2D–dimensional transition metal dichalcogenides (2D TMDs) namely molybdenum disulfide (MoS_2) nanostructures have received widespread interest in the scientific community because of their unique optical and physicochemical properties including ease of functionalization via simple chemistry and high surface to volume ratio, better bio-functionality, chemical and thermal stability along with the possibility of interactions with various organic and inorganic compounds. Currently, there is renewed interest especially on metal or metal-based nanostructures with respect to their various sensing and biological applications. On the other hand, most of the organic dye molecules are small fluorescent emitters which generally consist of rich π–conjugated ring structures such as xanthene, pyrene or cyanine etc. These commercially available fluorophores exhibit fluorescence emission from ultraviolet to the near infrared wavelength (300–900 nm) region. Over the past decade, various organic fluorescent dyes played the central role in the field of molecular level sensing applications. However, in many cases direct labelling with the fluorescent probe alter the structural conformation of the target bioanalytes. Also due to the limited photostablity and aggregation of many organic fluorescent probes, there are some difficulties for their use in biosensing applications. In recent times metal nanoparticle/dye interactions have received much attention in the scientific community due to many interesting spectroscopic properties of the emitter molecules in the vicinity of nanoparticle. The unique surface chemistry of metal NP's efficiently interfere with the oscillating dipole of organic emitter molecules resulting the quenching of fluorescence signal of the emitter molecules. In many situation, this change in fluorescence signal is found to be highly specific in presence of guest molecular or ionic species. On the other hand, the sensing of toxic inorganic ion using self-fluorescent metal-based nanostructures such as MoS_2 both in aqueous solution and intracellular medium as studied in this present research work contributes significant and valuable information both for biomedical and environmental aspects.

A promising approach to probe a detectable change or a signal for molecular recognition is the spectrofluorometric method. Spectrofluorometric technique has a

great deal of fundamental importance about the knowledge of molecular behaviour and promotes the understanding of their detail photophysical properties at molecular level both in the ground and excited electronic states when light interacts with the molecules. This technique is highly sensitive and most informative analytical tool concerning with the different fields of material science. Various aspects of radiative and non–radiative transitions depend on nature, rigidity, intermolecular distance, molecular microenvironments, presence of any ionic and non-ionic species etc. In this thesis work the effect of noble metal nanoparticles such as gold nanoparticles on the photophysical characteristics of some organic fluorescent dyes in absence and presence of biological molecules (namely L, D-Cysteine, etc.) in aqueous environment have been systematically investigated. The highly selective and sensitive response of fluorescence signal due to interaction of metal nanoparticles with target biomolecules reveals the fact that dye/nanoparticle system may be an efficient sensing platform for various biomolecular species. In another study silver nanoparticles have been used to study their interaction organic biologically relevant organic probe acridine orange in presence DNA in aqueous environment. Results showed strong binding interaction of silver nanoparticles with DNA as evidenced by fluorescence spectroscopy. In recent times, 2D layered MoS_2 has attracted great interest among the researchers for their unique layered structures and interesting fluorescence properties in aqueous medium. These properties have been utilized for efficient detection of toxic heavy metal ions namely mercury ions using MoS_2 nanostructures via spectrofluorometric method and is presented in this thesis. The relative change of the electronic states of the fluorophores in presence of various metal nanostructures are systematically correlated with the exposure of various guest organic, inorganic and bio–molecular species in the studied medium. Also, the unique layered structure of MoS_2 enables them as a suitable candidate to selectively interact with guest ionic species for possible application in biological fields. Overall, the detailed and systematic investigations of the interactions of noble metal nanoparticles and layered nanostructures like MoS_2 with organic, inorganic and biological species as studied in this present thesis work may contribute valuable database both for fundamental and technological applications.

The research work which I performed are presented in different chapters of this thesis. A brief summary of the research is given here.

Chapter 1 represents a **general introduction** of the thesis work. The motivation and scope of the present thesis are also briefly summarized in this chapter.

Chapter 2 gives the **theoretical background** of the research relevant to the work presented in this thesis and various analytical approaches especially spectroscopic techniques utilized for experimental work. The quantum theory of the interaction between light and matter and also various spectroscopic phenomena at the molecular level are described in detail. The theoretical backgrounds of computational simulations (DFT, Quantum Espresso etc.) are briefly described in this chapter.

Chapter 3 represents a l**iterature review** for the status of previous and recent works by various eminent scientists and researchers both at the international and national levels in the relevant field of research along with some breakthrough and pioneering work. Some interesting research on sensing mechanisms as reported by various scientific research groups are also cited to realize the opportunity of further development in this area of research.

Chapter 4 deals with a detailed description of the e**xperimental methods and characterization techniques** used in the research work as presented in this thesis. The preparation of mixed solutions used in the sensing of biomolecules and metal ions is also described step by step. The working principles of various analytical equipment to characterize metal and metal–based nanostructure materials are also briefly described in this chapter.

Chapter 5 demonstrates the details of the sensing mechanism of important essential amino acid namely L-Cysteine (abbreviated as L-Cys) by using citrate capped gold nanoparticles (Au NPs) and cationic dye Rhodamine B (abbreviated as RhB) dye in their aqueous solution via spectrofluorometric assay method. The as-synthesized colloidal Au NPs of diameter ~27.5 nm were characterized by UV-vis absorption and transmission electron microscopic (TEM) measurements. The fluorescence emission intensity of RhB dye was strongly quenched by Au NPs in the aqueous solution due to closer association of dye molecules in the vicinity of NPs surface. However, when L-Cys aqueous solution was added with Au NPs/RhB mixed solution, fluorescence emission started to emerge. This might be due to the strong affinity of thiol (–SH) moiety of L-Cys with the Au NPs in the aqueous medium. Due to SH–Au interaction, RhB molecules were displaced from the surface of Au NPs and 'turn–on' the fluorescence emission was observed. This binding interaction between SH–Au was very selective as was evidenced by the selectivity study of other relevant interfering analytes with Au NPs/RhB mixed solution in the same optimized conditions. This

sensing mechanism of L-Cys was successfully employed for the detection of L-Cys in the real biosample of normal human urine.

Chapter 6 mainly focused on the comparative and selective interaction of the important amino acid D-Cysteine (D-Cys) with the colloidal gold nanoparticles (Au NPs) in the presence of a fluorescent probe namely rhodamine B (RhB) dye in their aqueous solution. Various analytical techniques such as UV–vis absorption and steady-state fluorescence emission, dynamic light scattering (DLS), Zeta potential, circular dichroism (CD), fourier transform infrared (FTIR) and atomic force microscopy (AFM) have been employed in the study. D-Cys showed higher fluorescence recovery efficiency from Au NPs/RhB mixed aqueous solution compared to the other relevant D- and L- amino acids, other thiol (–SH) containing biomolecules including L-Homocysteine, D-Homocysteine, Glutathione (GSH) etc. Also, the binding constant between D-Cys and Au NPs/RhB mixed solution was much higher when compared to its L- chiral part. Most interestingly, the selective interaction of A NPs/RhB mixed system with D-Cys is accompanied with distinct colour change of the assay medium after reaction when compared that with other interfering compounds as observed in the study. FTIR, DLS, Zeta potential, AFM and CD measurements confirmed the different nature of interactions between D-Cys and L-Cys with the Au NPs/RhB mixed aqueous solution. Also, this interaction mechanism was successfully employed to detect D-Cys from the normal human urine sample.

Chapter 7 demonstrates the interactions of silver nanoparticles with cationic dye acridine orange in presence of calf thymus DNA in aqueous solution. Results revealed the strong fluorescence quenching of dye molecules due to silver nanoparticles as dye molecules adsorbed onto the surface of nanoparticles. DLS and zetapotential results are also consistent with the observed spectroscopic results. Acridine orange dye molecules also binds with DNA in the solution but there was no significant change in the peak position of AO emission. However, most interestingly after addition of Ag NPs in dye/DNA mixed solution silver nanopartilces strongly attached with DNA by expulsion of dye molecules from DNA. The proposed study may reveal valuabale informations about the binding mechanism of silver nanoparticles with DNA in presence of fluorescent probe.

Chapter 8 describes the sensing of very toxic heavy metal ion namely mercury (Hg^{2+}) using fluorescent molybdenum disulfide (MoS_2) nanoflakes both in the aqueous solution and cellular milieu. The bio-inspired MoS_2 nanoflakes were synthesized using

L-Cysteine as a rich source of sulfur (S) via hydrothermal method. The as-synthesized MoS_2 nanoflakes were characterized by X-ray diffraction (XRD), field emission scanning electron microscope (FESEM), high-resolution transmission electron microscope (HRTEM), atomic force microscope (AFM), Raman scattering, UV-vis absorption, steady-state and time-resolved fluorescence emission techniques. XRD, FESEM and Raman results confirmed the formation of flower-like morphology of MoS_2 by the stacking of individual nanosheets. The time-resolved fluorescence emission spectroscopy (TCSPC) reveals the fluorescence decay profile of as-synthesized MoS_2 and the fluorescence was found to be ~2.97 ns. The fluorescent MoS_2 nanoflakes were successfully employed in the sensing of the Hg^{2+} ion in aqueous medium due to strong affinity of Hg^{2+} towards S atom in the MoS_2 nanostructured sample. The proposed sensing method is highly sensitive towards Hg^{2+} ion in aqueous solution. Also, this interaction was very much selective when compared with the other metal ions (Ca^{2+}, Cd^{2+}, Cu^{2+}, Mg^{2+}, Na^{+}, Ni^{2+}, Zn^{2+}, Al^{3+}, Fe^{2+} etc.) in the aqueous medium. We have further employed the proposed sensing mechanism to biological cell for detection of Hg^{2+} ion via fluorescence imaging microscopy and similar fluorescence quenching was observed. Density functional theoretical (DFT) calculations based on the Quantum Espresso (QE) package confirmed the binding between Hg^{2+} and S atom of MoS_2.

Chapter 9 presents the overall conclusion of the present thesis and future plan of research.

Contents

List of figures

List of Tables

List of abbreviations

Abbreviations	Full form
°C	Degree Celsius
µM	Micromolar
2-D	2-Dimensional
A	Absorbance
a.u.	Absorbance unit
AFM	Atomic force microscope
Ag NPs	Silver nanoparticles
ATR	Attenuated total reflection
Au NPs	Gold nanoparticles
CD	Circular dichroism
cps	Counts per second
CV	Cyclic voltammetry
DFT	Density functional theory
DLS	Dynamic light scattering
Eqn.	Equation
FE	Field emission
FRET	Fluorescence resonance energy transfer
FTIR	Fourier transform infrared
HR	High resolution
hrs.	Hours
hv	Energy of electromagnetic wave
L/D-Cys	L/D-Cysteine
LSPR	Localised surface plasmon resonance
M	Molar
min	Minute
mL	Milli Litter
MoS_2	Molybdenum disulfide

MTT assay	3-[4,5-dimethylthiazol-2-yl]-2,5 diphenyl tetrazolium bromide
nm	Nanometer
NPs	Nanoparticles
QE	Quantum Espresso
RhB	Rhodamine B
r.m.s.	Route mean square
SEM	Scanning electron microscope
SPR	Surface plasmon resonance
TCSPC	Time correlated single photon counting
TEM	Transmission electron microscope
UV	Ultraviolet
UV-vis	Ultraviolet-visible
XRD	X-ray diffraction
ΔG	Gibbs free energy
λ_{max}	Wavelength corresponding to maximum absorption/emission
K_a	Binding/association constant
K_q	Quenching rate constant
K_{SV}	Stern-Volmer constant
τ_{av}	Average lifetime
cm^{-1}	Wavenumber

CHAPTER ~ 1

General Introduction

This chapter gives a brief introduction of the motivation, objective and organization of the thesis

CHAPTER~1

General Introduction

1.1. Introductory remarks

Nanostructured materials and nanotechnology have attracted great attention in the scientific community since the last several decades. Over 50 years ago, the idea of construction of nanomaterials by arranging the atom over the atom was first put forwarded by famous physicist Richard Feynman (1918–1988) in his lecture entitled "There's plenty of room at the bottom" [1]. In general, the term "Nano" in "Nanotechnology" refers to the materials with dimensions in the range of 1–100 nm [2]. The nanomaterials possess different physical and physicochemical properties at the nano level when compared to their bulk counterpart. Moreover, in our surroundings, there exist highly optimized nanoscale systems which are created by millions of years of evolutionary scientific development. As an example, the photonic crystal of nanoparticles in the wings of a butterfly creates intricate colours [2]. The scientific, experimental, and technical advancements over the last few years have made the ability to synthesise, control, and measure the miracles in atomic scale. Although, there are lot of scientific challenges in the field of nanotechnology towards the development of the high potential and promise that nanotechnologies improve the today's life and mankind. The main challenges include the development of efficient synthesis methods which offer great control in both the shape and size of nanomaterials and the overall engineering of these nanomaterials for various applications. Among the various nanostructured materials, metal nanoparticles (NPs) especially noble metal NPs are being explored for their potential applications in the field of catalysis [3], sensing [4], cell imaging [5], antibacterial [6], antimicrobial [6] etc. applications. These noble metal NPs unveil some new optical, optoelectronic, magnetic, and many physicochemical properties that are very different from the constituent atoms or molecules. For example, the brilliant colours of colloidal dispersion of noble metal NPs such as silver (Ag) and

gold (Au) etc. are observed due to the surface plasmon resonance (SPR) band which in general lies in the domain of visible wavelengths in contrast to their bulk counterpart for which the absorption bands lie in the UV region. The SPR band in the absorption spectrum is originated due to the interaction of free electrons with light thereby creating collective oscillation of these electrons on the surface of the NPs [7]. The spectral properties of these SPR bands significantly depend on the size and morphology of such metal NPs as well as the dielectric constant of the NP's surrounding environment [8]. Control of size and shape of these NPs enable various significant electronic, optical, magnetic, and catalytic [3] properties. Soft chemical methods are very promising for the synthesis of such noble metal nanostructures with controlled shape and size. Also, their extinction coefficients are much higher than that of many of the traditional organic fluorophores, which confirms the suitable use of noble metals NPs in cell imaging and fluorescence resonance energy transfer (FRET) studies [9]. For example, Au NPs and Ag NPs have an extinction coefficient of 2.93×10^9 $Lmol^{-1}cm^{-1}$ and 5.6×10^9 $Lmol^{-1}cm^{-1}$ respectively [10, 11] that allows them to be used as excellent FRET-based fluorescence quenchers for the study of interactions with different organic fluorophores, biomolecules and also can efficiently probe many conformational changes in the molecular structures. Appart from noble metal nanoparticles, 2-dimensional (2-D) layered nanostructures such as Molybdenum disulphide (MoS_2) has also attracted considerable interest in recent times for their utility in various sensing and biological applications [12]. The molybdenum (Mo) and sulphur (S) atoms are connected through covalent bond in the molecular layer of MoS_2. Due to their unique fluorescence emission properties, well dispersibility in water and low cytotoxicity, MoS_2 nanostructures are very promising materials for their possibility of use in various cellular study and metal ion sensing applications. Development of efficient sensing platform using nanostructured materials via facile and cost-effective approach in a ultramolar detection range is essential both for biomedical and environmental aspects.

Organic compounds, namely the xanthene group of dyes also known as laser dyes are being widely explored during the last few decades due to their incredible applications in the fields of green energy harvesting with photocells, spectroscopy, bio-sensing, bio-assisted drug delivery, bio-imaging, and several indirect and direct medical purposes [13]. Due to the presence of light absorbing chromophores in organic dyes, they exhibit excellent photophysical characteristics as is easily understood with the help

of conventional electronic spectroscopic techniques. Most of the organic laser dyes are fluorescent which is extensively studied by various researchers since long back. However, in some cases, limited photostability and aggregations of dye molecules create difficulties for their applications especially in biological and sensing applications. Additionally, direct labelling of biological molecules with conventional dyes sometimes causes the structural alternation of the bioanalyte in bio-sensing applications.[14]. Various noble metal NPs such as Au NPs, Ag NPs etc. significantly interfare with the photoexcitation and affect the deactivation processes of such organic dye molecules in aqueous medium. Recently, the study of the energy transfer process between photo-excited organic dye and metal NPs in solution is attracted great attention due to their sensitivity to the different microenvironments such as temperature, pH etc. in the solution [15]. The photo-excited dipoles of the fluorophores directly interact with the surface of NPs to exchange the excited state energy from their chromophore to the NPs surface. The efficiency of energy transfer strongly depends upon the dye-nanoparticle separation in the range of 1–10 nm [16]. Among the various organic dyes, study of the interactions of various cationic dyes with noble metal NPs in aqueous environment have been attracted great interest among the researchers due to their immense technological importance in drug delivery, biomedicine, and fabrication of various sensors [17] and also to comprehend the basic physics involved in their molecular mechanism. Various studies on the interaction of metal nanostructured materials with organic emitter molecules can open a great avenue of application in several emerging field of biomedical applications. More precisely, the attachment of metal NPs with organic dyes may lead to efficient drug delivery [18], enhanced bio sensing activity [19], and better photo-response in green energy-harvesting [20] applications.

1.2. Motivation and objectives of the present thesis

Research in the field of sensing of several biomolecular species and metal ions is growing in the last few years for various biomedical and environmental aspects. Synthesis of stable and desired-size noble metal NPs boosted this field of research into a new dimension. Apart from noble metal NPs, florescent organic molecules played a crucial role in the scientific and technological demands for the development of cutting-edge techniques in the field of sensing and related biomolecular ineteractios [14]. As

mentioned earlier that, noble metals such as Ag NPs, Au NPs etc. show remarkable electrical, optical, antibacterial and catalytic properties which primarily depend on the shape and size of NPs [6]. Recently, various metal NPs are being widely used in the fields of biology, chemistry, cosmetics, foods, medicine etc. [21]. Therefore, the controlled synthesis of noble metal NPs with well-organised morphology is extremely important for their methodical utilities in the field of research and development of various sensors as well as to explore their interaction with biological molecule for future technological appliactions. NPs have been used in different fields of research including biology, chemistry, electric engineering, medical physics, and the textile industry in which the shape and size of nano colloids play a pivotal role in different applications such as the preparation of electronic and magnetic devices, anti-microbial gene expression, wound healing using nano-bio composition etc. [22].

Recent advancements and utilization of various inorganic nanoparticles in the biological fields also create renewed interest for sustainable research and development of new materials with tailored physical and physicochemical properties. Most noble metal NPs possess durable structures which can easily host different biological and organic guest molecules resulting various multifunctional properties [23]. NPs show unique characteristics when compared to bulk counterparts due to their large surface area to volume ratio which is especially favourable for various fields of applications such as medical diagnostics, biomolecular sensing, bioimaging, and treatment for various convoluted diseases [24].

As mentioned in the previous section, organic fluorophores are small fluorescent molecules, which are of particular interest as they can interact via electrostatic attraction or chemisorption with noble metal NPs resulting in aggregated or self-assembled structures in aqueous solution. These aggregated configurations of NPs show interesting and significant physical and physicochemical properties. Thus, a detailed study on the interactions of noble metal NPs with different organic fluorescent compounds is of utmost importance for various applications. Consideration of various cationic organic dyes to comprehend their aggregation behaviour when associated in the vicinity of NPs in aqueous solution. Literature reveals that both the ground state and excited state electronic properties of the organic dye molecules largely depend on the way of association with the NPs in their molecular proximity [25]. In many cases this dye-NPs interaction is very much sensitive and selective [25]. So, it is very much

important to understand the molecular mechanism of cationic organic dyes involved in their ground and excited states while interacting with noble metal NPs (Au, Ag etc) in an aqueous solution for fundamental and technological importance. Moreover, the overlaps between the UV-vis absorption spectrum of NPs and the fluorescence emission spectrum of some organic dye molecules indicate the possibility of transfer of photo-excited energy from the photoexcited dye molecules (donor) to NPs via some nonradiative energy transfer pathway [26]. Additionally, 2D layered nanomaterials such as MoS_2 is a very promising maaterials and are continoueously studied by various researchers across the globe. Their fascinating fluorescence emission properties led the scientist to focus their utility in various biomedical applications. Due to this fact, the research to probe the possible utility of MoS_2 in the field of molecular and ion sensing is gained considerable interest among the scientific communities for various applications.

Therefore, the main objectives of this thesis are summarized below:

- To synthesize noble metal NPs such as Au, Ag etc. via simple soft chemical route to explore their interaction with various organic fluorescent compounds namely some cationic dyes and the formation of their molecular aggregates in aqueous solution.
- To choose some suitable biomolecules which can significantly interact with NPs and efficiently control the aggregation or association behaviour of dye molecules in the dye-NPs assembly, which motivates to develop efficient biosensing platform in the aqueous environment or various fundamental interst in the field of nano-biotechnology.
- To optimize various parameters for the interaction involved in the dye-NPs ensemble and the systematic investigation of any selective binding of such metal NPs with bioanalyte towards the development of biosensing platform using fluorescence emission properties of dye molecules in presence of noble metal NPs..
- To synthesize 2D layered nanomaterials such as MoS_2 and to study their selective interaction with some inorganic compounds namely various salts towards the detection of metal ions in aqeous environment as well as in intra-cellular environment.

- Several analytical approaches such as UV-vis absorption spectroscopy, steady-state and time-resolved fluorescence emission spectroscopy methods will be utilized to investigate the detailed photophysical behaviour of the organic fluorophores while interacting with noble metal NPs in the aqueous solution. Moreover, with the help of these analytical methods, we want to understand the spectroscopic characterstics of such dyes in close proximity of metal NPs in solution phase. In some caeses vibrational spectroscopy such as Fourier-transformed infrared spectroscopy and Raman spectroscopy will be utilized in order probe the interaction between the organic and inorganic species to be used in the study.
- X-ray diffraction technique will be employed to get the crystalline nature of the as-synthesized nanomaterials.
- Various imaging methods such as Field emission scanning electron microscope, High-resolution transmission electron microscope, Atomic force microscopy etc. will be utilized to explore the structure and the morphology of the as-synthesized metal and metal-based nanostructures as well as the aggregated dye-nanostructures complex. Also, in some caes, fluorescence imaging microscopy will be used to visualize the interaction of biological cells with the some of the synthesized nanomaterials.
- Some quantum-chemical calculations such as Density functional theoretical calculations will be performed to understand different electronic states associated with the observed electronic transition in absorption and emission spectra of the dye molecules in the aqueous solution.

1.3. Organization of the thesis

Chapter 1 represents the **General Introduction** of this thesis work. The motivation and objective of the present thesis work are also briefly summarized in this chapter.

Chapter 2 gives the **Theoretical Background** of the research relevant to the work presented in this thesis and various analytical approaches especially spectroscopic techniques utilized for experimental work. The quantum theory of the interaction between light and matter and also various spectroscopic phenomena at the molecular

level are described in detail. The theoretical backgrounds of computational simulations (DFT, Quantum Espresso etc.) are briefly described in this chapter.

Chapter 3 represents the detailed **Literature review** of previous work by various eminent scientists and researchers both at the international and national levels in the relevant field of research along with some breakthrough and pioneering work. Some interesting sensing mechanisms as reported by various groups are also cited to realize the opportunity for further development in this area of research.

Chapter 4 deals with a detailed description of the **Experimental Methods and Characterization Techniques** used in the research work as presented in this thesis. The preparation of mixed solutions used in the sensing of biomolecules or to study the interaction with organic dye and metal ions is also described step by step. The working principles of various analytical equipment to characterize metal and metal-based nanostructure materials are also briefly described in this chapter.

Chapter 5 demonstrates the details of the sensing mechanism of important essential amino acid namely L-Cysteine (L-Cys) by using citrated capped gold nanoparticles (Au NPs) and rhodamine B (RhB) dye in their aqueous solution via spectrofluorometric assay method. The colloidal Au NPs of diameter ~27.5 nm were synthesized using gold auric chloride and tri-sodium citrate as the reducing and capping agent and were characterized by UV-vis absorption spectrum, dynamic light scattering (DLS), zeta potential and transmission electron microscope (TEM) measurements. RhB is a xanthene group of dye also known as laser dye. The fluorescence emission of RhB was strongly quenched in the presence of Au NPs in the aqueous solution due to the closer association of dye molecules in the vicinity of NPs. The photoexcited energy of RhB dye molecules was transferred to the Au NPs via some non-radiative path, which was confirmed by the large overlapped area of the UV-vis absorption spectrum of Au NPs and the fluorescence emission spectrum of RhB. Due to this energy transfer, the fluorescence emission of RhB was almost quenched. However, when L-Cys aqueous solution was added with the mixed solution of Au NPs/RhB, the fluorescence emission of RhB started to appear. This might be due to the strong affiliation of the thiol (–SH) moiety of L-Cys with the Au NPs in the aqueous medium. Due to SH–Au interaction,

RhB molecules were displaced from the surface of Au NPs and 'turn-on' the fluorescence emission. This binding between SH–Au was very selective as was evidenced by the selectivity study of other relevant analytes with the Au NPs/RhB mixed solution in the same optimized conditions. This sensing mechanism of L-Cys was successfully employed for the detection of L-Cys in the real biosample of normal human urine.

Chapter 6 mainly demonstares the comparative and selective interaction of the important amino acid D-Cysteine (D-Cys) with the colloidal gold nanoparticles (Au NPs) in the presence of a fluorescent probe namely rhodamine B (RhB) dye in their aqueous solution using UV-vis absorption and steady-state fluorescence emission, dynamic light scattering (DLS), Zeta potential, Circular dichroism (CD), Fourier transform infrared (FTIR) and atomic force microscopy (AFM) measurements. D-Cys showed higher fluorescence recovery efficiency from Au NPs/RhB mixed aqueous solution compared to the other relevant D- and L- amino acids, another thiol (–SH) containing biomolecules including L-Homocysteine, D-Homocysteine, Glutathione (GSH) etc. Also, the binding constant between D-Cys and Au NPs/RhB mixed solution was much higher when compared to its L- chiral part. Most notably, the selective fluorescence enhancement due to D-Cys is accompanied with a distinct colour change of the assay solution when compared to the interaction with other amino acids. FTIR, DLS, Zeta potential, AFM and CD measurements confirmed the segregate nature of interactions between D-Cys and L-Cys with the Au NPs/RhB mixed solution in the aqueous medium. Also, the interaction mechanism was successfully used to detect D-Cys from the normal human urine sample.

Chapter 7 demonstrates the interactions of silver nanoparticles with cationic dye acridine orange in presence of calf thymus DNA in aqueous solution. Results revealed the strong fluorescence quenching of dye molecules due to silver nanoparticles as dye molecules adsorbed onto the surface of nanoparticles. DLS and zetapotential results are also consistent with the observed spectroscopic results. Acridine orange dye molecules also binds with DNA in the solution but there was no significant change in the peak position of AO emission. However, most interestingly after addition of Ag NPs in dye/DNA mixed solution silver nanopartilces strongly attached with DNA by expulsion

of dye molecules from DNA. The proposed study reveals many fundamental informations about the interactios of silver nanoparticles with biological macromolecule DNA in presence of a fluorescent probe and also contribute significant database in the field of biotechnology.

Chapter 8 describes the sensing of toxic heavy metal ion namely mercury (Hg^{2+}) ion using fluorescent molybdenum disulfide (MoS_2) nanoflakes both in the aqueous solution and intracellular medium. The bio-inspired MoS_2 nanoflakes were synthesized using sodium molybdate dihydrate and L-Cysteine as a rich source of sulfur (S) via hydrothermal method. The as-synthesized MoS_2 nanoflakes were characterized by the X-ray diffraction (XRD), field emission scanning electron microscope (FESEM), high-resolution transmission electron microscope (HRTEM), atomic force microscope (AFM), Raman scattering, UV-vis absorption, steady-state and time-resolved fluorescence emission techniques. XRD, FESEM and Raman results confirmed the formation of flower-like morphology of MoS_2 by the stacking of individual nanosheets. The time-resolved fluorescence emission spectroscopy (TCSPC) confirmed the fluorescence decay time of MoS_2 was ~2.97 ns. The as-synthesized fluorescent MoS_2 nanoflakes were successfully employed in the sensing of the Hg^{2+} ion by using the strong affinity of the Hg^{2+} ion towards the S atom in the MoS_2. This sensing method showed good sensitivity towards Hg^{2+} ion both in aqueous solution and cellular milieu. Also, this interaction was very much selective when compared with the other metal ions (Ca^{2+}, Cd^{2+}, Cu^{2+}, Mg^{2+}, Na^{+}, Ni^{2+}, Zn^{2+}, Al^{3+}, Fe^{2+} etc.) in the aqueous medium. This study further revealed the limit of detection (LOD) as ~0.09 nM for Hg^{2+} ion corresponding to the concentration of $HgCl_2$ in the aqueous medium. The cell viabikity of using as synthesized MoS_2 nanoflakes for detection of Hg^{2+} ion in the intracellular medium have been tested by MTT assay. Density functional theoretical (DFT) calculations based on the Quantum Espresso (QE) package reveals a correlation of electronic band structure with observed spectroscopic results towards the binding between Hg^{2+} and S atom of MoS_2.

Chapter 9 presents the **Overall conclusion of the present thesis and future plan of research**.

References

[1] R. P. Feynman, *J. Microelectromech. Syst.*, 1 (1992) 60–66.

[2] R. Nagarajan, Nanoparticles: Building Blocks for Nanotechnology, *ACS Symp. Ser.*, 996 (2008) 2–14.

[3] A. Moores, F. Goettmann, *New J. Chem.*, 30 (2006) 1121–1132.

[4] D. Li, Y. Dong, B. Li, Y. Wu, K. Wang, S. Zhang, *Analyst*, 140 (2015) 7672–7677.

[5] G. Paramasivam, N. Kayambua, A. M. Rabe, A. K. Sundramoorthy, A. Sundaramurthy, *Acta Biomater.*, 49 (2017) 45–65.

[6] L. L. Tan, M. Wei, L. Shang, Y. W. Yang, *Adv. Funct. Mater.* 31 (2020) 2007277.

[7] R. Das, S. S. Nath, D. Chakdar, G. Gope, R. Bhattacharjee, *J. Exp. Nanosci.*, 5 (4) (2010) 357–362.

[8] S. Thomas, S. K. Nair, E. M. A. Jamal, S. H. Al-Harthi, M. R. Varma, M. R. Anantharaman, *Nanotechnol.*, 19 (2008) 075710.

[9] K. E. Sapsford, L. Berti, I. L. Medintz, *Angew. Chem. Int. Ed.*, 45 (2006) 4562–4588.

[10] X. Liu, M. Atwater, J. Wang, Q. Huo, *Colloids Surf. B*, 58 (2007) 3–7.

[11] D. Paramelle, A. Sadovoy, S. Gorelik, P. Free, J. Hobley, D. G. Fernig, *Analyst*, 139 (2014) 4855–4861.

[12] V. Yadav, S. Roy, P. Singh, Z. Khan, A. Jaiswa, *Small*, 15 (2019) 1803706.

[13] S. Sundar, V. Ganesh, *Sci. Rep.*, 10 (2020) 15071.

[14] L. Malfatti, T. Kidchob, D. Aiello, R. Aiello, F. Testa, P. Innocenzi, *J. Phys. Chem. C*, 112 (2008) 16225–16230.

[15] M. Chakraborty, S. Paul, I. Mitra, M. Bardhan, M. Bose, A. Saha, T. Ganguly, *J. Photochem. Photobiol. B, Biol.*, 178 (2018) 355–366.

[16] D. Dinda, A. Gupta, B. K. Shaw, S. Sadhu, S. K. Saha, *ACS Appl. Mater. Interfaces*, 6 (13) (2014) 10722–10728.

[17] U. Chakraborty, T. Singha, R. R. Chianelli, C. Hansda, P. K. Paul, *J. Lumin.*, 187 (2017) 322–332.

[18] B. L. Li, M. I. Setyawati, L. Chen, J. Xie, K. Ariga, C. T. Lim, S. Garaj, D. T. Leong, *ACS Appl. Mater. Interfaces*, 9 (18) (2017) 15286–15296.

[19] V. Georgakilas, J. N. Tiwari, K. C. Kemp, J. A. Perman, A. B. Bourlinos, K. S. Kim, R. Zboril, *Chem. Rev.*, 116 (9) (2016) 5464–5519.

[20] D. H. Wang, D. G. Choi, K. J. Lee, J. H. Jeong, S. H. Jeon, O. O. Park, J. H. Park, *Org. Electron.*, 11 (2) (2010) 285–290.

[21] S. Medici, M. Peana, A. Pelucelli, M. A. Zoroddu, *Semin. Cancer Biol.*, 76 (2021) 17–26.

[22] I. Khan, K. Saeed, I. Khan, *Arab. J. Chem.*, 12 (7) (2019) 908–931.

[23] J. Yao, M. Yang, Y. Duan, *Chem. Rev.*, 114 (12) (2014) 6130–6178.

[24] K. Sztandera, M. Gorzkiewicz, B. Klajnert-Maculewicz, *Mol. Pharmaceutics*, 16 (1) (2019) 1–23.

[25] S. R. Kavitha, M. Umadevi, S. R. Janani, T. Balakrishnan, R. Ramanibai, *Spectrochim. Acta A Mol. Biomol. Spectrosc.*, 127 (2014) 115–121.

[26] K. Sahu, A. Ali, A. K. Kar, *ECS J. Solid State Sci. Technol.*, 11 (2022) 086003.

****

CHAPTER ~ 2

Theoretical Background

This chapter describes the brief information about some theoretical background and overview of the research topic related to the thesis work

CHAPTER~2

Theoretical Background

2.1. Introductory remark

Let's look about some theoretical overview behind the research work presented in this Ph.D. thesis. Various noble metal nanoparticles and metal-based 2-dimensional layered nanostructured materials have been synthesized and characterized by different morphological and spectroscopic techniques. The research work has been performed to study various photophysical processes of electronically excited organic dye molecules in the vicinity of metal nanoparticles. The dye-nanoparticles interactions have been utilized to design various sensing platforms for important biomolecules as well as also to understand various nano-bio interaction for future technological purposes. Also, the hydrothermally synthesized 2-D layered nanostructures such as Molybdenum disulfide is used in the sensing of heavy toxic metal ions both in aqueous solution and intra-cellular medium. Theoretical overview of various spectroscopic approach utilized for the research performed and presented in this thesis are discussed. Different terminologies which are being used during the explanation of the experimentally and theoretically obtained research results are briefly discussed in this chapter.

2.2. Theoretical background of light-matter interactions

Light is the most important and essential part of the nature for living beings on the earth. It is an electromagnetic radiation consisting of oscillating magnetic and electric fields [1]. The subject of light-matter interactions is of huge importance in the field of atomic physics and quantum optics, which is already gained significant interest at the frontiers of research. All the matters consist of atoms or molecules. The photophysical phenomena mainly occur due to the interaction of light with matter and plays an instrumental role in spectroscopy, laser technology, different sensing techniques, quantum information, photodiodes, solar cells, high energy particle detectors etc. In these real life application, light is considered as the plane

electromagnetic wave which extracted the quantum mechanical information of matter by means of direct interaction with the free or bound electrons of the matter [2]. The interactions between light and matter are fundamentally quantum electrodynamical (QED) in nature accompanied by the quantum transitions of atomic or molecular electrons resulting absorption, reflection, refraction, emission, scattering etc. of photons, the quanta of electromagnetic waves [3]. Paul Dirac in 1927 first formulated the theory of the electron-photon interactions which was reformulated as in the present forms by Enrico Fermi in 1932 [4, 5]. For simplification, it is sufficient to describe that the electromagnetic radiation consists of photons travel at the speed of light with wavelength much higher than the typical size of wave functions of electrons in the matter. Different photophysical and physicochemical reactions may take place when the matters are encountered with light photons [6, 7]. The photosynthesis in plants (also in few animals) is the most commonly known light induced physicochemical phenomenon in nature in which the energy of electromagnetic radiation is converted into its useful chemical forms which is very essential for living being. In specific, the strong coupling between photon of incident radiation and electron of matter allow to investigate photophysical and physicochemical reactions in details. However, atoms in the matter and photons of electromagnetic radiation are usually treated by fully quantum-mechanical descriptions pillared on the Schrodinger dynamics [8]. The light-matter interaction is schematically shown in Figure 2.1.

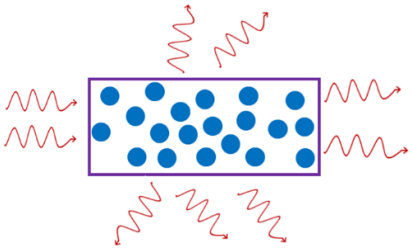

Figure 2.1. Schematic diagram represents the light matter interactions.

In the quantum mechanical model of light-matter interactions, both the energy of the atom and the electric field corresponding to the electromagnetic radiation considered as quantized [9]. Thus, photons are the quanta of electromagnetic field whereas, electrons are visualized as the quanta of atomic electric field. In general, atoms are considered as the positively charged nucleus surrounded by the cloud of electrons, as shown in Figure 2.2. In absence of electromagnetic wave, the centre of positive and negative charges coincide and there is no net dipole moment. However, a net dipole moment of $\vec{p} = q\vec{r}$ will be produced when the oscillating electric field of the incident

electromagnetic wave interacts with the electron cloud of the atom, where q is the charge, and $\vec{r}$ is the separation between displaced positive and negative charge centres [10]. According to the classical theory of electromagnetism, this dipole configuration has an energy of $U = -\vec{p}.\vec{E}$, where $\vec{E}$ is the oscillating electric field corresponding to the electromagnetic wave.

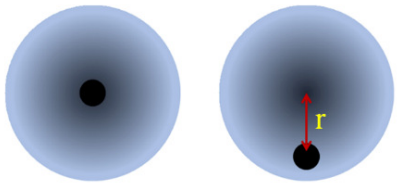

Figure 2.2. Schematic for the dipole moment of atom produce by the light-matter interaction.

Quantum mechanically, light-matter interaction, as described above, may be described by the simple interaction Hamiltonian H_I, such that, $H_I = -\hat{p}.\vec{E}(\hat{r},t)$, where, $\hat{p}$, $\hat{r}$, and t are the momentum operator, position vector operator and time respectively [11]. H_I may be considered as the perturbation to the actual Hamiltonian (H_0) of the actual atomic system [11]. The energy eigenvalue of the unperturbed atomic system may be given by the time-independent Schrodinger equation (eqn.) (2.1) [11],

$$H_0|n\rangle = E_0|n\rangle \dots\dots\dots\dots\dots\dots\dots (2.1)$$

where, E_0 and $|n\rangle$ are the energy eigenvalue and eigenstate corresponding to the unperturbed Hamiltonian H_0. The energy eigenvalue corresponding to the perturbed system can be written by the time-dependent Schrodinger eqn. (2.2) [12]

$$(H_0 + H_I)|\psi(t)\rangle = i\hbar\frac{\partial}{\partial t}|\psi(t)\rangle \dots\dots\dots\dots\dots\dots (2.2)$$

where, $|\psi(t)\rangle$ is the eigenstate corresponding to the perturbed atomic system which can be written in terms of the time-dependent expansion coefficient $c_n(t)$,

$$|\psi(t)\rangle = \sum_n c_n(t)e^{-iE_nt/\hbar}|n\rangle \dots\dots\dots\dots\dots\dots\dots\dots (2.3)$$

By substituting eqn. (2.3) in to eqn. (2.2) and taking inner product with another eigenstate $|k\rangle$, we may found,

$$i\hbar\dot{c}_k = \sum_n c_n(t)e^{-iE_{nk}t/\hbar}\langle k|H_I|n\rangle \dots\dots\dots\dots\dots\dots (2.4)$$

where, $\langle k|H_I|n\rangle$ is the matrix elements corresponding to the interaction Hamiltonian and $E_{nk} = E_n - E_k$.

Let us consider that, at time $t = 0$, the atomic system is in the ground state, i.e., $|1\rangle$, then, from eqn. (2.4) we may found that $c_1(0) = 1$. This is corresponds to the fact

that the probability of finding the atom in the ground state at $t = 0$ is unity. Also, for weak perturbation in case of light-matter interaction, the probability of finding the particle in the eigenstate $|k\rangle$ is very low as for very weak perturbation, the system has highest probability to remain in the ground state [13]. By using these two assumptions, we may neglect the interaction of $|k\rangle$ with any other states except $|1\rangle$. So, the eqn. (2.4) becomes,

$$i\hbar\dot{c}_k = e^{-i\omega_{1k}t/\hbar}\langle k|H_I|1\rangle \dots\dots (2.5)$$

where, $\omega_{1k} = E_{1k}/\hbar$.

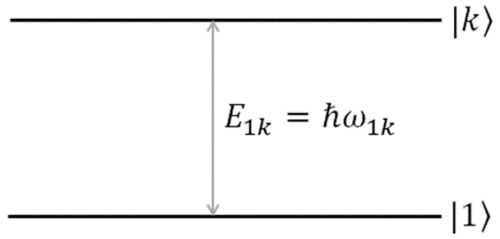

Figure 2.3. Schematic of simple two-level energy system of atom.

Thus, by the above assumptions, the atom now becomes a two level energy system or simply two state energy system as shown in Figure 2.3. When electromagnetic wave interacts with atoms or molecules of the matter, electrons of the atoms or molecules go to the higher energy state from their ground state. As the excited electronic state is less stable than ground state, the excited electrons immediately return to the ground state or lower energy state by emitting absorbed energy. This emitted energy may be into two forms: radiative and nonradiative emission [14]. The radiative emission corresponding to the emission of light, while in the nonradiative emission, energy of excitation will be lost in the form of heat. There are several processes such as absorption, emission, internal conversion, delayed emission etc. may takes place in the matter during the photophysical and physicochemical process induced by the light [14]. The transitions of excited electrons of atom or molecules between different electronic energy levels after interacting with the oscillating electric field of the incident electromagnetic wave is shown in Figure 2.4. The variation of periodic potential energy of the atomic system with the interatomic distance is shown in Figure 2.5. Atoms associated with this periodic potential behaves like an anharmonic oscillators [15]. As shown in Figure 2.5, each electronic energy level

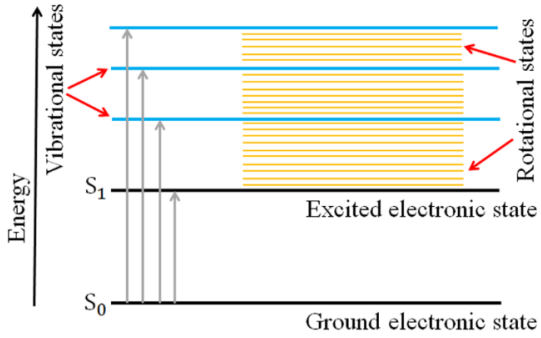

Figure 2.4. Schematic for the electronic, rotational, and vibrational energy levels.

consists of several vibrational levels each of which again comprises several rotational energy levels. The difference in energy between two consecutive levels i.e., the energy gap of vibrational levels is greater than that of the rotational levels. Again, the energy gap of electronic level is much higher than that of the vibrational levels [16]. The order of the energy gap may be written as, $\Delta E_e \gg \Delta E_{vib} > \Delta E_{rot}$ where ΔE_e , ΔE_{vib} and ΔE_{rot} are the electronic, vibrational and rotation energy gap respectively.

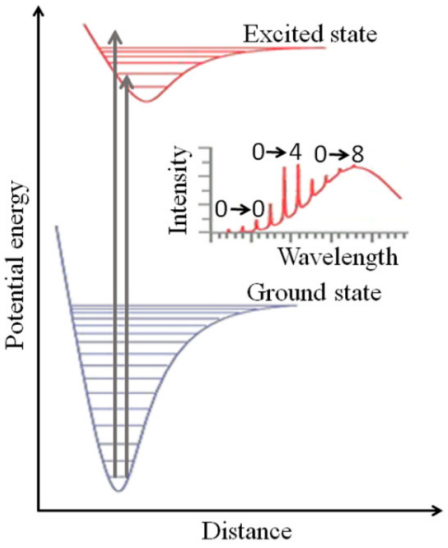

Figure 2.5. Variation of periodic potential energy with intermolecular distance and the transition between ground vibrational energy level of the ground electronic state to the excited vibrational energy level of excited electronic energy state.

Generally, the transitions between rotational and vibrational energy levels are induced by the microwave and infrared radiation of the electromagnetic wave respectively [16]. But, the transitions involved in the electronic energy levels are induced by the visible and ultraviolet part of the electromagnetic wave [16]. Thus, a particular electronic transition corresponding to the absorption of ultraviolet and visible radiation of light contains huge number of vibrational and rotational transitions as shown in Figure 2.5. The chemical composition and structure of a molecule generally determines its electronic energy levels. The electronic spectroscopy also known as the ultraviolet-visible spectroscopy (UV-vis spectroscopy) which is mainly due to the transition of electrons from lower energy level to higher energy level, gives the identity of the molecules precisely. Different spectroscopic techniques used in the field of research are briefly described in Table 2.1.

2.3. Ultraviolet-visible light absorption in polyatomic molecules

Ultraviolet-visible (UV-vis) or electronic absorption spectroscopy (200-800 nm) is often used in the quantitative analysis of matters [17]. When atoms or molecules are exposed to the electromagnetic radiation, they can absorb exact amount of energy

corresponding to the energy gap between the two particular orbitals and go to the higher energy states as shown in Figure 2.5. Due to this, intensity of the incident light (I_0) is attenuated after interacting with the matter. This attenuated intensity (I(x)) emerged from a linearly absorbing medium of optical path length x is shown in Figure 2.6 and is given by the Beer-Lambert's law (eqn. (2.6)) [18],

$$I(x) = I_0 e^{-\varepsilon(\lambda)xc} \ldots\ldots (2.6)$$

where c and $\varepsilon(\lambda)$ are the concentration of the linearly absorbing medium and molar extinction coefficient at a particular wavelength λ of the incident light respectively. The absorbance ($A(\lambda)$) (eqn. (2.7)) and transmittance ($T(\lambda)$) (eqn. (2.8)) of the linearly absorbing medium are defined as [18],

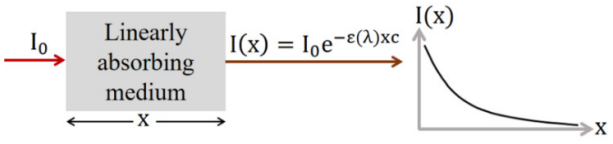

Figure 2.6. Process of absorption of photon in a linearly absorbing medium.

$$A(\lambda) = \log_{10}\left(\frac{I_0}{I(x)}\right) = \varepsilon(\lambda)xc \ldots\ldots\ldots\ldots\ldots\ldots\ldots\ldots\ldots\ldots\ldots (2.7)$$

and,
$$T(\lambda) = \left(\frac{I(x)}{I_0}\right) \ldots\ldots\ldots\ldots\ldots\ldots\ldots\ldots\ldots\ldots\ldots\ldots (2.8)$$

Table 2.1. Different spectroscopies used in the field of research.

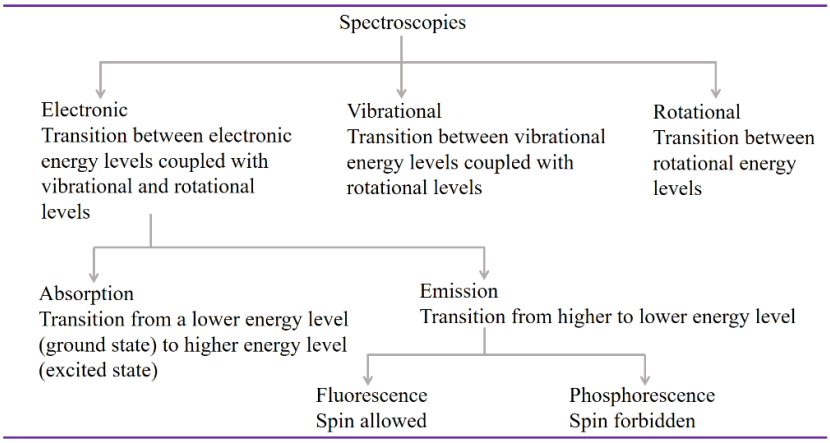

Typical absorption spectrum of linearly absorbing molecules is shown in Figure 2.7 in terms of both absorbance (A) and transmittance (T). λ_0 is the wavelength of incident light corresponding to the maximum absorbance of the incident electromagnetic radiation. In the absorbance vs wavelength curve, the continuous radiation from the source shows a peak at λ_0 whereas in transmittance vs wavelength curve, it shows dip

at λ_0. In molecular system, the characteristic feature such as shape and the position absorption bands strongly depend on the degree of distribution of electrons within the molecule [18]. Electrons are primarily localized in the chromophore of the organic materials. So, the absorption spectrum can be used to identify the molecular light absorbing units i.e., chromophores.

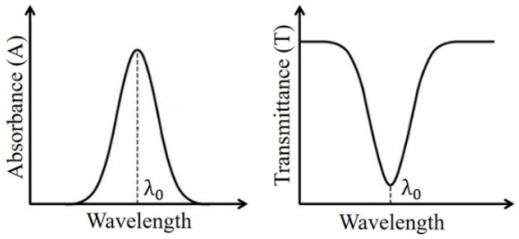

Figure 2.7. Absorption spectrum in absorbance and transmittance form.

There are different types of transitions of molecular electrons observed in several organic molecules [19]. These transitions are shown in Figure 2.8. Generally, the energy increases for different transitions in the sequence as $n \rightarrow \pi^*$, $\pi \rightarrow \pi^*$ and $\sigma \rightarrow \sigma^*$. A complex absorption spectrum consist of many absorption bands can be created by the complex organic molecule due to the various spectroscopic transitions involved in it. The frequency of the emitted spectral band position by the molecules depends on the energy gap between initial and final electronic states of after excitation. These transitions generally require multiple bonds, and occur in alkenes, alkynes, and aromatic compounds.

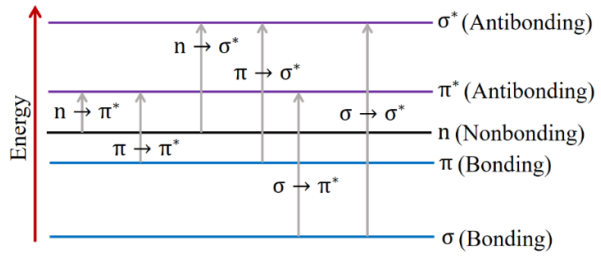

Figure 2.8. Schematic for the different types of electronic transitions involved in the molecular orbitals.

2.4. Radiative transitions

The emission of light from an electronically excited state of an atom or molecule is known as luminescence [20]. After absorbing energy exactly equal to the energy gap between two discrete energy levels of an atom or molecule, electron jumps to a higher energy state and stay there for a very short period of time and finally the electron returns to the lower possible energy levels by emitting its excited energy. In case of atoms, these energy levels have been constructed by following the charge distribution on the nucleus.

Whereas, for molecules, it depends on both charge distribution and arrangement of nuclei. Thus, in molecules, the vibrational de-excitation also known as vibrational relaxation occurs in the following steps: first electron absorbs photon and go to vibrational and rotational levels of electronic state with higher energy, then, loses its energy via some nonradiative process and comes back to lowest vibrational and rotational level of lower electronic energy state [21]. Finally, excited electron emits energy in terms of light photon and returns to the ground state via radiative transition. This phenomenon, in which light emission occurs from an excited atom or molecule is termed as photoluminescence. Depending upon the nature of excited state, photoluminescence is generally classified into two categories i.e., fluorescence and phosphorescence. The photophysical pathways for absorption and emission of light by molecules are described by the well-known Jablonski diagram [22] as shown in Figure 2.9. The electronic singlet states are labelled as S_0, S_1, S_2 etc. corresponding to the ground, first, second excited singlet states respectively. The triplet electronic states are denoted by T_1, T_2 etc. for first and second excited states respectively. Various vibrational energy levels associated with each electronic energy states are labelled by 0, 1, 2…etc. The transitions between different energy levels are depicted by the vertical lines as shown in the Jablonski diagram (Figure 2.9). As, the energy absorbed by the atom or molecule occurred in discrete quanta, the absorption spectrum shows a series of absorbance bands. In the simple Jablonski diagram (Figure 2.9), the rotational levels associated with different vibrational levels are neglected to avoid many of the possible absorption bands due to rotational transitions which are difficult to resolve with UV-vis absorption spectroscopy.

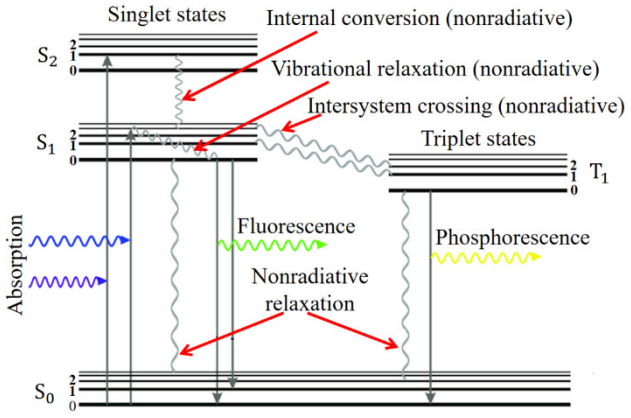

Figure 2.9. Jablonski diagram showing various pathways of absorption and emission of energy of a molecule.

2.4.1. Fluorescence:

In 1560, Bernardino de Sahagún and in 1565, Nicolás Monardes first observed and described the fluorescence in the infusion of *lignum nephriticum*, which was collected from the wood of Pterocarpusindicus and Eysenhardtiapolystachya [23,24]. The chemical component which was responsible for the fluorescence was the oxidation product also known as matlaline, which was the flavonoids components of that wood [23]. Edward D. Clarke in 1819 and René J. Haüy in 1822 described fluorescence in fluorites [25]. In 1833 and 1845, David Brewster and John Herschel explained the fluorescence phenomenon for chlorophyll and quinine respectively [26]. George G. Stokes in 1852 explained the 'refragibility' i.e., wavelength change phenomenon by uranium and fluorspar glass which were able to change the violet light into blue light [26]. He named this phenomenon as "fluorescence". The name "fluorescence" was derived from the europium containing mineral calcium difluoride, well known as fluorite, which mainly emits blue colour light.

Atoms or molecules are promoted to the higher excited electronic states (S_1, S_2, S_3 etc.) after photoexcitation or any other external perturbations. Basically this excitation can result the electrons in atoms or molecules to reach any of the vibrational levels associated with every electronic states and is typically occurs very fast ($\sim 10^{-15}$) after photoexcitation [27]. Then the excited electron quickly loses the excess vibrational energy (due to collision or interaction with incident photons) through vibrational relaxation and arrived at the ground vibrational level of the excited electronic state. During their return to the ground state, the loss of excited state energy of the electron may occur through different radiative and nonradiative transitions which are already schematically shown in the Jablonski diagram (Figure 2.9.). When the electron undergoes transition from the ground vibrational level of the excited singlet state to any of the vibrational levels of the ground electronic state, the remaining excited energy of electron is emitted in the form of light. This emission of light due to electronic transition is known as fluorescence. However, this return of excited electron to the ground state is spin allowed [28]. The rate of fluorescence emission is in the order of $\sim 10^8\ s^{-1}$, such that the fluorescence lifetime (τ_f), which is the average time of atom or molecule for staying in the excited electronic state and subsequent return to their ground state, is nearly of the order of ~ 10 ns [29]. The intrinsic character of a fluorescent molecule

may be represented by a parameter called quantum efficiency or fluorescence quantum yield (Φ_f) and is given by eqn. (2.9) [29],

$$\Phi_f = n_f/n_a \ldots\ldots\ldots\ldots\ldots\ldots\ldots\ldots\ldots\ldots\ldots\ldots (2.9)$$

where n_a and n_f are the number of absorbed and emitted photon per unit time during the process of fluorescence emission respectively. The minimum and maximum values of Φ_f are zero and one respectively. If the fluorescence emission takes place for all the excited electrons simultaneously after absorption of light, then the quantum efficiency of the material will be maximum. For any other process, other than radiative process, the value of Φ_f will be very less or may even be zero. However, due to vibrational relaxation the excited electrons reduce some of its excited sate energy before returning to ground sate. This implies that the energy of the emitted light is always less than that of absorbed light. Although, ideally, the absorption spectrum or more precisely, the fluorescence excitation spectrum and the emission spectrum of a particular material are mirror-image to each other, but, experimentally, always a shift is observed between fluorescence excitation and emission spectra [30] and is referred to as the stokes shift as shown in Figure 2.10. The radiative rate constant (k_f) of a fluorophore in the fluorescence emission is related to its average lifetime (τ_f) by the eqn. (2.10) [29]

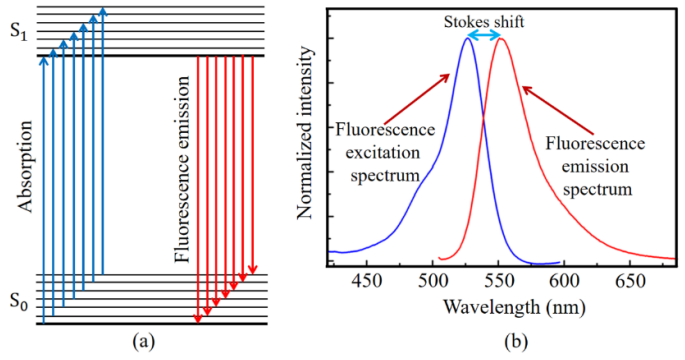

Figure 2.10. (a) Schematic represents for the vertical transition corresponding to the absorption and fluorescence emission. (b) Fluorescence excitation and emission spectra of organic fluorophore.

$$k_f = 1/\tau_f \ldots\ldots\ldots\ldots\ldots\ldots\ldots\ldots\ldots\ldots\ldots\ldots (2.10)$$

But, various nonradiative decay processes affected the average lifetime of the fluorophore. So, the overall fluorescence lifetime (τ_F) of the fluorophore in terms of radiative decay constants (k_f) and nonradiative decay constant (k_F) is given by the eqn. (2.11) [29]

$$\tau_F = 1/(k_f + k_F) \ldots\ldots\ldots\ldots\ldots\ldots\ldots\ldots\ldots (2.11)$$

The typical fluorescence emission spectrum is displayed in Figure 2.10. A particular photon emitted in the process of fluorescence emission, has single wavelength. Due to this, the intensity vs wavelength plot looks like a single vertical line situated on that particular wavelength of the emitted photon. But experimentally, the fluorescence emission spectrum looks like Gaussian distribution or Lorentzian distribution around that line [31] and is known as spectral line broadening. The broad spectrum pattern is generally produced by the overlapping of closely spaced spectral lines. There are many general useful rules which govern the process of fluorescence emission as given bellow:

- **Kasha's rule:** According to this rule, the quantum yield of fluorescence emission is independent of the wavelength of excitation [32]. This is due to the fact that, the molecular excitation usually deactivates to the lowest vibrational level of the excited electronic state prior to the emission of light as fluorescence.
- **Mirror image rule:** According to this rule, for many of the fluorophores, the optical absorption spectrum (or excitation spectrum) is a mirror image of the fluorescence emission spectrum [33]. This rule is also related with the Franck–Condon principle which states that electronic transitions between different energy levels of a molecule are vertical as represented by vertical line in Jablonski diagram, such that, the change in energy is occurred without changing the distance of nucleus.
- **Stokes shift:** According to Stokes, emitted fluorescence radiation has lower energy and a longer wavelength compared to that of the absorbed radiation [34]. The shift or difference in wavelengths of absorption and emission maxima is known as Stokes shift. The Stokes shift occurs due to the loss in energy of absorbed photon compared to that for emission. In general, the amount of Stokes shift depends on the nature of fluorophores and their microenvironments. The other reason behind the Stokes shift are the nonradiative decay or loss of the excited energy of atoms or molecules through the vibrational levels of the excited electronic state and the emission of light due to the electronic transition from the lowest vibrational level of excited state and the higher vibrational level of the ground electronic state.

2.4.2. Phosphorescence:

Phosphorescence is another type of light emission when excited electron undergoes a transition from triplet states (T_1, T_2 etc.) to the ground state (S_o) [35]. The

orientation of spin of an electron is conserved during the production of excited state via transitions from lower to higher energy orbitals. Electrons are arranged themselves in paired for molecules having even number of electrons. During the excitation, an electron does not disturb this parity. According to the Quantum Theory [36], a molecule can exist in three different forms of very slightly but indistinguishable energy. The molecule is then said to exist in a triplet energy state in which the electron has different spin symmetry than that in the ground state. The indirect transition from singlet to triplet electronic state takes place when the energy of lowest vibrational level of excited singlet state is equal to the energy of highest vibrational level of the triplet state. This type of indirect transition from singlet to triplet states in known as Intersystem Crossing (IC) and is shown in the Jablonski diagram (Figure 2.9). Theoretically, direct transition from the ground electronic state to a triplet state is forbidden for a molecule even with large number of electrons. Also, the reverse transition from triplet state to the ground state is less probable and the rate of emission is very slow (from 1000 to $100\ s^{-1}$) [37]. Thus, excited phosphors slowly return to the ground electronic state after excitation takes place and the corresponding emission lasts for much large duration compared to fluorescence since T_1 to S_o transition is forbidden due to spin-orbit interactions between singlet and triplet states. The typical lifetimes of the phosphorescence are in the order of milliseconds to second [38]. In the aqueous medium at room temperature, due to very fast deactivation excited energy of electron to lower energy states when compared with the time scale of emission process, the phosphorescence is usually not observed in solution [39]. The transition metal–ligand complexes (MLCs) containing one or more metal and organic ligands, shows phosphorescence from the transitions singlet to triplet and again singlet states. MLCs have phosphorescence lifetimes of the order of hundred nanoseconds to few microseconds which is visible by necked eyes [40].

2.5. Non-radiative transitions

If any electronic transition between different energy levels occurs without emitting light photon or radiation, then this type of transition is called radiationless or non-radiative transition. Also, the intensity of emission is less strong than the corresponding absorption. The weak intensity of the fluorescence emission of most of the materials is observed because of the dissipation of the excited state energy through various non-radiative channels such as dissipated as thermal energy in the surrounding environment. Also, the non-radiative transition may occur when the excited molecule

transfers all of its energy to neighbouring molecules or species while returning to their ground state. In general, the non-radiative transitions take place through different pathways such as internal conversion, vibrational relaxation, intersystem crossing, and non-radiative relaxation etc. [41] as shown in the Jablonski diagram (Figure 2.9).

2.5.1. Internal conversion

In this process, the excited electron goes to the vibrational level of electronic state of lower energy from the vibrational states of a higher electronic excited state without radiating light photon [42]. During internal conversion, excess energy of the electron is emitted as the thermal energy in the surrounding medium. This type of transition generally happens between the states having same spin multiplicity i.e., singlet to singlet or triplet to triplet states. The typical rate of transition of internal conversion is ~10^{12} s^{-1} which is faster than that of the rate of fluorescence emission (~10^{9} s^{-1}) [43]. Due to presence of higher number of vibrational transformations with increase in vibrational levels in the electronic states, more flexible molecular structure shows greater probability of internal conversion. Therefore, more rigid molecule exhibits comparatively higher fluorescence emission.

2.5.2. Vibrational relaxation

Vibrational relaxation occurs when excited electron goes from a higher vibrational level to the lowest vibrational level of the same excited electronic state [44]. The vibrational relaxation generally takes place by the photoexcited molecule before fluorescence emission.

2.5.3. Intersystem crossing

This type of non-radiative electronic transition occurs between two vibrational levels having nearly same energy but with different spin multiplicity (i.e., singlet, triplet) [35]. After excitation, electron goes from singlet to triplet energy state by flipping its spin via non-radiative transition. The probability of intersystem crossing is very less even in the high fluorescent material as singlet to triplet transitions are generally spin forbidden. However, the probability of intersystem crossing increases for the molecules having heavier atom in which large spin-orbit coupling exists. The average rate of intersystem crossing is nearly ~10^{12} s^{-1} [45], which is comparable with

the internal conversion. After intersystem crossing, the electron goes to the lowest vibrational level in the same triplet state followed by the internal conversion.

2.5.4. Non-radiative relaxation

In non-radiative relaxation, molecule can directly make transition from zero vibrational level of excited state to the ground state [46]. When the energy gap between the lower vibrational level of excited electronic state and upper vibrational level of the lower electronic state, the electron may tunnel from upper level to the lower level. The probability of tunnelling from upper level to the lower level is directly proportional to the energy difference between the corresponding vibrational levels. The non-radiative relaxation generally occurs between singlet-singlet and triplet-triplet states.

2.6. Molecular aggregation

Aggregation of molecules is a multi-molecular phenomenon which is affected by different parameters including, pH of solution, molar concentration, temperature etc. [47]. Various organic and biological compounds can associate to form some ordered structures (dimmer, trimer, etc.). In general, the π-conjugated organic molecules strongly take part in the molecular aggregation process via hydrophobic-hydrophilic, solute-solvent and intermolecular hydrogen bonding and noncovalent intermolecular interactions [48]. The photophysical and physiochemical properties due to molecular staking of π-conjugated molecules differs when compared to that of isolated molecule. In 1963, Kasha and his co-workers first elucidated the conception of molecular exciton coupling theory [32]. According to this theory, the absorption and emission properties of the molecular aggregates are treated as the reflection of interactions between molecular transition dipoles moments. In the exciton coupling model, the organic dye molecules are treated as "disk-like" or "card-like" flat structure and the aggregated structure of linear molecule can be visualized by the card packing model based on the coulomb coupling in between the neighbouring monomer units. There are commonly

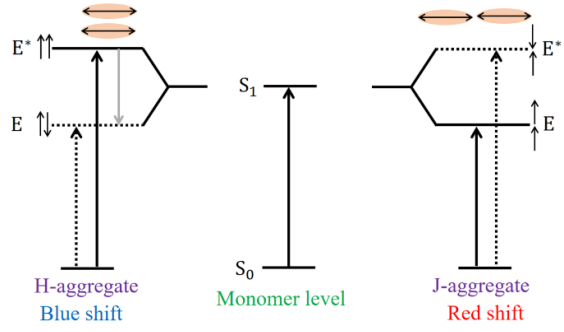

Figure 2.11. Schematics for the H-type and J-type molecular aggregates.

two types of molecular aggregates such as, H-type and J-type are observed. The molecular mechanism involved in the formation of these aggregates of organic dyes is schematically shown in Figure 2.11.

2.6.1. H-type aggregates

In H-type aggregates, the card-like planer dye molecules are coupled with each other in parallel or sandwich one upon the other [49]. For these molecular aggregates, both the UV-vis absorption and fluorescence emission bands are hypsochromically shifted (due to this, it is called H-type) or blue shifted compared to the monomeric unit. Also, in the excitonic band which is the highest energy electronic state, the dipole oscillator utilized all the molecular excitonic energy [49]. In most of cases H-type molecular aggregates do not emit fluorescence when compared to that due to monomeric unit as the fluorescence emission proceeds from the lowest excited electronic singlet state (S_1).

2.6.2. J-type aggregates

In J-type aggregates, molecules are arranged in head-to-tail pattern such that narrow molecular absorption band is obtained in the UV-vis absorption associated with stronger fluorescence emission at longer wavelength (bathochromic shift or red shift), compared to their monomer unit [49]. This type of molecular association was first reported by E. Jelley and named after Jelley [50]. In J-aggregates, the Coulomb coupling between aggregated molecules is negative. Also, the oscillator strengths are concentrated in the lower most energy of exciton and the fluorescence emission originated due to J-type aggregates are not generally suppressed [49].

2.7. Resonance energy transfer between organic fluorophore and metal nanoparticles

An excited molecule (donor) can donate all of its excitation energy to other molecules or metal nanoparticles (NPs) in a close proximity in the surrounding environment via fluorescence resonance energy transfer (FRET) [51]. FRET is a non-radiative process where an excited donor molecule can transfer its energy to a nearby acceptor molecule. The main pre-requisite for FRET to occur is the sufficient spectral overlap of the fluorescence emission of the donor and the absorption spectrum of the

acceptor, which is schematically shown in Figure 2.12. This type of energy transfer involves long range dipole-dipole interactions between excited donor and acceptor moieties without emitting photon [51]. In general, the name FRET is sometimes replaced by the resonance energy transfer (RET) as no photon is emitted in the energy transfer process [52]. The rate of energy transfer depends on various factors such as extend of spectral overlap between fluorescence emission spectrum of donor and absorption spectrum of the acceptor, the fluorescence quantum yield of the donor, the relative orientation of transition dipole moments of donor and acceptor and the distance in between donor and acceptor moieties in a medium [51]. The energy transfer efficiency (E_T) between a particular pair of donor and acceptor (donor-acceptor pair are separated by a fixed distance) is determined by the quenching of fluorescence emission of donor due to interaction with acceptor and is given by the eqn. (2.12) [51]

$$E_T = 1 - F_{DA}/F_D \dots\dots\dots\dots (2.12)$$

where F_D and F_{DA} are the fluorescence emission of donor in absence and presence of acceptor respectively. The value of E_T is also determined with help of eqn. (2.13) using the fluorescence lifetime data of donor [51] under the same required conditions as stated earlier,

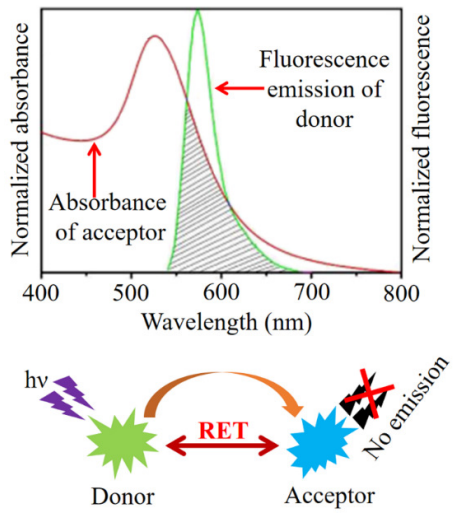

Figure 2.12. Schematic represents the resonance energy transfer (RET).

$$E_T = 1 - \tau_{DA}/\tau_D \dots\dots\dots\dots\dots\dots\dots\dots\dots (2.13)$$

where τ_D and τ_{DA} are the fluorescence lifetime of donor in absence and presence of acceptor respectively.

The fluorescence quenching of fluorophore are mainly two types, one is static quenching and another one is dynamic or collisional quenching [53]. In static quenching, donor and acceptor are at a fixed distance. This situation may occur in case whether the donor is directly adsorbed on the surface of acceptor. Donor-acceptor ground state complex is also formed in the static quenching. In case of dynamic quenching, fluorophore and quencher are in relative motion and continuously collides with each other. Quenching may also occur by a variety of trivial mechanism other than

static and dynamic methods. A fluorophore itself can attenuate its excited state energy and goes to the ground state after the removal of the incident radiation.

The quenching of fluorescence emission intensity of a fluorophore is described by the well-known Stern-Volmer relation (eqn. (2.14)) [53] as describe bellow,

$$\frac{F_D}{F_{DA}} = 1 + K_{SV}[Q] = 1 + K_q\tau_D[Q] \dots\dots\dots\dots\dots\dots\dots\dots (2.14)$$

where F_D and F_{DA} are the steady-state fluorescence emission intensity of donor in absence and presence of the acceptor. K_{SV} is referred to as the Stern-Volmer quenching constant which corresponds to the sensitivity of energy transfer from excited fluorophore to the quencher. K_q,τ_D and [Q] are the bimolecular quenching constant, and fluorescence lifetime of donor in absence of quencher and the concentration of quencher molecules respectively. A straight line Stern-Volmer plot (F_D/F_{DA} vs. [Q] plot) indicates either pure static quenching or pure dynamic quenching. Any deviation of the plot from straight line may correspond to the occurrence of both static and dynamic quenching of fluorescence of the fluorophore.

2.8. Infrared spectroscopy

Infrared spectroscopy belongs to a class of vibrational spectroscopy, which recognizes transition between different vibrational levels without electronic transition after excitation with infrared or near infrared light [54]. Also, the vibrational spectrum is very sensitive to the structure and molecular geometry. It provides many fundamental information including bond angle and bond length of the functional groups of a molecule. Molecular vibrations are two types, one is stretching vibrations, and another one is bending vibrations. In the stretching vibrations, molecule changes its bond lengths whereas in the bending vibrations, molecule changes its bond angles. Again, the stretching vibrations are of types, symmetric stretching and asymmetric stretching. In the symmetric stretching, bonds of the molecule vibrate in plane or out of plane direction with respect to the original molecular plane of vibration. In the asymmetric stretching, few bonds become shorter and few bonds become longer simultaneously. In the bending vibrations of a molecule, the change of angle between two neighbouring bonds occur. Bending vibrations are of four types, such as rocking, scissoring, wagging, and twisting.

2.9. Quantum-chemical calculations

Quantum-chemical computational calculations are the interlinked branch of both physics and chemistry [55] for organic and inorganic compounds. It mainly utilizes the high speed super computer incorporated with efficient computer programming based on theoretical chemistry models to solve various complicated physical and physicochemical problems. The theories behind the computational calculation have been refined and evolved gradually. Now, it is very efficient to explore variety of important ground and excited state molecular properties such as optimized geometry, various molecular orbitals namely highest occupied molecular orbital (HOMO) and lowest unoccupied molecular orbital (LUMO), equilibrium state between molecules, and energy corresponding to a particular reaction in many complex molecular systems. In the mathematical models, behind the chemical-computation, large number of coupled equations are solved simultaneously via iteration method [56]. In this convergence technique, iterations continue to run until a new equivalent outputs results are obtained as in the previous one by using particular set of mathematical and physical approximations. To obtained optimized geometry, molecular orbitals and corresponding energies different approximation methods have been marched with the programme algorithm and applied to the atomic orbitals with the help of well-defined basis set. The selection of theoretical model strongly depends on the dimension (i.e., number of atoms and bonds in the molecules), environment of the system and on the extent of approximation. The computational study generally complement various scientific and fundamental information obtained in the chemical experiments. Also, in some cases, it predicts hitherto chemical phenomena which are usually difficult to observe experimentally. In general, the quantum-chemical computational methods are mainly four types such as ab initio, semi-empirical, density functional, and molecular mechanics methods [57]. Among the various methods density functional theory is systematically used in the research presented in this thesis and is briefly discussed here.

2.9.1. Density functional theory (DFT)

In DFT method, calculations are performed based on the total electron density designated by $\rho(x, y, z)$, instead of wave function of the electrons as used in the Hartree-Fock method [57]. In DFT, the total electron density is the basis of whole methods of studying atoms and molecules. The results obtained in DFT method are

comparable with the ab initio method, but DFT method takes lower CPU time. In DFT calculation, there is an approximate Hamiltonian for the total electron density from which ground and excited state properties and detail potential energy surfaces are determined for the molecules [58]. Kohn and Sham formulated the presently used DFT method, where exchange correlation functional is used for any unknown energy configuration. According to the first Hohenberg-Kohn theorem, "any ground state property of a molecule can be represented by the ground state electron density functional" [57]. The second Hohenberg-Kohn theorem tells that "any trial electron density function will give an energy higher than (or equal to, if it is exactly the true electron density function) the true electronic ground state energy". There are mainly three methods used in the DFT calculation, which are B3LYP, PW91 and VWN.

- **B3LYP:** It includes Becke-3-parameters (B3), Lee–Yang–Parr (LYP) functional. It is the most popular method in the DFT calculation. B3LYP is called as a hybrid method, because it includes corrections for gradient and exchange correlations.
- **PW91:** It is a gradient-corrected method.
- **VWN:** The calculation performed in this method is based on local density approximation.

2.9.2. Molecular mechanics (MM)

In many cases, very large molecular systems are modelled using classical expression of energy of the harmonic oscillator by avoiding quantum mechanical calculations entirely [59]. In the MM simulations, atoms in the molecule are considered as spheres and bonds as springs. In the energy calculations, different algebraic equations are considered instead of electron density and wave function. The constants involved in the algebraic equations are generally obtained from the experimental data or other relevant calculations. The MM simulation is very simple computation, so that, one doesn't need complicated software of suit. Different types of MM simulations are given bellow.

- **Universal force field (UFF):** Generally, UFF method is used in Avogadro to explore different molecular properties of inorganic and organic compounds.
- **Merk molecular force field (MMFF):** MMFF is another important method, which is mainly used for some organic systems.

2.10. Binding constant and number of binding sites of metal-organic nanoassembles

The understanding of the formation of a complex between fluorophore with another molecules or some metal nanoparticles is of prime importance both for fundamental and technological aspects in various fluorometric measurements. The adsorption of the fluorophore on the surface of the metal NPs alter the different fluorescence properties such as fluorescence intensity, lifetime etc. The steady-state fluorescence emission spectra of the fluorophore of interest in presence of different concentrations of the quencher can be used to evaluate the binding constant between the fluorophore and the quencher (metal NPs) and the number of available binding sites in the fluorophore environment with help of the following eqn. (2.15) [60]

$$\mathrm{Log}\left\{\frac{F_D - F_{DA}}{F_{DA}}\right\} = \mathrm{Log}K_b + n_b \mathrm{Log}[Q] \dots\dots\dots\dots\dots\dots\dots (2.15)$$

where F_D and F_{DA} are the fluorescence emission intensity of the fluorophore (donor) in absence and presence of quencher (acceptor) respectively. K_b and n_b are the binding constant and number of binding sites respectively. [Q] is the concentration of the quencher. The values of K_b and n_b can be determined from the intercept and slope of $\mathrm{Log}\{(F_D - F_{DA})/F_{DA}\}$ vs. [Q] plot. If the value of K_b and n_b increase with increase in the value of quencher concentration, then fluorescence quenching will be dynamical in nature. This is because in the dynamical quenching, the rate of collision increases with increase in concentration of the quencher. But if K_b and $n_b$decrease with increase in quencher concentration, then quenching may be static in nature and there is a possibility of the formation of ground state complex between donor-acceptor pair. The Gibbs free energy change in the interaction can be determined by using the value of K_b from the following relationship (eqn. (2.16)) [61]

$$\Delta G = -RT\ln K_b \dots\dots\dots\dots\dots\dots\dots\dots (2.16)$$

where R and T are the universal gas constant and temperature respectively. The negative value of ΔG interaction between fluorophore and quencher is spontaneous.

References

[1] D. J. Panagopoulos, O. Johansson, G. L. Carlo, *Sci. Rep.*, 5 (2015) 14914.

[2] N. Rivera, I. Kaminer, *Nat. Rev. Phys.*, 2 (2020) 538–561.

[3] S. Scheel, S. Y. Buhmann, *Acta. Phys. Slovaca.*, 58 (5) (2008) 675.

[4] O. Keller, *Prog. Opt.*, 50 (2007) 51–95.

[5] S. Adams, Frontiers: Twentieth Century Physics. *CRC Press*, (1999).

[6] E. W. Helbling, H. Zagarese, UV Effects in Aquatic Organisms and Ecosystems. *Royal Society of Chemistry*, (2007).

[7] Z. Zhang, J. T. Yates, Jr, *Chem. Rev.*, 112 (10) (2012) 5520–5551.

[8] M. Pykal, P. Jurecka, F. Karlicky, M. Otyepka, *Phys. Chem. Chem. Phys.*, 18 (2016) 6351.

[9] M. Ruggenthaler, N. Tancogne-Dejean, J. Flick, et al., *Nat. Rev. Chem.*, 2 (2018) 0118.

[10] B. Carsten, J. M. Szarko, H. J. Son, W. Wang, L. Lu, F. He, B. S. Rolczynski, S. J. Lou, L. X. Chen, L. Yu, *J. Am. Chem. Soc.*, 133 (2011) 20468–20475.

[11] D. J. Griffiths, Introduction to Quantum Mechanics, 2nd ed., *Pearson Prentice Hall*, (2004).

[12] S. J. Axler, Linear Algebra Done Right, Undergraduate Texts in Mathematics, *Springer*, New York, (1997).

[13] M. Fox, Quantum optics: an introduction, Oxford master series in atomic, optical, and laser physics, *Oxford Univ. Press*, Oxford, (2006).

[14] P. A. Hobson, J. A. E. Wasey, I. Sage, W. L. Barnes, *IEEE J. Sel. Top. Quantum Electron.*, 8 (2) (2002).

[15] T. R. Rodríguez; R. García, *Appl. Phys. Lett.*, 84 (2004) 449–451.

[16] E. M. Kober, J. V. Caspar, R. S. Lumpkin, T. J. Meyer, *J. Phys. Chem.*, 90 (1986) 3722-3734.

[17] P. Dhatarwal, R. J. Sengwa, *Physica B Condens. Matter.*, 613 (2021) 412989.

[18] I. Oshina, J. Spigulis, *J. Biomed. Opt.*, 26 (10) (2021) 100901.

[19] J. R. Platt, *J. Opt. Soc. Am.*, 43 (4) (1953) 252-257.

[20] F. S. Richardson, J. P. RIEHL, *Chem. Rev.*, 86 (1) (1986) 1–16.

[21] I. Berlman, Handbook of florescence spectra of Aromatic Molecules. *Elsevier*, (2012).

[22] A. Jablonski, Efficiency of Anti-Stokes Fluorescence in Dyes. *Nature* 131 (1933) 839–840.

[23] A. U. Acuña, F. Amat-Guerri, P. Morcillo, M. Liras, B. Rodríguez, *Org. Lett.*, 11 (14) (2009) 3020–3023.

[24] W. E. Safford, "Lignum nephriticum". *Annual report of the Board of Regents of the Smithsonian Institution. Washington: Government Printing Office*, (1916) 271–298.

[25] J. Herschel, Philos. *Trans. Royal Soc. A.*, 135 (1845) 143–145.

[26] B. Valeur, B. Santos, Molecular Fluorescence: Principles and Applications. *Wiley-VCH*. (2012) 64.

[27] J. J. Cortés, J. H. Trujillo, Advances in Quantum Chemical Topology Beyond QTAIM, 1st ed. *Elsevier*, (2022) 165-192.

[28] X. Ai, E. W. Evans, S. Dong, et al. *Nature*, 563 (2018) 536–540.

[29] A. Margineanu, J. Hofkens, M. Cotlet, S. Habuchi, A. Stefan, J. Qu, C. Kohl, K. Mu1llen, J. Vercammen, Y. Engelborghs, T. Gensch, F. C. D. Schryver, *J. Phys. Chem. B*, 108 (2004) 12242-12251.

[30] M. Kollmannsberger, K. Rurack, U. Resch-Genger, J. Daub, *J. Phys. Chem. A*, 102 (1998) 10211-10220.

[31] E. J. G. Peterman, T. Pullerits, R. van Grondelle, H. van Amerongen, *J. Phys. Chem. B*, 101 (1997) 4448-4457.

[32] P. H. Heinermann, *Exp. Biol.*, 43 (2) (1984) 127-147.

[33] N. Michiels, N. Anthes, N. S. Hart, J. Herler, A. J. Meixner, F. Schleifenbaum, G. Schulte, U. E. Siebeck, D. Sprenger, M. F Wucherer, *BMC Ecol.*, 8 (2008) 16.

[34] T. Gerlach, D. Sprenger, N. K. Michiels, *Proc Biol Sci.*, 281(1787) (2014) 20140787.

[35] Q. Peng, H. Ma, Z. Shuai, *Acc. Chem. Res.*, 54 (2021) 940−949.

[36] L. Zhang, J. Han, H. Wang, R. Car, E. Weinan, *Phys. Rev. Lett.*, 120 (2018) 143001.

[37] J. Yuan, R. Chen, X. Tang, Y. Tao, S. Xu, L. Jin, C. Chen, X. Zhou, C. Zheng, W. Huang, *Chem. Sci.*, 10 (2019) 5031.

[38] J. Westermayr, P. Marquetand, *Chem. Rev.*, 121(16) (2021) 9873–9926.

[39] M. Baroncini , G. Bergamini, P. Ceroni, *Chem. Commun.*, 53 (2017) 2081.

[40] A. Sharmin, R. C. Darlington, K. I. Hardcastle, M. Ravera, E. Rosenberg, J. B. A. Ross, *J. Organomet. Chem.*, 694 (6) (2009) 988-1000.

[41] W. Bricker, P. Shenai, A. Ghosh, A. et al., *Sci. Rep.*, 5 (2015) 13625.

[42] B. Canny, D. Curie, Non-Radiative Relaxation of Solids: Different Pathways to the Ground State. In: B. Di Bartolo, (eds) Advances in Nonradiative Processes in Solids. NATO ASI Series, *Springer*, Boston, MA. 249 (1991).

[43] S. Rashev, *J. Chem. Phys.*, 101 (1994) 6632–6639.

[44] M. Head-Gordon; J. C. Tully, *J. Chem. Phys.*, 96 (1992) 3939–3949.

[45] L. Bañares, *Nat. Chem.*, 11 (2019) 103–104.

[46] A. Konrad, M. Metzger, A. M. Kern, M. Brechta, A. J. Meixner, *Nanoscale*, 8 (2016) 14541.

[47] Q. Y. Li, Z. F. Yao, J. Y. Wang, *J. Pei, Rep. Prog. Phys.*, 84 (2021) 076601.

[48] T. Ikeda, T. H. Ikeda, T. Haino, *Polymer*, 128 (2017) 243–256.

[49] S. Ma, S. Du, G. Pan, S. Dai, B. Xu, W. Tian, *Aggregate*, 2 (4) (2021) e96.

[50] E. E. Jelley, *Nature*, 138 (1936) 1009.

[51] C. Chen, N. Hildebrandt, *Trends Analyt. Chem.*, 123 (2020) 115748.

[52] S. Bhowmick, S. Saini, V. B. Shenoy, B. Bagchi, *J. Chem. Phys.*, 125 (2006) 181102.

[53] J. R. Lakowicz, (eds) Principles of Fluorescence Spectroscopy. *Springer*, Boston, MA. (2006).

[54] L.M. Ng, R. Simmons, Anal. Chem. 71 (1999) 343–350.

[55] K. Sugisaki, S. Nakazawa, K. Toyota, K. Sato, D. Shiomia, T. Takui, *Phys. Chem. Chem. Phys.*, 21 (2019) 15356.

[56] J. Westermayr, P. Marquetand, *Learn. Sci. Technol.*, 1 (2020) 043001.

[57] R. A. Friesner, *PNAS*, 102 (19) (2005) 6648–6653.

[58] H. Li, Z. Wang, N. Zou, et al., *Nat. Comput. Sci.*, 2 (2022) 367–377.

[59] M. Zgarbová, M. Otyepka, J. Šponer, P. Hobzaa, P. Jurečka, *Phys. Chem. Chem. Phys.*, 12 (35) (2010) 10476–10493.

[60] P. Yuvaraj, J. Ajantha, M. Karuppusamy, S. Easwaramoorthi, J. R. Rao, *ACS Sustainable Chem. Eng.*, 9 (2021) 10309−10317.

[61] N. Manjubaashini, M. P. Kesavan, J. Rajesh,T. D. Thangadurai, *J. Photochem. Photobiol. B, Biol.*, 183 (2018) 374–384.

****

CHAPTER ~ 3

Literature Survey

This Chapter gives a thorough literature review of the research related to this present thesis work both in international and national level.

CHAPTER~3

Literature Review

3.1. Introductory remarks

Noble metal nanoparticles (NPs) and metal-based 2D layered nanostructures have received wide spread interest among the scientific community of India and abroad because of their unique physical and physicochemical properties such as high surface area-to-volume ratios, high optical transparency, chemical and thermal stability [1-3]. In this context, gold (Au), silver (Ag) and Molybdenum disulfide nanostructures show remarkable potential in number of technological applications [3,4] in recent years. The unique localized surface plasmon resonance (LSPR) of Au and Ag NPs can efficiently modulate the intrinsic fluorescence properties of various organic compounds. The frequency of LSPR is found to depend on the properties of surface electrons of the NPs and their medium where they are dispersed. Also the photoinduced electron transfer between excited organic dye chromophores and inorganic metal or metal-based NPs open up a new avenue for the development of various molecular level sensing platform for wide variety of organic and inorganic analytes in different environment. Due to the coupling between photoexcited fluorophore and LSPR of such NPs, there may be quenching or enhancement of fluorescence emission of the fluorophore [5,6]. It is observed that the quenching or enhancement of fluorescence are influenced by the presence of guest biomolecules because of their strong affinity with metal nanoparticles in aqueous medium as reported by various researchers [7]. Currently, there is renewed interest especially on metal or metal-based nanostructures with regard to the possibility of various sensing as well as biological applications [8,9].

On the other hand, 2D layered nanostructures such MoS_2 is already attracted significant interest because of their tunable optical properties which are suitable for various technological applications [10]. During the last few years the research with layered MoS_2 nanostructures is increased and play a central role in materials research because of their considerable biocompatibility and easy exfoliation in aqueous

environment. Literature reveals that the unique fluorescence emission properties of MoS_2 nanostructures are very selective and sensitive in various environments containing ionic species (such as metal ions) assuring their potential to design various efficient sensing platform.

Among the various analytical techniques, spectrofluorometric method is now become a highly promising approach to selectively monitor a detectable change or a signal in molecular recognition processes. This technique has a great deal of fundamental importance about the knowledge of molecular behaviour and ensures a deeper understanding of their detail photophysical properties in nanoscale both in the ground and excited electronic states when light interacts with these molecules. Various aspects of radiative and nonradiative transitions depend on the nature, rigidity and shape of the molecules. Moreover, several photophysical properties are highly induced and affected by the local microenvironment of the molecules. It is also observed that in the aqueous environment of metal or metal-based NPs, the properties of various organic emitters are modified, which may alter their radiative deactivation process resulting the change in their electronic spectra [11-13]. The relative change of the electronic states of the organic emitters in presence of various metal or metal based NPs may be systematically investigated with the exposure of various guest molecular species in the same experimental condition. This strategy of understanding the fluorescence behaviour of organic emitters in presence of metal NPs plays significant role for desiging various molecular and biomolecular sensing platform with very high signal-to-noise ratio.

Various research groups both in national and international level are working in the broad area of this promising field for variety of important technological applications. So, in this chapter a brief overview of the research performed by various groups both in national and international level relevant to the research as presented in this thesis is highlighted.

3.2. International status

The study of nanoscience and nanotechnology has revolutionized the fields of materials research to create or tailor the properties of novel objects in nanometer sacle i.e., 1-100 nm. This interdisciplinary fileds of research significantly impact our life as it offers sustainable development through smart products for biomedical fields, environmental safety, better build quality, device miniaturization and as a whole the

improvement of our everyday life. However, among the various promising applications, nanotechnology provides facile and cost-effective approaches for molecular and biomolecular sensing applications by utilizing different specific and non-specific interactions with the target analytes. In this context novel metal NPs such as Au NPs,. and 2D layered MoS_2 nanostructures are in increasing demand as they play pevotal role in various sensing applications [14]. The unique optical properties of such nanomaterials assure their suitability to selectively control their interactions with wide variety of biological and inorganic species in different environments. These nanomaterials are found to significantly interact with various organic fluorescent compounds and can efficiently quench the fluorescence emission intensity in presence of guest molecular species. This strategy is successfully implemented for both lable and label free detection of various bioanalytes at very low molar concentration in aqueous medium as well as in real biological samples [15]. Additionally, the distinct colour of such metal and metal-based nanomaterials in solution facilitates sensing of analytes via colorimetric changes which are observed during the assay experiments [16]. Therefore, research in this emerging area of nanotechnology has attracted great deal of interest of the international scientific community during the last decades [17]. Some interesting research related to sensing and biological applications of such nanostructured materials and relevant photophysics as performed by various scientists and researchers at international level are briefly described in the following sub-sections.

3.2.1. Fluorescence-based sensing applications of dye-metal NPs system

Noble metals such as gold and silver are the naturally occurring elements and are found in the components of the Earth's crust. The study of interaction between noble metal NPs (Au NPs, Ag NPs etc.) with organic dye molecules has become growing interest towards the development of efficient sensing platforms for various important biological and inorganic compounds both in aqueous solution and biological environments [18]. The strong localised plasmonic oscillation of Au NPs and Ag NPs can strongly couple with the oscillating dipoles of various organic fluorophores in the vicinity of NPs resulting distinct change of fluorescence properties of the emitter molecules. These interactions are manifested in variety of spectroscopic observations such as energy transfer from organic molecules to metal NPs or vice versa, direct adsorption characteristics of the organic molecules onto the surface of metal NPs etc. [19]. All these processes significantly impact on the radiative and non-radiative

pathways of excited electronic states of the emitter molecules. Based on the metal NP-fluorophore interaction, number of applications have been developed such as solar cell, bio-imaging, medical therapies, biomolecule sensing, ion sensing etc. [20].

3.2.1.1 Gold nanoparticles for sensing and biological applications

Various researchers in the international level have given continuous efforts to design efficient sensing platforms using plasmonic Au nanostructures or their functionalization with appropriate fluorescent probe. Due to the high molar extinction coefficient and extremely broad energy bandwidth, Au NPs can be used as an excellent fluorescence quencher of organic probes in the resonance energy transfer (RET) based fluorometric assay methods for the sensing of biomolecules [21, 22].

The most common approach of desiging biosensor is based on fluoremetric assay using Au NPs, where Au NPs are functionalized with a suitable organic fluorophore molecule. Due to this, there will be some changes in the absorption band of Au NPs and the fluorescence emission of the fluorophore is quenched. This is known as the fluorescence "turn-off". After addition of analyst i.e., the target biomolecules, the fluorescence emission of the fluorophore may be retrieved and is called "turn-on" [23]. Tang et al. [24] have used β-cyclodextrin (β-CD) functionalized Au NPs to design RET based cholesterol sensor. Addition of fluorescein (FL) molecules with CD/Au NPs system forms CD/Au NPs/FL complex resulting in the fluorescence quenching of FL via RET process. However, after addition of cholesterol, the FL molecule is replaced by cholesterol in the CD/Au NPs/FL complex system due to the higher binding affinity between β-CD and cholesterol and consequently FL becomes free in the assay medium. This eventually restore the fluorescence emission of FL. They reported the fluorescence-based detection of cholesterol using this technique at nanomolar concentration level. Chang et al. [25] have constructed a fluoremetric assay using nile red (NR) with Au NPs for the sensing of biothiols at submicromolar concentration range. According to their study, NR is noncovalently attached to Au NPs in the aqueous medium. RET based Au NPs assay was also used by various group of researchers for the detection of Cysteine and Homocysteine [26]. C. C Huang et al. [27] reported a simple approach for the selective detection of Homocysteine thiolactone using fluorosurfactant (FSN) functionalized Ag NPs. Au NPs/FSN behaves as aminothiol removers and as sensors. They have used Au NPs/FSN mixed system for the detection of Homocysteine and Cysteine at 100 nM concentration levels. J. H. Lin et al. [28]

demonstrated a selective and sensitive sensing method based on fluorosurfactant-caped Au NPs (FSN-Au NPs) with o-Phthaldialdehyde (OPA). According to their report, the selectivity of FSN-Au NPs-OPA system is more than 100-fold for Homocysteine over any other aminothiols with a limit of detection of 180 nM. They also confirmed the selective binding interaction of FSN-Au NPs-OPA with Homocysteine in the real urine samples.

The remarkable quenching of organic dyes due to noble metal NPs has ensured enhanced sensitivity of the fluorescence resonance energy transfer (FRET) based biosensor [29]. L. Qin et al. [30] demonstrated fluorescence "turn-on" sensing of small protein molecule namely glutathione via FRET between Au NPs and amine-terminated gold nanorods. The energy transfer between gold nanorods capped glutathione and Au NPs was highly selective through the electrostatic interaction. Their result revealed a linear fluorescence enhancement with increasing glutathione concentration in the range of 2–100 nM.

Another interesting approach which is being recently investigated by various researchers [31,32] is the molecular beacons which utilize fluorescence labelled ssDNA functionalized with NPs forming hairpin structures for the development of biosensor. In this case the hairpin structure leads to the closer association of the fluorescent dye moiety around the surface of metal NPs resulting a drastic reduction of fluorescence via energy transfer between dye and NPs. However, in the presence of any complementary RNA and DNA target, the hairpin structure may be altered resulting the restoration of fluorescence signal [33]. Benia et al. [34] reported the use of molecular nano-beacons formed by 13 nm Au NPs for systematic detection of a genetic mutation associated with systic fibrosis considering only 1 nM of target analyte. Tseng et al. [35] demonstrated a highly selective turn-on fluorescence sensing of iodide ion using fluorescein 5-isothiocyanate (FITC) functionalized Au NPs in aqueous medium. They explored the selective binding affinity of I^- ion to Au NPs compared to other halides ions. Therefore, it is observed that most of the studies regarding the sensing of various biological and inorganic materials involves the proper functionalization of Au nanoparticles with fluorescent probes. However, it is still challenging to find the appropriate combination of fluorescent probes and Au NPs to design efficient sensing platform for variety of other important bio-analytes because of possible structural alternation of target biomolecular species while interacting with such funtionalized

metal nanoparticles in the assay medium. Also the effect of the external perturbation may influence the fluorescence signal in the fluorometric measurement. In contrast, a ratiometric approach of analysis of fluorescence signal in presence and absence of analytes can provide much accurate information of the analytes during the sensing experiment.

3.2.1.2. Silver nanoparticles for biological applications

Appart from Au NPs, Ag NPs have received great interest of the scientific community and researchers especially in the field of biosensing and bioimaging because of their unique physical and physicochemical properties when compared to their bulk counterpart. Dr. Muhammad Ismail and co-workers in North China Electric Power University, Beijing, China studied the role of Ag NPs on the highly sensitive detection of urea in real urine sample via a simple spectrofluorometric method [36]. They used a second order spectrofluorometric method to eliminate the possible effect of the interference in the real bioenviornment. Dr. Won-Gun Koh and his group at Yonsei University, South Korea developed highly sensitive polycaprolactone (PCL) fibers decorated with silica-coated silver nanoparticles as an efficient biosensing platform to study the immunoassay using IgG and fluorescence-labeled anti IgG. The significant fluorescence enhancement of these protein conjugated fluorophores was observed due to the presence of Ag NPs [37]. Prof. J. R. Lakowicz and his coworkers at the University of Meryland, USA successfully investigated the enhancement of the intrinsic fluorescence of tryptophan residue using Ag NPs for label free detection of protein namely avidin (which is present in the whites of eggs) via fluorometric method at submolar concentration [38]. Fluorescence based immunoassay is a conventional method in biomedical fields for sensitive detection of proteins associated with various antigen-antibody interactions. Prof. Jinhe Yang and his co-workers at Shandong University, china used CTAB-caped Ag NPs as an effective probe for determination of nucleic acid via resonance light scattering technique [39] Prof. Chang-Ping Yu , Institute of Urban Environment, Chinese Academy of Sciences, china studied the interaction of Nitrosomonas europaea ATCC 19718 with silver NPs having varying sizes. They fund the effective inhibition of Nitrosomonas europaea by addition of Ag NPs [40]

In recent times much emphasis has been given to Ag NPs for various ion sensing applications as well. Prof. Shao-Jung Wu and his co-workers at the Taipei Medical University in Taiwan [41] synthesized dual chitosan capped Ag NPs for designing fluorometric and colorimetric based sensor towards the selective detection of Hg^{2+} ion in aqueous medium. Prof. Victor Sánchez-Mendieta with his research group at Autonomous University of the State of Mexico, Mexico used green synthesized Ag NPs as an efficient sensing platform for detection of Cu^{2+} and Pb^{2+} in aqueous solution via fluorescence method [42]. Taihua Li et. al. at Korea Advanced Institute of Science and Technology (KAIST) studied the specific interactions of Ag NPs with various chiral biomolecules such as cysteine, glutathione and penicillamine etc by CD spectroscopy and such interactions was found using Au NPs . [43]

However, the information regarding the optimum condition as well as the proper combination of NPs and organic emitters are still in the early stage of research while considering their real applicability in the biomedical field [44]. Researchers [45] suggest that Ag NPs have relatively high cytotoxicity depending upon the size of the nanoparticles. Therefore, size of the metal NPs may be an important factor for the real application in fluorescence-based biological applications using metal NPs.

3.2.1.3. Metal nanoparticles based surface energy transfer (SET)

Surface energy transfer (SET) involves metallic surface such as metal nanoparticles (i.e., Au NPs, Ag NPs etc.) and a molecular dipole of an organic molecule and was theoretically first predicted by R. Chance et al. in 1978 [46] and experimentally reported by Y. Chen et al. in 2000 [47]. According to the theoretical model of Chance, in SET the rate of energy transfer (K_{SET}) from photoexcited dipole to metal surface is given by the following equation (eqn.) (3.1),

$$K_{SET} = \frac{1}{\tau_D}\left(\frac{d_0}{d}\right)^4 \dots\dots\dots\dots\dots\dots\dots (3.1)$$

where τ_D, d and d_0 are the life-time of the organic molecule (donor), distance between surface of metal NPs (acceptor) and organic molecule (donor) and a constant respectively. From this relation it is clear that the rate of energy transfer from donor to acceptor is proportional to $1/d^4$. According to B. N. Persson and N. D. Lang [48] the values of K_{SET} and d_0 for a photoexcited molecule with energy above the Fermi energy level of metal NPs, can be determined by using Fermi's golden rule when the molecule

goes to the ground energy state by the scattering of electron. However, SET process does not require overlapping between UV-vis absorption spectrum of the acceptor and fluorescence emission spectrum of the donor in contrast to that for FRET process. SET process is mainly originated from the electromagnetic interactions between the conduction electrons on the metal surface of the acceptor and excited dipole of the donor. The experimental observations of the various researchers suggest that FRET is generally limited to the distance of up to ~80 Å, however SET is effective for much larger distances [49-51].

3.2.2. Two-dimensional fluorescencent MoS_2 nanostructures for sensing and biomedical applications

After the discovery of graphene (one of the isotope of carbon) in 2004, two-dimensional (2D) nanostructured materials have gained much attention of the scientific community [52]. Since then, important physical and chemical properties of various 2D layered materials other than carbon have been discovered and studied with the potential applications in the fields of transistors, catalysis, optoelectronic devices, sensors, bioimaging, topological insulators, biomedical research and so on [53-55]. 2D layered materials derived from the transition metal dichalcogenides (TMDs) are very promising due to ease of synthesis, diverse physical and physicochemical characteristics. In the last decade, TMDs becomes the focus of both technological and fundamental research due to their different material properties, wide range of chemical composition, unique crystal and morphological features etc. [56,57]. TMDs are generally represented a MX_2, where M is a transition metal from the group 4 to group 10 of the periodic table (i.e., Hf, Mo, Nb, Ta, Ti, W, V) and X is the chalcogen (i.e., S, Se, Te). Transition metals have d-electrons. These d-electrons fill up the d-bands to different levels resulting the variety of spectroscopic and electronic properties [58]. The wide range of electronic structures of TMDs facilitates their applications not only in the electronic and optoelectronic devices but also in the fields of catalysis, sensors, bioimaging etc. The atomic arrangements of the TMDs also play important roles along with the chemical compositions in determining the 2D material properties. The bulk 2D TMDs are formed by the stacking of molecular layers via weak van der Waals interactions, whereas the transition metal and chalcogens are bonded covalently within the molecular layers [59]. The weak inter-layer and strong intra-layer interactions in the TMDs possesses the high

anisotropy which can tailor the material properties through various methodologies including intercalation, alloying, reducing dimension etc. [60]. There will be significant change in the band structures and band gap energies when 2D layers are thin down towards the single-layer limit [61,62]. Also, the intercalation of guest ion between the two layer of TMDs eventually change the carrier densities which may alter the optoelectronic properties of the materials [63].

Among different TMDs, nanostructured molybdenum disulphide (MoS_2) has received significant interest of the scientific community during the last several years because of their diverse potential in variety of fields such as catalysis, molecular and biomolecular sensing, ion sensing, bioimaging, nanomedicine, drug delivery etc. [64]. MoS_2 has been found to interact with wide variety of guest molecules or ionic species which may be easily intercalated between the layers of MoS_2. This eventually may change their charge carrier density resulting significant alternation of spectroscopic properties at nanoscale. MoS_2 posseses sheet like layered nanostructures wchich show very high photoluminescence yield in ambient condition. In 2010, A. Splendiani et al. [65] first reported the photoluminescence from MoS_2 NSs monolayer. According to them, bulk MoS_2 is an indirect bandgap semiconductor which shows negligible photoluminescence. When this rich d-electron crystal of MoS_2 is thinned to monolayer, a strong photoluminescence is obtained. The quantum confinement of the layered d-electrons creates photoemission, indicating the transition from indirect to direct bandgap materials provides new opportunities of applications at the nanoscale. Also, G. Eda et al. [66] showed 2D MoS_2 monolayer is a photoluminescent direct bandgap semiconductor when compared to its bulk counterpart.

As mentioned earlier, the significant and interesting optical properties of MoS_2 ensures their suitability in various promising technological applications. Among the various such interesting applications, sensing of wide spectrum of molecular and biomolecular and ionic species as well as biomedical applications have drawn much interest of the global scientific communities [67]. In recent times different forms of nanostructured MoS_2 have been investigated by various group of researchers for sensitive detection of ionic species both in aqueous solution as well as in biological environment.

According to the World Health Organization (WHO), mercury (Hg^{2+}), arsenic (As^{3+}), lead (Pb^{2+}), and cadmium (Cd^{2+}) are the highly toxic heavy metal ions [68].

These non-biodegradable heavy metal ions are serious concern to the lives in the environment as they represent major threats to human health and many aquatic lives. Recently, scientific community are very interested to design and develop spectrofluorometric sensors for the selective and sensitive detection of these toxic heavy metal ions to provide a better platform for the removal of these ions. X. Peng et al. [69] designed a visual detection and removal method for the Hg^{2+} by a ferrocene derivative. Q. Ji et al. [70] reported a chip device configured by 3D paper-based microfluidic for the fluorescence detection of Hg^{2+} and Cu^{2+} ions. Y. J. Kim et al. [71] developed a novel technique based on the Au NPs for spectroscopically silent heavy metal ions sensing. H. Sun et al. [72] reported $CdTe$ NPs based Hg^{2+} microsensor. They mainly used the dendrite structure of self-assembled $CdTe$ NPs in presence of Hg^{2+} ion. However, these methods require very sophisticated synthesis of the probe materials and very cross-sensitive towards the other ions while considering their practical applications. Prof. Giovanni Fanchini and co-workers [73] at University of Western Ontario, Canada developed solid-state chemiresistors using two-dimensional MoS_2 NSs which were functionalized with L-Cysteine for detection of heavy metal ion namely Cd^{2+} ion present in drinking water at ppb level. Another important metal element namely iron (Fe) which is an essential trace element for living being and is important as a constituent part of various proteins, enzymes etc. for regulating some biophysical and biochemical processes in our physiological system. However, the imbalance of Fe^{3+} ion in our body imparts many detrimental effects such as kidney diseases, anaemia, hepatitis, alzimers etc. Therefore, detection of the Fe^{3+} ion is essential and important for various biomedical interest. Jian Ma et. al. [74] developed highly efficient sensing platform using MoS_2 quantum dots for label free detection of Fe^{3+} ion in aqueous medium in the concentration range of $0–50\ \mu M/L$ via fluorometric method under the exposure of UV light. Prof. Chi Zhang and co-workers [75] at Jiangnan University, China also studied the use of MoS_2 quantum dots functionalized cysteine for detection of trivalent metal ions namely Fe^{3+} and Al^{3+} in aqueous solution using dual model photoluminescence switching of MoS_2 QD. Prof. Wei-Lung Tseng and his group [76] at National Sun Yat-sen University, Tiwan used 6-Mercaptopurine to selectively quench the fluorescence of MoS_2 nanodots. This selective fluoroscence response of MoS_2 has been utilized for various biological applications such as glutathione sensing, cell imaging, and drug delivery.

Unlike other 2D TMDs and graphene, the intrinsic fluorescence properties of MoS_2 nanostructures are very sensive to the interactions with many biomolecules which open a wider window for the use of MoS_2 in the field of biomedical applications ~~[85]~~ [77]. The high fluorescence of MoS_2 can be controlled by the interaction of the cation in between the layers of the MoS_2. As mentioned earlier, single or few layers of MoS_2 shows high photoluminescence compared to their bulk counterpart, which make them useful in the treatment and imaging of various cellular system. Long term live cell tracing is sometimes required to have better insights into the cellular system to understand the cell dynamics of the development of carcinogenic domains, immune responses, regenerative processes etc. For this purpose, proper and viable cellular imaging play the pivotal role to resolve such biomedical issues. Using organic probe in cellular imaging in many cases face difficulties due to limited photostability and photobleaching especially while using long term evaluation of cell dynamics. Prof. Weili Wei a co-researcher [78] at Chongqing University, China successfully used MoS_2 quantum dots as a fluorescent signalling agent to probe the long term live cell dynamics via the covalent linkage of MoS_2 with intracellular thiol compounds. Additionally, they suggested that due to extraordinary surface-area to volume ratio, MoS_2 will be an effective candidate for loading of functional molecules for many further biomedical applications. Prof. Joseph Wang and his group at University of California, San Diego, USA [79] explored MoS_2 as an advanced surface material in the synthesis of powerful tubular microengines with a diverse array of capabilities such as delivery of drug doxorubicin, highly sensitive detection of nucleic acid namely miRNA-21 via fluorescence TURN-OFF mechanism. Their study reveals MoS_2 as advanced material for the development of multifunctional micromachines for diverse biomedical applications.

The other advantages of MoS_2 over other 2D TMDs and graphene are good biocompatibility and very low cytotoxicity. Wei et al. [80] conduct the cell viability tests on human lung carcinoma epithelial cells (A549) incubated for 24 hrs with varying concentrations of the graphene and three TMDs including MoS_2. They observed that, at the concentration of MoS_2, 1.6 times higher than that of graphene, A549 cells are viable incubated with MoS_2 NSs than that of graphene. Thus MoS_2 could be less hazardous and more biocompatible compared to graphene and other TMDs for potential biomedical applications.

3.3. National status

Apart from the International status on the research in this emerging area of nanotechnology, in India there are various research groups working and exploring some application of fluorescence based on the detail study of photophysical and physicochemical behaviours of some fluorescent organic dyes namely rhodamine B (RhB), safranin O (SO), methylene blue (MB), rhodamine 6G (R6G), acridine orange (AO) etc. in presence of inorganic noble metal NPs such as gold nanoparticles (Au NPs), silver nanoparticles (Ag NPs), titanium dioxide nanoparticles (TiO_2 NPs), zinc sulphide nanoparticles (ZnS), zinc oxide nanoparticles (ZnO). Also, these NPs-dye interactions are have been investigated for various applications like sensing, cellular imaging etc. as being investigated extensively by the several group of researchers.

The drastical change in the fluorescence emission properties and shortening of the excited state life-time of R6G dye while interacting with Au NPs in the aqueous solution was reported by Prof. A. Patra and his research group in the Indian Association for the Cultivation of Science in Kolkata [81]. According their study, the energy transfer from photoexcited dye to NPs was occurred via surface energy transfer (SET) process. Prof. T. Pal et al. [82] in the Indian Institute of Technology, Kharagpur, for the first time, reduced the metal silver (I) to Ag NPs via photochemical reduction method in presence of ascorbic acid in the aqueous medium of Triton X-100. They showed that the synthesized string-like assembly of Ag NPs was extremely stable and efficient to show SERS soignal. The bio-functionalization of Ag NPs, Au NPs was reported by Prof. A. Mukherjee and his research group in the Indian Institute of Science in Bangalore [83]. According to their study, the bio-functionalization of the inorganic noble metal NPs is very essential to achieve the biocompatibility in the specific biomedical applications. Prof. S. K. Kailasa and his research group in the National Institute of Technology in Surat [84] had investigated the influence of the concentrations of reagents, reaction time and temperature on the morphology and electronic properties of Au NPs. They used ascorbic acid functionalized Au NPs as a colorimetric probe for the selective and sensitive sensing of glutathione (GSH) and cysteine (Cys) in the aqueous medium. The localized surface plasmon resonance (LSPR) of lauryl sulfate modified Au NPs have been successfully utilized as the colorimetric probe for the detection of arsenic in aqueous solution by the research group of Prof. K. Dewangan of Indira Gandhi National Tribal University in Amarkantak [85].

This colorimetric probe changes its colour from pink to blue after addition of arsenic solution resulting the red-shift in LSPR via coupling between NPs. Au NPs are being increasingly used in biosensing applications owing to excellent optoelectronic properties. Prof. C. Raman Suri and his research group in the Institute of Microbial Technology (CSIR) in Chandigarh [86] developed a novel electrochemical detection technique for cardiac troponin I using citrate caped Au NPs and troponin I biointerface. In recent years, this technique has attracted much attention in India for biomedical engineering and drug delivery system as well. However, another important work in the field of drug delivery system based on noble metal NPs had been reported at the Bose Institute in Kolkata [95]. V. Banerjee et al. [87] reported that the research on Ag NPs have been emerged with increasing applications in biological systems, for example as antimicrobial agents and potential candidates for controlled drug delivery systems. In all such applications various interactions between proteins and other biomolecules with Au NPs have been explored. Hence, the study of such interactions is of considerable importance for wide spectrum of biological application. They have studied experimentally that the LSPR band profile is dependent on protein concentration for a number of proteins. They explained that protein dependent LSPR signal is an interesting phenomenon and it is independent of size and structure of protein. Another group of researchers from the Indian Institute of Science in Bangalore [88] successfully developed the nanocomposite films of reduced graphene oxide-silver (RGO-Ag) on kapton sheet. This RGO-Ag based flexible film demonstrated good scalability in the sensing of temperature. The tendency of agglomeration of RGO nanosheets had been removed by incorporating the Ag NPs in the nanosheets, which showed excellent thermal conductivity suitable for the applications like temperature sensor. In the very recent time, a novel electrochemical immunosensors had been developed by Prof. R. Khan and his research group in the Advanced Materials and Processes Research Institute (CSIR), Bhopal [89] using the nanocomposites of graphene oxide-gold (GO-Au) for the dual detection of severe acute respiratory syndrome coronavirus 2 (SARS-CoV-2) antigen and SARS-CoV-2 antibody. Development of various photoplasmic platform using some hetro-nano hybrids for the augmentation of fluorescence signals of emitter molecules in the close vicinity of hybrid nanostructures is attracted recent interest in the field of photonics and related applications. Prof. S. S. Rammamurthy at Sri Satya Sai Institute of Higher Learning, Andhrapradesh, [90] studied hybrid nanostructure with Au NPs and Ag NPs for attomolar level detection of biologically

relevant organic material namely, mefenamic acid with very high sensitivity via cell-phone based fluorescence detection method.

On the other hand, Transition metal Dichalcogenides (TMDs) like molybdenum disulfide (MoS_2) nanostructures are attracted much attention of the national scientific communities due to their unique optical, physicochemical and electrical properties of such layered 2D nanostructures. Also, recently, the biocompatibility and biological applicability of MoS_2 has been extensively explored by the various group of researchers in the national level. Prof. N. C. Das and his research group of the Indian Institute of Technology, Kharagpur [91] reported for the first time the synthesis of MoS_2/vinyltrimethoxysilane (MoS_2/VTMS) coated poly(vinylidene fluoride) (PVDF) sponge via reverse immersion precipitation (IP) method. They showed that this sponge had oil/water separation and broad antibacterial properties. Recently, MoS_2 has considered as one of the best promising materials as a co-catalyst for photocatalytic hydrogen evolution over the more-expensive platinum and other conventional materials. A group of researchers from the Indian Institute of Technology, Mandi [92] reported an easy method for the preparation of ultrathin defect-rich MoS_2 nanostructures coated N-doped ZnO nanorods. They showed that this catalyst had a greater potential in the photocatalytic generation of H_2 under solar light irradiation. Also, the surface functionalization of MoS_2 using the noble metal NPs such as Ag NPs, Au NPs is an emerging field of research in the field of chemical sensing and electronic devices. Prof. A. Singha of Bose Institute, Kolkata [93,94] successfully reported Au NPs decorated MoS_2 nanoflowers (Au-MoS_2 NFs) as an efficient biosensor. Recently, electrochemical deposition technique has been widely used for the deposition of MoS_2 thin films on the ITO glass substrate using the method of carboxylation on MoS_2 nanostructures (MoS_2-COOH). C. Pal et al. [95] reported that synthesized MoS_2-COOH showed sulfur vaciencies on the outer layer of the nanosheets which eventually make this material hydrophilic with enhanced conductive and charge transfer properties. They also reported that after proper functionalization with single stand DNA (ssDNA), MoS_2-COOH behaves as an excellent material for the selective and sensitive detection of mercury (II) ions at the femtomoler level of concentration in the aqueous medium.

Therefore, in the light of above literature review, the study of the interactions of various novel metal NPs namely Au, Ag NPs etc. and 2D layered nanostructures such as MoS_2 with organic and inorganic species both in solution and real bio-environment become an emerging topic of research for fundamental as well as

technological interest. Although various studies are performed in national and international level, but still needs continuous development to explore further possibility of metal NPs or their various nanostructures while considering the wide spectrum of sensing and biological applications. It is also very crucial to study the important factors which may affect the viability of such application in diverse technological fields.

References

[1] A. Angelova, B. Angelov, R. Mutafchieva, S. Lesieur, *J. Inorg. Organomet. Polym.*, 25 (2015) 214–232.

[2] B. Angelov, A. Angelova, M. Drechsler, V. M. Garamus, R. Mutafchieva, S. Lesieur, *Soft Matter*, 11 (2015) 3686–3692.

[3] A. S. Aricò, P. Bruce, B. Scrosati, J. M. Tarascon, W. Schalkwijk, *Nat. Mater.*, 4 (2005) 366–367.

[4] D. Gupta, V. Chauhan, R. Kumar, Inorg. *Chem. Commun.*, 121 (2020) 108200.

[5] O. Mondal, M. Pal, *J. Mater. Chem.*, 21 (2011) 18354–18358.

[6] E. A. F. Van Doren, P. R. H. D. Temmerman, M. A. D. Francisco, J. Mast, *J. Nanobiotechnol.*, 9 (2011) 17.

[7] S. Chatterjee, X. Y. Lou, F. Liang, Y. W. Yang, *Coord. Chem. Rev.*, 459 (2022) 214461.

[8] L. Zerkoune, S. Lesieur, J. L. Putaux, L. Choisnard, A. Gèze, D. Wouessidjewe, B. Angelov, C. Vebert-Nardin, J. Doutchh, A. Angelova, *Soft Matter*, 12 (2016) 7539–7550.

[9] J. A. Nash, A. L. Kwansa, J. S. Peerless, H. S. Kim, Y. G. Yingling, *Bioconjugate Chem.*, 28 (2017) 3–10.

[10] J. Ping, Z. Fan, M. Sindoro, Y. Ying, H. Zhang, *Adv. Funct. Mater.*, 27 (19) (2017) 1605817.

[11] S. K. Arya, S. Saha, J. E. Ramirez Vick, V. Gupta, S. Bhansali, S. P. Singh, *Anal. Chim. Acta*, 737 (2012) 1–21.

[12] I. Willner, B. Willner, E. Katz, *Bioelectrochemistry*, 70 (2007) 2–11.

[13] N. Narband, M. Uppal, C. W. Dunnill, G. Hyett, M. Wilson, I. P. Parkin, *Phys. Chem. Chem. Phys.*, 11 (2009) 10513–10518.

[14] F. Mo, Q. Zhou, Y. He, *Sci. Total Environ.*, 829 (2022) 154644.

[15] M. Hasanzadeh, N. Shadjou, *Mater. Sci. Eng. C*, 71 (2017) 1313−1326.

[16] Z. Ali, R. Ullah, M. Tuzen, S. Ullah, A. Rahim, T. A. Saleh, *Trends. Environ. Anal. Chem.*, 37 (2023) e00187.

[17] N. Baig, I. Kammakakam, W. Falath, *Mater. Adv.*, 2 (2021) 1821−1871.

[18] C. Pin, S. Ishida, G. Takahashi, K. Sudo, T. Fukaminato, K. Sasaki, *ACS Omega*, 3 (2018) 4878−4883.

[19] B. Auguié, B. L. Darby, E. C. L. Ru, *Nanoscale*, 11 (2019) 12177.

[20] T. Hu, Z. Chen, G. Zhang, N. Sun, P. Zhao, X. Liu, Y. Xie, *J. Colloid Interface Sci.*, 614 (2022) 468−477.

[21] P. K. Jain, I. H. El-Sayed, M. A. El-Sayed, *Nano Today*, 2 (2007) 18.

[22] K. E. Sapsford, L. Berti, I. L. Medintz, *Angew. Chem., Int. Ed.*, 45 (2006) 4562.

[23] Z. Ebrahimnezhad, N. Zarghami, M. Keyhani, S. Amirsaadat, A. Akbarzadeh, M. Rahmati, et al., *Bioimpacts.*, 3 (2013) 67–74.

[24] N. Zhang, Y. Y. Liu, L. L. Tong, K. H. Xu, J. H. Zhuo, B. Tang, *Analyst*, 133 (2008) 1176.

[25] S. J. Chen, H. T. Chang, *Anal. Chem.*, 76 (2004) 3727.

[26] Y. Chu, T. Han, A. Deng, L. Li, J. J. Zhu, *Trends Analyt. Chem.*, 123 (2020) 115745.

[27] C. C. Huang, W. L. *Tseng, Anal. Chem.*, 80 (2008) 6345.

[28] J. H. Lin, C. W. Chang, W. L. Tseng, *Analyst*, 135 (2010) 104.

[29] P. Błaszkiewicz, M. Kotkowiak, A. Dudkowiak, *J. Lumin.*, 183 (2017) 303–310.

[30] L. Qin, X. He, L. Chen, Y. Zhang, *ACS Appl. Mater. Interfaces*, 7 (2015) 5965−5971.

[31] N. Bellassai, R. D'Agata, G. Spoto, *Anal. Bioanal. Chem.*, 413 (2021) 6063–6077.

[32] A. Shibata, S. L. Higashi, M. Ikeda, *Polym. J.*, 54 (2022) 751–766.

[33] P. C. Ray, G. K. Darbha, A. Ray, J. Walker, W. Hardy, *Plasmonics*, 2 (2007) 173–183.

[34] V. Beni, K. Hayes, T. M. Lergaa, C. K. O'Sullivan, *Biosens. Bioelectron.*, 26 (2010) 307–313.

[35] Y. M. Chen, T. L. Cheng, W. L. Tseng, *Analyst*, 134 (2009) 2106–2112.

[36] M. Ismail, W. Xiangke, G. Cazzato, H. A. Saleemi, A. Khan, A. Ismail, M. Zahid, M. F. Khan, *Spectrochim. Acta A Mol. Biomol. Spectrosc.*, 271 (2022) 120889.

[37] B. J. Yun, J. E. Kwon, K. Lee, W. G. Koh, *Sens. Actuators B Chem.*, 284 (2019) 140–147.

[38] H. Szmacinski, K. Ray, J. R. Lakowicz, *Anal. Biochem.*, 385 (2009) 358–364.

[39] J. Zheng, X. Wu , M. Wang, D. Ran, W. Xu, J. Yang, Talanta 4 (2008) 526-532.

[40] Z. Yuan, J. Li, L. Cui, B. Xu, H. Zhang, C.P. Yu, Chemosphere 90 (2013) 1404-1411.

[41] F. L. Mi, S. J. Wu, W. Q. Zhong, C. Y. Huang, Phys. *Chem. Chem. Phys.*, 17 (2015) 21243.

[42] L. E. S. D. Hoyos, V. Sánchez-Mendieta, A. R. Vilchis-Nestor, M. A. Camacho-López, Univers. *J. Mater. Sci.*, 5 (2) (2017) 29–37.

[43] T. Li, H. G. Park, H.S. Lee, S.H. Choi, Nanotechnology 15 (2004) S660–S663.

[44] J. Li, Y. Liu, Y. Xu, L. Li, Y. Sun, W. Huang, *Coord. Chem. Rev.*, 415 (2020) 213318.

[45] A. R. Gliga, S. Skoglund, I. Odnevall Wallinder, et al., *Part. Fibre. Toxicol.*, 11 (2014) 11.

[46] R. Chance, A. Prock A, R. Silbey, *Adv. Chem. Phys.*, 60 (1978) 1.

[47] Y. Chen, M. B. O'Donoghue, Y. F. Huang, H. Kang, J. A. Phillips, X. Chen, *J. Am. Chem. Soc.*, 132 (46) (2010) 16559–16570.

[48] B. N. Persson, N. D. Lang, *Phys. Rev. B*, 26 (1982) 5409.

[49] S. Saraswat, A. Desireddy, D. Zheng, L. Guo, H. Peter Lu, T. P. Bigioni, D. Isailovic, *J. Phys. Chem. C*, 115 (2011) 17587–17593.

[50] A. A. Deniz, M. Dahan, J. R. Grunwell, T. Ha, A. E. Faulhaber, D. S. Chemla, S. Weiss, P. G. Schultz, *BBCB*, 96 (7) (1999) 3670–3675.

[51] T. Pons, I. L. Medintz, K. E. Sapsford, S. Higashiya, A. F. Grimes, D. S. English, H. Mattoussi, *Nano Lett.*, 7 (10) (2007) 3157–3164.

[52] K. S. Novoselov, *Science*, 306 (5696) (2004) 666–669.

[53] L. Ci, L. Song, C. Jin, D. Jariwala, D. Wu, Y. Li, A. Srivastava, Z. F. Wang, K. Storr, L. Balicas, F. Liu and P. M. Ajayan, *Nat. Mater.*, 9 (2010) 430–435.

[54] Y. L. Chen, J. G. Analytis, J. H. Chu, Z. K. Liu, S. K. Mo, X. L. Qi, H. J. Zhang, D. H. Lu, X. Dai, Z. Fang, S. C. Zhang, I. R. Fisher, Z. Hussain, Z. X. Shen, *Science*, 325 (2009) 178–181.

[55] H. Zhang, C. X. Liu, X. L. Qi, X. Dai, Z. Fang, S. C. Zhang, *Nat. Phys.*, 5 (2009) 438–442.

[56] Q. H. Wang, K. Kalantar-Zadeh, A. Kis, J. N. Coleman, M. S. Strano, *Nat. Nano*, 7 (2012) 699–712.

[57] B. Hinnemann, P. G. Moses, J. Bonde, K. P. Jørgensen, J. H. Nielsen, S. Horch, I. Chorkendorff, J. K. Nørskov, *J. Am. Chem. Soc.*, 127 (2005) 5308–5309.

[58] M. Chhowalla, H. S. Shin, G. Eda, L. J. Li, K. P. Loh, H. Zhang, *Nat. Chem.*, 5 (2013) 263–275.

[59] B. Radisavljevic, A. Radenovic, J. Brivio, V. Giacometti, A. Kis, *Nat. Nano*, 6 (2011) 147–150.

[60] D. Jariwala, V. K. Sangwan, L. J. Lauhon, T. J. Marks, M. C. Hersam, *ACS Nano*, 8 (2014) 1102–1120.

[61] D. Kong, H. Wang, J. J. Cha, M. Pasta, K. J. Koski, J. Yao, Y. Cui, *Nano Lett.*, 13 (2013) 1341–1347.

[62] M. S. Dresselhaus, Intercalation in layered materials, *Plenum Press*, New York, (1986).

[63] Q. Zhang, L. Mei, X. Cao, Y. Tang, Z. Zeng, *J. Mater. Chem. A*, 8 (2020) 15417–15444.

[64] Z. Wang, B. Mi, *Environ. Sci. Technol.*, 51 (2017) 51, 15, 8229–8244.

[65] A. Splendiani, L. Sun, Y. Zhang, T. Li, J. Kim, C. Y. Chim, G. Galli, F. Wang. *Nano Lett.*, 10 (2010) 1271–1275.

[66] G. Eda, H. Yamaguchi, D. Voiry, T. Fujita, M. Chen, M. Chhowalla, *Nano Lett.*, 11 2011, 11, 5111–5116

[67] T. Rasheed, M. Bilal, F. Nabeel, H. M. N. Iqbal, C. Li, Y. Zhou, *Sci. Total Environ.*, 615 (2018) 476–485.

[68] https://www.who.int/news-room/fact-sheets/detail/mercury-and-health

[69] X. Peng, H. He, J. Xia, Z. Lou, G. Chang, X. Zhang, S. Wang, *Tetrahedron Lett*, 55 (2014) 3541–3544.

[70] Q. Ji, L. Bowei, W. Xinran, Z. Zhong, W. Zhuo, H. Jinglong, C. Lingxin, *Sens. Actuators B Chem.*, 251 (2017) 224–233.

[71] Y. J. Kim, R. C. Johnson, J. T. Hupp, *Nano Lett.*, 1 (2001) 165–167.

[72] H. Sun, H. Wei, H. Zhang, Y. Ning, Y. Tang, F. Zhai, B. Yang, *Langmuir*, 27 (2011) 1136–1142.

[73] P. Bazylewski, S. V. Middelkoop, R. Divigalpitiya, G. Fanchini, *ACS Omega*, 5 (2020) 643−649.

[74] J. Ma, H. Yu, X. Jiang, Z. Luo, Y. Zheng, *Sens. Actuators B Chem.*, 281 (2019) 989–997.

[75] H. Lin, C. Wang, J. Wu, Z. Xu, Y. Huang, C. Zhang, *New J. Chem.*, 2015, 39, 8492.

[76] S. C. Chen, C. Y. Lin, T. L. Cheng, W. L. Tseng, *Adv. Funct. Mater.*, 27 (2017) 1702452.

[77] K. Zhou, Y, Zhang, Z, Xia, W, Wei, *Nanotechnology*, 27 (2016) 275101.

[78] H. Yang, X. Jie, L. Wang, Y. Zhang, M. Wang, W. Wei, *Mikrochim. Acta*, 185 (2018) 512.

[79] V. V. Singh , K. Kaufmann, B. E. F. de Ávila , E. Karshalev, J. Wang, *Adv. Funct. Mater.*, 26 (2016) 6270–6278.

[80] K. Zhou, Y. Zhang, Z. Xia, W. Wei, *Nanotechnology*, 27 (2016) 275101.

[81] T. Sen; S. Sadhu; A. Patra, *Appl. Phys. Lett.*, 91 (2007) 043104.

[82] A. Pal, T. Pal, *J. Raman Spectrosc.*, 30, (1999) 199–204.

[83] A. Ravindrana, M. Elavarasi, T. C. Prathna, A. M. Raichur, N. Chandrasekarana, A. Mukherjee, *Sens. Actuators B Chem.*, 166–167 (2012) 365–371.

[84] J. Bhamore, K. A. Rawat, H. Basu, R. K. Singhal, S. K. Kailasa, *Sens. Actuators B Chem.*, 212 (2015) 526–535.

[85] K. Shrivas, R. Shankar, K. Dewangan, *Sens. Actuators B Chem.*, 220 (2015) 1376–1383.

[86] V. Bhallaa, S. Carrara, P. Sharmaa, Y. Nangiaa, C. Raman Suri, *Sens. Actuators B Chem.*, 161 (2012) 761–768.

[87] V. Banerjee, K. P. Das, *Colloids Surf. B*, 111 (2013) 71–79.

[88] N. Neella, V. Gaddam, M. M. Nayak, N. S. Dinesh, K. Rajanna, *Sens. Actuator A Phys.*, 268 (2017) 173–182.

[89] Md. A. Sadique, S. Yadav, P. Ranjan, R. Khan, F. Khan, A. Kumar, D. Biswas, *ACS Appl. Bio Mater.*, 5 (5) (2022) 2421–2430.

[90] S. Bhaskar, A. Rai, K. M. Ganesh, R. Reddy, N. Reddy, S. S. Ramamurthy, *Langmuir*, 38 (2022) 12035−12049.

[91] S. Remanan, N. Padmavathy, R. Rabiya, S. Ghosh, T. Kanti Das, S. Bose, R. Sen, N. C. Das, *Ind. Eng. Chem. Res.*, 59 (45) (2020) 20141–20154.

[92] S. Kumar, A. Kumar, V. N. Rao, A. Kumar, M. V. SHankar, V. Krishnan, *ACS Appl. Energy Mater.*, 2 (8) (2019) 5622–5634.

[93] S. S. Singha, S. Mondal, T. S. Bhattacharya, L. Das, K. Sen, B. Satpati, K. Das, A. Singha, *Biosens. Bioelectron.*, 119 (2018) 10–17.

[94] S. S. Singha, D. Nandi, T. S. Bhattacharya, P. K. Mondal, A. Singha, *J. Alloys Compd.*, 723 (2017) 722e728.

[95] C. Pal, T. T. Suzuki, S. Majumder, *Chem. Phys. Lett.*, 784 (2021) 139115.

****

CHAPTER ~ 4

Experimental Methods and Characterizations Techniques

This chapter demonstrates the detail description of the materials used, experimental methods and various characterization techniques used in the research presented in this thesis.

CHAPTER~4

Experimental Methods and Characterizations Techniques

4.1. Introductory remarks

In this thesis work, various materials such as organic fluorescent dyes, surfactants, inorganic metal salts along with other chemical reagents and various analytical instruments have been used to study the sensing and biological applications of the novel metal or some metal based nanomaterials. For the synthesis of metal-based nanostructures such as gold nanoparticles (Au NPs), silver nanoparticles (Ag NPs) and molybdenum disulfide (MoS_2) nanoflakes soft chemical and hydrothermal synthesis methods are used. The morphological characterizations of the as-synthesized nanostructures samples have been thoroughly investigated using X-ray diffraction (XRD), field emission scanning electron microscope (FESEM), transmission electron microscope (TEM), atomic force microscope (AFM), dynamic light scattering (DLS), UV-vis absorption spectroscopy, steady-state and time-resolved fluorescence emission spectroscopy, Raman spectroscopy etc. The spectroscopic investigation on the interaction metal and metal-based nanostructures with various organic dyes and inorganic compounds such as various metal-based inorganic salts has been systematically studied using UV-vis absorption, steady-state and time-resolved fluorescence emission spectroscopic measurements. In some work, fourier transform infrared (FTIR) in attenuated total reflectance (ATR) mode, circular dichroism (CD) and cyclic voltammetry (CV) are also used to probe the interaction and association between the metal-based nanostructured materials with organic and inorganic compounds in the aqueous medium. To understand and visualize the morphology of the nanomaterials for their interaction with organic and inorganic compounds, TEM and AFM methods are employed. The experimental results are analyzed and correlated with some theoretical study as performed by different software packages. The discussion

about materials used, experimental methods adopted and various analytical methods used for all the research work of this thesis are discussed in detail in this chapter.

4.2. Materials

4.2.1. Organic materials used

❖ Rhodamine B (RhB)

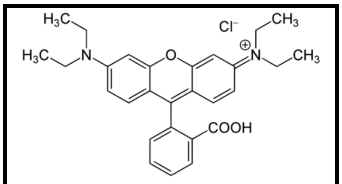

Figure 4.1. Chemical structure of Rhodamine B.

Rhodamine B $(C_{28}H_{31}N_2O_3Cl, M.W.: 479.01\ gmol^{-1})$ abbreviated as RhB is a xanthene dye having very good spectral properties and is widely used as a fluorescent probe in various biomolecular and chemical sensing, biological staining applications [1,2]. The chemical structure of RhB dye is shown in Figure 4.1. In aqueous medium, RhB has absorption and fluorescence emission maximum at around 555 nm and 575 nm respectively [2].

❖ Acridine orange

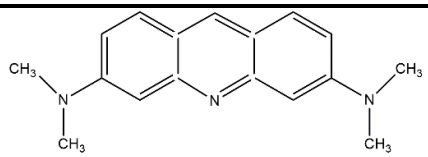

Figure 4.2. Chemical structure of Acridine orange

The acridine orange (AO) is a an organic dye and in solution is a cationic in nature. This dye belongs to the family of xenthane class of molecules and is also an aromatic compound. It has high fluorescence quantum yield and high stability. This dye is a nucleic acid selective dye as reported in the literature [3]. It is widely used biological field for cell study, bacterial staining etc.[4]. The molecular structure of AO is shown in the figure 4.2.

4.2.2. Biomaterials used

❖ Deoxyribonucleic acid

Deoxyribonucleic acid (abbreviated as DNA) is a biopolymer and is responsible for function of various organ of living being and also carries various genetic informations. This consists to strands which are wind together as double helical type. Each strands has phosphate bakbone which has alternative sugars. Different base pairs such as adenine (A), cytosine (C), guanine (G) or thymine (T) are connected with the sugar

group. The sequence of the base pairs control the synthesis of proteins moecules which regulate development and the functions of different organs in our body.

- Various amino acids such as L-Cysteine, D-Cysteine, L-Aspartate (L-Asp), L-Histidine (L-His), L-Methionine (L-Met), L-Serine (L-Ser), L-Tryptofan (L-Try), L-Alanine (L-Ala), L-Arginine (L-Arg), L-Glycine (L-Gly), L-Isolevcine (L-Iso), L-Proline (L-Pro), L-Threonine (L-Thr), L-Valine (L-Val), L-Asparagine (L-Aspa), L-Glutamic Acid (L-Glu), L-Glutamine (L-Glut), L-Phenylalanine (L-Phe), L-Leucine (L-Leu), L-Tyrosine (L-Tyr) L-Lysine (L-Lys) and L-Homocysteine (L-HomoCys) and antioxidant glutathione (GSH) have used in the research presented in theis thesis.

4.2.3. Inorganic materials used

Gold nanoparticles (Au NPs)

Nanoparticles (NPs) have already opened up versatile avenues to explore the new horizon in the field of materials science. NPs show different and various distinct and interesting properties such as high surface-to-volume ratio, strong response to incident electromagnetic radiation etc. when compared to their bulk counterpart [5]. The focus on the emerging aspects of novel metal NPs has paved the way for a new dimension in the research [6]. Noble metal NPs, like gold nanoparticles (Au NPs), have attracted considerable interest for several decades. When Au NPs interact with electromagnetic radiation of suitable wavelengths, the free electrons in their conduction band perform collective oscillations giving rise to the strong plasmonic band which is generally observed by UV-vis absorption spectroscopy [7]. This type of collective oscillation of electrons is termed surface plasmon resonance (SPR). Au NPs were synthesized by the reduction of gold salt ($HAuCl_4$, $3H_2O$) using citrate salt of sodium ($Na_3C_6H_5O_7$) as the reducing and capping agent in the aqueous medium [8]. The aqueous dispersion of Au NPs is reddish-wine in colour and stable at ambient condition. The synthesized Au NPs had an average diameter of $\sim$27.5 nm with an absorption band of $\sim$528 nm.

Silver nanoparticles (Ag NPs)

Among the various noble metal NPs, silver nanoparticle (abbreviated as Ag NPs) is also attracted significant attention of the researchers because of their unique optical and antimicrobial properties [9]. Since the last few decades, the quenching and

enhancement of fluorescence emission of various fluorophores due to the SPR of colloidal Ag NPs and other properties of Ag NPs bring them to the centre of interest of the scientific community. The colloidal Ag NPs were synthesized by simple chemical methods as described elsewhere [10]. In a typical synthesis, the aqueous solution of silver nitrate ($AgNO_3$) was added dropwise into the aqueous solution of sodium borohydride ($NaBH_4$). The bright yellow colour of the reaction mixture indicated the reduction of $AgNO_3$ and the formation of stable colloidal Ag NPs. The prepared Ag NPs had an average diameter of ~8.71 nm with a strong absorption band at ~400 nm.

❖ Molybdenum disulfide (MoS_2) nanoflakes

The evolution of nanomaterials by altering the shape and size at the nanoscale levels confirm their various applications in day-to-day life. The most optimistic two-dimensional (2D) materials such as carbon nanotubes (CNT), 2D honeycomb silicon, 2D layered materials like graphene and graphite, 2D layered transition metal dichalcogenides (TMDs) like tungsten disulfide (WS_2) and molybdenum disulfide (MoS_2) draw the center of attention of global scientific community for their significant use in various fields including electronic, biomolecular and chemical sensing, bioimaging, cancer treatments etc. [11-13]. Among the different 2D-TMDs, MoS_2 nanoflakes were considered as the multipurpose materials for their physical and physicochemical properties at the nanoscale level. In the hexagonal structure of MoS_2 nanoflakes, the S-Mo-S atomic layers were bonded by covalent attraction, whereas the adjacent NSs layers are stacked with each other by weak van der Waal interactions [14]. These promising characteristics of MoS_2 nanoflakes make them suitable for various practical applications. The layered MoS_2 nanoflakes can be prepared by chemical exfoliation of bulk MoS_2. Also, MoS_2 NSs can be synthesized by the chemical reduction of molybdenum salt in the presence of some rich source of sulfur (S) in the control hydrothermal environment. In this research work, MoS_2 nanoflakes were synthesized via hydrothermal method by using sodium molybdate dihydrate (Na_2MoO_4, $2H_2O$) as the salt of Mo and L-Cysteine ($C_3H_7NO_2S$) as the rich source of sulfur (S) by placing the mixed solution in a Teflon-lined stainless-steel autoclave heated at 180°C for 36 hrs [15]. The as-synthesized MoS_2 nanoflakes showed promising photophysical properties which confirmed their use in metal ion sensing applications.

❖ Metal-based salts

To study the effects of various metal ions on the spectroscopic properties of 2D layered nanostructed compound namely MoS_2, various metal based salts have been choasen. This includes $HgCl_2$, AgCl, NaCl, $CaCl_2$, $MgCl_2$, $CdCl_2$, $PbCl_2$, $MnCl_2$ and many others relevant metal salts.

4.2.4. Other materials used

❖ To change pH

Hydrochloric acid (HCl) and sodium hydroxide (NaOH) were used to control the pH of the aqueous solvent medium for specific experiments performed during this thesis work.

❖ Solvent

Ultrapure triple distilled deionized milli-Q water (collected from Synergy integrated with an Elix-Advantage set-up, make: Millipore SAS, France) was used to prepare the solutions of the compounds as used in different spectroscopic and other relevant analytical studies. All the prepared solutions were kept in airtight conditions to maintain their fixed concentrations and to avoid any contamination as it can affect the experimental results.

4.3. Methods

4.3.1. Preparation of mixed solutions for fluorometric measurements

All the mixed solutions of Au NPs, Ag NPs and MoS_2 nanomaterials and the various organic dyes used are prepared in 1:1 volume ratio prior to the spectrofluorometric measurements. All the solutions of pure and mixed samples are preserved in air-tight condition in different glass made conical flask at room temperature and used for the various analytical measurements. All the colorimetric changes of the mixed samples as prepared are captured by digital camera immediately after mixing.

4.3.2. Spectroscopic studies in aqueous solution

Organic materials including dyes are dissolved in ultrapure milli-Q water (resistivity ~18.2MΩ-cm). Metal nanoparticles such as Au NPs, Ag NPs, etc., and metal-based nanostructures namely MoS_2 nanoflakes are not fully soluble in aqueous

medium, they are in normally dispersed in aqueous medium. The MoS_2 layers were exfoliated in aqueous medium by rigorous ultrasonication for few minutes at room temperature. For UV-vis absorption, steady-state, and time-resolved fluorescence emission measurements of organic fluorophores, an appropriate volume of their aqueous solution (with required molar concentration) was taken in high quality quartz cuvette of 1 cm path length.

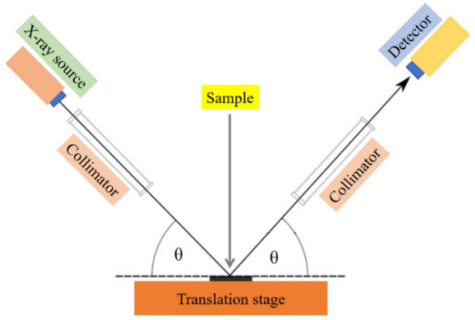

Figure 4.3. Schematic diagram of the working principle of X-ray diffraction.

4.3.3. Morphological and topographical studies on the solid surface

Morphological and topographical studies were performed on the drop-cast films of our samples with the help of XRD, FESEM, HRTEM and AFM measurements. For XRD, FESEM and AFM studies, sample solutions were drop casted on smooth quartz glass substrates and dried at room temperature (25°C). In the case of the TEM study, sample solutions were spread onto the copper microgrids by drop casting and then were dried sufficiently at room temperature before the microscopic measurements.

4.4. Characterization techniques

4.4.1. X-ray diffraction

The X-ray diffraction (XRD) technique is a powerful constructive method to determine the compositions and crystalline structures of the samples [16]. A commercially available X-rays powder diffractometer (model: D8, , WI, Bruker AXS, USA) which is available in our department was used in this study. XRD studies give the information on crystal texture, phases, average grain size, crystal strain, and defects for the too-small crystal. This technique is very well known and can easily be applied to determine the structure and arrangements of atoms in macromolecules and inorganic compounds. In this elegant method, high energetic X-rays are passed through the sample. Some part of the incident beam bouncing-off after the collision with atoms in the materials and goes to different angle other than the incident one. This angle of the

emergent beam from the material is known as the angle of diffraction (θ). Figure 4.3 represents the schematic diagram of the working principle of the X-ray diffraction method. In 1912, Max von Laue et al. observed that the crystalline materials behave like 3D diffraction gratings in the range of X-ray wavelength [17]. A monochromatic beam of X-ray produces constructive interference after being scattered at a certain diffraction angle from the specific lattice plane of the material. The intensity of the diffraction peaks is the fingerprint of periodic atomic arrangements in the given sample. Highly crystalline materials exhibit number of sharp peaks with significant intensity in their XRD spectra. The diffraction angle (θ) can be used to determine the separation between different atomic layers (d) in the material by using Bragg's law of diffraction (eqn.) (4.1)

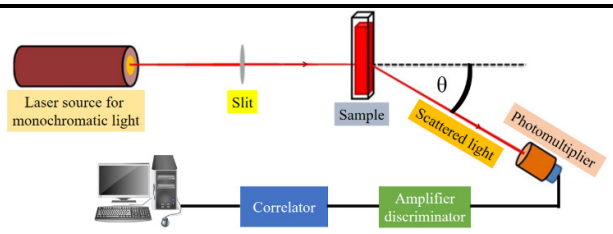

Figure 4.4. Schematic diagram of the working principle of dynamic light scattering method.

$$2dSin\theta = n\lambda \dots\dots\dots\dots\dots\dots\dots\dots\dots (4.1)$$

where n and λ are the integer number and wavelength of incident X-ray respectively. X-ray diffraction technique is vastly used in the rapid development of the field of material science, microelectronics, glass industry, forensic science, pharmaceutical industry, geological applications, etc.

4.4.2. Dynamic light scattering and Zeta potential spectroscopy

Dynamic light scattering (DLS) method is used to determine size distribution of nanoscale particles and polymers based on their diffusion behaviour in the dispersion medium or in solution respectively [18]. The working principle of DLS is schematically shown in Figure 4.4. A monochromatic beam of laser of suitable wavelength is entered into the sample compartment after passing through a polarizer (slit). The scattered light is collected by a photomultiplier after passing through a second polarizer. The resulting spectrum is correlated by a correlator and projected onto a screen. The scattering of the laser photons occurs through the quasi-elastic technique. In this technique, the hydrodynamic radii of the colloidal particles are correlated with the diffusion coefficient via temporal fluctuations of the scattered photons of the laser beam. The DLS method is widely used in the characterization of nanoscale particles including

polymers, protein cages, micelles, virus-linked nanoparticles, biological cells, carbohydrates, vesicles, etc. [19, 20].

On the other hand, Zeta (ζ) potential measurements have been using by the scientific communities over the centuries for their fascinating applications in the field of colloidal chemistry. The interface between the attached and moving fluid in the vicinity of a surface in the colloidal dispersion is known as the slipping plane. The electrokinetic potential at the slipping plane is known as the ζ potential. On the other hand, the ζ potential is also defined as the potential difference between boundary layer of the dispersive medium on the dispersed particle and that of dispersive medium [21]. Figure 4.5 represents the schematic diagram of ζ potential on the surface of metal nanoparticle dispersed in the aqueous medium. The value of the ζ potential of the colloidal dispersion generally indicates the stability of the dispersed solution. More the value of ζ potential, higher the stability of the colloidal dispersion i.e., the colloidal dispersion will resist the particle aggregation in dispersion medium [22]. The accurate determination of the pK_a value of complex polymer systems is very difficult using conventional methods. The pK_a value of these complex systems can be estimated precisely by using the value of Zeta potential [23].

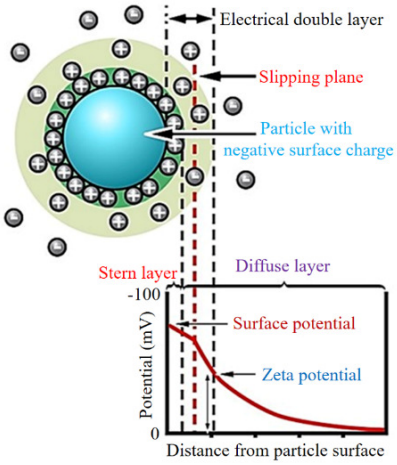

Figure 4.5. Schematic diagram of Zeta potential on the surface of the metal nanoparticle.

4.4.3. Circular dichroism spectroscopy

In the first half of the 19th century, the phenomenon of circular dichroism (CD) was discovered by Jean B. Biot, Augustin Fresnel and Aimé Cotton [24]. The optical activity of the inorganic and organic molecules can be determined by using CD spectroscopic measurements and is manifested as the absorption band in the CD spectrum. The electromagnetic radiation used for the measurement of the optical activity, consists of polarization including left-handed and right-handed circular signals [25]. Left-handed circular (LHC) and right-handed circular (RHC) polarized light consists of two possible states of spin angular momentum. Due to this CD is referred to as the dichroism for spin angular momentum. The CD has a wide range of applications in a variety of research fields including biochemistry and inorganic chemistry [26,27]. The secondary

structure of proteins can be investigated using ultraviolet CD. The charge transfer induced transition involved in the inorganic materials can be determined with the help of ultraviolet-visible CD spectrum. The near-infrared CD spectroscopy can be utilized to investigate electronic structure by probing the metal d → d transitions. The working principle of a commercially available CD spectrometer is schematically shown in Figure 4.6. The solution of the sample is placed in a cuvette on the path of a circular polarized electromagnetic wave. Firstly, the sample solution is illuminated by LHC polarized radiation and the absorbance is measured. A second radiation consisting of RHC polarized radiation is used to irradiate the sample solution. The chiral substance then reacted differently with the circularly polarized radiation due to the intrinsic asymmetry of the chiral molecules. The difference in the absorbance of LHC and RHC polarized light gives the CD spectrum of sample.

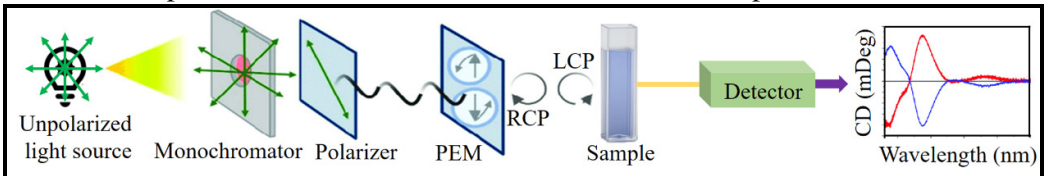

Figure 4.6. Schematic diagram of the working principle of circular dichroism spectroscopy.

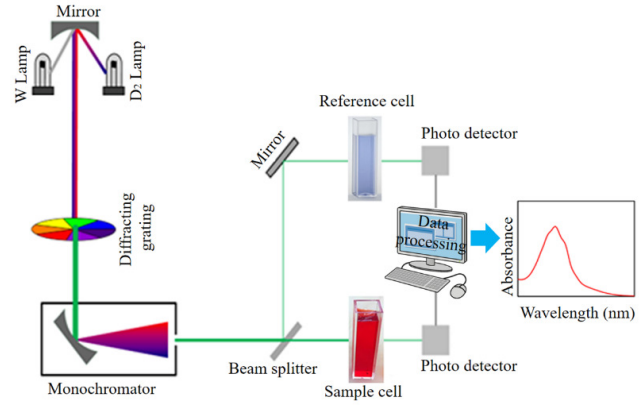

Figure 4.7. Schematic diagram of the working principle of UV-vis absorption spectroscopy.

4.4.4. Ultraviolet-visible absorption spectroscopy

Ultraviolet-visible (UV-vis) absorption spectroscopy is the oldest, most useful, and most conventional characterization method in the fields of physics, chemistry, biology, medicine, and many more. In UV-vis absorption spectroscopic measurements, the various properties of the sample are investigated via the interaction of electromagnetic radiation in the ultraviolet and visible region with the atoms or molecules of the matter [28]. The fraction of light that comes out the sample

compartment is compared with the reference beam of light, which informs how much of the photon is absorbed which is schematically shown in Figure 4.7. This above process is spectrophotometrically repeated for each wavelength. The UV-vis absorption spectrum is generally coming out as a broad spectrum instead of a sharp line due to the associated transitions between several vibrational and rotational states along with the electronic transitions. In the absorption spectrophotometer, the incident light splits into two beams after passing through a beam splitter and passes through two sample compartments which mount two quartz cuvettes. One of the cuvettes contains a background solvent and the light passes through it acts as a reference. Whereas, another cuvette which contains the sample solution. Also, some substrates coated with thin films may also be mounted in the sample compartments for specific measurements. The beams of light reach the detectors (Silicon photodiode, photomultiplier tube etc.) after passing through the sample and reference. The working principle of a typical UV-vis absorption spectrophotometer is schematically shown in Figure 4.7. Generally, in an absorption spectrophotometer, deuterium, and tungsten lamps are used as the source of light. After passing through a diffraction grating used as a monochromator, a beam of light with a specific wavelength goes in two directions. Generally, an UV-vis absorption spectrophotometer works between the ultraviolet (170 – 350 nm) and visible (360 – 800 nm) regions of the electromagnetic spectrum. The transition of electrons between the discrete electronic energy states is mainly responsi ble for the observed electronic absorption spectrum by UV-vis absorption spectroscopy. Due to this, the UV-vis absorption spectrum is also known as the electronic spectrum [29]. According to the Beer-Lambert law (eqn. 4.2) [30], the observed intensity of the absorption peak at a particular wavelength is directly proportional to the presence of absorbing species in the sample i.e., this intensity depends on the concentration of the samples in the medium. When a material is illuminated by electromagnetic radiation, some fraction of radiation will be absorbed and some will be transmitted. The amount of electromagnetic radiation absorbed or transmitted depends exponentially on the

Figure 4.8. Typical image of UV-vis absorption spectrophotometer installed in our laboratory.

concentration (c) and optical path length (l) of sample. Therefore, the absorbance of light by the sample can be represented by eqn. 4.2

$$A = \log_{10}(I_0/I) = \varepsilon cl \ldots\ldots\ldots (4.2)$$

where, I_0, I and ε are the original intensity of the incident radiation, the intensity of the radiation after exiting from the sample, and the coefficient of molar absorptivity. The transmittance (T) is defined by the eqn. 4.3,

$$T = \frac{I_0}{I} \ldots\ldots\ldots\ldots\ldots\ldots\ldots\ldots\ldots\ldots\ldots\ldots (4.3)$$

A commercially available dual beam UV-vis absorption spectrophotometer (model: UV-1800, make: Shimadzu Corporation, Japan) was used in the measurements related to this thesis work, and Figure 4.8 shows the real image of this instrument.

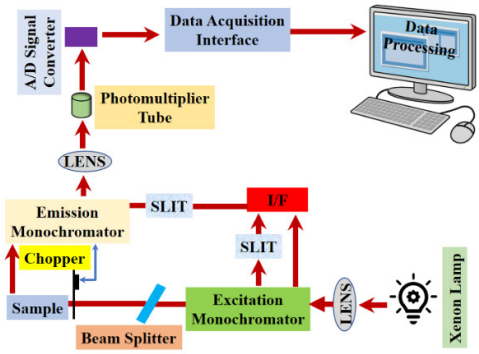

Figure 4.9. Schematic diagram of the working principle of a steady state fluorescence emission spectroscopy.

4.4.5. Steady-state fluorescence emission spectroscopy

As discussed in the previous section, when an electron absorbs energy from the incident photon of electromagnetic radiation, gives the absorption spectrum. When the photoexcited electrons return from the excited electronic state to the ground state via radiative pathways, an emission spectrum may be observed depending upon nature of the electronic states of the material. The steady-state fluorescence emission spectroscopy belongs to class of electronic spectroscopy operated in the wavelength range of 200 – 1100 nm. Figure 4.9 shows the schematic diagram of the working principle of steady-state fluorescence emission spectroscopy. Firstly, light from the Xenon lamp passes through the monochromator for the selective wavelength for a particular sample. Also, Mercury- arc lamps, light-emitting diode (LED), and lasers maybe used as source of night.

The electron of the sample's molecules absorbs energy from the incident monochromatic radiation and goes to the higher vibrational level of excited singlet electronic state. However, within very short interval of time (~10^{-12} s), the excited electron goes to the lower vibrational level from the higher vibrational level of the excited state, which is referred to as the vibrational relaxation. Finally, the electron returns to the ground electronic state from the higher electronic state and emits the excited energy in the form of fluorescence emission [31]. There are also some nonradiative transitions, the energy for which is generally dissipated in the form of heat. The photomultiplier tube is commonly used as a detector which is placed at an angle of 90° relative to the excitation radiation to collect only the scattered light from the sample. Commercially available fluorescence emission spectrophotometer (model: Fluoromax 4, make: Horiba Scientific incorporated, USA was used in the measurements related to this thesis work, and Figure 4.10 shows the real image of this instrument.

4.4.6. Time-resolved fluorescence emission spectroscopy

The fluorescence decay lifetime of the samples was performed in time domain using the Time-correlated single photon counting (TCSPC) method [31] with the help of time-resolved fluorescence spectrometer. TCSPC is a statistical counting method in which time-resolved fluorescence data is recorded. Also, this method provides information about the excited state properties of the light emitting species. In this method method, light-emitting diode (LED) or pulsed laser were used as the source for excitation of the samples at a particular wavelength. The excitation wavelength is generally considered near the wavelength corresponding to absorption maximum.

Figure 4.10. Typical steady-state fluorescence emission Spectrophotometer installed in our laboratory.

After phtoexcitation the corresponding emission is monitored at the maximum emission wavelength as obtained in the steady-state measurement. Unlike steady-state fluorescence emission measurements, in TCSPC, a single photon is counted and its time of arrival through the sample is correlated with that of the photon used during the excitation. This process is repeated many times to get the distribution of photons over time. The details of the working principle of TCSPC are schematically shown in Figure 4.11. The fluorescence signal from the sample is collected and detected with a single-photon counting high-gain photodetector after passing through a monochromator. Mainly, an avalanche photodiode or a multi-channel plate, or a photomultiplier is used as a photodetector. The count rate of photons is kept at less than 5 % compared to that of the frequency of the excitation signal to confirm the measurement of a maximum of one photon per excitation cycle.

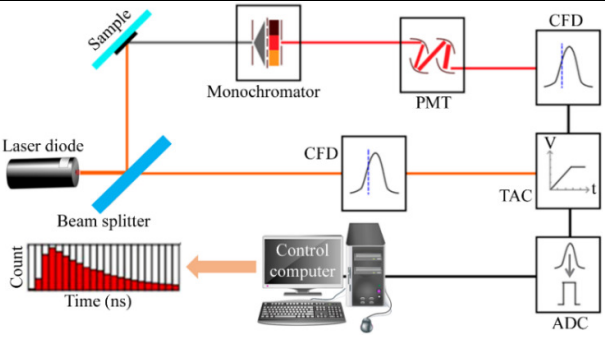

Figure 4.11. Schematic diagram of working principle of time-resolved fluorescence emission spectroscopy (TCSPC).

4.4.7. Fourier transform infrared spectroscopy

Fourier transform infrared (FTIR) spectroscopy belongs the class of vibrational spectroscopy operated in the region of near infrared to microwave of electromagnetic radiation. [32]. The working principle of a commercially available FTIR spectrometer is schematically shown in Figure 4.12. In an FTIR spectrometer, there is interference between two IR beams of light from the same source with a change in path length [33]. The change in path length between the two beams is generally achieved by using a Michelson interferometer, which consists of a source of light (mercury arc or tungsten lamp), two perpendicular mirrors, and a semi-reflecting beam-splitter. After that, the beams are decomposed into frequencies by using a Fourier Transform (FT) algorithm.

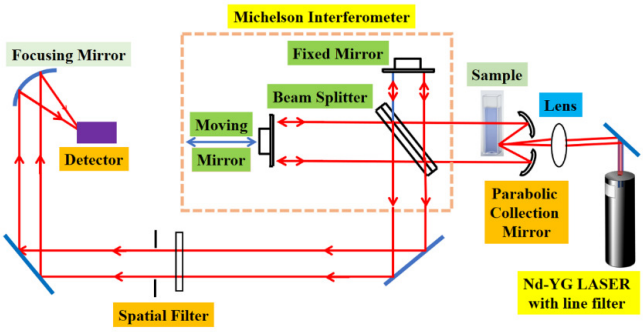

Figure 4.12. Schematic diagram of the working principle of FTIR spectroscopy.

FTIR spectroscopy is usually used to get the structural information including the presence of any functional group, bond types, bond length, type of interactions between molecular species, etc. of an IR active material. An FTIR spectrometer measures the changes in the intensity and frequencies of the beams of light after interacting with the sample. The amount of intensity absorbed by the sample is measured by the Beer-Lambert law (eqn. 4.2). Figure 4.13 shows the image of an FTIR spectrometer installed in our department (model: IRAffinity-1S, make: Shimadzu Corporation, Japan). Attenuated total reflectance (ATR) is an accessory of the commercially available FTIR spectrophotometer to measure the surface properties of thin film or solid samples. In the ATR-FTIR, the interfering beams have a penetration depth of ~1 to 2 µm depending on the conditions of the sample.

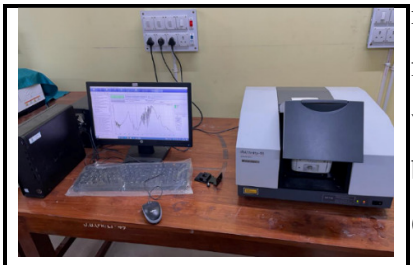

Figure 4.13. Typical photograph of the FTIR instrument installed in our department.

4.4.8. Field emission scanning electron microscopy

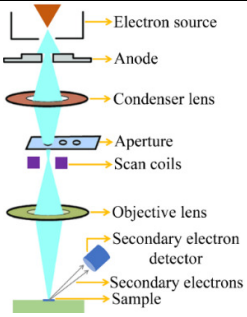

Figure 4.14. Schematic diagram of the working principle of FESEM.

There are mainly two types of microscopy available, one is optical microscopy (OM) or also known as light microscopy and another one is scanning electron microscopy (SEM) [34]. Optical microscopy is the oldest and simplest microscopic technique which is continuously used for the last two centuries with limited capabilities. Field emission scanning electron microscopy (FESEM) is an elegant and promising imaging technique used worldwide in many disciplines. The working principle of a FESEM is shown schematically in Figure 4.14. In the FESEM technique, a highly focused beam of electrons with a very shorter wavelength created by the high vacuum field emission scans the sample and produces high-resolution micrographs [35]. The nanoscale resolution (~1 nm) of the images is obtained due to very shorter wavelength of electron beam. This beam of the electron is accelerated through the high electric field gradient. Then, the beams are modified into narrower and focused by accelerating potential through the condenser lens and a few other arrangements. These sharp focused electron beams then hit the sample placed on a metallic stage in the same vacuum chamber. To improve the image quality and confirm the conductivity of the sample, the gold coating is used during the sample preparation for FESEM measurements. Depending upon the electronic distribution of the atoms of the sample, secondary electrons, back-scattered electrons, X-rays, etc. are produced when the focused beams of electrons interacted with the sample. The detector mainly collects the secondary electrons to visualize the micrograph of the sample. The secondary electron contains detailed information about the surface morphology, chemical composition, and a rough idea about the crystal nature of the sample.

Figure 4.15. Typical photograph of the FESEM instrument installed in our department.

In the research work related to this thesis, the morphology, topography, size distribution, and purity of as-synthesized various noble metal nanoparticles and metal-based two-dimensional nanostructured materials namely MoS_2 were obtained by using FESEM equipment installed in our department (model: Inspect F50, make: FEI, Netherland) and a typical image of this equipment is shown in Figure 4.15. For the FESEM microscopic measurements, the sample solutions were drop-casted on the glass

substrate and subsequently dried at ambient temperature. After proper drying, these substrates were coated with gold with the help of mini DC sputter coater and subsequently the gold coated sample is mounted on a movable stage in FESEM sample chamber under proper vacuum condition.

4.4.9. High-resolution transmission electron microscopy

In the early 20th century, Transmission electron microscopy (TEM) was designed and developed shortly after the verification of the wave-particle duality characteristics of the electron to overcome the drawbacks of optical microscopy [36]. The TEM techniques bring a revolution in the understanding of materials. It provides crystallographic, structural, phase, and compositional information on the atomic scale [37]. TEM analysis has become a major tool in the fields of materials science, chemistry, and biology due to its versatility and high spatial resolution. The working principle of high-resolution transmission electron microscopy (HRTEM) is schematically shown in Figure 4.16. In HRTEM, a beam of electrons is passed through several apertures and lenses. After passing through the sample, the beam of electrons is focused on a phosphor screen. The accelerating voltage used for the beam of electrons in HRTEM is in the range of 150–250 kV, which is much higher than that used for FESEM (5–30 kV). This high energy is mainly required to pass the sample during TEM imaging. A sample of thickness <100 nm gives good images in HRTEM. A photograph of commercially available HRTEM equipment is shown in Figure 4.17. A TEM (model: JEM-2100, make: JEOL Ltd., Japan) was used in the analysis of metal nanoparticles and metal-based

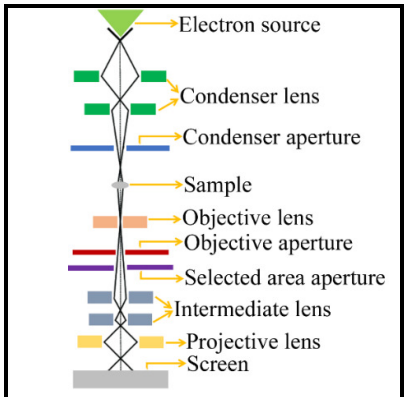

Figure 4.16. Schematic diagram of the working principle of HRTEM.

Figure 4.17. Typical Photograph of the TEM instrument.

nanosheets. To proceed with TEM study, a small amount of sample was drop cast on a carbon-coated copper grid and dried for 24 hrs at room temperature.

4.4.10. Atomic force microscopy

The Atomic Force Microscopy (AFM) was invented in the year of 1985 by G. Binnig and H. Rohrar. [38] It is used to determine the surface morphology of various types of samples, especially thin films. It provides 3-dimensional information, i.e., roughness of the surface of the sample. In addition to its superior resolution, the AFM has advantages when compared with SEM, that it provides 3D imaging of the surfaces of almost any type of sample with extraordinary topographic contrast, direct height measurements, and undistorted views of surface features. In AFM measurement, no surface coating is required. AFM may be operated in the ambient condition in the air or under high vacuum (for specific measurements). The mechanical properties of the sample at nanoscale resolution can also be estimated by this elegant imaging method. In the special arrangement, the surface potential is also determined for a large variety of samples.

The basic working principle of AFM is simple and is schematically shown in Figure 4.18. A sharp tip is put in contact or close vicinity to a sample surface by spring loaded cantilever and scans systematically. It gets deflected if the tip encounters changes in the roughness of the sample surface while scanning. Different types of force such as van der Walls, electrostatic, mechanical contact force, etc. may be responsible for the deflection of the tip while scanning through the specimen surface. A very sharp laser beam focused on the back of the tip will amplify the atomic scale deflection onto a position-sensitive photodiode. A very sharp tip is required to obtain a high-resolution image. There are two commonly used modes for AFM topographic study: (i) static or contact mode and (ii) dynamic mode (non-contact mode or tapping mode).

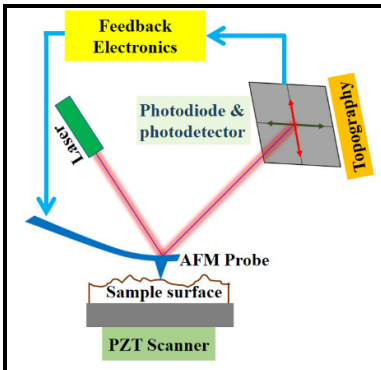

Figure 4.18. Schematic diagram of the operation principle of the AFM.

4.4.11. Raman spectroscopy

Raman spectroscopy is a branch of vibrational spectroscopic technique typically used to interpret various chemical structures based on their vibrational characteristics of atoms in a sample. It generally measures the shift in frequency between incident electromagnetic radiation and inelastically scattered radiation produced from the sample. If the scattered photon has a frequency lower than the incident radiation, then this scattering is known as the Stokes-Raman scattering [39]. On the other hand, if the scattered photon has a higher frequency compared to that of the incident photon and in that case, it is known as the anti-Stokes Raman scattering [39]. Generally, molecules in the excited state produce anti-Stokes lines during the Raman scattering, where the photon will get vibrational energy from the molecule [40]. The shift in frequency between incident photon and scattered photon depends on the chemical compositions (functional groups) present in the molecule which is responsible for the Raman scattering. The energy level diagram involved in the Stokes and anti-Stokes Raman scattering is schematically shown in Figure 4.19. The working principle of a commercially available Raman spectrometer is schematically shown in Figure 4.20. Fundamentally, the Raman spectrum can be treated as a fingerprinting tool to study chemical bonding and intramolecular bonds and identify the corresponding molecules. So the Raman spectrum of the unknown samples can be analyzed to get information about the compound present in the sample.

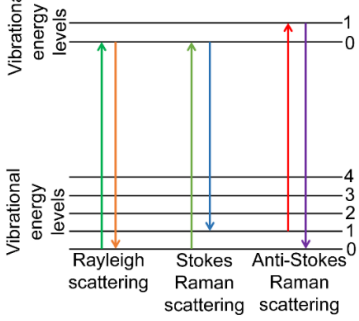

Figure 4.19. Vibrational energy levels involved in the Raman spectroscopy.

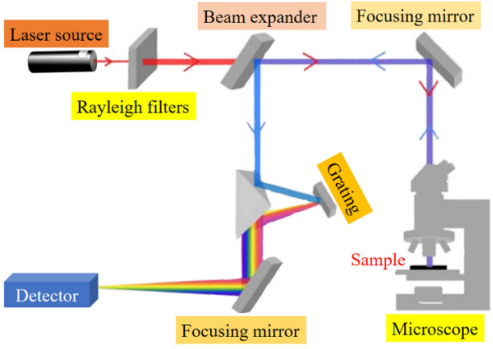

Figure 4.20. Schematic diagram of the working principle of Raman spectroscopy.

4.4.12. Cyclic voltammetry

Cyclic voltammetry (CV) is the widely used electroanalytical technique in the fields of electrochemistry, organic chemistry, inorganic chemistry, biochemistry, etc. to study the electroactive nature of the sample in solution or of an adsorbed molecule onto the electrode. [41]. The rapidly obtained voltammograms in the CV are mainly based on the redox behaviour of the sample over a wide range of potential. In the CV experiments, potential in the working electrode is linearly ramped over time during each phase which is known as the scan rate (V/s) of the experiment. The trace of the cyclic voltammogram is obtained by plotting current vs. potential in the working electrode. The voltammogram carries information about the redox behaviour and electrochemical reaction rate of the sample which are the function of the energy scan. Figure 4.21 schematically shows the working principle of electrodes in the CV measurement. As shown in this figure, the potential difference between reference and working electrodes is ramped and the current is measured between the counter and the working electrodes.

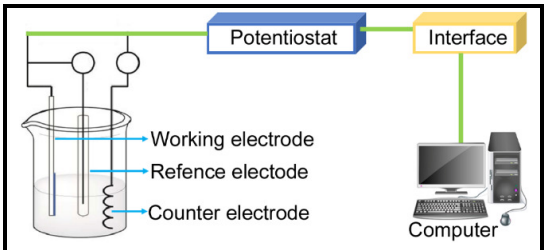

Figure 4.21. Schematic diagram of the working principle of cyclic voltammetry.

4.4.13. Fluorescence imaging microscopy

Fluorescence microscopy is an optical imaging technique that uses fluorescence emission instead of absorption, scattering, or reflection of signals in the details study of the inorganic or organic sample [42]. The fluorescence microscope is of two types, one is a simple fluorescence imaging microscope and another one is a confocal microscope. The design and working principle of a confocal microscope is more complicated than an epifluorescence microscope. However, the

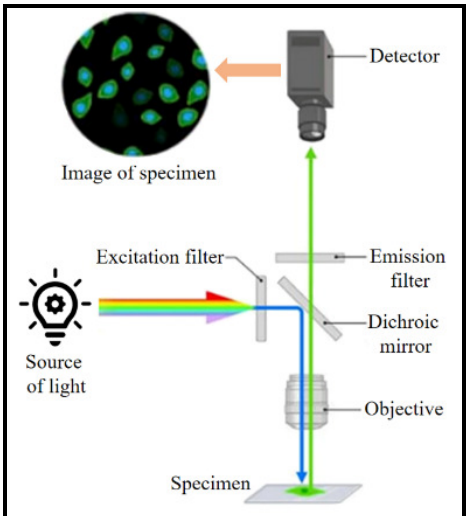

Figure 4.22. Schematic diagram of the working principle of fluorescence imaging microscopy.

resolution of fluorescence image is much better in a confocal microscope which mainly uses optical sectioning for better resolution. The specimen emits a fluorescence signal at a higher wavelength after photo-excitation with specific electromagnetic radiation of a lower wavelength. Excitation and emission filters are generally used to separate the weak fluorescence emission from the sample from that of the strong excitation signal [42]. Figure 4.22 schematically shows the working principle of an epifluorescence microscope in which electromagnetic radiation with excitation wavelength illustrates the sample through the objective. The fluorescence emission from the specimen goes to the detector via the same objective, due to this an objective of large aperture is mainly used in a simple optical microscope. A dichroic mirror or filter is a wavelength-specific beam splitter that mainly transmits fluorescence radiation through the detector and eyepiece but cut out or reflects any remaining exciting radiation toward the source.

4.5. Computational techniques

OriginPro 8.5 software was utilized to plot and analyze the experimental data as presented in the present thesis.

Density functional theoretical (DFT) simulation was also carried out using Gaussian 09 and GaussView 06 software to optimize the stable geometry of the studied organic dye molecule. Gaussian and GaussView simulations are often used in quantum chemical calculations. The details of these methods are already discussed in Chapter 2. The name is Gaussian comes from the use of Gaussian orbitals to speed up molecular simulation and energy calculations to know the electronic structure of a compound instead of using Slater-type orbitals. This choice can speed up, especially the Hartree-Fock calculation. In GaussView 06, molecules are drawn, and several parameters are assigned such as calculating methods, e.g., DFT, Hartree-Fock, semi-empirical, etc., basis sets, assigning spin, charge, determining energy, NMR spectra, optimizing molecular geometry, etc. After setting all the required parameters, the job is submitted to run to perform the calculation. Then job is taken care of by Gaussian 09 from GaussView 06. Gaussian 09 then calculates this and gives calculated results and files. These files are opened by GaussView 06, and calculated parameters are visualized through it. Not only parameters like electronic energy and transition states, bond length, UV-vis spectra, NMR spectra, etc. can be seen through this, but also we can have visualized the optimized molecular structure and orbitals, animate the molecular vibrations, generate electron cloud, etc.

Theoretical simulation for the periodic crystalline material is also carried out with the help of the QUANTUM ESPRESSO (QE) suite of computer codes. QE is a quantum-mechanical material modeling for electronic structure calculations. QE is mainly based on the DFT, plane waves modelling and pseudopotentials approximation.

References

[1] J. Bordini, I. Calandreli, G. O. Silva, K. Q. Ferreira, D. P. S. Leitão-Mazzi, E. M. Espreafico, E. Tfouni, *Inorg. Chem. Commun.*, 35 (2013) 255–259.

[2] S. Claucherty, H. Sakaue, *Sens. Actuators B Chem.*, 240 (2017) 956–961.

[3] Z. Darzynkiewicz, *Methods in Cell Biology*, 33 (1990) 285-298.

[4] G. Kronvall, E. Myhr, *Acta path. microbiol. scand. Sect. B*, 85 (1977) 249-254.

[5] N. C. Lucena, C. M. Miyazaki, F. M. Shimizu, C. J. L. Constantino, M. Ferreira, *Appl. Surf. Sci.*, 436 (2018) 957–966.

[6] S. P. Deshmukh, S. M. Patil, S. B. Mullani, S. D. Delekar, *Mater. Sci. Eng. C*, 97 (2019) 954–965.

[7] A. Campos, N. Troc, E. Cottancin, M. Pellarin, H. C. Weissker, J. Lermé, M. Kociak, M. Hillenkamp, *Nat. Phys.*, 15 (2019) 275–280.

[8] G. Frens, *Nat. Phys.*, 241 (1973) 20–22.

[9] S. K. Kailasa, T J. Park, J. V. Rohit, J. R. Koduru, Chapter 1: Nanoparticles in Pharmacotherapy, *Elsevier*, (2019) 461–484. ISBN: 978-0-12-816504-1.

[10] S. Iravani, H. Korbekandi, S. V. Mirmohammadi, B. Zolfaghari, *Res. Pharm. Sci.*, 9 (2014) 385–406.

[11] X. Li, H. Zhu, *J. Mater.*, 1 (1) (2015) 33–44.

[12] D. Burman, H. Raha, B. Manna, P. Pramanik, P. K. Guha, *ACS Sens.*, 6 (9) (2021) 3398–3408.

[13] D. J. Late, Y. K. Huang, B. Liu, J. Acharya, S. N. Shirodkar, J. Luo, A. Yan, D. Charles, U. V. Waghmare, V. P. Dravid, C. N. R. Rao, *ACS Nano*, 7 (6) (2013) 4879–4891.

[14] D. Gupta, V. Chauhan, R. Kumar, *Inorg. Chem. Commun.*, 121 (2020) 108200.

[15] K. Chang, W. Chen, *ACS Nano*, 5 (2011) 4720.

[16] A. A. Bunaciu, E. G. U. Tioiu, H. Y. A. Enein, *Crit. Rev. Anal. Chem.*, 45 (2015) 289–299.

[17] W. Friedrich, P. Knipping, M. von Laue, Sitzungsberichte der Mathematisch-Physikalischen Classe der Königlich-Bayerischen Akademie der Wissenschaften zu München, (1912) 303.

[18] B. J. Berne, R. Pecora, *Courier Dover Publications*, (2000). ISBN: 0-486-41155-9.

[19] P. R. Bhut, N. Pal, A. Mandal, *ACS Omega*, 4 (23) (2019) 20164–20177.

[20] H. K. Waghwani,T. Douglas, *J. Mater. Chem. B*, 9 (14) (2021) 3168–3179.

[21] IUPAC, Compendium of Chemical Terminology, 2nd ed. (the "Gold Book") (1997). DOI: 10.1351/goldbook.E01968.

[22] D. Hanaor, M. Michelazzi, C. Leonelli, C. C. Sorrell, *J. Eur. Ceram. Soc.*, 32 (1) (2012) 235–244.

[23] A. J. Barbosa, M. S. Abdelsadig, B. R. Conway, H. A. Merchant, *Int. J. Pharm.*, 1 (2019) 100024.

[24] G. D. Fasman, *Springer*, (1996) 3. ISBN: 978-0-306-45142-3.

[25] P. Atkins; J. Paula, Elements of Physical Chemistry (4th ed.). *Oxford University Press*, (2005). ISBN: 978-0-7167-7329-0.

[26] K. Nakanishi, N. Berova, R. Woody, *VCH*, (1994) 473. ISBN: 978-1-56081-618-8.

[27] N. Solomon, A. T. Wecksler; G. Schenk; T. R. Holman, *J. Am. Chem. Soc.*, 129 (24) (2007) 7531–7537.

[28] D. A. Skoog, F. J. Holler, S. R. Crouch, (6th ed.), Belmont, CA: Thomson Brooks/Cole. (2007) 169.

[29] R. S. Drago, Physical Methods for Chemists, 2nd ed., W. B. Saunders (ed), (1992). ISBN: 0030751764.

[30] W. J. Jasper, M. Günay, Modelling, Simulation and Control of the Dyeing Process, *Woodhead Publishing Series in Textiles*, (2014) 206–221. DOI: 10.1533/9780857097583.206.

[31] L. Arnaut, Chemical Kinetics: From Molecular Structure to Chemical Reactivity, (2nd ed.), (2021) 37–91. DOI: 10.1016/B978-0-444-64039-0.00004-2

[32] B. Stuart, Infrared spectroscopy: fundamentals and applications. *John Wiley & Sons, Ltd.*, (2005). DOI: 10.1002/ 0470011149.

[33] A. A. Michelson, Studies in optics. *Chicago, IL: University of Chicago Press*, (1927).

[34] A. Mohammed, A. Abdllah, Scanning Electron Microscopy (SEM): A Review, Proceedings of 2018 International Conference on Hydraulics and Pneumatics – HERVEX, ISSN: 1454–8003.

[35] J. R. Banbury, *J. Phys. E: Sci. Instrum.*, 5 (1972) 798, DOI: 10.1088/0022-3735/5/8/025.

[36] D. B. Williams, C. B. Carter, The transmission electron microscope. In Transmission Electron Microscopy; *Springer: New York, NY, USA*, (1996) 3–17.

[37] A. Alhamidi, Z. Horita, *Mater. Sci. Eng. A*, 622 (2015) 139–145.

[38] M. Marrese, V. Guarino, L. Ambrosio, *J. Funct. Biomater.*, 8 (2017) DOI: 10.3390/jfb8010007.

[39] S. A. Asher, *Anal. Chem.*, 65(4) (1993) 201A–210A.

[40] A. Kudelski, *Surf Sci.*, 603 (10) (2009) 1328–1334.

[41] P. T. Kissinger, W. R. Heineman, *J. Chem. Educ.*, 60 (9) (1983) 702.

[42] F. Rost, Fluorescence Microscopy, Applications, *Encyclopedia of Spectroscopy and Spectrometry*, (3rd ed.) (2017) 627–631.

****

CHAPTER ~ 5

Selective and sensitive detection of L-Cysteine via fluorometric assay using gold nanoparticles and Rhodamine B in aqueous medium

Characterizations of synthesized colloidal gold nanoparticles and their interaction with rhodamine B dye towards the development of essential amino acid namely L-Cysteine sensor are highlighted in this chapter.

A research paper based on the work presented in this chapter has been published in ***Materials Chemistry and Physics 234 (2019) 158–167***
http://doi.org/10.1016/j.matchemphys.2019.06.001

CHAPTER~5

Selective and Sensitive Detection of L-Cysteine via Fluorometric assay using Gold nanoparticles and Rhodamine B in Aqueous Medium

5.1. Introductory remarks

The thiol containing amino acid L-Cysteine (abbreviated as L-Cys) generally found in human plasma is well known as the building block of proteins and is involved in verity of important biological processes [1]. Normally a small amount of L-Cys is present in human body in the form of N-acetyl-L-cysteine (NAC) commonly known as L-Cys and is naturally derived from the amino acids serine and methionine [2]. It is widely used in pharmaceutical industry as medicine to treat different type of physiological complications [3–6]. The body prepares the important antioxidant from NAC by converting it firstly into L-Cys and then into glutathione [7]. Antioxidants such as or ascorbic acid (vitamin C) fight against the free radicals in our body and reduce oxidative stress before damage of the vital molecules. For healthy adults about 4.1 mg/kg/day of L-Cys is required as recommend by Joint FAO/WHO/UNO expert consultation [8]. Although L-Cys has a number of health benefits, the elevated amounts of such amino acid may cause neurotoxicity [9], promotes urinary stone formation [10] etc. and it can also be regarded as the biological marker for various diseases [11–13]. Therefore, it is of utmost importance to detect the concentration of L-Cys by a highly sensitive, selective and convenient method with high degree of accuracy in order to prevent its adverse effects in our health. Various analytical methods such as immunoassay, electrochemistry, chromatography etc. are recently being explored for the detection of L-Cys and are performed in conjugation with liquid chromatography,

fluorimetry, colorimetry, differential pulse voltammetry and spectrofluorimetry etc. [14–19]. But immunoassay and chromatography required expensive biological reagents and complicated instrumentations. Also, the electrochemical methods show relatively low selectivity to L-Cys. Some methods utilize the fluorometric detection after direct labeling of suitable fluorescent probe with target bio-analyst. However direct labeling sometimes causes structural alternation of the biological species resulting erroneous information. Also, these detection methods directly utilizing the absolute fluorescence intensity sometimes may include unwanted noise due to environmental perturbation in the measurement. In recent times the colorimetric methods are attracted great attention but are still limited because of their lack of effectiveness at very low concentration. Therefore, it is of crucial importance to design the appropriate sensing platform for the detection of L-Cys both selectively and quantitatively with high degree of accuracy in the physiological range. In this direction, the method based on the fluorometric assay may offer great advantages for the detection of L-Cys as they enable a direct and level free detection in an aqueous environment even at very low concentration. Also, the ratio-metric fluorescence recovery from the fully quenched state of any suitable fluorescent probe in presence of the analyst biomolecule ensures the elimination of any external perturbation involved in the measurements. Metal nanoparticles (NPs) are attracted considerable attention for their excellent ability to modulate the spectroscopic properties of various interesting cationic organic dyes in the aqueous environment [20,21]. The ground and excited state electronic properties of such dye molecules adsorbed onto the surface of gold nanoparticles (Au NPs) or silver nanoparticles (Ag NPs) show significant physical and physicochemical behavior which sometimes enable their use in many biomolecular recognition processes [22]. The reduction of excited state fluorescence life time down to several hundreds of picoseconds has been attributed to energy or electron transfer processes [23,24] from excited dye molecules to these NPs. The resonant coupling between the oscillatory electric dipole of plasmonic electrons and the dipole of excited dye molecules may be a possible reason for ultra-fast energy transfer [25]. These interesting photophysical processes of small organic dyes assembled on to the noble nanoparticle's surfaces are sometimes very sensitive to the specific guest-host geometry in a particular environment, which allows their possible application in the field of biosensors [26]. On the other hand, these NPs may aggregate in solution while interacting with many biological molecules namely protein,

enzyme, amino acids etc. [27] resulting substantial effect on the surface plasmonic band under optical irradiation. In this chapter, a highly sensitive and selective method for detection of L-Cys via fluorescence turn-off and turn-on mechanism based on the interaction of RhB and Au NPs in aqueous media have been studied. The cationic dye RhB belongs to xanthene family of organic dyes and has high fluorescence quantum yield (0.71) in water with good photo-stability [28,29]. The fluorescence emission of RhB was turned on from its initial quenched state and was recovered (approximately 68 fold) after addition of L-Cys to RhB/Au NPs mixed solution at a concentration range between 0.01 μM and 1000 μM. Most interestingly this fluorometric method was accompanied with a significant and noticeable color changes of the final solution and is therefore direct visual evidence for selective determination of L-Cys over all other associated amino acids in the aqueous medium.

5.2. Experimental

5.2.1. Materials

The amino acid of our interest i.e., L-Cys ($C_3H_7NO_2$, M.W: 121.15 $gmol^{-1}$) along with all other essential and non-essential amino acids used in this present work, RhB ($C_{28}H_{31}ClN_2O_3$, M.W: 479.02 $gmol^{-1}$), chlorauric acid ($HAuCl_4$, $3H_2O$, M.W: 339.79 $gmol^{-1}$), glutathione (M.W: 307.32 $gmol^{-1}$), ascorbic acid ($C_6H_8O_6$, M.W: 176.12 $gmol^{-1}$), uric acid ($C_5H_4N_4O_3$, M.W:168.11 $gmol^{-1}$) were purchased from Sigma Aldrich chemical company, USA and used without further purification. The purity of RhB was checked via spectroscopic method prior to use in the experiment. Trisodium citrate ($Na_3C_6H_5O_7$, M.W: 258.06 $gmol^{-1}$), sodium chloride (NaCl, M.W: 58.44 $gmol^{-1}$), potassium chloride (KCl, M. W: 74.5513 $gmol^{-1}$) were purchased from Merck Chemical Company, Germany. All the glasswares were cleaned with freshly prepared aquaregia solution (3:1 mixture of hydrochloric acid (HCl) and nitric acid HNO_3) followed by subsequent rinsing with triple distilled deionized Milli-Q water (resistivity 18.2 MΩ cm, pH~7, collected from Synergy integrated with an Elix®-Advantage set-up, Millipore SAS, France) and then were autoclaved for 24 hrs before use. Aqueous solutions of the chemicals were also prepared with the same triple distilled Milli-Q water.

5.2.2. Synthesis of Au NPs

Au NPs were synthesized by citrate reduction method as described elsewhere [30]. In a typical procedure, 50 mL aqueous solution of $HAuCl_4$, $3H_2O$ (concentration of 0.25 M) was heated to boiling and 1.2 mL of $Na_3C_6H_5O_7$ (1%) was added into the solution under vigorous stirring for preparing gold nanocolloidal solution. Within a time of 70 s, the boiling solution turned faintly to blue color and after 120 s the blue color changed to deep red. The solution was then set aside to cool down at room temperature. The final concentration of the gold nanocolloidal solution became 0.1 mM at pH~7.

5.2.3. Characterizations techniques

The UV–vis absorption spectra of the samples were recorded in the wavelength range of 200–800 nm by a double beam UV–vis absorption spectrophotometer (UV-1800, Shimadzu, Japan) after proper baseline correction for the solvent background. Steady state fluorescence spectra of the samples were recorded in the range of wavelength 545–700 nm by using a Horiba Spectrofluorometer (Fluoromax-4C, Horiba Scientific Incorporated, USA). An excitation light source of wavelength 530 nm emerged through a slit having width of 2 nm was used for all the steady state fluorescence emission measurements. Both the absorption and emission spectra were collected from the sample solution in quartz cell (Kozima, Japan) of 1.0 cm path length at room temperature (25°C). The hydrodynamic nanoparticle size distribution and the effective surface Zeta (ζ) potential of the as-synthesized Au NPs were obtained by a Zetasizer (Zetasizer Nano ZS, Malvern Instruments Ltd, UK) via dynamic light scattering method (DLS) at an ambient condition. High resolution TEM study of the Au NPs was carried out on a Transmission Electron Microscope (TEM) operated at 200 kV (JEM-2010 TEM, JEOL Ltd., Japan). For TEM study, the sample solutions were incubated for 15 min and then a small drop was spread onto the carbon coated copper microgrid (PELCO 300 Mesh Grids, Ted Pella Inc. USA) and subsequently dried at room temperature. Time resolved fluorescence emission measurements were acquired by using time-correlated single photon counting (TCSPC) method (Fluorolog, Horiba Jobin Yvon, USA) to obtain the excited state fluorescence lifetime of the samples. In this method, the sample solutions were excited at 510 nm by using a picosecond pulsed diode laser. The fluorescence decay data were collected over 200 channels which were

calibrated on a non-linear time scale with increasing time according to an arithmetic progression with a Hamamatsu photomultiplier tube (R928P). The raw decay data as obtained were analyzed using IBH DAS6 software.

5.3. Results and discussions

5.3.1. Characterizations of synthesized Au NPs

Figure 5.1A shows the UV–vis absorption spectrum of the citrate-stabilized Au NPs in aqueous colloidal solution and shows distinct absorption band with its maximum at around 528 nm along with two weak humps at 251 nm and 356 nm. The former is due to the strong characteristic surface plasmon resonance (SPR) while the other two are due to the intra-band electronic transitions of gold and can be related with the traces

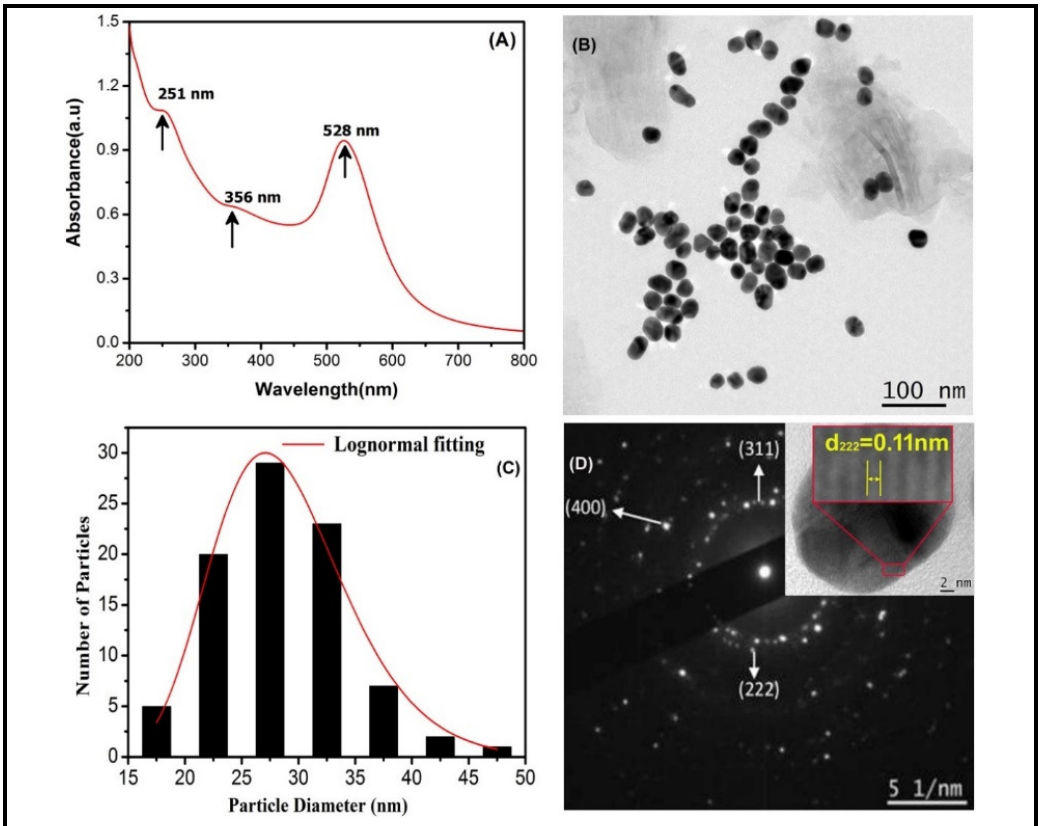

Figure 5.1. (A) UV–vis absorption spectrum of as-synthesized Au NPs in aqueous colloidal solution. (B) TEM micrograph of Au NPs. (C) Lognormal fitting of the particle size distribution. (D) SAED pattern with the Miller-indices of Au NPs. Inset of (D) shows the HR TEM micrograph with crystal spacing.

of such bands as similarly reported for Ag NPs by some researchers [31,32]. The well resolved and sharp SPR maximum band is basically due to both longitudinal and transverse SPR equivalently, which reveals a sign of the formation of spherical Au NPs. The molar extinction coefficient of Au NPs (with maximum SPR observed at 528 nm) was calculated as 540 x 10^7 $M^{-1}cm^{-1}$ [33].

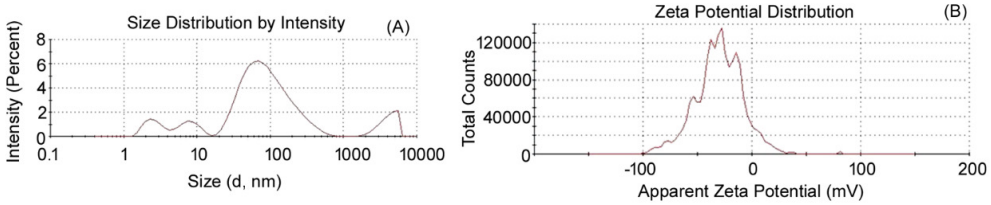

Figure 5.2. (A) DLS and (B) Zeta potential spectra of as-synthesized Au NPs in aqueous solution at room temperature and pH ~7.

The DLS study (Figure 5.2A) revels that the average hydrodynamic size of Au NPs was about 53.78 nm. To have further knowledge about the homogeneity of NPs distributions the surface ζ potential was measured (Figure 5.2B) and was found to be -30 mV at room temperature and solution pH~7. These results suggest that Au NPs could overcome the van der Waals attraction through the strong electrostatic repulsion between the negatively-charged citrate coronas around the NPs surface in the aqueous medium and therefore Au NPs remained effectively stabilized prior to their use in the experiment [34].

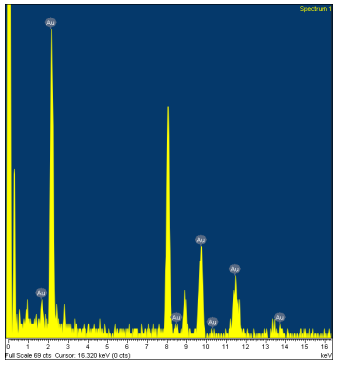

Figure 5.3. EDS spectrum of as-synthesized Au NPs.

However, to have a more precise and clear understanding of the size and morphology of Au NPs, TEM study was performed. Figure 5.1B shows that Au NPs were mono-dispersed with nearly spherical in shape and the average particle diameter was ~27.5 nm as calculated from the size distribution curve (Figure 5.1C). The selected area electron diffraction (SAED) (Figure 5.1D) reveals the good crystalline nature of Au NPs. The rings as seen in SAED pattern were indexed and corresponds to the electron diffractions originated from (311), (222), (400) etc. planes of FCC gold crystal. The interplaner spacing as calculated (Figure 5.1D) was about 0.11 nm corresponding to the lattice plane (222). The High-resolution TEM

micrograph was also shown in the inset of Figure 5.1D. The energy dispersive X-ray spectrum (EDS) curve (Figure 5.3) shows the nucleation of Au NPs without any impurities and the presence of large number of Au NPs in its colloidal solution used for the experiment.

5.3.2. UV-vis absorption spectroscopy

The cationic dye RhB is a well-known laser dye from the xanthene family of organic dyes and its molecular structure is shown as the inset of Figure 5.4A. The UV–vis absorption spectrum of pure RhB solution (concentration of 6 μM) as shown in Figure 5.4A (curve 3) exhibits a strong absorption band at around 554 nm which is attributed to the characteristic π-π* transition of dye monomer units and a very weak band observed at around 520 nm is assigned to the dimeric states of RhB molecules due to the n-π* transition [29]. In aqueous solution at low concentration (i.e., 6 μM) RhB dimmers are in equilibrium with the monomers and their mean numbers should remain constant at a particular concentration [29]. However, in our work, the concentration of RhB solution was about 0.1 μM for the detection of L-Cys. So, it was

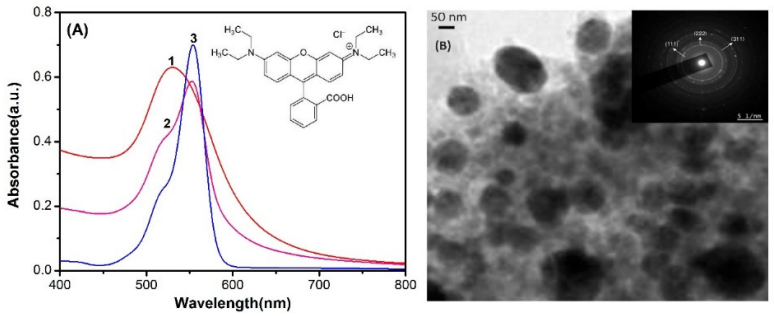

Figure 5.4. (A) UV–vis absorption spectra of (1) aqueous colloidal dispersion of Au NPs, (2) mixed aqueous solution of RhB and Au NPs, (3) aqueous solution of RhB. (B) TEM micrograph of Au NPs/RhB mixed sample. Insets of (A) and (B) show the molecular structure of RhB dye and SAED pattern of RhB/Au NPs mixed sample, respectively.

presumed that most of the RhB molecules might exist as monomer units in the studied aqueous solution because of their very low concentration. RhB/Au NPs mixed solution (1:1 vol. ratio) (Figure 5.4A, curve 2) showed that the main characteristic absorption band position (554 nm) of RhB was almost unaltered but with decreased intensity along

with an increase in absorbance of dimeric band (520 nm) compared to that of pure RhB. This change in the absorption spectrum of RhB in presence of Au NPs was possibly due to their adsorption on to the NPs surface. More precisely this aggregation effects were manifested as the close packing of RhB dye molecules around the Au NPs surface and this eventually induced enhanced dye-dye intermolecular interaction. Some authors [20–22] also reported this type of aggregations of other xanthene family dyes on the Au NPs surface via strong electrostatic interaction. In fact, addition of Au NPs to the aqueous solution of RhB certainly changed the microenvironment around the electronic states of the dye molecules and this might have altered their electric transition dipole-moment. The interaction of molecular dipoles of RhB with the plasmonic field produced by Au NPs eventually affected the excitation energies of the individual dye molecules resulting decrease in absorbance of dye monomeric band at 554 nm.

The closer association of dye molecules on the Au NPs surface additionally induced the aggregations of NPs in the mixed sample which was also observed from TEM analysis (Figure 5.4B). It is clearly observed that different size of dye/Au composite systems were formed in the mixed ensembles which have been correlated with the observed UV–vis results. The DLS measurement shows that the hydrodynamic diameter of the NPs increases after addition of RhB and the negative charges on the surface of citrate stabilized Au NPs were reduced as evidenced from Figure 5.5A,B respectively.

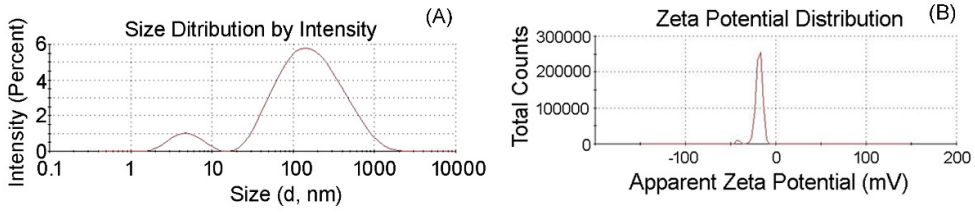

Figure 5.5. (A) DLS and (B) Zeta potential spectra of Au NPs/ RhB mixed aqueous solution at room temperature and pH~7.

5.3.3. Sensing of L-Cys based on fluorometric assay

In this work we systematically design a highly sensitive sensing platform for the quantitative as well as selective recognition of L-Cys using fluorometric assay of RhB/Au NPs in the aqueous medium. The sensing of L-Cys via fluorometric assay mechanism is schematically shown in Figure 5.6.

The fluorescence emission spectra of RhB/Au NPs mixed aqueous solution (1:1 vol. ratio) in absence (curve a) and presence (curve b) of L-Cys (concentration of 100 μM) was shown in Figure 5.7A. It is observed that RhB/Au NPs mixed aqueous solution had negligibly small value of emission intensity because of efficient fluorescence resonance energy transfer (FRET) from excited dye molecules to the Au NPs surface as well as also the decrease in radiative rate

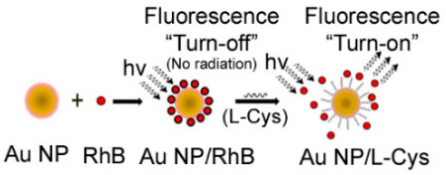

Figure 5.6. Mechanism of detection of L-Cys using fluorometric assay of Au NPs and RhB.

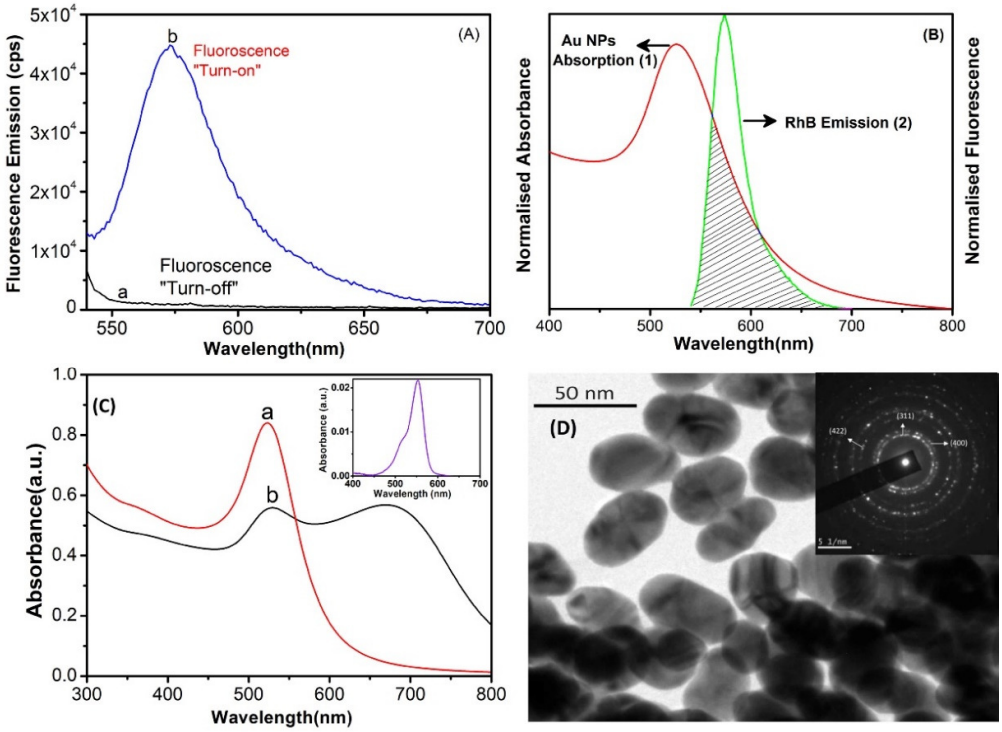

Figure 5.7. (A) Fluorescence emission spectrum from RhB/Au NPs mixed solution in absence (curve a) and presence (curve b) of L-Cys. (B) Spectral overlapping between normalized absorption of Au NPs and fluorescence emission of RhB. (C) UV–vis absorption spectra of RhB/Au NPs in absence (curve a) and presence (curve b) of L-Cys. (D) TEM micrograph of RhB/Au NPs/L-Cys mixed sample. Insets of (C) and (D) show the UV–vis absorption spectrum of RhB in presence of L-Cys and SAED pattern of RhB/Au NPs/L-Cys mixed sample, respectively.

constant of individual RhB molecules adsorbed on NPs surface. The energy transfer from donor RhB to acceptor Au NPs is mainly due to FRET process which is clearly perceived from the large overlap between the emission of RhB and absorbance of Au NPs as shown in Figure 5.7B. However, most interestingly after addition of L-Cys solution to the RhB/Au NPs mixed solution the fluorescence emission at around 574 nm was found to emerge with much increased intensity from its quenched state as shown in Figure 5.7A (curve b). This observation clearly suggests that the emission of RhB molecules which were adsorbed onto the Au NPs surface before addition of L-Cys was recovered to a great extent and was possibly due to a strong interaction between L-Cys and Au NPs through the thiol moiety (–SH) [35]. Due to this strong affinity of thiol to Au NPs, the L-Cys molecules were strongly bound to NPs resulting the escape of RhB molecules away from NPs surface. Because the attachment of RhB molecules with Au NPs were due to electrostatic interaction whereas L-Cys tend to attach with Au NPs by Au–S bond via chemisorption which is relatively much stronger. As a result, the electrostatic charge distribution around the NPs surface was disrupted causing the release of RhB molecules from Au NPs surface resulting the decrease of fluorescence quenching via nonradiative energy transfer. Thus, addition of L-Cys eventually restored the fluorescence band intensity of RhB at around 574 nm. However, the control experiment (Figure 5.8) (i.e., fluorescence emission of RhB/L-Cys mixed aqueous solution without Au NPs) reveals a negligible effect of L-Cys on the emission profile of RhB molecules in the studied aqueous medium as the unaltered emission band position and no such significant rise and fall of emission intensity with increase or decrease of L-Cys concentration. But the slight decrease in emission intensity of RhB after addition of L-Cys solution of different concentrations might only be due to the dilution of the RhB concentration in the mixed solution and not due to any interaction in their ground or excited electronic states.

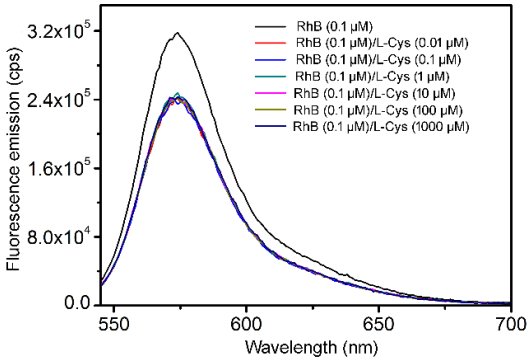

Figure 5.8. Fluorescence emission spectra of RhB in absence and presence of different concentrations of L-Cys.

In order to support the above results as obtained from fluorometric assay method, TEM study (Figure 5.7D) was also performed for the RhB/Au NPs/L-Cys mixed solution at the same ambient condition. We already observed that the dye molecules were adsorbed on the Au NPs surface resulting some aggregation of Au NPs and the distribution became inhomogeneous (Figure 5.4B). However, from Figure 5.7D it is clearly observed that after addition of L-Cys in RhB/Au NPs mixed aqueous solution, the distribution of NPs became more homogeneous but the average size of the particle increased to about 40 nm. This increased size distribution of Au NPs was basically due to some aggregation of individual NPs in the relatively higher viscous medium after addition of L-Cys. However, the crystallinity of Au NPs after addition of L-Cys possibly was not altered as distinct diffraction rings was observed from SAED images (Inset of Figure 5.7D). DLS study as shown in Figure 5.9A further reveals the increase in the hydrodynamic particle size distribution (~67.84 nm) of Au NPs in presence of RhB and L-Cys compared to pure Au NPs (~53.78 nm). Also, ζ potential as measured for RhB/Au NPs/L-Cys mixed solution was found to be -13.0 mV (Figure 5.9B) which is much lower than that of pure Au NPs (-30.1 mV) as well as RhB/Au NPs mixture (-20.0 mV). The reduced ζ potential of Au NPs in RhB/Au NPs/L-Cys mixture eventually favored further aggregation of NPs. More precisely the addition of L-Cys to the RhB/Au NPs mixed aqueous solution might have displaced the negatively charged citrate around NPs surfaces resulting the decrease in negative ζ potential of Au NPs. This in turn also favored the aggregation of Au NPs in aqueous medium [35].

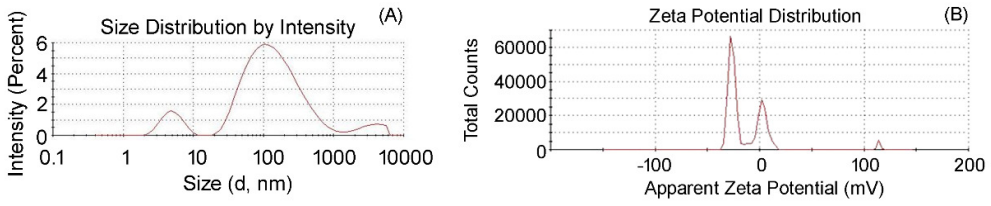

Figure 5.9. (A) DLS and (B) Zeta potential spectra of Au NPs/RhB/L-Cys mixed sample in aqueous solution at room temperature and pH~7.

5.3.3.1. Sensitivity of the proposed method

In the present work, we have also studied the quantitative detection of L-Cys via fluorometric assay of RhB/Au NPs assembly in the same aqueous environment. Figure 5.10 demonstrates the fluorescence spectra of RhB/Au NPs mixed aqueous solution in presence of various L-Cys concentrations viz. 0.01 µM, 0.1 µM, 1.0 µM, 10 µM, 100 µM and 1000 µM. From this figure, we immediately see that the fluorescence emission band of RhB at 574 nm was recovered and their intensity increased systemically with increase in L-Cys concentration. Also, the increase in fluorescence recovery efficiency with the concentration of L-Cys was almost linear (Inset of Figure 5.10). The systematic recovery of fluorescence from RhB/Au NPs mixed solution in presence of L-Cys was highly sensitive with the change in the concentration of L-Cys. Therefore, this fluorometric assay in aqueous medium may be a suitable and efficient sensing platform for quantitative detection of amino acid L-Cys. The increased number of L-Cys molecules with increase in their concentration in RhB/Au NPs mixed solution definitely segregates more number of dye molecules from the surface of Au NPs and this has been manifested as the systematic linear increase in the fluorescence emission intensity. In fact, the initial quenched fluorescence emission of RhB due to Au NPs via FRET process was gradually decreased as the concentration of L-Cys was increased. A very good linear relationship between the fluorescence recovery efficiency (at 574 nm) and the concentration of L-Cys can be used to calibrate the proposed method of L-Cys detection in the concentration range of 0.01 µM–0.1 mM as obtained from the inset of Figure 5.10. The calibration equation (eqn. (5.1)) for this approach can be written as

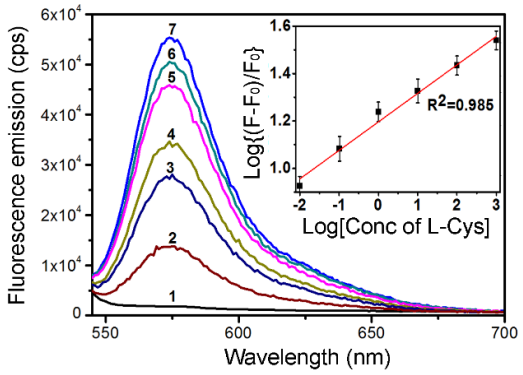

Figure 5.10. Fluorescence recovery from assay of Au NPs/RhB in presence of L-Cys of various concentration viz. 0 µM (1), 0.01 µM (2), 0.1 µM (3), 1.0 µM (4), 10 µM (5), 100 µM (6) and 1000 µM (7). Inset shows the plot of Log{(F-F_0)/F_0} vs. Log[Conc of L-Cys].

$$\mathrm{Log}[(F - F_0)/F_0] = \mathrm{Log}[C] + \mathrm{Constant} \ldots\ldots\ldots\ldots\ldots\ldots\ldots (5.1)$$

where C is the concentration of L-Cys which was added into RhB/Au NPs mixed solution during the fluorometric assay experiments. The linear fitted plot as shown in inset of Figure 5.10 is almost passed through the initial point of the calibration curve and hence the limit of detection (LOD) may be approximately considered as 0.01 μM.

Table 5.1. Comparison with other reported methods for detection of L-Cys.

Probe	Detection principle	Range (in μM)	LOD (in μM)	Ref.
TCEP & CMQT[a]	HPLC-UV	20–300	0.5	[14]
Fluorescein–modified Au NPs	Fluorescence	0.8–4.1	0.1	[15]
Ficin	Colorimetry	0.05–14	0.02	[16]
Poly(p-coumaric acid)/ MWNT/GCE[b]	Differential pulse voltammetry	7.5–1000	1.1	[17]
Cu^{2+}–caclein	Fluorimetry	0.3–12	0.04	[18]
Tl(III)[c]	Spectrofluorimetry	0.1–5.5	0.1	[19]
Rhodamine B Coated Au NPs	Fluorometric assay	0.01– 100	0.01	**This work**

[a]TCEP–tris(2-carboxyethyl)phosphinehydrochloride, CMQT–2-Chloro-1-thylquinolinium tetrafluoroborate. [b]MWNT/GCE–multi-walled carbon nanotubes modified glassy carbon electrode. [c]Tl(III)–Thallium(III).

The sensibility or the LOD of the proposed L-Cys detection method can be comparable with the results reported in the literature as cited in Table 5.1. Furthermore, the present technique utilizes the ratiometric fluorescence response of the fluorescent probe (RhB). Hence the effect of any impurity or external perturbation on the fluorescence was automatically discarded during the calibration of the proposed assay. Also, the range of detection in the present method is comparable to the concentration of L-Cys present in the blood plasma [37] (near about micromolar), which suggests that our detection technique will have great potential with the diagnostic impact for biomedical interest.

5.3.3.2. Selectivity of the proposed method

In the practical purposes a good biosensor should selectively responds to a particular biological analyte which is to be sensed at a given time otherwise the sensing

process will be failed to give the desired output. To evaluate the selectivity of the proposed method towards L-Cys, the interference of various other twenty amino acids such as L-Aspartate (L-Asp), L-Histidine (L-His), L-Methionine (L-Met), L-Serine (L-Ser), L-Tryptofan (L-Try), L-Alanine (L-Ala), L-Arginine (L-Arg), L-Glycine (L-Gly), L-Isolevcine (L-Iso), L-Proline (L-Pro), L-Threonine (L-Thr), L-Valine (L-Val), L-Asparagine (L-Aspa), L-Glutamic Acid (L-Glu), L-Glutamine (L-Glut), L-Phenylalanine (L-Phe), L-Leucine (L-Leu), L-Tyrosine (L-Tyr) L-Lysine (L-Lys) and L-Homocysteine (L-HomoCys) and antioxidant glutathione (GSH) were tested via the same fluorometric assay method in aqueous medium. Apart from these amino acids, the interactions of other relevant biosamples such as uric acid and ascorbic acid and some neurotransmitters (K^+ and Na^+) are also examined with the proposed assay method.

5.3.3.3. Colorimetric response of the assay

The most interesting observation was that just after addition of equal amounts of various amino acids including L-Cys separately to the RhB/ Au NPs mixed aqueous solution the color of the final solution became nearly bluish-black (as shown in Figure 5.11) only in case of L-Cys and could be clearly visualized with the naked eye.

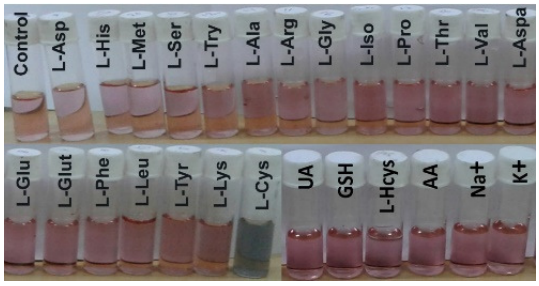

Figure 5.11. Digital photographs of Au NPs/RhB mixed solution before (Control) and after adding of relevant analytes of same concentration.

The concentrations of aqueous solutions of all the amino acids, other biosamples and neurotransmitters were same (0.1 mM) for these colorimetric observations. This was the initial visual evidence that L-Cys could selectively bind to Au NPs thereby changing the color of the final solution. It is already evident from Figure 5.7C (curve b) that the addition of L-Cys to RhB/Au NPs mixed aqueous solution causes the emergence of the new absorption band of Au NPs at around 670 nm which implies a very fast and strong interaction between L-Cys and Au NPs in presence of probe RhB in the ground electronic states resulting the change of color of RhB/Au NPs mixed solution from wine to bluish-black.

Figure 5.12A shows the fluorescence emission spectra from RhB/Au NPs mixed system for various amino acids including L-Cys as well as glutathione, uric acid, ascorbic acid and some neurotransmitters like Na^+, K^+ etc. and the corresponding change in fluorescence recovery efficiency as a function of various analytes are shown

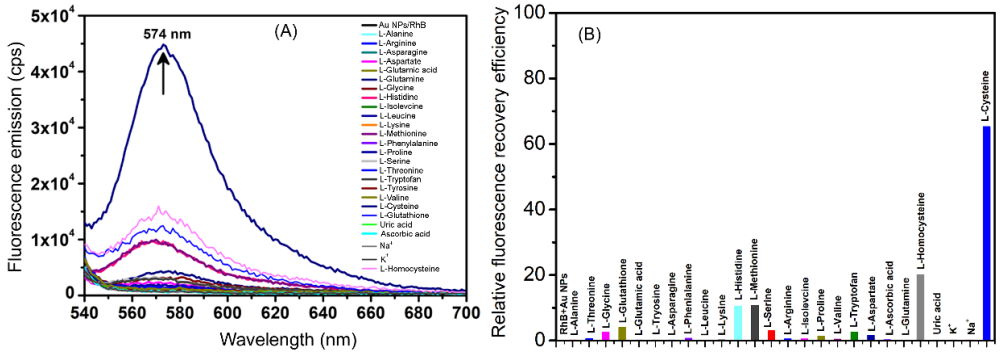

Figure 5.12. (A) Fluorescence emission spectra of Au NPs/RhB mixed solution in absence and presence of interfering relevant analytes. (B) Relative fluorescence recovery efficiency of the assay of Au NPs/RhB at 574 nm upon addition of L-Cys and all other relevant interfering analytes.

in Figure 5.12B. From this plot it is clearly observed that the fluorescence recovery efficiency of RhB/Au NPs system in presence of L-Cys was significantly maximum compared to the rest of the amino acids although the concentration of all the amino acids remained same. The all-other amino acids showed almost negligible effect on the quenched state of RhB adsorbed onto Au NPs surface resulting no noticeable change in fluorescence intensity of the dye molecules. Additionally, there was no significant enhancement of fluorescence recovery efficiency while using the other amino acids of concentration of at least 100 times higher than that of pure L-Cys (Figure not shown). However, only other three essential amino acids namely L-Histidine, L-Methionine and L-Homocysteine showed slightly greater fluorescence recovery efficiency but still very less compared to the L-Cys. The slight difference of the fluorescence recovery efficiency in presence of L-Histidine and L-Methionine as shown in Figure 5.12B might be due to the electrostatic interaction of $-NH_2^+$ with the negatively charged Au NPs and very minimal interaction through the less accessible intra-bond S-atom resulting a slight decrease in overall fluorescence quenching via FRET between excited RhB molecules and Au NPs during photo excitation [38]. It is also relevant to mention here that it was

unlikely for Au NPs to self-assemble with these two amino acids via covalent combination through S–Au bonds in the same aqueous environment as compared to L-Cys [39]. However, for L-Cys, the thiol moiety (–SH) is the head group and more exposed to aqueous environment causing greater extent of interaction with Au NPs. Although L-Homocysteine is a homologue of the amino acid L-Cys but differing with additional methylene bridge, it still shows almost 1/3 less fluorescence recovery efficiency compared to L-Cys while considering same molar concentrations for both the amino acids during the assay experiments. Additionally, the concentration of L-Homocysteine used was 0.1 mM which is much higher compared to its presence in real blood plasma. So, it is expected that in real biosample it would leave negligible effect in the detection of L-Cys by the proposed method.

In this work it is therefore highly important to study the relative fluorescence

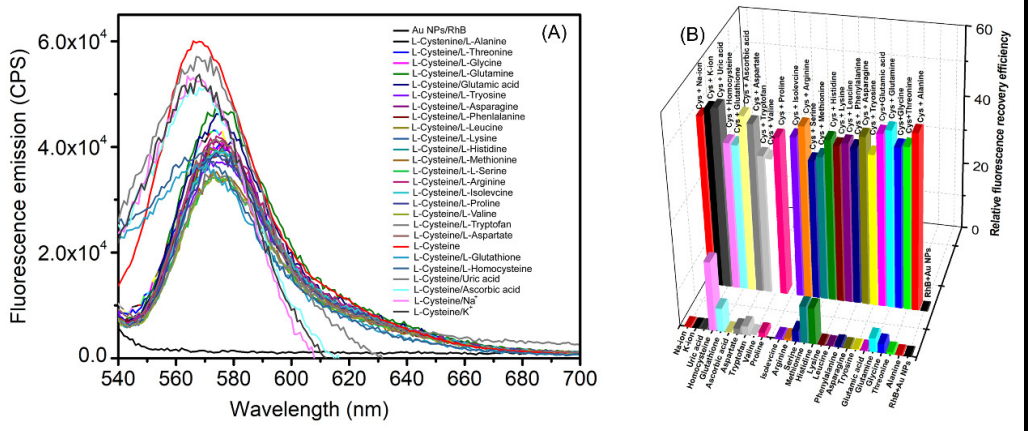

Figure 5.13. (A) Fluorescence emission spectra of Au NPs/RhB mixture in absence and presence of mixture of L-Cys with relevant amino acids, glutathione, ascorbic acid, uric acid and neurotransmitters. (B) The plot of relative fluorescence recovery efficiency (at 574 nm) from the assay of Au NPs/RhB when exposed to the aqueous solution of L-Cys mixed with various analytes. Figure also represents the relative fluorescence recovery efficiency of the assay when added separately with other amino acids, glutathione, uric acid, ascorbic acid and neurotransmitters.

recovery efficiency of RhB/Au NPs system when exposed to L-Cys in presence of other interfering essential and non-essential amino acids. This is because of the fact that the

physiological plasma medium contains other amino acids as well along with L-Cys. So, the study of fluorescence recovery from RhB/Au NPs mixed aqueous solution was carried out in presence of L-Cys mixed with other amino acids (0.1 mM) and is shown in Figure 5.13A. The corresponding fluorescence recovery efficiencies are also shown in Figure 5.13B. Interestingly it has been observed that the fluorescence recovery efficiency from RhB/Au NPs mixed solution in presence of L-Cys mixed with various other amino acids was nearly equal or close to that obtained with pure L-Cys only. These results suggest that in the presence of L-Cys, approximately 20-fold enhancement of the fluorescence recovery efficiency was obtained when compared to that in presence of other amino acids without L-Cys in the mixture. From this study it can also be concluded that the presence of more freely assessable –S atoms in L-Cys compared to that in case of all other amino acids, L-Cys binds to Au NPs surface via S–Au bonding competitively and selectively in faster way resulting the displacement of RhB molecules from Au NPs surface. Consequently, the fluorescence quenching due to FRET between RhB and Au NPs was reduced. This is why fluorescence intensity became much higher when L-Cys was present with other amino acids in aqueous medium. Therefore, the proposed technique may be an efficient sensing platform for highly selective determination of amino acid L-Cys in aqueous medium.

5.3.3.4. Real bio-sample analysis by using the fluorometric assay

The proposed fluorescence-based sensing mechanism for detection of L-Cys is also tested with real biosample in the present work. The L-Cys may present in both human blood plasma and urine. In our experiments we have used normal urine sample which was provided by our laboratory volunteer research student (male) having no renal complications. These experiments were performed with extra precaution to avoid any type of contamination or direct human contact with the urine sample. It is already known that [40] the excess amount of free L-Cys in urine causes the disease Cystinuria which leads to the formation of L-Cys stones in the renal system. The same assay condition was maintained while doing the real sample analysis. The fluorescence recovery was measured from the RhB/Au NPs system in presence of pure human urine, L-Cys and other amino acid mixed urine and are shown in Figure 5.14A. The corresponding fluorescence recovery efficiencies are shown in Figure 5.14B.

From Figure 5.14B it is observed that, the assay experiment with just pure urine sample shows nearly 35% fluorescence recovery whereas addition of L-Cys (0.1 mM,

200 µL) to the urine shows enhancement of fluorescence recovery efficiency up to 62%. The normal level of L-Cys in human urine is about 0.13 mmol/day [41] and any excess amount of L-Cys in the urine is therefore manifested as several health issues.

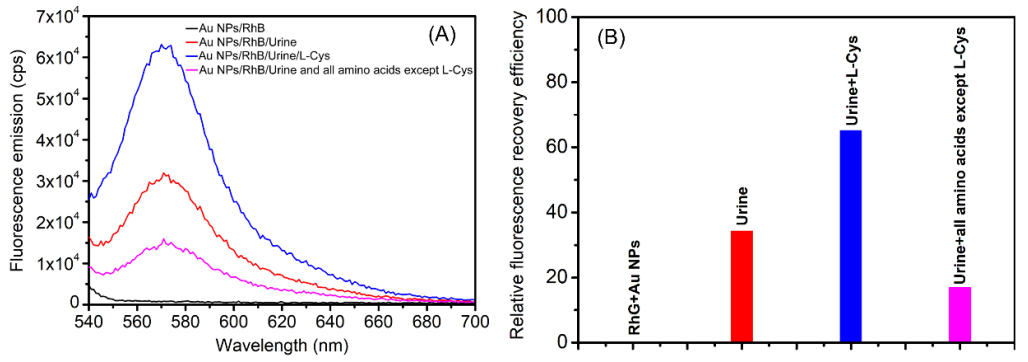

Figure 5.14. (A) Fluorescence emission spectra from the assay of Au NPs/RhB in absence and presence of normal human urine, mixed solution of L-Cys and urine and mixed solution of urine and other amino acids except L-Cys. (B) Plot of relative fluorescence recovery efficiency (at 574 nm) from the assay of Au NPs/RhB when exposed to the normal human urine, mixed solution of urine and L-Cys and urine and other amino acids except L-Cys.

Therefore, the initial fluorescence recovery with pure urine sample is basically due to usual presence of L-Cys in the urine. However, the increase of fluorescence recovery efficiency after addition L-Cys in the urine is a confirmation of selective detection of L-Cys because presence of all other amino acid did not show any significant rise in fluorescence recovery efficiency as observed from Figure 5.14B. Thus, the present mechanism may be a suitable method for the determination of L-Cys in the human urine sample in order to diagnose the disease Cystinuria.

5.3.4. Time resolved fluorescence emission spectroscopic study

The time resolved fluorescence emission spectroscopy is a useful and powerful method to know the excited state life time of fluorophore and the nature of quenching whether it is dynamic or static. In this study, the time resolved fluorescence emission of RhB aqueous solution (0.1 µM) was measured by using TCSPC method in absence and presence of Au NPs and L-Cys respectively using an excitation laser source of

wavelength of 510 nm and the corresponding fluorescence emission was monitored at 574 nm. The fluorescence decay plots as obtained were fitted by two exponential functions according to eqn. (5.2) and are shown in Figure 5.15. The average lifetimes of the samples were calculated according to eqn. (5.3) [23] and are summarized in Table 5.2.

$$I(t) = \alpha_1 e^{-t/\tau_1} + \alpha_2 e^{-t/\tau_2} \quad \ldots\ldots\ldots (5.2)$$

$$\tau_{av} = \frac{\sum_i \alpha_i \tau_i^2}{\sum_i \alpha_i \tau_i} \quad \ldots\ldots\ldots\ldots\ldots\ldots\ldots (5.3)$$

where α_1, α_2 are the normalized pre-exponential factors of the molecules with lifetime τ_1 and τ_2 respectively. τ_{av} is the average fluorescence life time. The average fluorescence life time of pure RhB was calculated as 1.384 ns [29] but it was decreased to 1.225 ns after the addition of Au NPs (0.1 mM). This decrease in fluorescence lifetime might be related to the reduced excited state energy of RhB molecules due to their adsorption onto Au NPs surface in solution as well as the non-radiative energy transfer from RhB to Au NPs and some extent of dye aggregation. The relationship between the intensity of fluorescence emission and the life time of fluorophore may be given as in eqn. (5.4) [36].

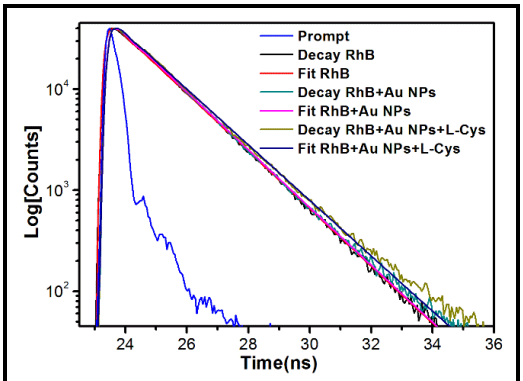

Figure 5.15. Fluorescence decay plots of RhB aqueous solution and of RhB/Au NPs mixed solution in absence and presence of L-Cys.

$$\tau_{obs} = \frac{1}{K_{obs}} = \frac{1}{K_r + K_{nr} + K_{et}} \quad \ldots\ldots\ldots\ldots\ldots (5.4)$$

That is the observed lifetime τ_{obs} is the inverse of the observed decay rates, radiative decay rate K_r, non-radiative decay rate K_{nr} and the rate of energy transfer K_{et}. For a particular organic dye in specific environment, both the radiative and non-radiative decay rates are normally considered as constant. From the steady state measurement, it was already observed that the decrease in radiative rate of RhB upon adsorption on to Au NPs was only 20% to the overall fluorescence quenching. Thus, the rate of energy transfer K_{et} is the major contributor to the decreased fluorescence lifetime of the fluorophore in presence of Au NPs which played the dominant role in fluorescence quenching. However, the most interesting observation was that when L-Cys solution

was added to the RhB/Au NPs mixed solution the average fluorescence lifetime of RhB molecules was again enhanced significantly to 1.342 ns which is almost close to that of pure dye molecules. More precisely the reversal of the fluorescence lifetime of RhB after addition of L-Cys is basically attributed to the availability of free RhB molecules in the surrounding aqueous medium of Au NPs/L-Cys conjugated systems. Therefore, this result also supports the fluorescence recovery of RhB molecules from their quenched state in the surface of Au NPs when exposed to L-Cys solution. The very small difference in the average lifetime in this case as compared to that of pure RhB may be due to the different microenvironment of the surrounding medium of dye molecules after addition of L-Cys because the dielectric properties of the medium might have changed [42]. This may slightly affect the decay path of the excited RhB molecules.

Table 5.2. Fluorescence life time parameters as obtained from the fitted data of pure RhB and RhB/Au NPs mixed solution in absence and presence of L-Cys. Corresponding fluorescence emission was monitored at 574 nm.

Sample name	Number of Exponential	λ_{ex} (nm)	τ_1 (ns)	α_1	τ_2 (ns)	α_2	τ_{av} (ns)	χ^2
RhB	2	510	0.066	0.375	1.522	0.156	1.384	1.276
RhB/Au NPs	2	510	0.037	1.311	1.517	0.129	1.225	1.156
RhB/Au NPs/L-Cys	2	510	0.048	0.788	1.577	0.132	1.342	1.279

λ_{ex}= Excitation wavelength

5.4. Conclusions

We have successfully developed a sensing platform for selective and quantitative detection of important bio-thiol namely L-Cys via fluorometric assay of RhB and Au NPs in aqueous medium as well as in real biosample (human urine). The LOD for L-Cys was found to be 0.01 μM in our experimental range of concentration. The initial fluorescence quenching of RhB in presence of Au NPs without L-Cys in the mixture was possibly dominated by FRET mechanism which depends upon the relative distance between dye and NPs. As the decrease in the radiative rate of RhB/Au NPs complex systems contributed only 20% of the overall fluorescence quenching, which also suggests that the excited state energy transfer was dominant factor for the drastic

fluorescence quenching. The selective fluorescence response of RhB/Au NPs complex molecular assemblies in presence of L-Cys in the mixture was also accompanied with a color change from wine to bluish-black which was not observed for all other amino acids including other thiol containing compounds, namely L-Methionine, L-Homocysteine, glutathione in the same aqueous environment. Additionally, the other relevant biosamples such as uric acid, ascorbic acid, neurotransmitters have shown negligible interference over the selective determination of L-Cys. However, the assay with real biosample shows about 35% fluorescence recovery occurred from the mixture. This is basically due to the usual presence of L-Cys in normal urine. In aqueous solution the thiol moiety in L-Cys formed strong bonding with the citrate caped Au NPs and might have displaced RhB molecules from the surface of Au resulting the aggregation of individual NPs as confirmed by UV–vis absorption spectroscopy. The TEM study confirmed that our synthesized Au NPs was nearly spherical with average diameter of 27.5 nm. DLS and Zeta potential studies revealed the homogeneity of Au NPs distribution in aqueous solution and did not aggregate prior to their use in the experiments. Fluorescence lifetime of RhB adsorbed onto Au NPs surface was reduced compared to that of pure RhB in aqueous solution as confirmed by TCSPC study. Addition of L-Cys in the mixture restored the fluorescence lifetime of pure RhB resulting the decrease of fluorescence quenching via FRET. Therefore, the present study may be proposed as an efficient sensing platform for selective and highly sensitive detection of L-Cys via fluorometric assay mechanism using Au NPs and RhB.

References

[1] E. G. Schulz, H. R. Schirmer, Principles of Protein Structure, (1st ed.), *Springer, New York*, 1978.

[2] W. Wang, O. Rusin, X. Xu, K. K. Kim, O. J. Escobedo, O. S. Fakayode, A. K. Fletcher, M. Lowry, M. C. Schowalter, M. C. Lawrence, R. F. Fronczek, M. I. Warner, M. R. Strongin, *J. Am. Chem. Soc.*, 127 (2005) 15949–15958.

[3] K. J. Nicholson, J. Connelly, C. J. Lindon, E. Holmes, *Nat. Rev. Drug Discov.*, 1 (2002) 153–161.

[4] K. R. Atkuri, J. J. Mantovani, L. A. Herzenberg, L. A. Herzenberg, *Curr. Opin. Pharmacol.*, 7 (2007) 355–359.

[5] S. K. Biswas, I. Rahman, *Mol. Asp. Med.*, 30 (1–2) (2009) 60–76.

[6] R. V. Kondratov, O. Vykhovanets, A. A. Kondratova, M. P. Antoch, *Aging*, 1 (12) (2009) 979–987.

[7] V. I. Lushchak, *J. Amino Acids*, 2012 (2011) 1–26.

[8] http://www.who.int/iris/handle/10665/43411.

[9] R. Janaky, V. Varga, A. Hermann, P. Saransaari, S. S. Oja, *Neurochem. Res.*, 25 (9–10) (2000) 1397–1405.

[10] J. D. Rimer, Z. An, Z. Zhu, M. H. Lee, D. S. Goldfarb, J. A. Wesson, M. D. Ward, *Science*, 330 (6002) (2010) 337–341.

[11] B. Halliwel, *Am. J. Med.*, 91 (1991) 14–22.

[12] J. T. Jarrett, *J. Biol. Chem.*, 290 (2015) 3972–3979.

[13] E. Mukwevho, Z. Ferreira, A. Ayeleso, *Molecules*, 19 (2014) 19376–19389.

[14] R. Glowacki, J. Stachniuk, K. Borowczyk, *Acta Chromatogr.*, 28 (2016) 333–346.

[15] M. Bouri, R. Salghi, A. Rios, M. Zougagh, *Anal. Lett.*, 49 (2016) 1221–1232.

[16] Z. Huang, Y. Yang, Y. Long, H. Zheng, *Anal. Methods*, 10 (2018) 2676–2680.

[17] G. Ziyatdinova, E. Kozlova, H. Budnikov, *Electrochim. Acta*, 270 (2018) 369–377.

[18] L. Chang, T. Wu, F. Chen, *Microchim Acta*, 177 (2012) 295–300.

[19] A. A. Ensafi, B. Rezaei, S. Nouroozi, *J. Braz. Chem. Soc.*, 20 (2009) 288–293.

[20] N. Narband, M. Uppal, C. W. Dunnill, G. Hyett, M. Wilson, I. P. Parkin, *Phys. Chem. Chem. Phys.*, 11 (2009) 10513–10518.

[21] N. Kometani, M. Tsubonishi, T. Fujita, K. Asami, Y. Yonezawa, *Langmuir*, 17 (2001) 578–580.

[22] M. C. Daniel, D. Astruc, *Chem. Rev.*, 104 (2004) 293–346.

[23] J. R. Lakowicz, Principles of Fluorescence Spectroscopy, (3rd ed.), *Plenum Press*, New York, 1983.

[24] D. Gust, T. A. Moore, A. L. Moore, *Acc. Chem. Res.*, 26 (1993) 198–205.

[25] F. Tam, G. P. Goodrich, B. R. Johnson, N. J. Halas, *Nano Lett.*, 7 (2007) 496–501.

[26] P. C. Ray, *Chem. Rev.*, 110 (9) (2010) 5332–5365.

[27] R. A. Sperling, W. J. Parak, *Philos. Trans. Royal Soc. A*, 368 (2010) 1333–1383.

[28] T. Karstens, K. Kobs, *J. Phys. Chem.*, 84 (14) (1980) 1871–1872.

[29] N. K. M. N. Srinivas, S. V. Rao, D. N. Rao, *J. Opt. Soc. Am. B*, 20 (12) (2003) 2470–2479.

[30] G. Frens, *Nat. Phys.*, 241 (1973) 20–22.

[31] X. C. Ma, Y. Dai, L. Yu, B. B. Huang, *Light Sci. Appl.*, 5 (2016) 16017–16029.

[32] S. D. Roy, M. Ghosh, J. Chowdhury, *J. Raman Spectrosc.*, 46 (2015) 451–461.

[33] N. R. Jana, L. Gearheart, C. J. Murphy, *Langmuir*, 17 (2001) 6782–6786.

[34] W. Zhao, M. A. Brook, Y. Li, *Chembiochem*, 9 (2008) 2363–2371.

[35] F. Chai, C. Wang, T. Wang, Z. Ma, Z. Su, *Nanotechnology*, 21 (2010) 25501–25506.

[36] A. Mocanu, I. Cernica, G. Tomoaia, L. D. Bobos, O. Horovitz, M. T. Cotisel, *Colloid. Surf. Physicochem. Eng. Asp.*, 338 (2009) 93–101.

[37] J. W. Olney, C. Zorumski, M. T. Price, J. Labruyere, *Science*, 248 (1990) 596–599.

[38] R. Cao, B. Li, *Chem. Commun.*, 47 (2011) 2865–2867.

[39] M. Bahram, E. Mohammadzadeh, *Anal. Methods*, 6 (2014) 6916–6924.

[40] E. Kaniowska, G. Chwatko, R. Głowacki, P. Kubalczyk, E. Bald, *J. Chromatogr. A*, 798 (1998) 27–35.

[41] C. S. Biyani, J. J. Cartledge, *EAU-EBU Update Ser.*, 4 (2006) 175–183.

[42] H. Chen, S. S. Ahsan, M. E. B. S. Berrios, H. D. Abrun, W. W. Webb, *J. Am. Chem. Soc.*, 132 (2010) 7244–7245.

****

CHAPTER ~ 6

Comparative and Selective Interaction of Amino Acid D-Cysteine with Colloidal Gold Nanoparticles in the Presence of a Fluorescent Probe in Aqueous Medium

This chapter demonstrates the study of comparative and selective interaction of amino acid D-Cysteine (D-Cys) with colloidal gold nanoparticles (Au NPs) and cationic dye Rhodamine B (RhB) in aqueous solution.

A research paper based on the work presented in this chapter has been published in ***ACS Omega 7 (2022) 29013−29026***
http://doi.org/10.1021/acsomega.2c02725

CHAPTER~6

Comparative and Selective Interaction of Amino Acid D-Cysteine with Colloidal Gold Nanoparticles in the Presence of a Fluorescent Probe in Aqueous Medium

6.1. Introductory remarks

The fundamental part of antibodies, signaling molecules, enzymes, hormones, receptors, and protein structures present in all living organisms is amino acids. They also act as biochemical rulers in the neurotransmission [1,2]. All of the amino acids present in the nature exist mainly in two forms: dextrorotatory (D) and levorotatory (L) enantiomers. On the basis of the protein-creating efficiency, there are in total 20 amino acids that have been reported. Previously, it was presumed that only L-amino acids were necessary in mammals, including humans, in the formation of components for proteins and peptides. However, various sensitive and selective analytical approaches developed for detecting chiral amino acids [3,4] suggested that diverse D-amino acids are also present in mammalian tissues. Different studies have been performed to explore the physiological functions of D-amino acids. The physiological and the biochemical activities of different D-amino acids such as D-cysteine (D-Cys), D-aspartate (D-Asp), Dalanine (D-Alan), D-serine (D-Ser) etc. in our nerve cells, skin, arterial walls, bones, other tissues, and body fluids, including amniotic fluid, urine, blood plasma, cerebrospinal fluid (CSF), saliva etc., have been systematically studied by various researchers in the last several years [5,6]. The semi-essential, proteinogenic amino acid cysteine ($C_3H_7NO_2S$) (abbreviated as Cys) contains thiol ($-SH$), amine ($-NH_2$), and carboxylic ($-COOH$) functional groups. The $-SH$ moiety mainly takes part in the nucleophilic enzymatic reactions [7]. Also, the $-SH$ group plays an important structural

role in the formation of many proteins by creating the disulfide derivative of Cys [8]. D-Cys creates hydrogen sulfide (H_2S) and decreases the disulfide bonds present in the receptors [8]. This may act synergistically and increase the responsiveness of neurotransmitters specifically to a particular activity. The deviant activity of receptors causes diseases in the central nervous system (CNS) such as amyotrophic lateral sclerosis, Alzheimer's disease, schizophrenia etc. [9,10] In the endocrine gland, H_2S prevents discharge of insulin due to glucose generation by the pernicious β cells [11]. Tong et al. showed that the biofilm formation of Streptococcus mutans and Streptococcus sanguinis on the surface of teeth could be controlled by free D-Cys [12].

In recent times, the study of the interactions of various proteins and amino acids with nanoparticles (NPs) has attracted great attention in the field of nano-biotechnology [13]. Among the various amino acids, D-Cys is also responsible for the growth of various diseases and disorders in the human body. Thus, the selective and quantitative recognition of D-Cys is very important for the diagnosis and treatments of various diseases. D-Cys can interact and be functionalized with several interesting metal NPs [13,14] because NPs possess significant adsorption capabilities due to their large surface area to volume ratio [15]. Sometimes this type of biomolecules can bind with such NPs via selective covalent interactions [16]. Among the various metal-based NPs, [17,18] noble metal NPs such as gold nanoparticles (Au NPs) show significant prospects regarding their potential in various fields of biomedical applications such as drug delivery [19], biomolecular sensing [20–22] etc. The high extinction coefficient of Au NPs in the visible region renders them as an efficient platform for signaling molecular recognition processes through their color change [21]. The small sizes of these metal NPs with a large surface curvature facilitate their binding with various organic dyes, proteins [16,18] etc. The degree of structural perturbation of the protein molecules due to their interaction with NPs varies for different protein species [23]. As the amino acids are the basic structural units of protein molecules, the study of the interaction of amino acids with Au NPs via a simple spectrofluorometric technique is of particular importance. The −SH-containing amino acid D-Cys is recognized as an important regulator of neurotransmitters and the overall neural cell dynamics in our physiological system. Therefore, a comparative study of the interaction of various forms of Cys and their chiral discrimination while interacting with Au NPs is important for both fundamental and biomedical interests.

This chapter demonstrates the interaction or reactivities of D-Cys and L-Cys as well as all other relevant amino acids, neurotransmitters etc. with citrate caped Au NPs in the presence of a fluorescent probe, namely rhodamine B (RhB), in aqueous medium as studied in my thesis work. RhB is a cationic organic dye with a high fluorescence quantum yield and has been used as an interesting signaling agent for various biomolecular recognition events [24,25]. The fluorescence emission of the RhB dye is almost fully quenched by the colloidal solution of Au NPs and the mechanism of the quenching has been described in detail in this work. The fully quenched fluorescence emission of this dye due to Au NPs in the aqueous solution is recovered via selective interaction with the amino acid D-Cys through SH−Au bond formation and aggregation of Au NPs. This interaction is also reflected as a distinct color change of the assay medium from red-wine to bluish-black, which is different from the interaction with L-Cys or any other interfering compounds studied in this work. The ratio-metric determination of the fluorescence recovery efficiency [26,27] in the presence of various analytes in the assay medium automatically eliminates the perturbation from any external influences during the assay. However, there are few recent reports on the detection of D-Cys based on various methods such as SRM-chromatography, colorimetric, ultra-high-performance liquid chromatography (UHPLC)-URMS-chromatography, electrokinetic chromatography [28−32] etc. However, the proposed fluorometric method, which is free from any direct leveling, offers great advantages for the detection of D-Cys, especially up to the nanomolar level. The aggregations of the Au NPs/RhB system in the presence of both the −SH-containing amino acids, D- and L- Cys, have been visualized by transmission electron microscopy (TEM) and atomic force microscopic (AFM) studies and are correlated with the observed Fourier transform infrared (FTIR), UV−vis absorption, and steady state fluorescence spectroscopic results. The different extents of interaction of D-Cys and L-Cys with the proposed Au NPs/RhB mixed system in aqueous medium are also distinguished by the chiral properties using the circular dichroism (CD) spectroscopic technique. Au NPs and the RhB-based fluorescence turn-on sensing platform are also tested with normal human (male) urine as a real biosample to realize the same selective response of the D-Cys present in urine.

6.2. Experimental section

6.2.1. Materials

All of the chemicals used in this work were of analytical grade and were used as obtained without further purification. Gold (III) chloride acid trihydrate ($HAuCl_4 \cdot 3H_2O$, MW: 393.83 $gmol^{-1}$), RhB ($C_{28}H_{31}ClN_2O_3$, MW: 479.02 $gmol^{-1}$), D-Cys ($C_3H_7NO_2S$, MW: 121.15 $gmol^{-1}$), and other D- and L-amino acids, ascorbic acid (AA) ($C_6H_8O_6$, MW: 176.12 $gmol^{-1}$), uric acid (UA) ($C_5H_4N_4O_3$, MW: 168.11 $gmol^{-1}$), glutathione (GSH) ($C_{10}H_{17}N_3O_6S$, MW: 307.33 $gmol^{-1}$), and homocysteine (Hcys) ($C_4H_9NO_2S$, MW: 138.18 $gmol^{-1}$), were purchased from Sigma-Aldrich Chemical Company. Trisodium citrate ($Na_3C_6H_5O_7$, MW: 258.06 $gmol^{-1}$), sodium chloride (NaCl, MW: 58.44 $gmol^{-1}$), and potassium chloride (KCl, MW: 74.5513 $gmol^{-1}$) were purchased from Merck Chemical Company, Germany. All of the glasswares were cleaned with freshly prepared aqua regia (mixture of HCl and HNO_3 in 3:1 ratio) followed by subsequent rinsing with triple distilled deionized Milli-Q water (resistivity 18.2 MΩ cm, pH~7 at 25°C, collected from Synergy integrated with an Elix Advantage setup; make: Millipore SAS, France) and then were autoclaved for 24 hrs before use. Aqueous solutions of the samples were also prepared with the same triple distilled deionized Milli-Q water.

6.2.2. Synthesis of Au NPs

The well-documented Frens' soft chemical reduction method has been used to obtain monodispersed gold nanocolloids with the desired particle size distribution [21,33]. In brief, an aliquot of a 50 mL aqueous solution of $HAuCl_4 \cdot 3H_2O$ (0.25 M) was heated to boil and 1.2 mL of $Na_3C_6H_5O_7$ (1%) was added into the solution under vigorous stirring for the formation of gold nanocolloids. In about 100 s, the boiling solution turned faintly blue. After 120 s, the blue color changed to deep red, which indicates the formation of the spherical Au NPs. The synthesized nanocolloidal solution was set aside to cool down to room temperature and stored at 4°C for future use. The final concentration of the aqueous gold nanocolloidal solution was 0.1 mM at pH~7 in ambient temperature.

6.2.3. Characterization techniques

High-resolution transmission electron microscopy (HRTEM) measurements, energy-dispersive spectroscopy (EDS) images, and selected area electron diffraction (SAED) patterns of the Au NPs were collected using a field emission transmission electron microscope (JEM-2010 TEM, JEOL Ltd., Japan) operated at an accelerating voltage of 200 kV. For the HRTEM study, the sample solutions were incubated for 15 min and then a small drop from each solution was spread onto the carbon-coated copper microgrid (PELCO 300 Mesh Grids, Ted Pella Inc.) and subsequently dried at room temperature (25°C). The hydrodynamic nanoparticle size and the effective surface ζ potential of the as-synthesized Au NPs were obtained by a Zetasizer (Zetasizer Nano ZS, Malvern Instruments Ltd., U.K.) via the dynamic light scattering (DLS) method at ambient condition. The UV−vis absorption spectra of the samples were obtained in the wavelength range of 200−800 nm by a double beam UV−vis absorption spectrophotometer (UV-1800, Shimadzu, Japan) after proper baseline correction for the solvent background. The steady-state fluorescence emission spectra of the sample solutions were recorded using a spectrofluorometer (Fluoromax-4C, Horiba Instruments Incorporated, USA) under the following conditions: excitation and emission monochromator slit widths of 2 nm each, excitation wavelength of 530 nm, emission wavelength range of 540−700 nm, and experimental temperature of 25°C. Fluorescence-grade quartz cuvettes (path length 1.0 cm, Kozima, Japan) were used in all of the absorption and fluorescence emission measurements. CD spectroscopic measurements were carried out using a JASCO J-815 CD spectrometer (JASCO International Co., Ltd., Japan). The surface morphology and roughness measurement of the samples were performed using a commercially available atomic force microscope (AFM) (NaioAFM, Nanosurf, Germany) in tapping mode in a humidity-controlled environment. For AFM analysis, the freshly prepared Au NPs aqueous colloidal dispersion and a mixture of Au NPs/RhB in the presence of D-Cys and L-Cys, respectively, were deposited onto smooth glass substrates. FTIR spectra of the samples were recorded using a FTIR spectrometer (model: Spectrum Two, make: Perkin Elmer Inc.) in attenuated total reflection (ATR) mode at ambient temperature. The pH of the aqueous solutions was measured using a digital pH meter (FiveEasy Plus, Mettler Toledo, Germany).

6.2.4. Sample preparation for the spectrofluorometric measurements

The Au NPs/RhB mixed solution was prepared by adding 2 mL of freshly prepared Au NPs of concentration 0.1 mM into 2 mL of freshly prepared RhB of concentration 0.1 μM at ambient condition. Thus, the final concentrations of the Au NPs and RhB in the total 4 mL mixed solution were 0.05 mM and 0.05 μM, respectively. The pH of the RhB aqueous solution was 7.0 and remained approximately constant through the whole analysis. Then, a freshly prepared 200 μL aqueous solution of each concentration of D-Cys (concentration range from 1000 μM to 1 nM) was added to the Au NPs/RhB mixed ensemble separately and incubated for 3 min at room temperature (25°C). Also, the D-Cys aqueous solution was prepared by using ultrapure triple distilled Milli-Q water at pH∼7.0. The final concentrations of D-Cys in all of the Au NPs/RhB/D-Cys mixed solutions were in the range 0.0476 nM to 47.6 μM. After the incubation period of 3 min, colorimetric images, the UV−vis absorption, and steady-state fluorescence emission spectra of the Au NPs/RhB/D-Cys complex were recorded immediately. Also, aqueous solutions (fixed concentration of 0.1 mM) of other relevant D- and L- amino acids such as D-arginine (D-Arg), L-arginine (L-Arg), D-histidine (D-His), L-histidine (L-His), D-methionine (D-Met), L-methionine (L-Met), D-proline (D-Pro), L-proline (L-Pro), D-tryptophan (D-Trp), L-tryptophan (L-Trp), D-tyosine (D-Tyr), L-tyosine (L-Tyr), L-cysteine (L-Cys), and other −SH-containing compounds like glutathione (GSH) and homocysteine (Hcys) as well as some different biomolecules such as ascorbic acid (AA), uric acid (UA), and neurotransmitters (Na^+ and K^+) were prepared in the same ambient condition. A 200 μL aqueous solution of each compound was added separately to the Au NPs/RhB mixed solution and incubated for 5 min at ambient condition prior to the spectrofluorometric measurements. The 5 min incubation time used for other analytes except D-Cys was just to confirm whether these other compounds have any effect on the proposed interaction even after a longer time of incubation compared to that of D-Cys.

6.3. Results and discussions

6.3.1. Characterizations of the Au NPs

The UV−vis absorption spectroscopic data were recorded to explore the optical absorption properties of the as-synthesized citrate stabilized colloidal aqueous

dispersion of Au NPs and are shown in Figure 6.1a. The figure shows a distinct absorption band with its maximum at around 528 nm due to the strong characteristic surface plasmon resonance (SPR) of the Au NPs. Also, there are two weak humps observed at 251 and 356 nm, which are mainly attributed to the intra-band electronic transitions of gold [34]. The sharp and well-resolved SPR maximum band is originated basically due to both the longitudinal and transverse SPR equivalently, which is an

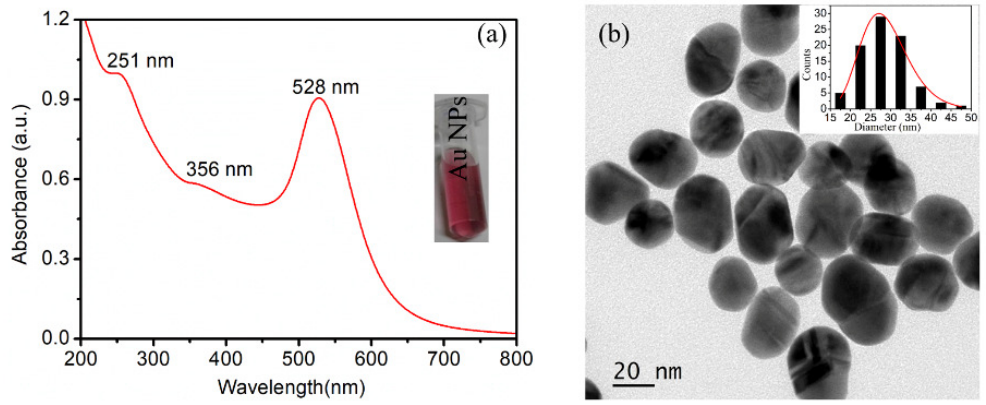

Figure 6.1. (a) UV−vis absorption spectrum of as-synthesized Au NPs' colloidal dispersion and (b) TEM micrograph of the as-synthesized Au NPs. The insets of (a) and (b) show the digital micrographs of the vial containing as-synthesized Au NPs' dispersion and lognormal fitting of the NPs' size distribution curve, respectively.

indication of the formation of spherical Au NPs [35]. The average hydrodynamic diameter of the colloidal Au NPs as obtained from the DLS study was about 48.04 nm (as shown in Figure 6.2a). The surface ζ potential of the Au NPs was found to be −30.1

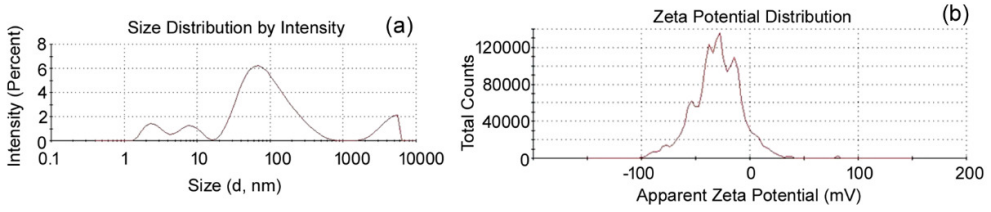

Figure 6.2. (a) Dynamic light scattering (DLS) and (b) Zeta potential spectra of as-synthesized citrate caped Au NPs colloidal dispersion at room temperature (25 °C) and pH∼7.

mV (as shown in Figure 6.2b). The high negative ζ potential reveals the homogeneity and stability of the NPs in the aqueous colloidal dispersion.

On the other hand, the TEM micrograph as shown in Figure 6.1b gives the visual evidence that Au NPs were monodispersed with nearly spherical shape and the average particle diameter was ~27.5 nm, as is evidenced from the lognormal fitting of the particles' size distribution curve (the inset of Figure 6.1b and Figure 6.3a). The good crystalline nature of the Au NPs was shown by the SAED pattern (as shown in Figure 6.3b). The rings as shown in SAED were indexed as (311), (222), and (400) and correspond to the electron diffractions originated from the planes of the face-centered cubic (FCC) gold crystal [36]. The interplanar spacing of the as-synthesized FCC Au NPs was 0.11 nm for the (222) plane as calculated from the HRTEM micrograph (as shown in Figure 6.3c). The EDS spectrum (as shown in Figure 6.3d) reveals that the nucleation of Au NPs occurred without any impurities and confirms the presence of a large number of NPs in its aqueous colloidal dispersion.

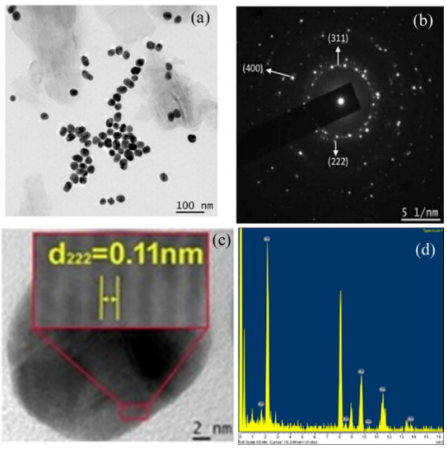

Figure 6.3. (a) TEM micrograph, (b) SAED pattern with lattice plane indices, (c) HRTEM image and (d) EDS spectrum of as-synthesized citrate caped Au NPs.

6.3.2. UV–vis absorption spectroscopic study

The UV–vis absorption spectroscopic measurements were carried out by adding D-Cys and other D- and L-amino acids, neurotransmitters, AA, UA, including other –SH-containing compounds such as Met, HCys, GSH etc., to the mixed solution of Au NPs and RhB (aqueous mixture of Au NPs (0.1 mM) and RhB (0.1 μM) in 1:1 volume ratio). Figure 6.4a shows the UV–vis absorption spectra of pure RhB (0.1 μM) (curve 1) along with the mixture of RhB and Au NPs in aqueous solution (curve 2). The concentrations of Au NPs and RhB in the mixed solution were 0.05 mM and 0.05 μM, respectively. The inset of Figure 6.4a shows the molecular structure of the laser dye

RhB. The UV−vis absorption spectrum of pure RhB exhibits a strong absorption band at around 554 nm, which is attributed to the π−π* transition of the dye monomer unit, and a weak hump is observed at around 520 nm, which is originated from the n−π* transition due to the presence of dimeric units [24]. The UV−vis absorption results of the mixed solution further reveal that the monomeric absorption peak of RhB remains unaltered but with decreased intensity, whereas the dimeric band intensity (520 nm) increases. This variation of the absorption intensity may possibly be due to the closure association of the RhB molecules adsorbed onto the NPs' surface. As RhB is a cationic

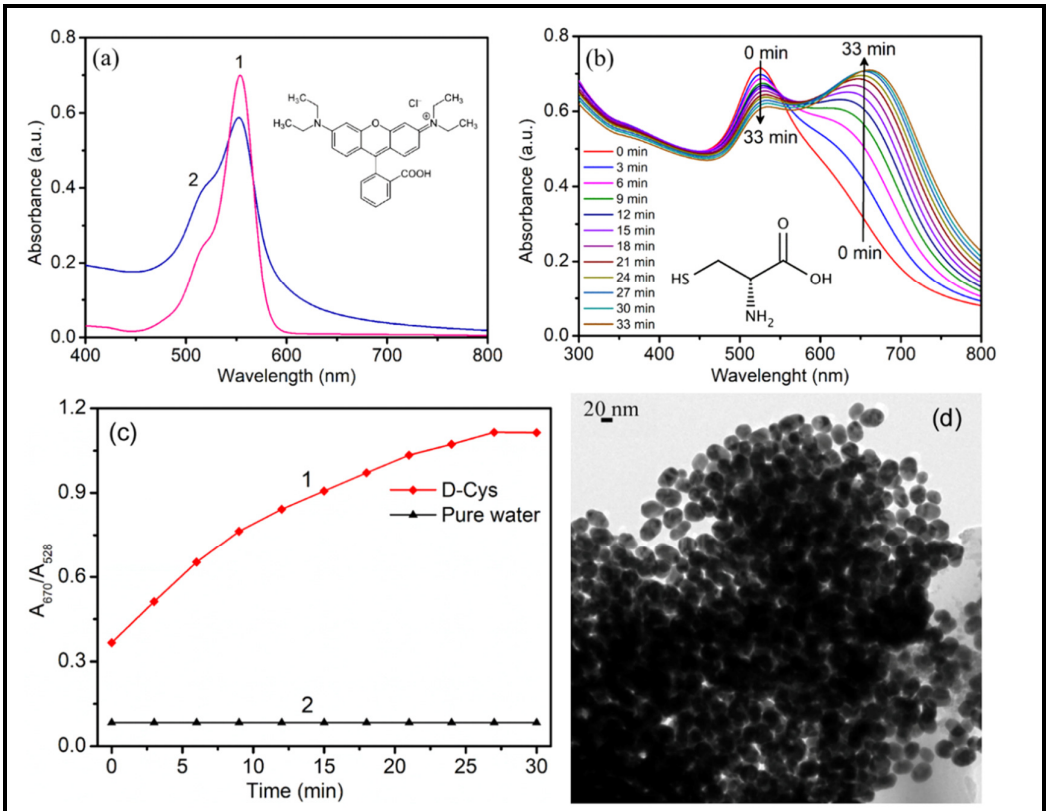

Figure 6.4. UV−vis absorption spectra of (a) pure RhB aqueous solution (curve 1), Au NPs/RhB mixed solution (curve 2) and (b) mixed solution of Au NPs and D-Cys recorded at different intervals of time. (c) Ratio of the absorbance at 670−528 nm of Au NPs after addition of D-Cys (curve 1) and pure water (200 µL) (curve 2). (d) TEM micrograph of Au NPs/D-Cys mixed sample. The insets of (a) and (b) show the molecular structure of RhB and D-Cys, respectively.

dye and citrate caped Au NPs have a large negative surface ζ potential, the strong electrostatic interaction between Au NPs and RhB is mainly responsible for the adsorption of the dye molecules on the NPs' surface, resulting in the change in the absorption behavior of the dye molecules in their aqueous mixed solution. The number of dye molecules (N_{dye}) linked with each Au NP is determined using the relation [37] (equation 6.1) (eqn. 6.1)

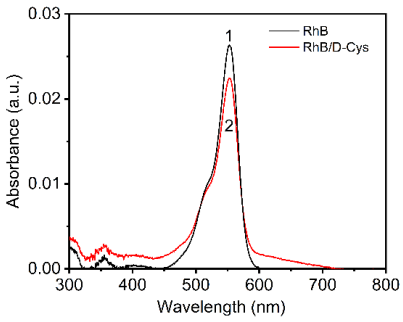

Figure 6.5. UV-vis absorption spectra of RhB aqueous solution in absence and presence of D-Cys.

$$N_{dye} = \frac{n_{Au}}{\{[\text{Au NPs}]/[\text{RhB}]\}} \quad \ldots\ldots\ldots (6.1)$$

where n_{Au} is the number of gold atoms in each NP. The number of gold atoms per NP (n_{Au}) is calculated by using the expression [37,38] $n_{Au}=(\pi/6)(59\ \text{nm}^{-3})(dav)^3$, where d_{av} is the mean diameter of the Au NPs. Thus, in this case, an Au NP of average diameter 27.5 nm is composed of 642138 gold atoms. In the mixed solution of Au NPs (0.1mM) and RhB (0.1 μM), 642 dye molecules are adsorbed on each Au NP surface.

On the other hand, the UV−vis absorption spectrum of RhB in the presence of D-Cys as shown in Figure 6.5 reveals that there is no appreciable effect of D-Cys on the absorption behavior of RhB in the mixed solution of RhB and D-Cys. The concentration of RhB was kept fixed for all of these mixed solutions, which were prepared using RhB and the Au NPs solution in 1:1 volume ratio. The UV−vis absorption spectra of the Au NPs (concentration of 0.1 mM) recorded at different intervals of time after addition of the aqueous solution of D-Cys (concentration of 0.1 mM) are shown in Figure 6.4b. The respective concentrations of Au NPs and D-Cys in the mixed solution were 0.09 mM and 6.25 μM. The inset of Figure 6.4b shows the molecular structure of D-Cys. The additional band of Au NPs observed at around 670 nm is originated due to the strong interaction of D-Cys with the citrate caped Au NPs in the mixed aqueous solution. The absorbance of the main SPR band at around 528 nm gradually decreases and the new band at 670 nm systematically increases with the incubation time for the mixed solution. The absorbance ratio (A_{670}/A_{528}) of the Au NPs colloidal dispersion, as shown in Figure 6.4c, increases with the incubation time in the

presence of D-Cys. This is possibly due to the strong cooperative metal ion-ligand interactions [39]. Because of this interaction, the citrate layer on the NP's surface may be displaced and the interparticle separations of the NPs are possibly reduced due to the subsequent cross-linking through the amino groups of D-Cys. As a consequence, the increased dipole–dipole interactions and the coupling between neighboring plasmons eventually induced the formation of aggregates or clusters [39,40] of Au NPs. This aggregation is manifested as the emergence of the additional band at around 670 nm in the UV–vis absorption spectra [41,42]. In order to have direct visual evidence for the formation of aggregates or clusters of NPs, TEM analysis was also performed. Figure 6.4d shows the TEM image of the Au NPs/RhB/D-Cys mixed sample and clearly shows very dense and aggregated domains of the NPs when compared to the TEM image of pure Au NPs as shown in Figure 6.1b. This aggregation eventually induces enhanced dye–dye intermolecular interaction in the mixed solution of Au NPs and RhB. As a result, the RhB molecules might have altered electric transition dipole moments in the microenvironment of Au NPs [43].

6.3.3. Interaction of D-Cys with the Au NPs/RhB mixed solution

To understand the interaction of D-Cys with the Au NPs/RhB mixed ensemble in aqueous medium and the related photophysical properties, steady-state fluorescence emission measurements were performed. It is observed from Figure 6.6a that the steady-state fluorescence emission intensity of the peak at around 574 nm of RhB in the Au NPs/RhB mixed aqueous solution (1:1 volume ratio) is almost quenched for an Au NP concentration of 0.05 mM in the mixed solution at ambient condition. It is important to mention that the electrostatic interaction between the dye molecules and the negatively charged citrate layer on the Au NPs or any formation of H bonds does not change the electronic transition dipole moment of the xanthene moiety of the RhB molecules [44] as there is no shift of the emission band (574 nm) of dye molecules after photoexcitation of the Au NPs/RhB mixed ensemble in the absence or presence of D-Cys. Therefore, the effect of direct molecule on nanoparticle interaction may be excluded from the initial fluorescence quenching of RhB molecules in the presence of Au NPs. Additionally, the possibility of dynamic collisional quenching of fluorescence may be less due to the existence of a strong electrostatic interaction between the RhB molecules and negatively charged citrate caped Au NPs in the studied aqueous medium.

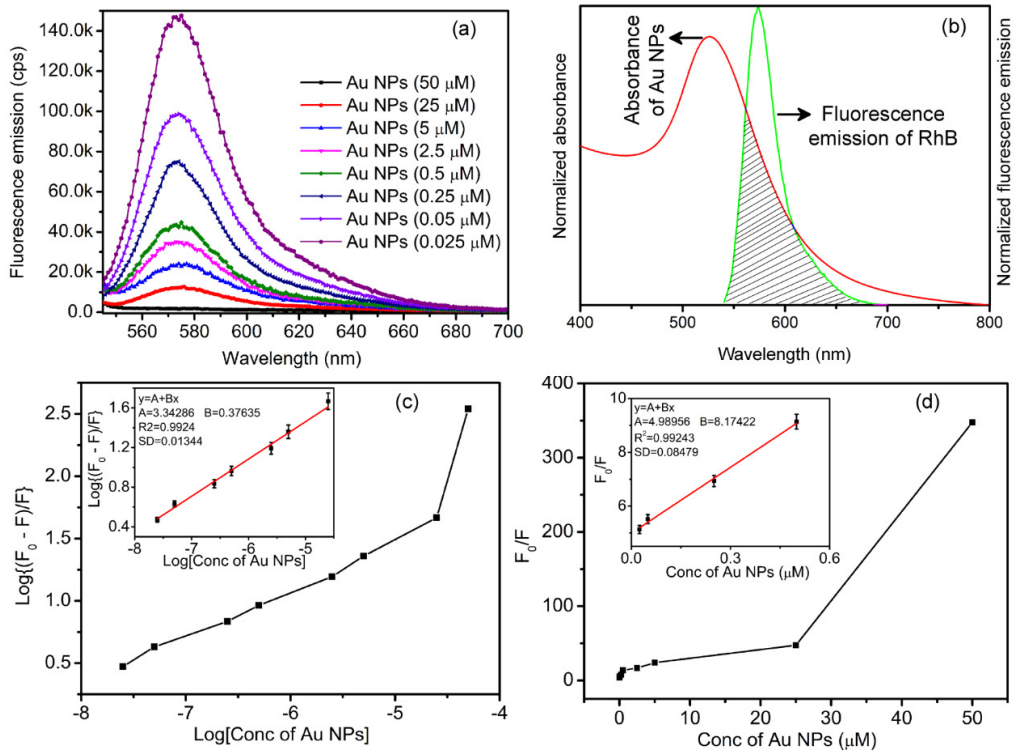

Figure 6.6. (a) Fluorescence quenching of RhB in presence of Au NPs of different concentrations (b) Spectral overlap between absorption and fluorescence emission spectra of Au NPs and RhB respectively. (c) Plot of Log{(F_0–F)/F} vs. Log[Conc of Au NPs]. Inset shows the straight-line region of the Log{(F_0–F)/F} vs. Log[Conc of Au NPs] plot. (d) Stern-Volmer (SV) plot. Inset shows the straight-line region of the SV plot.

Interestingly, there is a sufficient spectral overlap between the absorption spectrum of Au NPs and fluorescence emission spectrum of RhB as shown in Figure 6.6b. So, the observed quenching of fluorescence emission (574 nm band) of RhB in the Au NPs/ RhB mixed solution is mostly due to the efficient nonradiative energy migration through the resonance energy transfer (RET) process using the dipole–dipole resonance interaction between the excited RhB dye (donor) molecules and Au NP surface (acceptor), as well as the decrease in the radiative rate constant of individual RhB molecules when they are adsorbed onto the NPs' surface [21,43]. This resonance energy transfer process is a distance-dependent phenomenon and therefore the concentration

of the Au NPs (acceptor) plays a significant role in controlling the relative distance between the donor and acceptor sites in the mixed solution. The RET efficiency (E) is calculated using the expression [44,45] (eqn. 6.2)

$$E = 1 - \frac{F}{F_0} \ldots\ldots\ldots\ldots\ldots\ldots\ldots\ldots (6.2)$$

where F_0 and F are the fluorescence emission intensity of RhB in the absence and presence of Au NPs, respectively. The value of energy transfer efficiency (E) is estimated as 0.9989, considering the fluorescence spectrum of Au NPs/RhB with concentrations of RhB and Au NPs as 0.05 μM and 0.05 mM in the mixed solution, respectively. The value of the binding constant (K_b) to a binding site and the number of binding sites (n) per RhB molecule in the Au NPs/RhB mixed aqueous solution are determined from the fluorescence quenching data of RhB in the presence of Au NPs by using the following eqn. 6.3 [46]

$$Log\left\{\frac{F_0 - F)}{F}\right\} = LogK_b + nLog[Q] \ldots\ldots\ldots\ldots\ldots\ldots\ldots\ldots (6.3)$$

where [Q] is the corresponding quencher (Au NPs) concentration. The values of K_b and n are calculated from the intercept and slope of the plot as shown in Figure 6.6a,c and are found to be 2.202×10^3 M^{-1} and 0.376, respectively. The change in Gibbs free energy (ΔG) for the interaction between RhB and Au NPs at room temperature ($25°C$) is obtained using the Gibbs–Helmholtz relation [46] $\Delta G = -RTlnK_b$, where R is the universal gas constant and T is the temperature. The calculated value of ΔG is -19.07 kJ mol^{-1}. The negative ΔG value indicates that the interaction between RhB and Au NPs is spontaneous. Also, the quenching of the fluorescence emission of RhB by Au NPs is further described by the well-known Stern–Volmer eqn. 6.4 [47]

$$\frac{F_0}{F} = 1 + K_{SV}[Q] \ldots\ldots\ldots\ldots\ldots\ldots\ldots\ldots (6.4)$$

where K_{SV} is the Stern–Volmer quenching constant. The deviation from linearity of the Stern–Volmer plot at higher quencher concentration implies that the fluorescence quenching of the RhB dye is a mixture of static and dynamic (diffusion) quenching [48]. Considering the slope of the straight line region of the F_0/F vs [Q] plot (i.e., at lower concentrations of Au NPs) as shown in Figure 6.6a,e, the value of K_{SV} is calculated as 8.174×106 M^{-1}. The bimolecular fluorescence quenching rate constant (K_q) and K_{SV} are related by the relation [49] $K_q = K_{SV}/\tau_0$, where τ_0 is the fluorescence emission lifetime of pure RhB (1.384 ns) [21]. The value of K_q is calculated as 5.906

$\times$ 1015 $M^{-1}s^{-1}$ for this fluorometric titration experiment. The high values of both K_{SV} and K_q substantiate the efficient quenching of RhB (donor) fluorescence by Au NPs in the aqueous medium. All of the above calculated photophysical parameters are summarized in Table 6.1.

Table 6.1. Binding constant (K_b), binding sites (n), Gibbs free energy (ΔG), Stern-Volmer constant (K_{SV}), quenching rate constant (K_q) for Au NPs/RhB mixed aqueous solution. R^2 is the corresponding correlation coefficient.

K_b (M^{-1})	n	R^2	ΔG (kJmol^{-1})	K_{SV} (M^{-1})	R^2	K_q ($M^{-1}s^{-1}$)
2.202×10^3	0.376	0.9924	-19.07	8.174×10^6	0.9924	5.906×10^{15}

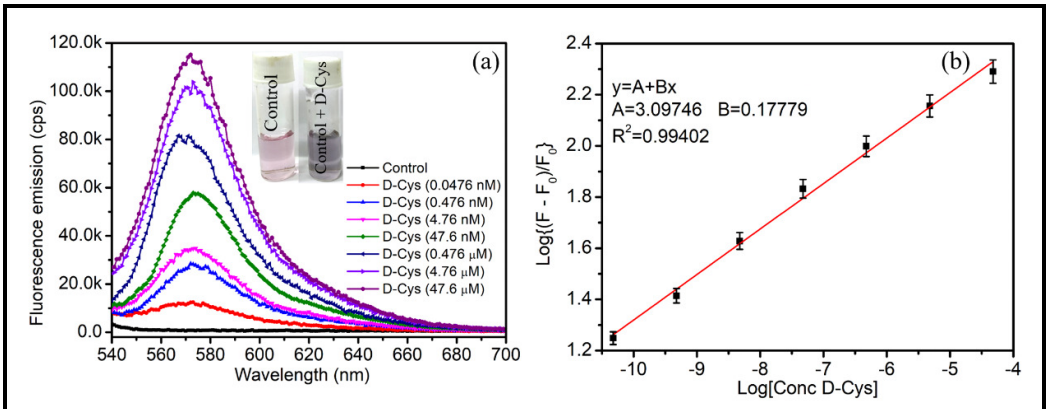

Figure 6.7. (a) Recovery of fluorescence emission from the Au NPs/RhB mixed solution when added with D-Cys of various concentrations. (b) Plot of fluorescence recovery efficiency from Au NPs/RhB mixed solution for various concentrations of D-Cys. The inset of (a) shows the digital micrographs of the vial containing the Au NPs/RhB mixed solution before (control) and after incubation with D-Cys.

However, interestingly, after addition of D-Cys to the mixed solution of Au NPs and RhB, the original fluorescence emission (574 nm) of dye molecules is recovered from their quenched state as shown in Figure 6.7a. The concentrations of RhB and Au NPs for the assay experiments were optimized in such a way that there is an almost complete quenching of the fluorescence emission of RhB in the Au NPs/RhB mixed system before addition of the D-Cys solution when excited with light of wavelength 530 nm and recovery of fluorescence signal in the presence of D-Cys at ambient

condition. This "turn-off" and "turn-on" mechanism of fluorescence emission due to the presence of D-Cys in the assay medium is schematically shown in Figure 6.8.

For the assay experiments, the concentrations of RhB and Au NPs in their aqueous mixture were fixed at 0.05 μM and 0.05 mM, respectively. These selected concentrations of RhB and Au NPs in their aqueous solution at ambient condition may be considered as an optimized condition for the fluorescence recovery from the mixed ensemble when exposed to D-Cys in aqueous medium. Here we have studied the recovery of fluorescence emission from the Au NPs/RhB mixed solution in the absence (control) and presence of various concentrations of D-Cys. Also, there is a distinct color change of the mixed final solution from red-wine (control) to bluish-black (after addition of D-Cys) as shown in the inset of Figure 6.7a. From the fluorescence emission of RhB in the presence of different concentrations of D-Cys (viz. 0.06 nM to 62.5 μM in the mixed solution) as shown in Figure 6.9, it is further confirmed that there is no significant effect of D-Cys on the fluorescence emission properties of RhB in aqueous solution as the emission spectra of the RhB/D-Cys mixed solution for all concentrations of D-Cys are almost unaltered.

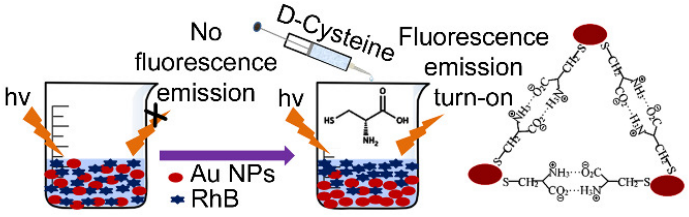

Figure 6.8. Schematic presentation of the proposed fluorescence "off–on" mechanism and chemical coordination between the D-Cys molecules and citrate caped Au NPs.

Therefore, RhB dye has been considered as a good and efficient fluorescent probe for recognition of the amino acid D-Cys in aqueous medium via a simple spectrofluorometric method in the present work. It is known that at neutral or under near-physiological pH,

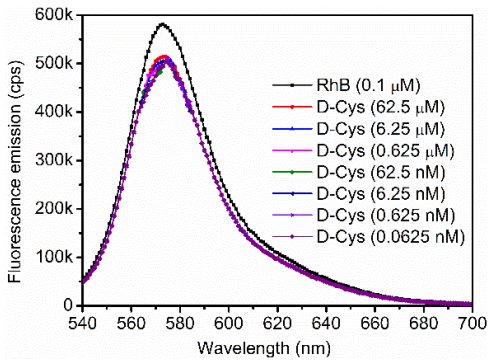

Figure 6.9. Fluorescence emission spectra of RhB in absence and presence of different concentrations of D-Cys.

citrate caped Au NPs possess three carboxylated ($-COO^-$) groups [50], whereas the D-Cys molecule has $-SH$, $-COO^-$ groups, and the amino group (NH_3^+) in the same aqueous environment. The citrate layer surrounding the Au NPs in aqueous dispersion gives an overall strong negative surface potential as is already confirmed by the ζ potential study (as shown in Figure 6.2b). It is already reported elsewhere that at neutral pH (7.0) cysteine is neutral [51], due to which there will be very less possibility of citrate caped Au NPs having direct interaction with D-Cys through its $-NH_2$ group via electrostatic attraction [42]. However, due to the strong affinity of the $-SH$ moiety of D-Cys towards the Au NPs' surface, they try to encapsulate [41] Au NPs by thiolate–Au bond formation via chemisorption [39], which eventually displaces the original citrate layer of Au NPs. As a consequence, the RhB molecules that were adsorbed onto the citrate caped nanoparticles' surface by electrostatic interaction [52] now become free in the surrounding environment. This is why the intrinsic fluorescence emission of RhB with peak centered at 574 nm is retrieved after photoexcitation. However, the displacement of the citrate layer of Au NPs should depend upon various factors like the concentration of D-Cys molecules in the assay medium, overall charge distribution, surface potential around the nanoparticle surface, temperature etc. Immediately after the reaction of D-Cys with Au NPs/RhB systems, the presence of amino acid molecules in the encapsulating shell of NPs starts to induce crosslinking (as shown schematically in Figure 6.8 between the neighboring encapsulated Au NPs) in the mixed solution, resulting in the formation of Au NP aggregates or clusters, which causes a color change of the mixed solution from red-wine to bluish-black [53,54] after the reaction. The aggregation of Au NPs in the presence of D-Cys is already evidenced by the UV–vis absorption (Figure 6.4b) and TEM study (Figure 6.4d) as discussed earlier. From the above discussion, it is clear that the fluorescence emission band intensity at 574 nm of the mixed solution of Au NPs and RhB is recovered after addition of D-Cys and this fluorescence recovery is most probably due to the availability of free RhB molecules in the mixed ensemble. Overall, due to the interaction of D-Cys with the Au NPs/RhB system in solution, the relative distance between the dye molecules and Au NPs might have increased, resulting in the decrease of fluorescence quenching via nonradiative energy transfer pathways.

6.3.4. Sensitivity of the interaction of the Au NPs/RhB mixed ensemble towards D-Cys

In this work, it is important to understand the sensitivity of the interaction of D-Cys with Au NPs/RhB mixed aqueous solution. It is observed that under the optimized experimental condition, the fluorescence emission intensity obtained from the Au NPs/ RhB/D-Cys mixed solution increases almost linearly with the increase in concentrations of D-Cys. The relative fluorescence recovery efficiency is defined by $[(F-F_0)/F_0]$ and is given by the following linear eqn. 6.5 [52]

$$\mathrm{Log}\left[\frac{(F-F_0)}{F_0}\right] = \mathrm{Log}\,[C] + A \ldots\ldots\ldots\ldots\ldots\ldots\ldots\ldots \quad (6.5)$$

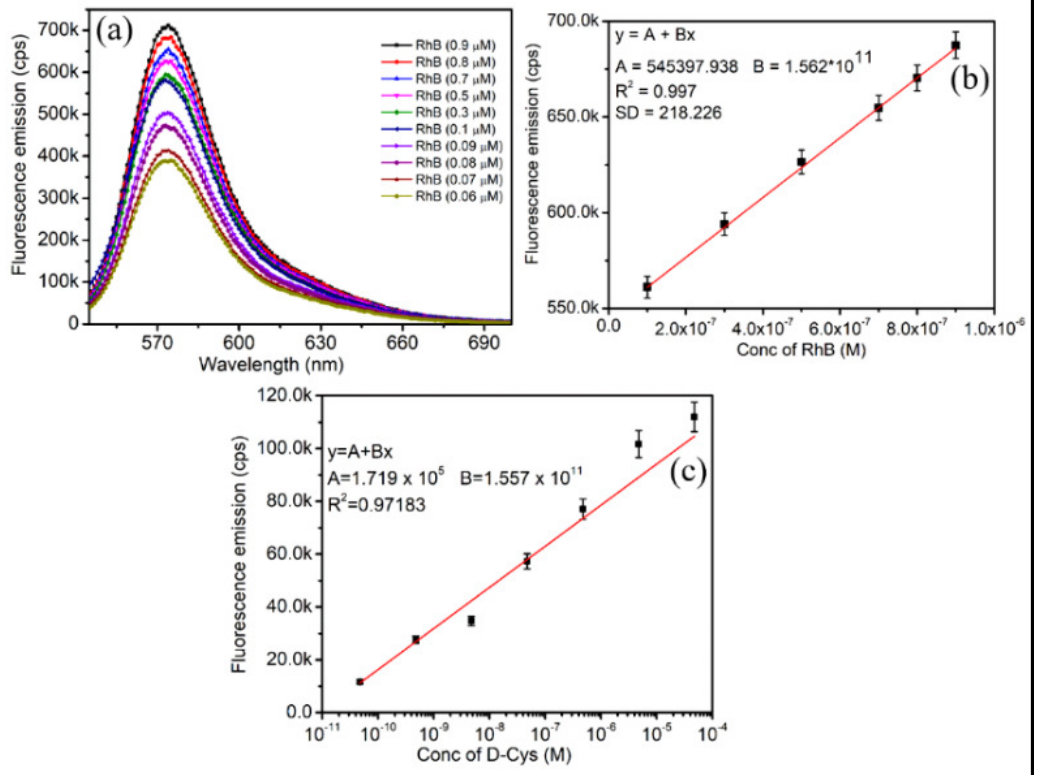

Figure 6.10. (a) Fluorescence emission spectra of different concentration of RhB. (b) Plot of fluorescence emission vs. concentration of RhB. (c) Plot of recovered fluorescence emission from Au NPs/RhB mixed solution vs. concentrations of D-Cys.

where C is the concentration of D-Cys and A is an arbitrary constant. The relative fluorescence recovery efficiency and the concentration of D-Cys follow the linear equation $y = 3.09746 + 0.17779[C]$ with a correlation coefficient (R^2) of 0.99402 as shown in Figure 6.7b, and the concentration range of 0.004 nM to 47.6 μM in the Au NPs/RhB mixed ensemble. Thus, this method of recovery of fluorescence emission shows very high sensitivity to a broad linear range of concentrations of D-Cys.

To compare the sensitivity of Au NPs/RhB towards D-Cys, the limit of detection (LOD) has been determined by the 3σ method [55] using the expression LOD=(k×SD)/S, where S is the slope of the recovered fluorescence emission from the Au NPs/RhB vs concentration of D-Cys (in M) plot. The LOD value of D-Cys (as shown in Figure 6.10a-c) is found to be 4.2 nM. This LOD value indicates that the proposed Au NPs/RhB mixed ensemble is highly sensitive towards D-Cys for spectrofluorometric measurement. The linear range and LOD of D-Cys determination as previously reported in the different studies have been compared with the present work and summarized in Table 6.2.

Table 6.2. Comparisons of the Analytic Methods for the Determination of D-Cysteine.

Probe/systems	Detection principle	Range (in μM)	LOD (in nM)	Ref.
4-fluoro-7-nitrobenzofurazan	SRM-Chromatogram	0 – 300	–	[28]
Ag NPs-embedded nanopaper	Colorimetric	–	4880	[29]
NCS-OTPP[a]	UHPLC-HRMS-Chromatograms	0.098 – 1000	19.20	[30]
Polar ionic elution[b]	Chiral UHPLC-MS	0.413 – 4.13	165.08	[31]
L-Carnitine methyl ester bis	Electrokinetic Chromatography	10 – 150	1100	[32]
Au NPs/RhB mixed system	Colorimetric & Fluorometric assay	0.001 – 100	4.2	**This work**

[a](R)-(5-(3-isothiocyanatopyrrolidin-1-yl)-5-oxopentyl)triphenylphosphonium,
[b]MeOH/MeCN/H_2O 49/49/2 v/v/v

6.3.5. Selectivity study of the proposed bio-nano interactions

The selectivity of the interaction of the Au NPs/RhB mixed solution towards D-Cys in the presence of other relevant interfering analytes such as AA, UA, neurotransmitters, other D- and L-amino acids including D-Arg, L-Arg, D-His, L-His,

D-Met, L-Met, D-Pro, L-Pro, D-Trp, L-Trp, D-Tyr, L-Tyr, L-Cys, –SH-containing compounds like GSH and Hcys etc. is tested under the same optimized experimental conditions of the Au NPs/RhB mixed solution and the corresponding fluorescence emission spectra are illustrated in Figure 6.11a. The chemical structures of all of the

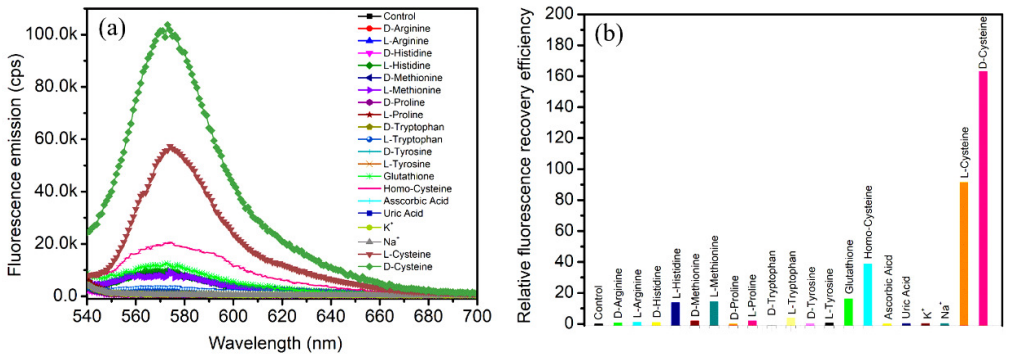

Figure 6.11. (a) Recovery of fluorescence emission from the Au NPs/RhB mixed solution in the presence of all of the relevant analytes. (b) Relative fluorescence recovery efficiency of the Au NPs/RhB mixed solution due to each analyte as calculated from the corresponding emission intensities.

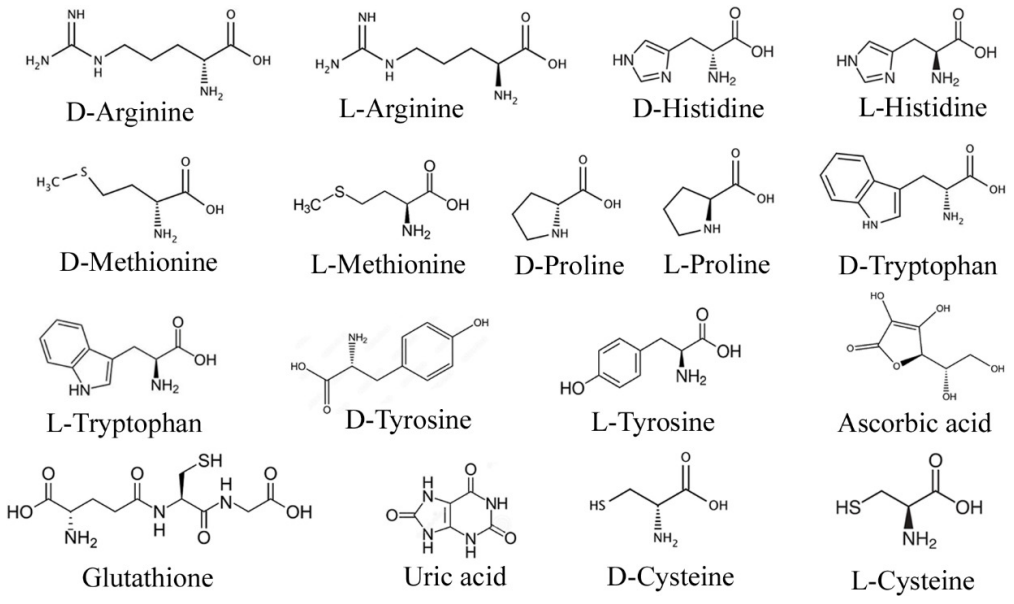

Figure 6.12. Molecular structure of different D- and L-amino acids, glutathione, ascorbic acid and uric acid.

interfering compounds are shown in Figure 6.12. From Figure 6.11a it is observed that the fluorescence emission intensities of the Au NPs/RhB mixed solution in the presence of D-Cys and L-Cys are significantly high compared to those for other interfering compounds, although the concentrations of all of the analytes were the same in these spectrofluorometric measurements. However, when the Au NPs/RhB mixed solution is added with D-Cys, the final solution turns red-wine to bluish-black in color, which is different when mixed with L-Cys solution separately, as shown in Figure 6.13. The relative fluorescence recovery efficiency $[(F-F_0)/F_0]$ as shown in Figure 6.11b becomes remarkably high for D-Cys compared to that for all other relevant interfering species or elements. From the above observations it is clear that the interaction of the Au NPs/RhB mixed ensembles with D-Cys in aqueous medium is selective due to the high fluorescence recovery as well as distinct color change of the Au NPs/RhB mixed solution when compared to the interactions with L-Cys and all other D- and L-amino acids, physiologically relevant interfering elements etc. as studied in this experiment. It is important to mention that the difference between fluorescence recovery efficiencies for D-Cys and L-Cys might be attributed to the different chiralities in the molecular structure of these amino acids, as is evidenced from the CD spectra shown in Figure 6.14a. The high selectivity of the interaction of the Au NPs/RhB mixed solution with D-Cys may be attributed to the change in structural configuration of the amino acid D-Cys, which is manifested as the observed change in the peak position of the CD spectrum. This is because any change in the configuration of the functional group (−SH) while interacting with the Au NPs/RhB mixed ensemble in aqueous medium possibly disrupts the chiral properties in the structure of D-Cys. As a result, there is a blue shift of the peak position at 210 nm in the CD spectrum as shown in Figure 6.14a. On the other hand, when L-Cys is added to the Au NPs/RhB mixed solution, the peak position observed at 216 nm in the CD spectrum is not altered except for a slight reduction of intensity. These observations clearly indicate that the chiral properties of L-Cys were possibly less affected while interacting with the Au NPs/RhB

Figure 6.13. Digital photographs of vials showing distinct colour changes for the interactions of D-Cys and L-Cys with Au NPs/RhB mixed solution.

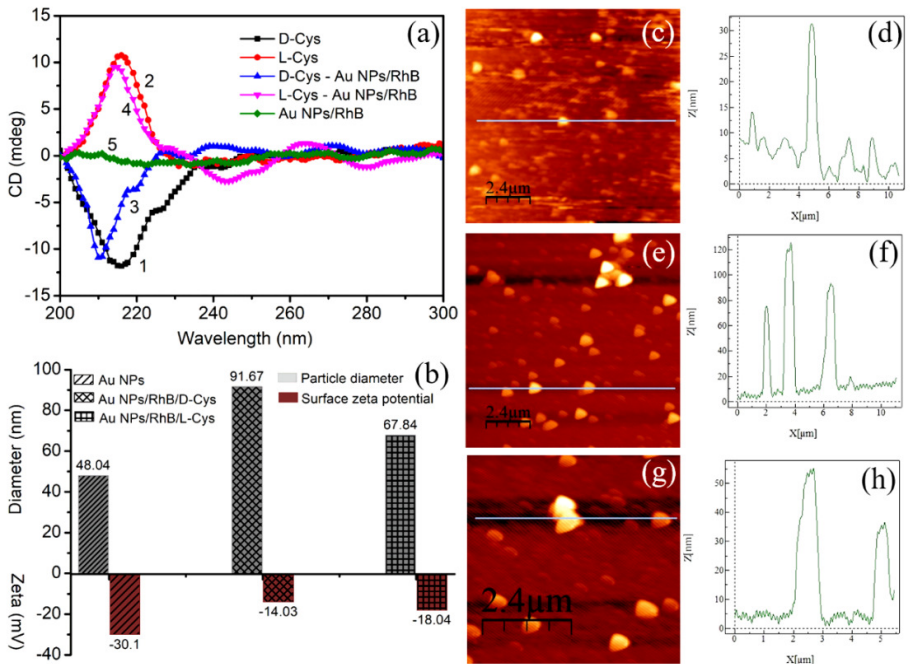

Figure 6.14. (a) CD spectra of the aqueous solution of D-Cys (curve 1), L-Cys (curve 2), mixed solution of Au NPs/RhB/D-Cys (curve 3), Au NPs/RhB/L-Cys (curve 4), and Au NPs/RhB (curve 5). (b) Column plot of the hydrodynamic diameter and surface ζ potential of the NPs as obtained from Au NPs, Au NPs/RhB/D-Cys, and Au NPs/RhB/L-Cys system. AFM topographic micrographs and surface roughness plot of (c,d) Au NPs, (e,f) Au NPs/RhB/D-Cys and (g,h) Au NPs/RhB/L-Cys mixed systems. The RMS surface roughness has been measured along the chosen lines as shown in the figures.

mixed ensemble compared to those of D-Cys. From the DLS study, as shown in Figures 6.14b, 6.15a, and 6.15c, it is observed that the particle size of Au NPs increases in the presence of both D- and L-Cys. However, for D-Cys, the increase in hydrodynamic particle diameter is higher (91.67 nm) compared to that of L-Cys (67.84 nm). This observation implies the possibility of a high degree of aggregation of Au NPs while interacting with D-Cys when compared to that due to L-Cys. As mentioned earlier, amino acids basically displace the citrate layer of the Au NPs during interaction and induce interparticle cross-linking, which favors rapid aggregation of Au NPs. However, the rate or extent of interparticle cross-linking is possibly higher for D-Cys than for L-Cys. Additionally, the less negative ζ potential (Figures 6.14b, 6.15b, and 6.15d) of the

Au NPs/RhB mixed solution containing D-Cys (−14.03 mV) compared to that with L-Cys (−18.04 mV) confirms the higher aggregation of NPs in the case of D-Cys [56]. To have a better understanding and direct visual evidence of the formation of aggregates or clusters, AFM topographical imaging is performed in a tapping mode. Figure 6.14c–h shows the AFM topographical image and surface roughness plot of the drop-casted film deposited onto smooth glass substrates from the Au NPs/RhB mixed solution in the presence of D-Cys and L-Cys, respectively. For all of these measurements, Au NPs/RhB mixed solutions were prepared in 1:1 volume ratio and their concentrations in the mixed solution were 0.05 mM and 0.05 μM, respectively. These images show that D-Cys facilitates a higher extent of aggregation or formation of clusters of Au NPs in the mixed solution. The root-mean-square (RMS) surface roughness of the Au NPs/RhB film is estimated as 4.4 nm, whereas for L-Cys and D-Cys it becomes 7.25 and 18.92 nm, respectively. That is, the surface roughness of the film having D-Cys is much higher compared to that of L-Cys. Our AFM analysis revels that D-Cys induces a much greater degree of nanoparticle aggregation. Also, the hydrogen bond between the neighboring D-Cys molecules in the aqueous solution is

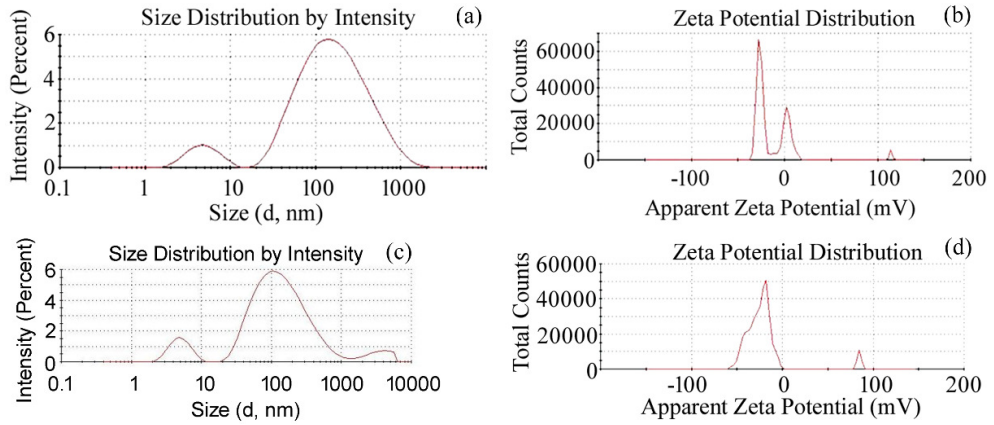

Figure 6.15. DLS and Zeta potential spectra of Au NPs/RhB mixed solution in presence of D-Cys (a,b) and L-Cys (c,d) respectively.

highly affected by the steric hindrance due to the presence of Au NPs. The high extent of aggregation of NPs in the aqueous mixture of Au NPs/RhB facilitated higher fluorescence recovery from the quenched state due to the release of more number of RhB dye molecules from the Au surface.

Interestingly, our proposed Au NPs/RhB mixed platform does not show any significant or appreciable fluorescence recovery by other aminothiols such as Hcys and

GSH in the same aqueous medium as studied in this work. In case of Hcys and GSH, we observe a slight recovery of fluorescence emission from the Au NPs/RhB matrix in aqueous medium. Although Hcys is a homologue of the amino acid Cys, it differs with an additional methylene bridge in its molecular structure. It is also known that [57] nearly at physiological pH, Hcys contains one amino group ($-NH_3^+$), one $-COO^-$ group, and one $-SH$ group in aqueous medium, whereas citrate caped Au NPs possess three $-COO^-$ groups in the same aqueous medium. Therefore, the direct electrostatic binding between Hcys and Au NPs is minimal. Due to the presence of the $-SH$ group in Hcys, there will be still some interaction via thiolate–Au bond formation, but the rate of displacing the citrate layer on which the cationic RhB molecules are bound might be limited due to the difference in the orientation of the amino acid groups or in the interfacial free energies when compared to D-Cys or L-Cys in the studied aqueous environment [41]. As a consequence, the fluorescence emission recovery from the Au NPs/RhB mixed ensemble is less compared to D-Cys and L-Cys. On the other hand, GSH has two $-COOH$ groups associated with glutamic acid and glycine residues and three amino groups ($-NH_3^+$) in three amino acids, and one sulfur atom present in the Cys residue. It is expected that at intermediate or higher pH the disassociation of $-COOH$ groups may hinder [58] the binding of GSH with Au nanocolloids via the α amine group. This results in a very little cross-linking between the $-SH$ group and Au colloids. As we have studied the binding interactions at neutral pH (7.0), less interaction between Au and GSH results in lower fluorescence recovery in the Au NPs/RhB aqueous medium. Additionally, the GSH molecule is relatively bulky in size compared to cysteine or Hcys, and therefore, the interfacial reactivity may be less probable due to energetic consideration. However, literature revels that the amino acid Trp can selectively bind with Au NPs [59]. In the present work, we did not find any significant fluorescence recovery from the Au NPs/RhB mixed solution in the presence of D- and L-Trp. This is possibly due to the formation of the nonfluorescent Trp–RhB complex [60].

The binding constant, sometimes referred to as the association constant (K_a), of the Au NPs/RhB system with D-Cys and L-Cys in the aqueous medium has been determined using the Benesi–Hildebrand eqn. 6.6 [61,62]

$$\frac{1}{(F_X - F_0)} = \frac{1}{(F_{max} - F_0)} + \frac{1}{K_a[M](F_{max} - F_0)} \dots\dots\dots\dots\dots\dots (6.6)$$

where F_0, F_x, and F_{max} are the fluorescence emission intensities obtained from the mixture of Au NPs/RhB in the absence of D-Cys (or L-Cys), with an intermediate concentration of D-Cys (or L-Cys) and the concentration of D-Cys (or L-Cys) at saturation level, and [M] is the concentration of D-Cys (or L-Cys). The magnitude of the binding constant (K_a) gives an indication about the strength of interaction between the guest and host for their complexation in a medium and is related to the change in

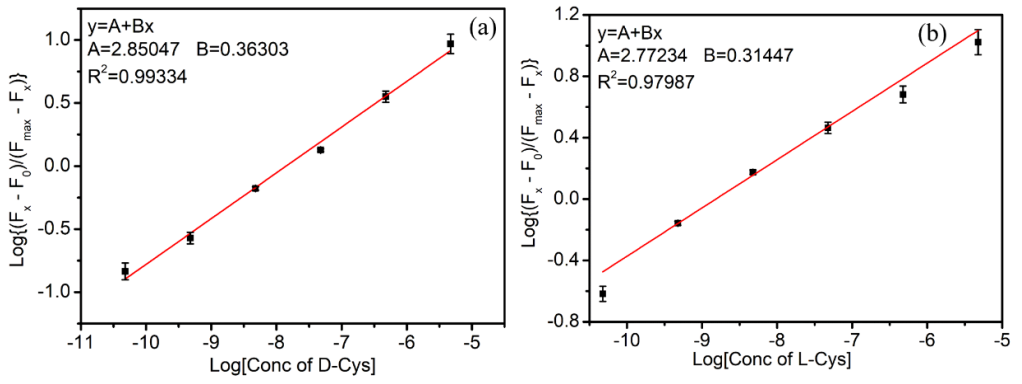

Figure 6.16. Plot of (a) $Log\{(F_x-F_0)/(F_{max}-F_x)\}$ vs. Log[Conc of D-Cys] and (b) $Log\{(F_x-F_0)/(F_{max}-F_x)\}$ vs. Log[Conc of L-Cys] to determine the binding constants of the Au NPs/RhB system with D-Cys and L-Cys, respectively.

Gibbs free energy [46] ($\Delta G=-RTlnK_a$) for the process. The values of K_a have been obtained from the intercept of the plot of $Log\{(F_x-F_0)/(F_{max}-F_x)\}$ vs. Log[M] as shown in Figure 6.16 for both D-Cys and L-Cys, and are summarized in Table 6.3. These values confirm that both D-Cys and L-Cys can bind to the Au NPs/RhB system in aqueous solution. But, in the case of D-Cys, this interaction is stronger than that for L-Cys. Therefore, due to the strong binding interaction between D-Cys and citrate caped Au NPs in aqueous medium, the fluorescence recovery efficiency is much higher compared to L-Cys. The values of the Gibbs free energy ΔG and binding constant K_a for Au NPs/RhB/D-Cys and Au NPs/RhB/L-Cys complexes have been calculated from the steady-state fluorescence emission spectra and are summarized in Table 6.3. The negative ΔG indicates that the interactions of both D-Cys and L-Cys with the Au NPs/RhB system are spontaneous. However, the higher negative value of ΔG reveals the faster rate of interaction in the case of D-Cys with the assay medium compared to that for L-Cys.

Table 6.3. Binding constant (K_a), Gibbs free energy (ΔG) for the D-Cys and L-Cys with the Au NPs/RhB mixed systems in aqueous solution. R^2 is the corresponding correlation coefficient.

Chiral amino acids	K_a (M^{-1})	R^2	ΔG ($kJmol^{-1}$)
D-Cys	708.712	0.9933	-16.261
L-Cys	592.025	0.9798	-15.816

For further investigation on the selectivity and interaction mechanism of Au NPs/RhB with D- and L-Cys, FTIR spectroscopic measurements in ATR mode were performed and are shown in Figure 6.17. The FTIR spectra of pure D-Cys and L-Cys (curve 1 in (a) and (b), respectively) are very similar and show IR bands with peaks centered at 3166, 1582, and 1390 cm^{-1}, which are attributed to the stretching of $-NH_3^+$ and the asymmetric and symmetric stretching of the $-COO^-$ functional groups of Cys molecules, respectively. In addition, Cys molecules have a weak IR vibrational band near 2550 cm^{-1}, which is originated due to the characteristic stretching vibration of the S−H bond (thiol group). Other vibrational bands are observed at 2968 cm^{-1} (CH_2 stretching, asymmetric), 2078 cm^{-1} (NH_3 bending, asymmetric), 1522 cm^{-1} (N−H bending), 1340 cm^{-1} (NH_3 bending, symmetric), 1294 cm^{-1} (CH_2 wagging), 1195 cm^{-1} (CH_2 twisting), 1130 cm^{-1} (SO_2 stretching), 1062 cm^{-1} (NH_3 rocking), 941

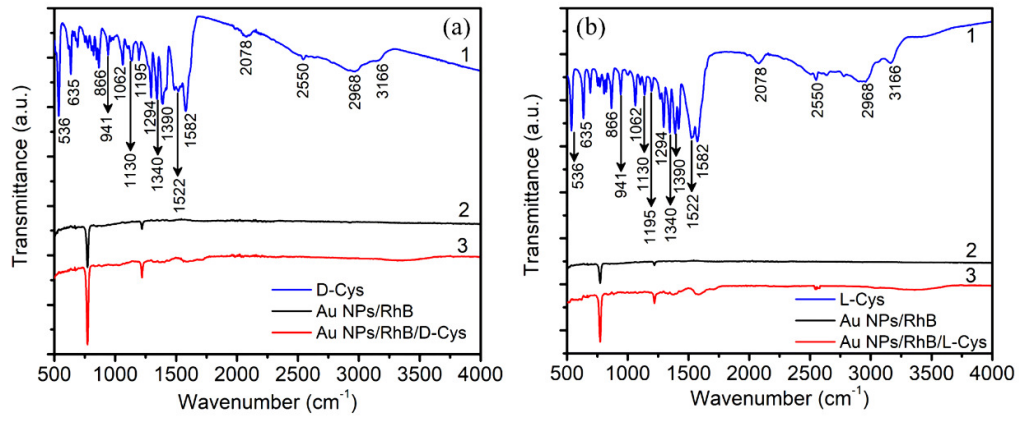

Figure 6.17. ATR-FTIR spectra of (a) D-Cys (b) and L-Cys in the absence and presence of Au NPs/RhB, respectively.

cm^{-1} (S−H bending), 866 cm^{-1} (N−O stretching), 635 cm^{-1} (COOH bending), 536 cm^{-1} (COOH rocking) etc. These results are consistent with the FTIR spectra of amino acids reported elsewhere [63–65]. Interestingly, for the Au NPs/RhB/D-Cys system, the IR bands corresponding to the stretching of $-NH_3^+$ and $-COO^-$ groups of D-Cys are almost absent, possibly due to their cross-linking with other cysteine molecules attached to the neighboring Au NPs. However, for the Au NPs/RhB/L-Cys system, the bands of these stretching vibrations are also abruptly reduced compared to pure L-Cys but the peaks are still visible. These observations may reveal that the interparticle cross-linking is much stronger in the case of D-Cys in the assay medium, resulting in a rapid and greater extent of nanoparticle aggregations, which is reflected in the different color change of the final solution. This may also be due to the change in their dipole moments when binding with a high electron density of the metal surface. But the most significant observation is that the S−H stretching vibration band (2550 cm^{-1}) totally disappears for D-Cys after interacting with the Au NPs/RhB mixed system in aqueous medium (Figure 6.17a curve 3). This indicates that S−H bonds are cleaved in the presence of the metal NPs, which further indicates the strong binding interaction of D-Cys with Au NPs. On the other hand, the S−H stretching vibration band is not totally absent for L-Cys when interacted with the Au NPs/RhB system but it appears as a weak band near 2550 cm^{-1} as shown in Figure 6.17b (curve 3). Therefore, it is clear that the interaction of D-Cys with the Au NPs/RhB mixed system is stronger compared to that of L-Cys in the studied aqueous medium. Additionally, the FTIR spectra of the Au NPs/RhB mixed system (curve 2 in Figure 6.17a,b, respectively) confirm that there is no such significant effect of RhB molecules on the interaction of D-Cys or L-Cys molecules with Au NPs in the assay medium.

6.3.6. Real biosample analysis

The proposed nano-bio interaction is also studied in the presence of normal human urine. The normal urine sample was collected from a healthy laboratory volunteer (male researcher) having no renal complications. In this investigation with the normal urine sample, we maintained the same optimized concentrations of RhB and Au NPs in their mixed solution as discussed earlier, and took extra precautions to avoid any direct contact or any type of contamination with the urine sample. D-Cys may present in both urine and blood plasma. It is already known that diseases like cystinuria leading to the formation of kidney and renal system stone occur due to the free presence

of Cys in the urine [66,67] The fluorescence emission spectra of the mixed solution of Au NPs/RhB (control) in the presence of normal urine (200 µL), mixture of normal urine (200 µL) and D-Cys (0.1 mM, 200 µL), and mixture of normal urine (200 µL) and all other analytes (0.1 mM) used in the present work except D-Cys are shown in Figure 6.18a. The concentrations of D-Cys and all other analytes in the final assay medium containing urine were 2.38 µM, respectively. The corresponding fluorescence recovery efficiency is shown in Figure 6.18b. From this figure it is clear that, the normal urine shows fluorescence recovery efficiency of 42% but mixture of normal urine and D-Cys shows fluorescence recovery efficiency of 73%. Therefore, the usual presence of Cys in the normal urine gives the initial fluorescence recovery from Au NPs/RhB system. It is also observed that when all other D and L-amino acids along with the other relevant interfering compounds as considered are mixed with the proposed assay matrix, the fluorescence recovery efficiency is slightly higher than that due to pure normal urine. This may be due to the presence of L-Cys as was added with all other interfering compounds. Additionally, there is also a distinct color change (from red-

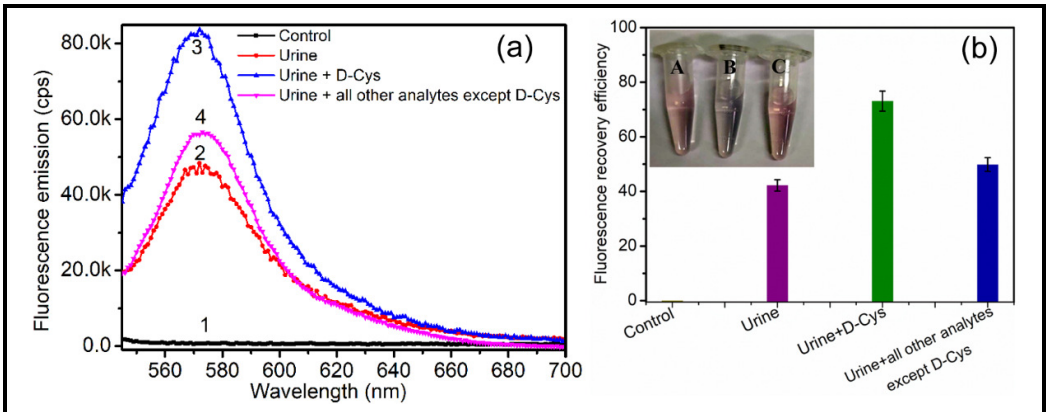

Figure 6.18. (a) Fluorescence emission spectra of Au NPs/RhB mixed solution (control) (curve 1), mixed with normal humane urine (curve 2), urine and D-Cys (curve 3), urine and all other analytes used in this work except D-Cys (curve 4). (b) Plot of the fluorescence recovery efficiencies for the Au NPs/RhB mixed solution in the presence of normal human urine and all other analytes relevant to the present work. The inset shows the digital photograph of vials containing the Au NPs/RhB mixed solution with (A) urine, (B) mixture of urine and D-Cys, and (C) mixed solution of urine and all other analytes except D-Cys.

wine to bluish-black) of the assay solution after addition of D-Cys compared to all other analytes including L-Cys as shown in the inset of Figure 6.18b. This study confirms the proposed nano-bio interaction is manifested as the selective binding of D-Cys with Au NPs/RhB in in human urine as well. Therefore, the proposed Au NPs/RhB system in aqueous medium under the appropriate and optimized condition may be used as an efficient platform for rapid detection of D-Cys in human urine in a ratio-metric approach to diagnose various renal complications.

6.4. Conclusions

In conclusion, we demonstrate a simple fluorometric method to explore the comparative and selective interaction of the amino acid D-Cys among various other D- and L-amino acids, neurotransmitters, relevant biological compounds etc., with citrate caped gold nanoparticles (27.5 nm) in the presence of the fluorescent dye RhB. Au NPs are found to almost fully quench the fluorescence emission of RhB dye in the optimized concentrations of both Au NPs and RhB via a nonradiative energy transfer pathway from the excited RhB molecules to Au NPs in aqueous solution at neutral pH. This quenched fluorescence is selectively recovered with high efficiency after addition of D-Cys to the Au NPs/RhB mixed solution and there was a distinct color change of the assay medium after reaction with D-Cys when compared to the effect of other interfering compounds studied in this work. The degree of aggregation of Au NPs is greater due to the interaction with D-Cys compared to L-Cys due to strong thiolate–Au bond formation via chemisorption and possibly greater interparticle cross-linking compared to that due to L-Cys and in aqueous solution. The higher value of binding constant and higher negative value of Gibbs free energy for D-Cys interacting with the Au NPs/RhB mixed system compared to those for L-Cys as estimated from the fluorescence recovery results confirm the stronger interaction of D-Cys with the nanoparticle system in the studied aqueous medium. The difference in aggregations of D-Cys and L-Cys while interacting with Au NPs/RhB mixed systems in solution is correlated with the ζ potential results and chiral properties of the amino acids, as evidenced by the ζ potential study and CD spectroscopic characterization, respectively. The ATR-FTIR study further distinguishes the difference of interactions of both D-Cys and L-Cys with the assay matrix through the change in vibrational signatures of the S–H bond as well as other relevant functional groups and is consistent with the

observations by the other analytical methods used in this present work. The interaction of D-Cys with the proposed nanoparticle-based platform is highly sensitive and lies in the broad linear range of concentration of 1 nM to 100 μM. The LOD for D-Cys is found to be 4.2 nM, which is lower compared to many available detection methods cited in the literature. The normal human urine sample when mixed with the assay matrix (Au NPs/RhB) and D-Cys exhibits a higher fluorescence recovery and distinct color change (red-wine to bluish-black) of the assay medium after reaction compared to that for L-Cys or all other interfering compounds as studied. Therefore, the proposed bio-nano interaction may be realized as an efficient approach for the selective recognition of the amino acid D-Cys in the aqueous environment.

References

[1] W. Widlak, Molecular Biology Not Only for Bioinformaticians; *Springer*, (1998). DOI:10.1007/978-3-642-45361-8.

[2] A. Kessel, N. B. Tal, Introduction to Proteins Structure, Function, and Motion, (2nd ed.), *CRC Press*, (2018).

[3] R. Kimura, H. Tsujimura, M. Tsuchiya, S. Soga, N. Ota, A. Tanaka, H. Kim, *Sci. Rep*., 10 (2020) 804.

[4] G. Carenzi, S. Sacchi, M. Abbondi, L. Pollegioni, *Amino Acids*, 52(6–7) (2020) 849–862.

[5] J. Liu, B. Fu, Z. Zhang, *Anal. Chem.*, 92 (2020) 8670–8674.

[6] S. Karakawa, K. Shimbo, N. Yamada, T. Mizukoshi, H. Miyano, M. Mita, W. Lindner, K. Hamase, *J. Pharm. Biomed. Anal.*, 115 (2015) 123–129.

[7] D. Liu, Y. Lv, M. Chen, D. Cheng, Z. Song, L. Yuan, X. Zhang, *J. Mater. Chem. B*, 7 (2019) 3970–3975.

[8] J. R. Winther, C. Thorpe, Biochim. *Biophys. Acta, Gen. Subj.*, 1840 (2014) 838–846.

[9] X. Chen, Y. Hu, Z. Cao, Q. Liu, Y. Cheng, *Front. Immunol.*, 9 (2018) 02122.

[10] A. L. Kjældgaard, K. Pilely, K. S. Olsen, S. W. Pedersen, A. O. Lauritsen, K. Moller, P. Garred, *Mol. Immunol.*, 102 (2018) 14–25.

[11] J. Pichette, J. Gagnon, *Oxid. Med. Cell. Longevity*, 2016 (2016) 3285074.

[12] Z. Tong, L. Ni, J. Ling, *Peptides*, 60 (2014) 32–40.

[13] M. Zhang, B. C. Ye, *Anal. Chem.*, 83 (2011) 1504–1509.

[14] P. R. Zamora, B. S. Angeles, F. Buendía, C. C. Silis, J. Fabila, J. B. Díaz, L. M. F. Díaz, L. P. O. Borbón, G. Díaz, I. L. Garzón, *J. Raman Spectrosc.*, 51 (2020) 243−255.

[15] J. Klein, *Proc. Natl. Acad. Sci. U.S.A.*, 104 (2007) 2029−2030.

[16] J. Lei, H. Ju, *Chem. Soc. Rev.*, 41 (2012) 2122−2134.

[17] J. Zhu, J. Shen, B. Hu, L. Yang, C. Jiang, *Anal. Chem.*, 94 (2022) 1126−1134.

[18] M. L. Goas, J. Saber, S. G. Bolívar, J. M. Rabanel, J. M. Awogni, D. C. Boffito, X. Banquy, *Nano Today*, 45 (2022) 101516.

[19] J. Li, J. Liu, C. Chen, *ACS Nano*, 11 (2017) 2403−2409.

[20] G. Maduraiveeran, M. Sasidharan, V. Ganesan, *Biosens. Bioelectron.*, 103 (2018) 113−129.

[21] P. Maiti, T. Singha, U. Chakraborty, S. D. Roy, P. Karmakar, B. Dey, S. A. Hussain, S. Paul, P. K. Paul, *Mater. Chem. Phys.*, 234 (2019) 158−167.

[22] H. M. Dizman, E. O. Kazancioglu, T. Shigemune, S. Takahara, N. Arsu, *Spectrochim. Acta, Part A*, 264 (2022) 120294.

[23] A. A. Shemetov, I. Nabiev, A. Sukhanova, *ACS Nano*, 6 (2012) 4585−4602.

[24] A. Bigdeli, F. Ghasemi, S. A. Moayed, M. Shahrajabian, N. F. Kashani, S. Jafarinejad, M. A. F. Nejad, M. R. H. Nezhad, *Anal. Chim. Acta*, 1079 (2019) 30−58.

[25] X. F. Yang, X. Q. Guo, Y. B. Zhao, *Talanta*, 57 (2002) 883.

[26] S. Han, L. Yang, Z. Wen, S. Chu, M. Wang, Z. Wang, C. Jiang, *J. Hazard. Mater.*, 398 (2020) 122894.

[27] F. Yang, D. Lin, L. Pan, J. Zhu, J. Shen, L. Yang, C. Jiang, *Anal. Chem.*, 93 (2021) 14506−14513.

[28] S. Ferré, V. G. Ruiz, J. Zangari, S. Girel, J. C. Martinou, R. Sardella, S. Rudaz, *J. Pharm. Biomed. Anal.*, 209 (2022) 114539.

[29] E. Zor, *Talanta*, 184 (2018) 149−155.

[30] Q. Ma, C. Qi, X. L. Li, Q. Shi, C. Y. Xu, T. Jin, J. Z. Min, *J. Pharm. Biomed. Anal.*, 196 (2021) 113939.

[31] L. Pucciarini, V. González-Ruiz, J. Zangari, J. C. Martinou, B. Natalini, R. Sardella, S. Rudaz, *J. Pharm. Biomed. Anal.*, 177 (2020) 112841.

[32] M. Greño, M. L. Marina, M. C. Puyana, *Microchem. J.*, 169 (2021) 106596.

[33] G. Frens, *Nat. Phys. Sci.*, 241 (1973) 20.

[34] S. D. Roy, M. Ghosh, J. Chowdhury, *J. Raman Spectrosc.*, 46 (2015) 451–461.

[35] M. R. Jones, K. D. Osberg, R. J. Macfarlane, M. R. Langille, C. A. Mirkin, *Chem. Rev.*, 111 (2011) 3736–3827.

[36] J. Zhang, B. Zhao, L. Meng, H. Wu, X. Wang, C. Li, *J. Nanopart. Res.*, 9 (2007) 1167–1171.

[37] N. Chandrasekharan, P. V. Kamat, J. Hu, G. Jones, *J. Phys. Chem. B*, 104 (2000) 11103–11109.

[38] R. G. Acres, V. Feyer, N. Tsud, E. Carlino, K. C. Prince, *J. Phys. Chem. C*, 118 (2014) 10481–10487.

[39] T. Wang, X. Hu, S. Dong, *Chem. Commun.*, (2008) 4625–4627.

[40] H. P. Wu, C. C. Huang, T. L. Cheng, W. L. Tseng, *Talanta*, 76 (2008) 347–352.

[41] F. X. Zhang, L. Han, L. B. Israel, J. G. Daras, M. M. Maye, N. K. Ly, C. J. Zhong, *Analyst*, 127 (2002) 462–465.

[42] L. Li, B. Li, *Analyst*, 134 (2009) 1361–1365.

[43] N. Alarcos, B. Cohen, M. Ziolek, A. Douhal, *Chem. Rev.*, 117 (2017) 13639–13720.

[44] D. S. Tira, M. Focsan, S. Ulinici, D. Maniu, S. Astilean, *Spectrosc. Lett.*, 47 (2014) 153–159.

[45] S. Chu, H. Wang, X. Ling, S. Yu, L. Yang, C. Jiang, *ACS Appl. Mater. Interfaces*, 12 (2020) 12962–12971.

[46] N. Manjubaashini, M. P. Kesavan, J. Rajesh, T. D. Thangadurai, *J. Photochem. Photobiol., B*, 183 (2018)374–384.

[47] V. Chandrakar, K. Tapadia, S. K. Gupta, *Inorg. Nano-Met. Chem.*, (2022) 1–9.

[48] B. Prusti, M. Chakravarty, *Analyst*, 145 (2020) 1687–1694.

[49] S. Prasanth, R. D Raj, T. V. Vineeshkumar, R. K. Thomas, C. Sudarsanakumar, *RSC Adv.*, 6 (2016) 58288.

[50] I. I. S. Lim, W. Ip, E. Crew, P. N. Njoki, D. Mott, C. J. Zhong, Y. Pan, S. Zhou, S. *Langmuir*, 23 (2007) 826–833.

[51] B. Saroha, A. Kumar, R. R. Maurya, M. Lal, S. Kumar, H. K. Rajor, I. Bahadur, D. S. Negi, *J. Mol. Liq.*, 349 (2022) 118197.

[52] S. H. Hung, J. Y. Lee, C. C. Hu, T. C. Chiu, *Food Chem.*, 260 (2018) 61–65.

[53] S. Link, M. A. E. Sayed, *Int. Rev. Phys. Chem.*, 19 (2000) 409–453.

[54] C. G. Blatchford, J. R. Campbell, J. A. Creighto, *Surf. Sci.*, 120 (1982) 435–455.

[55] H. Wang, L. Yang, S. Chu, B. Liu, Q. Zhang, L. Zou, S. Yu, C. Jiang, *Anal. Chem.*, 91 (2019) 9292−9299.

[56] J. V. Jokerst, T. Lobovkina, R. N. Zare, S. S. Gambhir, *Nanomedicine*, 6 (2011) 715−728.

[57] I. I. S. Lim, D. Mott, W. Ip, P. N. Njoki, Y. Pan, S. Zhou, C. J. Zhong, *Langmuir*, 24 (2008) 8857−8863.

[58] S. Basu, P. Pal, *J. Nanosci. Nanotechnol.*, 7 (2007) 1904−1910.

[59] L. Zhang, C. Xu, C. Liu, B. Li, *Anal. Chim. Acta*, 809 (2014) 123−127.

[60] Y. Feng, W. Liu, R. M. Prieto, X. D. Chen, *J. Photochem. Photobiol. A*, 408 (2021) 113092.

[61] P. Yuvaraj, J. Ajantha, M. Karuppusamy, S. Easwaramoorthi, J. R. Rao, *ACS Sustainable Chem. Eng.*, 9 (2021) 10309−10317.

[62] H. A. Benesi, J. H. Hildebrand, *J. Am. Chem. Soc.*, 71 (1949) 2703−2707.

[63] M. S. Lodhi, M. T. Khan, S. Aftab, Z. Q. Samra, H. Wang, D. Q. Wei, *Cancer Nanotechnol.*, 12 (2021) 26.

[64] V. Andal, G. Bhuvaneswari, *Mater. Res. Innovations*, 24 (2020) 202−209.

[65] A. Pawlukojć, J. Leciejewicz, A. J. R. Cuesta, J. N. Scheibe, *Spectrochim. Acta, Part A*, 61 (2005) 2474−2481.

[66] A. G. Shtukenberg, J. Hu, A. Sahota, B. Kahr, M. D. Ward, *Acc. Chem. Res.*, 55 (2022) 516−525.

[67] D. J. Claes, E. Jackson, *Pediatr. Nephrol.*, 27 (2012) 2031−2038.

****

CHAPTER ~ 7

Interaction of Silver nanoparticles with cationic dye Acridine orange in presence of DNA in aqueous environment

This chapter describes how silver nanoparticle influence the photophysical properties of biologically relevant cationic dye acridine orange in aqueous solution. Also the binding interaction of silver nanoparticles with calf thymas DNA in presence of fluorescent probe acridine orange is explored.

CHAPTER~7

Interaction of Silver nanoparticles with cationic dye Acridine orange in presence of DNA in aqueous environment

7.1. Introductory remark

During the last several decades' novel metal nanoparticles (NPs) have drawn much interest because of their fascinating optical and electronic characteristics [1,2]. These interesting properties led the researchers to motivate towards number of promising applications in biomedical fields, cosmetics, food industries, textiles, paints etc. [3,4]. Most noticeable the unique surface plasmon resonance (SPR) of metal NPs can efficiently modulate the photophysical properties of various organic molecules both in their ground and excited electronic states [5]. The observed changes of such photophysical behaviour of organic moieties located in the vicinity of metal NPs sometimes found to show very selective while interacting with various target biomolecular species in the same environment leading to various promising applications in biomedical field [6,7]. Literature reveals that size and shape of such novel metal NPs are two important factors because these correspond to the different surface plasmonic oscillation which may interfere with the fluorescence of guest organic species in their close proximity [8]. The plasmonic field may overlap with the oscillating dipole of neighbouring organic fluorophores resulting the enhancement or quenching of fluorescence of the organic emitter molecules around the NPs depending upon their relative separation [9]. As the spherically shaped metal NPs do not possess any dipole moment compared to organic dye molecules, therefore energy transfer may occur from the excited dye chromophore to metallic surface. The large absorption cross-section of NPs also favours this energy migration towards the surface of metal [10].

The energy transfer is also manifested as the fluorescence quenching of the dye molecules.

In recent times dye-conjugated metal NPs assembly have been shown to be efficient platform for selective recognition of various biomolecular species at various environments [11,12]. Among the various metal NPs, Silver nanoparticles (Ag NPs) have drawn immense interest among the researchers due to their good catalytic properties, antibacterial properties, ability of interacting with wide variety biomolecular species through different specific and non-specific interactions [13,14,15]. The strong SPR of Ag NPs enable them to modulate physical and physicochemical properties of organic dye molecules.

The study of the interaction of Ag NPs with deoxyribonucleic acid (DNA) and its constituents became a great interest among the scientists in the interface nanobiotechnology [16]. Nucleic acids containing various base pairs are carrying the characteristic genetic information and recognition of the structure of DNA is of particular importance for the diagnosis of various genetically induced health complications [17,18]. As both DNA and Ag NPs do not possess fluorescence emission, therefore it is difficult to discriminate the nature of form of DNA just utilising their direct interaction. In this regard spectrofluorometric method using an organic probe (generally dye) is an excellent choice to discriminate the structure or form of DNA present in a particular medium by observing the unique change in fluorescence properties of dye in the Ag NPs/DNA medium involving various specific and non-specific interactions [19].

In this chapter, I have studied the photophysical behaviour of cationic laser dye Acridine Orange (abbreviated as AO) in presence of Ag NPs in aqueous solution. Additionally, the binding interaction of Ag NPs and AO in presence of Calf Thymas DNA in the mixed solution have been explored. UV-vis absorption and fluorescence spectroscopic studies provides many useful information about the nano-bio interaction in this present work, which can contribute as scientific database in biological research and various biotechnological applications. Ag NPs strongly quench the fluorescence emission of AO in aqueous solution and UV-vis absorption study is evident that there was binding between DNA and Ag NPs. Most interestingly in presence of DNA the fluorescence of AO is not quenched rather it binds with DNA either by intercalation or

groove binding. As AO is planner molecule it can easily intercalate between the sugar bases of DNA double helix structure [20]. Addition of Ag NPs solution in AO/CT-DNA mixed solution reveals the strong interaction with DNA and induces the expulsion of AO dye from the DNA duplex structure as is anticipated from the steady-state fluorescence spectroscopic study. Density functional study are also have been performed to understand the electronic energy of level of the dye molecules.

7.2. Experimental methods

7.2.1. Materials

The cationic organic dye acridine orange (abbreviated as AO) ($C_{17}H_{19}N_3$, M.W.: 265.36 $gmol^{-1}$) and silver nitrate ($AgNO_3$, M.W.: 169.87 $gmol^{-1}$) were purchased from Sigma Aldrich chemical company, USA and have been used without further purification. However, their purity was checked by UV-vis absorption and steady-state fluorescence method before use in the experiment. Sodium borohydride ($NaBH_4$, M. W.: 37.83 $gmol^{-1}$) were purchased from Merck chemical company, Germany. Calf Thymas DNA was supplied by SRL chemical company, India. The purity of DNA was confirmed by the ratio of absorbance (~1.8) at ~260 nm and ~280 nm. Triple distilled deionized Milli-Q (resistivity 18.2 MΩcm) water was prepared by Synergy integrated with an Elix-Advantage set-up (Millipore SAS, France) and have been used to prepare all the sample solution. The glassware used for the experiment have been thoroughly cleaned and autoclaved before use. pH of all the solution were measured with the help of a high precision digital pH meter (Five easy, Metler Toledo, Germny).

7.2.2. Synthesis of Ag NPs

Ag NPs was prepared by the reduction of $AgNO_3$ aqueous solution by $NaBH_4$ according to the method available in the literature [21,22]. At first, 70 mL aqueous solution $AgNO_3$ of concentration of 0.05 mM was mixed to 110 mL solution of $NaBH_4$ (concentration of 1.5 mM) drop-wise and the mixture was stirred rigorously at room temperature (25ºC). Then the mixed solution has been chilled in the ice bath. At the early stage during reaction, the colour of the mixture was light yellow and gradually turned to very bright yellowish type after adding all the $AgNO_3$ solution. Finally, Ag NPs was obtained in the colloidal solution which shows clear yellow colour. A typical

image of vial containing Ag NPs colloidal dispersion is shown in the inset of Figure 7.1a.

7.2.3. Characterizations

High resolution transmission electron microscopy (HRTEM) and selected area electron diffraction (SAED) measurements of as-synthesized Ag NPs were performed on a transmission electron microscope (TEM) (JEM-2100, JEOL. Ltd, Japan) operated at accelerating voltage 200 kV. For HRTEM study, the sample solutions were incubated for 15 min at room temperature (25ºC) and then a small drop of sample solution was spread onto the carbon coated copper microgrid (PELCO 300 Mesh Grids, Ted Pella Inc. USA) and subsequently dried at the same ambient temperature. All the absorption spectroscopic measurements were performed by using a double beam UV–vis absorption spectrophotometer (UV-1800, Shimadzu, Japan). However, before taking the sample spectrum, a proper baseline correction was done. A steady state fluorescence spectrometer (Fluoromax 4, Horiba Scientific, USA) was used to obtain all the emission spectroscopic measurements of the sample solution. The sample solutions were exited at 475 nm and the emission was scanned in the wavelength of 490-700 nm region at ambient condition. Both the UV-vis absorption and fluorescence emission spectra of the sample solutions were collected using quartz cell (Kozima, Japan) of 1.0 cm path length at room temperature (25ºC). Dynamic light scattering study and zeta potential of as-synthesised Ag NPs, Ag NPs/AO and Ag NPs/AO/DNA samples were characterised by Zetasizer (Zetasizer Nano ZS, Malvern Instruments Ltd, UK).

7.2.4. Computational details

The ab initio geometry optimization and quantum-chemical calculation of AO dye in the solvent medium (water) have been performed by the density functional theoretical approach (DFT) using the Gaussian 09 software [23]. The geometry of AO was optimized in aqueous medium using the Becke's three-parameter (B3) with Lee−Yang−Parr (LYP) hybrid correlation energy (B3LYP functional) [24] and 6-31+G(d,p) basis set [24]. Water was incorporated as an implicit solvent using the conductor-like continuum polarized model (CPCM) at room temperature (25ºC). The

geometry optimized structures of AO was obtained by the fully relaxed method, and the corresponding molecular orbitals such as HOMO and LUMO levels were visualized with the help of time dependent density functional theory (TD-DFT) using the same level of theory as was used for geometry optimization in the GaussView 6.0.16 software [25]. After the geometry optimization, frequency check was carried out to confirm the fully relaxed mode of the AO molecule by attaining the local minima of the potential energy surfaces.

7.3. Results and discussions

7.3.1. Characterization of as-synthesized Ag NPs

The as-synthesized Ag NPs have been characterized UV-vis absorption, DLS and Zeta potential, TEM etc. measurements. All these methods have been described in the previous section. Figure 7.1. Shows the UV-vis absorption spectrum of stable aqueous colloidal solution of Ag NPs. The absorption spectrum shows distinct

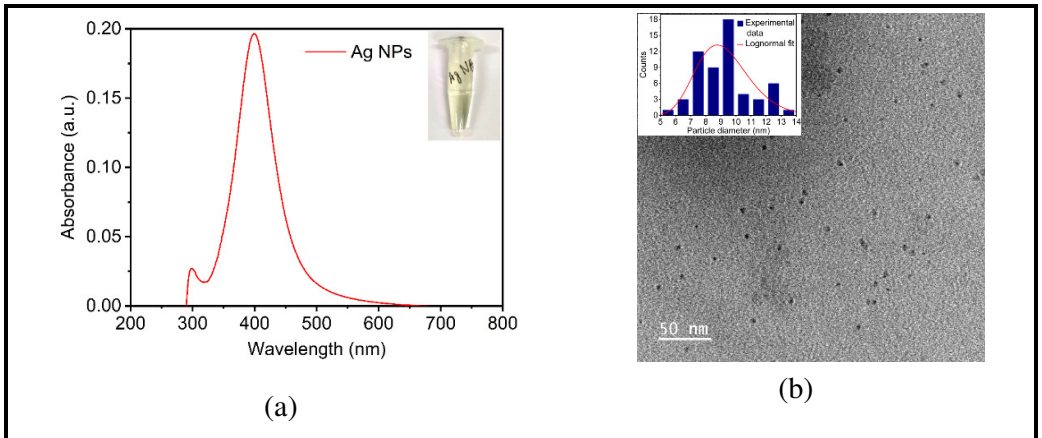

Figure 7.1. (a) UV-vis absorption spectrum of Ag NPs aqueous colloidal dispersion. (b) Transmission electron microscopic image of as-synthesized Ag NPs. Inset of (b) shows the lognormal particle size distribution.

absorption peak at around ~400 nm which is attributed to the characteristic surface plasmon resonance band of Ag NPs in the colloidal solution after photoexcitation [26]. Other small absorption band observed at ~300 nm is ascribed to the intraband electronic transition of silver [27]. However, the nature and position of these bands should depend upon various factor such as NPs size, shape as well as the surrounding environment

[28]. We have also performed transmission electron microscopy of the as-synthesized Ag NPs as shown in Figure 7.1b. TEM images shows the well dispersed merely spherical shaped Ag NPs and the average size of the nanoparticles is found to be ~9.264 nm with slandered deviation of ~1.798 nm as obtained from lognormal distribution. The as-synthesized Ag NPs was further characterized by DLS and Zeta potential study. Figure 7.2 shows the DLS spectrum of Ag NPs colloidal solution. From this figure the average hydrodynamic particles size is approximately estimated as ~91 nm. The contributions from other to small peaks are very less which implies that Ag NPs colloidal solution was mostly homogeneous with very minimal polydispersity in the studies medium. Also, to have an idea about the stability of Ag NPs in the aqueous medium, surface zeta potential is investigated as shown in Figure 7.3. Zeta potential of Ag NPs is found to be -33 mV which reveals that the Ag NPs in the solution were mostly stable and did not form aggregates or clusters. This also corresponds to the fact that the Ag NPs could easily balance the weak van der Waals force of attractions and the strong electrostatic interactions between borohydrate layer on the surface of Ag NPs in the aqueous colloidal dispersion.

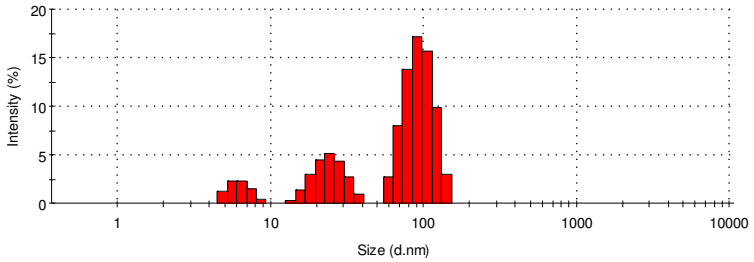

Figure 7.2. DLS spectrum of colloidal dispersion of Ag NPs

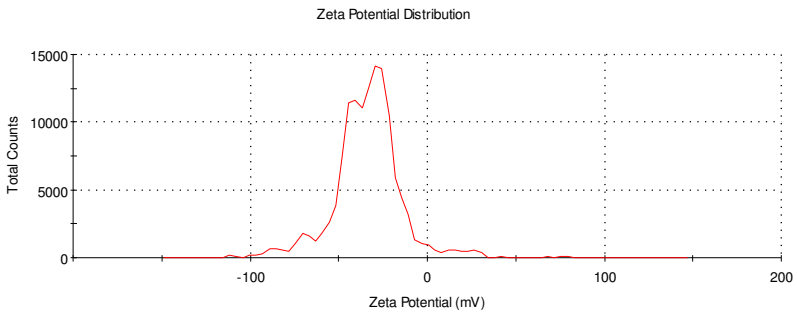

Figure 7.3. Zeta potential spectrum of Ag NPs colloidal solution.

7.3.2. UV-vis absorption spectroscopic study

The cationic dye AO is highly photophysically active organic compound and is attracted significant attention of the researchers due to their wide range of applications such as, textile industry, biomedical field especially in the flow cytometry to discriminate denaturation of DNA and various intracellular contents or to diagnose the alternation of genetic components in the cell [29,30]. This dye in the dilute solution mostly exists in their monomeric structures. However, at higher concentration (>10 μM) they have tendency to form dimeric structures which show different spectral and photophysical properties in different microenvironment [31]. AO is widely used in bacterial staining for fluorescence microscopy [29]. Therefore, the photophysical studies of this dye is prime importance from the point of view of their various biomedical applications. Figure 7.4a shows the UV-vis absorption spectrum of pure AO aqueous solution (concentration of 1 μM). Inset of Figure 7.4a shows the molecular structure of AO. Aqueous solution of AO exhibits prominent absorption bands in the wavelength region of 350-550 nm. The highly strong absorption band observed at ~490 nm is attributed to the monomeric forms of the dye molecules whereas weak shoulder at ~470 nm is possibly due to the presence of some aggregates (namely dimer) of dye molecules in the studied concentration of AO solution [31]. All these observations are in well consistent with the results reported elsewhere. Literature reveals that the intensity of this dimeric band increases with increase in concentration of dye solution [31].

In this work we have basically studied the interaction of Ag NPs with AO dye in absence and presence of DNA by using electronic spectroscopy. In recent times Ag NPs has been explored as various gene delivery agent in vivo and found to be biocompatible when properly functionalized. The unique plasmonic properties of Ag NPs can modulate various physical and physicochemical properties of organic emitter molecules which are used as fluorescence probe system to diagnose the structure and conformation of biomolecules. Therefore, keeping in mind the potential application of such Ag NPs in biological field, the interaction of Ag NPs with biologically relevant organic dye namely AO is important. Figure 7.4b represents the UV-vis absorption spectra of AO aqueous solution (1 μM) for various concentrations of Ag NPs colloidal solution. From the figure it is observed that the ~490 nm band of AO is shifted to ~500

nm and intensity of this band also increases with increase in concentration of Ag NPs in the mixed solution. Additionally, the main absorption peak of the Ag NPs gradually increases with increase of nanoparticle concentrations. The shift of the absorption band of AO at ~500 nm reveal the binding of Ag NPs with AO dye molecules in the mixed aqueous solution. Ag NPs in the solution carries net negative charges as evidenced from the Zeta potential study (Figure 7.3) and AO is a cationic dye. So the electrostatic interactions may play the dominant role in the binding AO and Ag NPs in the solution. Due to this interactions AO dye molecules might have adsorbed on to the NPs surface in the ground state resulting the change in the electronic properties of dye molecules. Also due to this interaction the average hydrodynamic size of the nanoparticle as

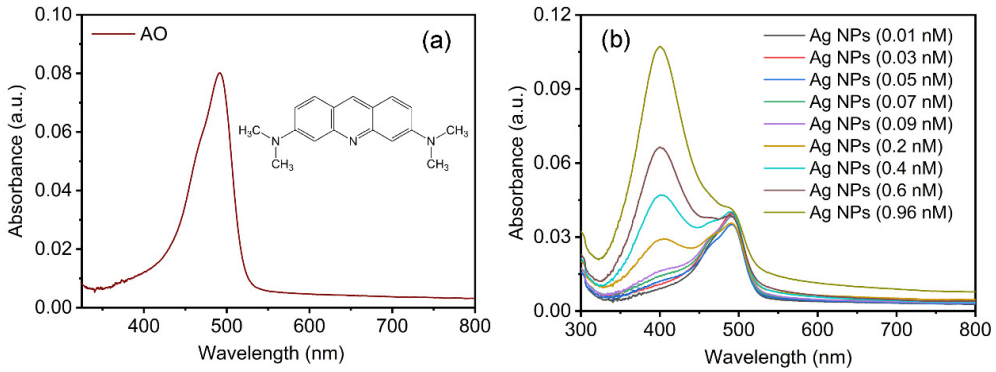

Figure 7.4. UV-vis absorption spectra of (a) AO aqueous solution (concentration of 1 µM) and (b) AO (1 µM) and Ag NPs mixed solutions for various concentrations of Ag NPs. Inset of (a) shows the molecular structure of AO.

obtained from DLS study (Figure 7.5) is increased to ~105 nm confirming the adsorption of dye molecules on the surface of NPs. Furthermore, the Zeta potential of AO/Ag NPs mixed solution becomes less negative (-16 mV) when compared to pure Ag NPs. Both these results confirm the binding of Ag NPs with AO in aqueous solution.

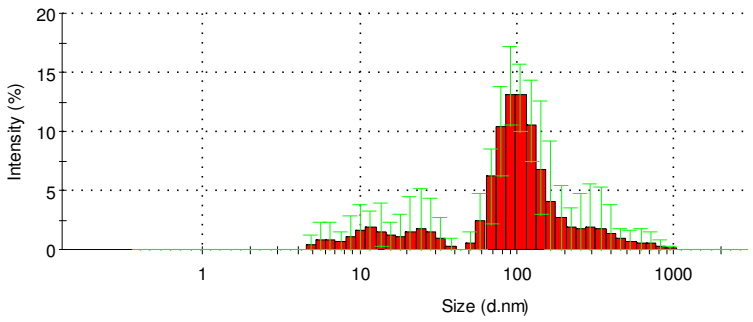

Figure 7.5. DLS spectrum of Ag NPs/AO mixed aqueous solution

Ag NPs have been explored as the carrier of various biomolecules including delivery of theraptic materials for biomedical interest. In this study we also aim to understand the effect of Ag NPs/AO mixed solution on the spectroscopic properties of DNA. It is a biological macromolecules and in aqueous solution it is negatively charged [32]. Figure 7.6 shows the UV-vis absorption spectra of pure DNA solution, AO/DNA mixed solution, Ag NPs/DNA mixed solution and Ag NPs/AO/DNA mixed solution. Pure DNA shows the characteristic absorption band at around ~262 nm which is due to π-π^* transition of the nucleic acid base pairs of DNA [33] The transition dipole moments due to this absorption generally oriented along the short axis of the base pair [34]. AO/DNA mixed absorption spectrum as shown in Figure 7.6 reveals that the characteristic band of DNA is shifted to ~267 nm and the monomeric band of AO (~490 nm) is also slightly shifted to higher wavelength i.e., at ~500 nm. This change of the absorption spectrum gives an indication of the interaction of DNA with AO dye molecules in the aqueous solution. The difference in ionic character of DNA and AO is possibly responsible for the interaction. On the other hand, when Ag NPs is mixed with DNA solution the ~262 nm band is totally disappeared with no appreciable change of the plasmonic band (~400 nm) of Ag NPs. This results confirms the binding of DNA with Ag NPs as well. Most interestingly absorption spectrum of Ag NPs/AO/DNA shows that the ~262 nm of DNA is shifted to ~267 nm as well as AO monomeric absorption peak is slightly shifted. Additionally, the intensity of plasmonic band (~400 nm) of Ag NPs is sufficiently decreased. This observation reveals the bind of both Ag NPs and AO dye with DNA in the aqueous solution.

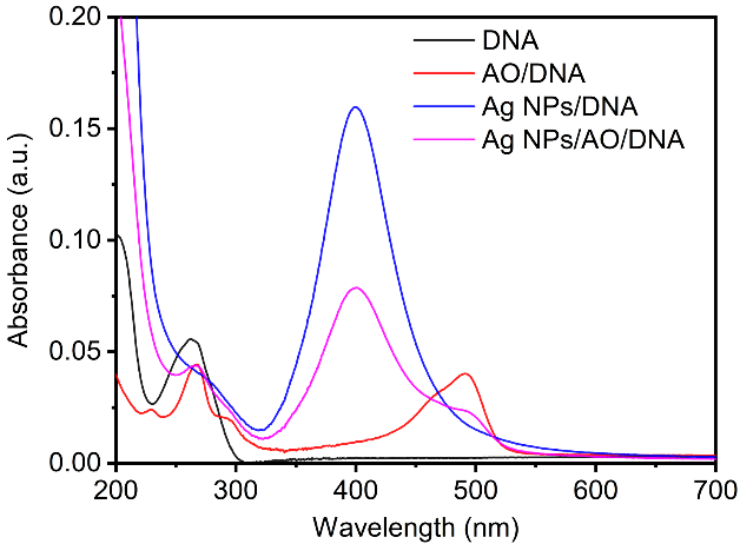

Figure 7.6. UV-vis absorption spectra of pure DNA aqueous solution; AO/DNA, Ag NPs/DNA and Ag NPs/AO/DNA mixed aqueous solution.

7.3.3. Steady state fluorescence spectroscopic study

Steady fluorescence emission technique is an elegant approach of understanding the molecular level interactions in the excited state between various molecular species. Figure 7.7a shows the steady-state fluorescence emission spectrum of AO aqueous solution (concentration of 1 μM). This emission spectrum shows distinct and prominent emission peak of AO dye at around ~525 nm. The sample solution was exited at wavelength of 475 nm. The 525 nm peak is attributed to the monomeric emission of AO in aqueous solution [31]. However, when Ag NPs solution with varying concentrations are added to AO solution, the intensity of monomeric band (~525 nm) is gradually decreased as shown in Figure 7.7b. This gradual quenching of fluorescence of AO due to addition of Ag NPs in the mixed solution might have happened due to the adsorption of dye molecules on to NP's surface resulting the decrease in radiative rate of the dye molecules while interacting with NP's surface.

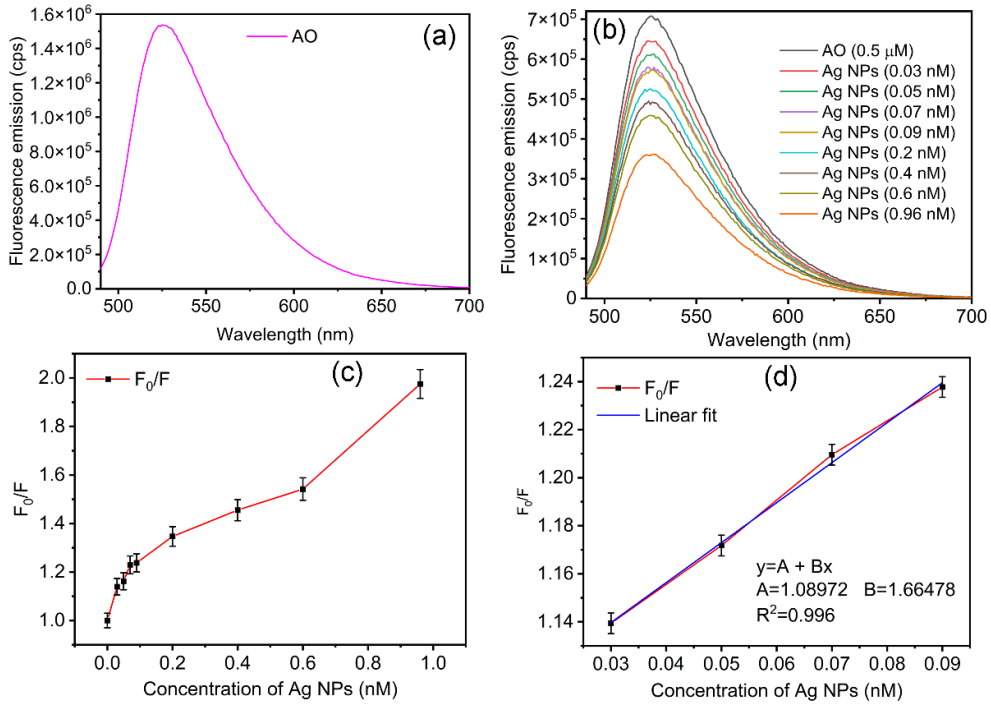

Figure 7.7. Steady-state fluorescence emission spectrum of (a) AO aqueous solution (concentration 1 μM) and (b) AO (0.5 μM) and Ag NPs mixed solution for various concentrations of Ag NPs. (c) Stern-Volmer plot for Ag NPs/AO mixed solution for various concentrations of Ag NPs. (d) Linear region of Stern-Volmer plot. Excitation wavelength was 475 nm.

The quenching of the observed fluorescence of AO due to Ag NPs depends on the nature of interactions between dye molecules and NPs. The quenching may be static or dynamic. For static quenching, a ground state complex may be formed and this does not emit fluorescence [31]. On the other hand, in dynamic or collisional quenching molecules encounter with the quencher due to diffusion resulting change in the radioactive rate of the emitter molecules [35]. The nature or type quenching may be described by well-known Stern-Volmer (SV) equation [36],

$$\frac{F_0}{F} = 1 + K_{SV}[Q] \qquad \ldots\ldots\ldots\ldots\ldots\ldots\ldots (7.1)$$

where F_0 and F are steady state fluorescence intensity of dye molecules in absence and presence of quencher i.e., Ag NPs respectively. K_{SV} is known as SV quenching constant and measure the extent of fluorescence quenching of the emitter molecules in a

particular medium. The plot of F_0/F versus concentration of Ag NPs as shown in Figure 7.7c gives the nature of fluorescence quenching. From this figure it is observed that at lower concentration range the plot is almost linear as shown in Figure 7.7d. The value of K_{SV} is calculated as 1.73209×10^9 M^{-1} from this linear SV plot. However, at higher concentration the plot deviates from the linearity. This results reveal that both static and dynamic quenching might have occurred in the Ag NPs/AO mixed solution under photoexcitation. Actually, at higher Ag NPs concentration, the collision between the nanoparticle and dye molecules increases resulting a dynamic change of the excited state of AO molecules. However, the overall radiative rate constant might have decreased resulting the quenching of the fluorescence intensity of AO in presence of Ag NPs.

The main interest in this study is to understand the interaction behaviour of Ag NPs/AO mixed system with DNA in aqueous environment. The study of the interaction of NPs with biological molecules or systems has become an active area of research for different biological applications during the last several years [29]. The fluorescence emission study of the Ag NPs/AO mixed system in presence DNA gives some interesting results. As both DNA and Ag NPs do not show fluorescence emission, therefore the interaction of such biomolecules with Ag NPs may be understood through the change of fluorescence emission properties of AO in presence of Ag NPs. Figure 7.8 shows the steady state fluorescence emission spectra of pure AO solution, AO/DNA mixed solution, AO/Ag NPs mixed solution and AO/Ag NPs/DNA mixed solution respectively. The emission spectra give some interesting results. The emission spectra of pure AO and AO/DNA are almost similar. AO molecule may intercalate between the double helix of DNA and the complexation is stabilized by π-π stacking interaction [37] although very small amount of DNA (400 μL) was added to AO solution. However, exact binding mechanism is not readily understood and further studies are required. Emission spectrum of AO/Ag NPs mixed solution shows sufficient quenching of the emission. The possible reason of this quenching is already described earlier. However, after addition of DNA in the AO/Ag NPs mixed solution the emission intensity at ~525 nm is further quenched. It is therefore concluded that Ag NPs strongly binds with DNA and forms complex [38] when compared to AO as reflected in the emission results. The reduction of fluorescence intensity of AO/DNA mixed solution after addition of Ag NPs may possibly due to the fact that Ag NPs were trying to associate with DNA

molecules by means of several possible ways such as groove binding, hydrophobic or hydrogen bonding interactions or via electrostic interactions [39]. Also the drastic reduction of fluorescence intensity of AO/DNA mixed solution in presence of Ag NPs implies that the Ag NPs induces rapid exclusion of AO molecules from the double helix structure of DNA and replacing Ag NPs via strong interaction. Literature reveal that this type quenching may be static quenching as Ag NPs forms complex with DNA [40].

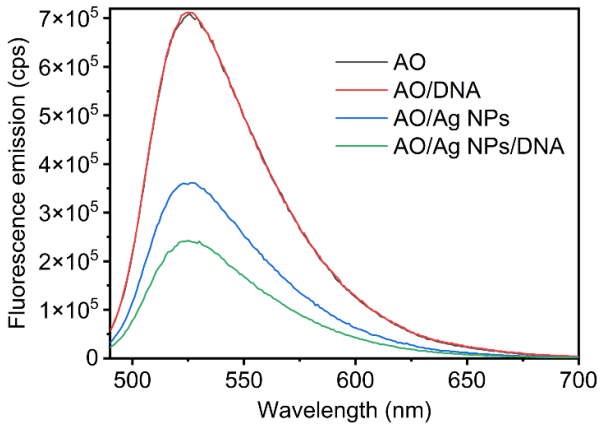

Figure 7.8. Steady-state fluorescence emission spectra of AO aqueous solution (0.5 µM) in presence of DNA (400 µL, 10 µM), Ag NPs (0.96 nM).

7.3.4. DFT study

DFT is an important theoretical approach for studying the frontier molecular orbital structure and molecular orbital energies responsible for various photophysical properties in different microenvironments. Figure 7.9 shows the geometry optimized structure of AO dye in the solvent (water) background using the CPCM model. The AO dye was optimized by the B3LYP/6-31+G(d,p) level of theory using the Gaussian 09 software [23,24]. The TD-DFT calculation was also performed using the same level of theory as already used in case of geometry optimization. Frontier molecular orbitals (HOMO, LUMO etc.) energies or the excitation energies were also obtained for AO and their corresponding contour map was visualized by GaussView 6.0.16 software [25] as shown in Figure 7.9. The HOMO and LUMO energy difference or the energy corresponding to the excitation of singlet electronic state of AO was estimated as ~3.411 eV. The theoretical study also reveals that the main strong characteristic

transition of AO dye is attributed to the π–π* transition of the xanthene moiety and the result is consistent with the experimental UV–vis absorption study of the dye aqueous solution. The resultant transition dipole moments for the ground state to the first excited state transition of AO was 0.422 Debye. Therefore, the well converging nature of this theoretical study signifies various important information on the electronic structures and molecular mechanism involved in their ground electronic states.

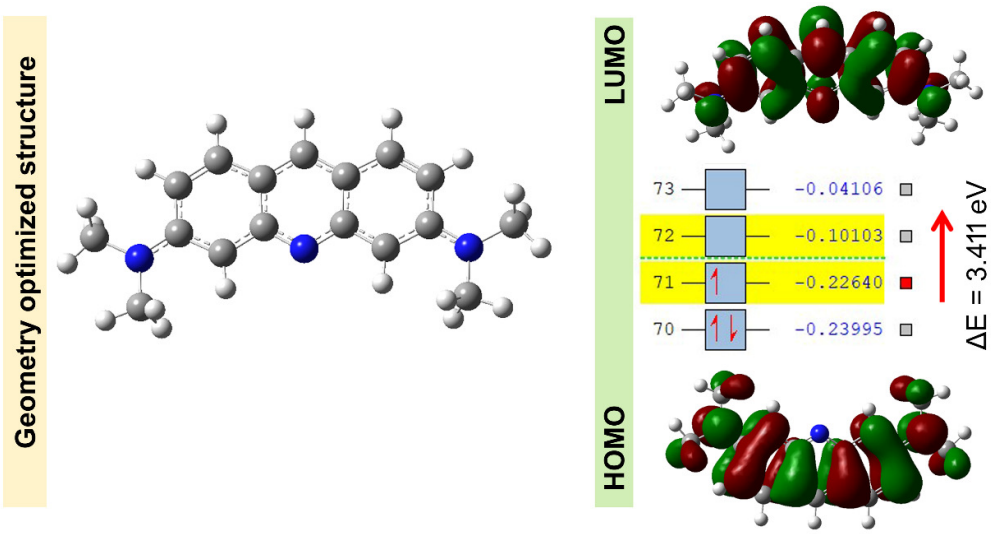

Figure 7.9. Geometry optimized structure and frontier molecular orbitals (HOMO and LUMO) associated with the electronic states of AO dye molecule as obtained by using the B3LYP/6-31+G(d,p) level of theory. The excitation energies (ΔE) is calculated from the TD-DFT calculation using the same level of theory.

7.4. Conclusion

In conclusion the present study reveals the interaction of as-synthesized silver nanoparticles (Ag NPs) with cationic organic dye namely Acridine orange (AO) in presence of biological macromolecule DNA in aqueous medium. DLS studies reveals the hydrodynamic particle size of the Ag NPs as 91 nm. When Ag NPs interacts with AO molecules the hydrodynamic size of the nanoparticles also increases which confirms the adsorption of dye molecules on the surface of nanoparticles. Ag NPs strongly quench the fluorescence emission of dye molecules in the solution. UV-vis studies confirm the binding of both Ag NPs and dye molecules with DNA molecules.

However, addition of Ag NPs to AO/DNA mixed solution gives the strong quenching of emission of AO dye molecules. However, this quenching of fluorescence of AO molecules by Ag NPs in presence of DNA corresponds to striving interaction of Ag NPs with DNA through the expulsion of intercalated AO molecules from the DNA molecules. DFT results reveals the energy gap between the HOMO and LUMO levels of AO dye molecule as 3.41 eV. The proposed study provides valuable fundamental information about nano-bio interactions and may have possible implications for various biotechnological applications.

References

[1] C. Gao, Z. Guo, J. H. Liu, X. J. Huang, *Nanoscale*, 4 (2012) 1948.

[2] R. G. Saratale, I. Karuppusamy, G. D. Saratale, A. Pugazhendhi, G. Kumar, Y. Park, G. S. Ghodake, R. N. Bharagava, J. R. Banu, H. S. Shin, *Colloids Surf. B*, 170 (2018) 20–35.

[3] Y. K. Mishra, R. Adelung, *Mater. Today*, 21 (6) (2018) 631–651.

[4] R. Reshmy, E. Philip, S. A. Paul, A. Madhavan, R. Sindhu, P. Binod, A. Pandey, R. Sirohi, *Rev. Environ. Sci. Biotechnol.*, 19 (2020) 779–806.

[5] S. Patnaik, D. P. Sahoo, K. Parida, *Renew. Sustain. Energy Rev.*, 82 (1) (2018) 1297–1312.

[6] J. Yao, M. Yang, Y. Duan, *Chem. Rev.*, 114 (12) (2014) 6130–6178.

[7] F. Hu, S. Xu, B. Liu, *Adv.Mater.*, 30 (2018) 1801350.

[8] Y. Wang, B. Yan, L. Chen, *Chem. Rev.*, 113 (2013) 1391−1428.

[9] S. T. Kochuveedu, D. H. Kim, *Nanoscale*, 6 (2014) 4966.

[10] A. Schroter, S. Märkl, N. Weitzel, T. Hirsch, *Adv. Funct. Mater.*, 32 (2022) 2113065.

[11] Q. Cui, F. He, L. Li, H. Möhwald, *Adv. Colloid Interface Sci.*, 207 (2014) 164–177.

[12] D. Kim, K. Shin, S. G. Kwon, T. Hyeon, *Adv. Mater.*, 30 (2018) 1802309.

[13] I. Khan, K. Saeed, I. Khan, *Arab. J. Chem.*, 12 (7) (2019) 908–931.

[14] P. K. Dikshit, J. Kumar, A. K. Das, S. Sadhu, S. Sharma, S. Singh, P. K. Gupta, B. S. Kim, *Catalysts*, 11 (8) (2021) 902.

[15] N. K. Sharma, J. Vishwakarma, S. Rai, T. S. Alomar, N. Al Masoud, A. Bhattarai, *ACS Omega*, 7 (2022) 27004−27020.

[16] A. Samanta, I. L. Medintz, *Nanoscale*, 8 (2016) 9037–9095.

[17] P. E. Nielsen, *Acc. Chem. Res.*, 32 (1999) 624–630.

[18] J. Liu, Y. Zhang, H. Xie, L. Zhao, L. Zheng, H. Ye, *Small*, 15 (2019) 1902989.

[19] K. Supabowornsathit, K. Faikhruea, B. Ditmangklo, T. Jaroenchuensiri, S. Wongsuwan, S. Junpra-ob, I. Choopara, T. Palaga, C. Aonbangkhen, N. Somboonna, J. Taechalertpaisarn, T. Vilaivan, *Sci. Rep.*, 12 (2022) 14250.

[20] S. Bi, C. Qiao, D. Song, Y. Tian, D. Gao, Y. Sun, H. Zhang, *Sens. Actuators B Chem.*, 119 (1) (2006) 199–208.

[21] S. D. Solomon, M. Bahadory, A. V. Jeyarajasingam, S. A. Rutkowsky, C. Boritz, L. Mulfinger, *J. Chem. Educ.*, 2007, 84 (2) 322–324.

[22] S. Shikhaa, S. Durejaa, R. Saprab, J. Babub, V. Haridas, S. K. Pattanayek, *RSC Adv.*, 11 (2021) 32286–32294.

[23] M. J. Frisch, G. W. Trucks, H. B. Schiegel, G. E. Scuseria, M. A. Robb, J. R. Cheeseman, Jr. J. A. Montgomery, T. Vreven, K. N. Kudin, J. C. Burant, et al. Gaussian 09, Gaussian, Inc.: Pittsburgh, PA, 2009.

[24] T. Casalini, M. Salvalaglio, G. Perale, M. Masi, C. Cavallotti, *J. Phys. Chem. B*, 115 (2011) 12896−12904.

[25] R. Dennington, T. Keith, J. Millam, GaussView 6.0.16; Semichem Inc.: Shawnee Mission, KS, 2018.

[26] Y. K. Mo, O. Kankavi, P. P. Masci, G. D. Mellick, M. W. Whitehouse, G. M. Boyle, P. G. Parsons, M. S. Roberts, S. E. Cross, *J. Invest. Dermatol.*, 127 (2007) 381−386.

[27] P. Maiti, T. Singha, U. Chakraborty, S. Dutta Roy, P. Karmakar, B. Dey, S. A. Hussain, S. Paul, P. K. Paul, *Mater. Chem. Phys.*, 234 (2019) 158−167.

[28] U. P. Azad, V. Ganesan, M. Pal, *J. Nanopart. Res.*, 13 (2011) 3951–3959.

[29] V. A. Byvaltsev, L. A. Bardonova, N. R. Onaka, R. A. Polkin, S. V. Ochkal, V. V. Shepelev, M. A. Aliyev, A. A. Potapov, *Front. Oncol.*, 9 (2019) 925.

[30] E. Iessi, M. Logozzi, L. Lugini, T. Azzarito, C. Federici, E. P. Spugnini, D. Mizzoni, R. Di Raimo, D. F. Angelini, L. Battistini, S. Cecchettid, S. Fais, *J. Enzyme Inhib. Med. Chem.*, 32 (1) (2017) 648–657.

[31] J. Bhattacharjee, S. A. Hussain, D. Bhattacharjee, *Spectrochim. Acta A Mol. Biomol. Spectrosc.*, 116 (2013) 148–153.

[32] P. Prentø, *Biotech. Histochem.*, 76 (3) (2001). https://doi.org/10.1080/bih.76.3.137.161

[33] N. Higashi, T. Inoue, M. Niwa, *Chem. Commun.*, 1997, 1507–1508. https://doi.org/10.1039/A701265I

[34] H. M. Wu, N. Dattagupta, D. M. Crothers, *Biochem.*, 78 (1981) 6808–6811.

[35] D. Genovese, M. Cingolani, E. Rampazzo, L. Prodi, N. Zaccheroni, *Chem. Soc. Rev.*, 50 (2021) 8414.

[36] P. Maiti, U. Saren, U. Chakraborty, T. Singha, S. Paul, P. K. Paul, *ACS Omega*, 7 (2022) 29013−29026.

[37] S. A. Hussain, P. K. Paul, D. Dey, D. Bhattacharjee, S. Sinha, *Chem. Phys. Lett.*, 450 (2007) 49–54.

[38] Komal, Sonia, S. Kukreti, M. Kaushik, *J. Photochem. Photobiol. B, Biol.*, 194 (2019) 158–165.

[39] M. Sirajuddin, S. Ali, A. Badshah, *J. Photochem. Photobiol. B, Biol.*, 124 (2013) 1–19.

[40] Z. Sohrabijam, M. Saeidifar, A. Zamanian, *Colloids Surf. B*, 152 (2017) 169–175.

CHAPTER ~ 8

Hydrothermal Synthesis of Bio-Inspired MoS_2 Nanoflakes for Highly Sensitive Fluorescence-based Detection of Mercury Ion in Aqueous Solution and Cellular Milieu

This chapter describes the synthesis and characterization of fluorescent MoS_2 nanoflakes. As-synthesized nanoflakes are utilized to detect toxic metal ion namely mercury both in aqueous solution and human cell via highly sensitive fluorescence method.

A research paper based on the work presented in this chapter has been communicated to an international journal for publication.

CHAPTER~8

Hydrothermal Synthesis of Bio-Inspired MoS_2 Nanoflakes for Highly Sensitive Fluorescence-based Detection of Mercury Ion in Aqueous Solution and Cellular Milieu

8.1. Introductory remarks

Heavy metal ion such as mercury (Hg) is one of the most dangerous non-biodegradable metal pollutant is known to be highly toxic for biological system as suggested by World Health Organisation (WHO) [1]. Elemental mercury (Hg^0) is easily oxidized into divalent mercuric ion (Hg^{2+}) form and is widely released to the environment by means of various emission such as industrial activities, vehicles, power-plants using fossil fuels etc. [2]. Also, Hg^{2+} dissolved in water is the most abundant form of inorganic Hg [3]. Trace amount of Hg^{2+} ion in drinking water may also contribute to the detrimental effects on our physiological health due to disruption in both neurological and immunological responses [4,5]. US Environmental Protection Agency (USEPA) already set a maximum permissible limit of inorganic Hg in drinking water as 0.002 ppm [6]. It is well known that the prevalence of Hg in the earth surface is occurred from volcanic activity, weathering of rocks, sea water etc. [7]. Human activity is also an another predominant factor for the release of Hg into the environment particularly by the thermal power stations, residential coal burning, medical wastes, pharmaceutical wastes etc. [8]. High exposer of Hg to human body in many specific geographical locations are also due to gold mining, deforestations etc. [9]. However, chronic low dose of Hg exposer is associated with the dietary intake of methyl-mercury (CH_3Hg) from various sea-foods and due to significant bio-activity of the Hg^0, Hg^{2+} ion can easily be accumulated in the biological cells [9]. The toxic effect of Hg depends on

the difference in the bio-accessibility and the toxico-kinetics in the biological environment [10]. Hg^{2+} ion tends to bind with nucleobase pairs resulting the conformal change in DNA, which may depend upon the sequence of the base pairs [11]. Various studies suggest that thymine-thymine (T-T) interactions are specific to Hg [12,13]. Due to the above reasons, Hg pollution is being considered as one of the greatest threats to the public health and environmental safety [4,5,8]. Therefore, a precise and facile approach for highly sensitive and selective detection of Hg^{2+} ion in aqueous medium as well as in biological cells is of utmost important both for our health and environment.

In recent time, various two-dimensional (2D) metal-based nanosheets (NSs) have gained significant attention of the global scientific community for metal ions sensing applications [14]. The important physical and physiochemical properties of 2D-layered materials other than carbon have already been discovered for various fields of applications such as transistors, supercapacitors, optoelectronic devices, sensors, bioimaging and so on [15,16]. The 2D-layered nano-structures derived from Transition-metal dichalcogenides (TMDs) exhibit distinct optical, electronic and catalytic properties due to their wide range of chemical composition and unique crystal structures [17,18]. Transition metals have d-electrons which fill up the d-bands to different energy levels resulting significant spectroscopic and electronic properties [19]. Single layered TMD such as molybdenum disulphide (MoS_2) is attracted particular attention in the field of electronics and biomedical research due to their specific structural, morphological, optical and catalytic properties [20,21]. On the other hand, bulk 2D structures of this type of TMDs are also formed by stacking of large number of molecular layers via weak van der Waals interactions. The molybdenum (Mo) and sulfur (S) atoms are bonded covalently within the molecular layers of the transition metal chalcogens MoS_2 [22]. But, various nanostructures of 2D MoS_2 have gained great attention because of their well dispersibility in aqueous medium through easy exfoliation by disrupting the weak van der Waals forces between the consecutive stacked layers [23]. The presence of intrinsic S-atom in MoS_2 NSs makes them a suitable platform for adsorbing various heavy metal ions. In contrast, due to lower specific surface area in bulk MoS_2 as well as the limited accessibility of divalent sulfur (S^{2-}) ion, bulk MoS_2 is generally inefficient for the detection of metal ions [24]. Thus, it is of prior importance to synthesize suitable MoS_2 nano-structures with higher specific surface area and maximum number of accessible S^{2-} ion for efficient selective

interactions with heavy metal ions. Nanostructured MoS_2 has been explored as a suitable material for electrochemical sensing of Hg^{2+} ion in DMF solution [25]. But, as most of the metal ions are abundant in aqueous medium in the environment as well as in our physiological system, a suitable, cost effective and facile approach for the detection of Hg^{2+} ion in aqueous environment is a great deal of importance both for biomedical and environmental aspect. Among the various available analytical approaches of detection of metal ions using 2D MoS_2 or their nanocomposites with other materials, label-free fluorescent detection technique in real cellular system is attracted considerable interest in recent times because this technique is highly sensitive towards analytes [26,27]. Also, measuring the fluorescence signal of the probe via a ratiometric approach in absence and presence of analytes can give accurate information of sensing due to the cancelation of the any external perturbations during measurement [28].

As it is already mentioned earlier that, the presence of Hg^{2+} ion in cellular system may have detrimental effects, therefore, a proper and highly sensitive method of detecting of such metal ion in biological system is of prime importance in the scientific community [12]. Although MoS_2 nanostructures have been explored for the detection of Hg^{2+} ion in different media via various analytical methods, the information regarding the use of nanostructured MoS_2 for the detection of such Hg^{2+} ion in biological cells via a label-free fluorometric method is limited. The main issue of using MoS_2 nanostructured materials for effective biomedical applications is restricted due to their low fluorescence quantum yield (QY) and poor readability of the optical signal from the biological medium. Therefore, the consideration of many critical parameters is highly essential while synthesis of nanostructured MoS_2 with high fluorescence QY especially for biological applications. Y. Wang et. al. [29] reported the enhancement of QY of MoS_2 nanoflakes by reducing their lateral dimension. They also showed that the QY yield can also be increased by adjoining the MoS_2 nanoflakes [30].

In this chapter, the synthesis of highly fluorescent MoS_2 nanoflakes using sodium molybdate dihydrate and biological compound namely L-Cysteine (L-Cys) for sensitive detection of Hg^{2+} ion both in aqueous medium, normal and cancer cells (H9c2 and A549 cell lines) through the fluorescence quenching effect of MoS_2 are demonstrated. Nanoflakes like structures of MoS_2 due to stacking of NSs have been visualized by Field emission scanning electron microscopy (FESEM), Transmission

electron microscopy (TEM), Atomic force microscopy (AFM) etc. The crystallographic information of MoS_2 nanoflakes are explored by the X-ray diffraction (XRD) and high resolution TEM (HRTEM) study. UV-vis absorption, steady-state and time-resolved fluorescence emission (TCSPC), Raman spectroscopic and Cyclic voltammetry (CV) studies were employed to understand the electronic properties and the interaction of MoS_2 with Hg^{2+} ion in aqueous medium. The fluorescence microscopic imaging technique was used to detect the presence of Hg^{2+} ion in the studied cells. Density functional theoretical calculations (DFT) have been performed using Quantum Espresso (QE) software package in order to correlate the band structures and electronic properties of MoS_2 nanoflakes in absence and presence of Hg^{2+} ion with the experimental observations.

8.2. Materials and experimental methods

8.2.1. Materials

All the chemicals were in analytical grade and used in this work as received without further purification. Sodium molybdate dihydrate (Na_2MoO_4, $2H_2O$, M.W.: 241.95 $gmol^{-1}$, ≥99.5%) and L-Cysteine ($C_3H_7NO_2S$, M.W.: 121.16 $gmol^{-1}$, ≥98%) were purchased from Sigma-Aldrich (USA). Mercury (II) chloride ($HgCl_2$, M.W.: 271.5 $gmol^{-1}$). All the required metal salts used in ion sensing application described in this present study were obtained from Merck Chemical Company (Germany). Aqueous solutions of all the chemicals were prepared with triple distilled deionized milli-Q water (resistivity ~18.2 MΩ cm, pH ~7 at temperature of 25 °C, collected from Synergy integrated with an Elix Advantage setup; make: Millipore SAS, France). All the glasswares were cleaned by rinsing with Milli-Q water and then autoclaved at 60 ºC for 24 hrs before use in the experiments.

8.2.2. Synthesis of fluorescent MoS_2 nanoflakes

MoS_2 nanoflakes sample was prepared by a facile hydrothermal approach [31,32] using $C_3H_7NO_2S$ as the rich sulfur (S) precursor. The procedure of synthesis is schematically shown in Figure 8.1. In brief, 0.25 g of Na_2MoO_4, $2H_2O$ was dissolved in 25 mL of milli-Q. After continuous ultrasonication for 30 min at room temperature, the solution pH was adjusted to ~6.5 using 0.1 M HCl. Then 0.5 g of $C_3H_7NO_2S$ and 50 mL of milli-Q were added to the solution followed by continuous ultrasonication for

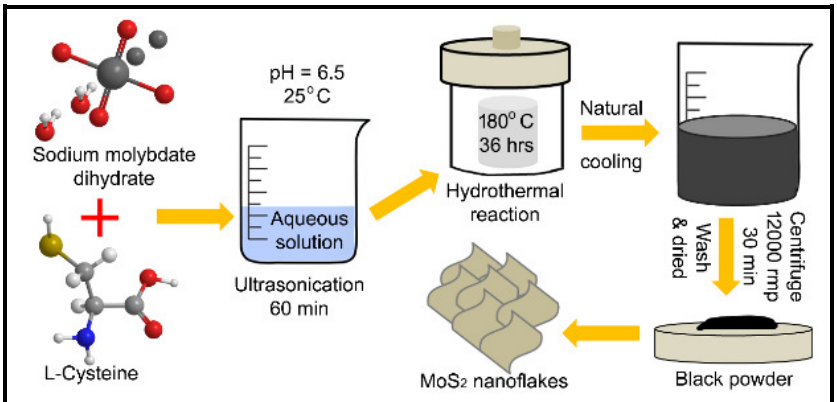

Figure 8.1. Schematic representation of synthesis of highly fluorescent MoS_2 nanoflakes.

an additional 60 min. The mixture was then transferred into a 100 mL Teflon-lined stainless-steel autoclave and heated at 180 °C for 36 hrs. To complete the reaction, the solution cooled naturally to room temperature and the supernatant containing MoS_2 nanoflakes was collected followed by centrifugation for 30 min at 12000 rpm. The collected MoS_2 sample were washed, dried and stored in dark place for further studies.

8.2.3. Characterizations

High-resolution transmission electron microscopy (HRTEM) measurement and selected area electron diffraction (SAED) study of the as-synthesized MoS_2 samples were obtained by using a transmission electron microscope (model: JEM-2100 Plus TEM, JEOL Ltd., Japan) operated at an accelerating voltage of 200 kV. For the HRTEM study, the sample solutions were ultrasonicated and incubated for 20 min and then a small drop from each solution was spread onto the carbon-coated copper microgrid (make: PELCO 300 Mesh Grids, Ted Pella Inc.) and subsequently dried at room temperature (25 °C). Field emission scanning electron microscopy (FESEM) (model: F50, INSPECT, Netherlands) operated at a bias voltage of 5–20 kV was also employed to visualize the morphological features of MoS_2 sample. The surface morphology and roughness measurement of the samples were performed on smooth mica sheets using a commercially available atomic force microscope (AFM) (model: Di Innova AFM, Bruker, USA) in tapping mode in a humidity-controlled environment. For FESEM and AFM measurements, the freshly prepared MoS_2 aqueous dispersion were deposited onto smooth Si substrates. The effective surface Zeta (ζ) potential of the as-synthesized MoS_2 nanoflakes was obtained by a Malvern Zetasizer (model: NanoZS90, Malvern

Instruments Limited, Worcestsershire, UK) via dynamic light scattering (DLS) method at an ambient condition.

The synthesized MoS_2 sample was further characterized by using a X-ray powder diffractometer (model: D8, Bruker AXS, WI, USA) for 2θ values ranging from ~10° to ~70°. The X-ray tube was operated at 35 kV and filament current of ~35 mA. CuK_α target was used to emit characteristic X-rays of wavelength of 1.5418Å. The scan speed for recording the X-rays diffraction data was 2 s per step. The UV−vis absorption spectra of the samples were obtained in the wavelength range of 200−800 nm by a double-beam UV−vis absorption spectrophotometer (model: UV−1800, Shimadzu, Japan) after proper baseline correction for the solvent background. The steady-state fluorescence excitation and emission spectra of the sample solutions were recorded using a spectrofluorometer (model: Fluoromax−4C, Horiba Instruments Incorporated, USA) keeping slit width of 2 nm for both excitation and emission monochromator. The sample solutions were excited at wavelength of 400 nm and the corresponding fluorescence emission spectra were recorded in the wavelength range of 410−700 nm at room temperature (25 °C). Fluorescence-grade quartz cuvettes of path length 1.0 cm (make: Kozima, Japan) were used in all of the absorption and fluorescence emission measurements. To estimate the fluorescence lifetime of MoS_2 sample time-resolved fluorescence lifetime measurements were carried via Time correlated single photon counting (TCSPC) technique using a modular time-resolved spectroflurometer (model: FluoroCube, make: Horiba Jobin Yvon, Horiba Scientific Incorporated, USA) having an instrument response time of ~1 ns. Sample solutions were excited at 370 nm using a nanosecond pulsed diode laser (model: nanoLED-07, IBH, UK) and TBX-04 as the detector. The fluorescence decay data were collected over 2000 micro channel plate photomultiplier tube (PMT) (model: R928P, make: Hamamatsu, Japan) by monitoring at the maximum steady-state fluorescence emission wavelength (i.e., ~465 nm). IBH DAS-6 fluorescence decay analysis software was used to deconvolute the decay data. The goodness of fit was judged by the reduced χ^2 values and residual plot. The fluorescent decay curve was fitted with bi-exponential decay profile as described by equation (eqn.) (8.1), [33,34]

$$I(t) = \alpha_1 e^{-t/\tau_1} + \alpha_2 e^{-t/\tau_2} \quad \ldots\ldots\ldots\ldots\ldots\ldots\ldots\ldots\ldots (8.1)$$

where τ_1 and τ_2 are the decay times and α_1 and α_2 are their normalized relative amplitudes respectively. The average fluorescence lifetime (τ_{av}) was analysed using the eqn. (8.2), [34]

$$\tau_{av} = (\alpha_1\tau_1 + \alpha_2\tau_2)/(\alpha_1 + \alpha_2) \ldots\ldots\ldots\ldots\ldots\ldots\ldots\ldots (8.2)$$

Raman spectroscopic study of MoS_2 nanoflakes were performed using a Raman spectrometer (model: Xplora Plus micro-Raman, Horiba, USA) with a 532 nm laser excitation source. Fourier transform infrared (FTIR) spectra of the samples were recorded using a FTIR spectrometer (model: IRAffinity-1S, Shimadzu, Japan) in attenuated total reflection (ATR) mode at ambient temperature. Cyclic Voltammetry (CV) study of as-prepared MoS_2 and Hg-adsorbed MoS_2 aqueous solution were performed by using a computer controlled potentiostat/galvanostat (model: AUTOLAB, PGSTAT101, Metrohm, Switzerland) using a conventional three electrode system and 50 mL electrochemical cell. The glassy carbon electrode, platinum (Pt) electrode and Ag/AgCl in satd. NH_4PF_6 electrode were used as the working, counter and reference electrodes respectively. The solutions in the electrochemical cell were de-aerated using argon (Ar) gas prior to run each CV experiment for a minimum period of 30 min. The CV data was collected and analysed with the help of NOVA 1.10.1.9 programme. The pH of all the sample's aqueous solutions were measured by using a digital pH meter (model: FiveEasy Plus, Mettler Toledo, Germany).

8.2.4. Sample preparation for fluorometric detection of Hg^{2+} ion

In a typical titration experiment, MoS_2 nanoflakes /Hg^{2+} mixed solution was prepared by adding 100 µL freshly prepared Hg^{2+} aqueous solution of concentration of 2 µM into 3 mL of freshly prepared aqueous dispersion of MoS_2 nanoflakes (concentration 1 mg/mL) and incubated for 3 min at room temperature (25 °C). The whole titration experiment was performed in total 10 steps at an ambient condition and in each step 100 µL of Hg^{2+} aqueous solution of concentration of 2 µM was sequentially micro-pipetted with the previous MoS_2/Hg^{2+} mixed solution. The resultant solution was mixed thoroughly and incubated for 3 min. Thus, the final concentrations of the Hg^{2+} in the mixed solution were viz. nM: ~64.5, ~127, ~187.6, ~246.4, ~303.5, ~359, ~413.1, ~465.7, ~416.3 and ~566.3. The pH of the MoS_2 aqueous dispersion was ~7.0 and remained approximately constant through the whole analysis. After the incubation period of 3 min, colorimetric images, UV−vis absorption and steady−state fluorescence emission spectra of the MoS_2/Hg^{2+} mixed solution were recorded immediately. Also,

the mixed solutions (concentration of ~566.3 μM in the mixed solution) of other relevant metal ions (described later) with the aqueous dispersion of MoS_2 sample (concentration of 1 mg/mL) were prepared in the same ambient condition prior to the spectrofluorometric measurements.

8.2.5. Method for the determination of quantum yield of MoS_2 nanoflakes

The relative fluorescence quantum yield (QY) of as-synthesized nanostructured MoS_2 sample was obtained by using a widely used method as reported in the literatures [35,36]. As a principle, aqueous solution of quinine sulfate (QY ~0.546 (54.6 %) for an excitation of 340 nm) in 0.1 M H_2SO_4 was considered as the reference. The aqueous solutions of quinine sulfate and MoS_2 were always diluted such that the absorption intensity were under 0.1 respectively to avoid the reabsorption effects. The QY of MoS_2 was determined using the following eqn. (8.3), given bellow.

$$Q_S = Q_R \left(\frac{OD_R}{OD_S}\right)\left(\frac{A_S}{A_R}\right)\left(\frac{\eta_S^2}{\eta_R^2}\right) \dots\dots\dots\dots\dots\dots (8.3)$$

where, S and R are the sample (i.e., MoS_2) and reference (i.e., quinine sulfate) respectively. OD, A, and η are optical density at the excitation wavelength, area under the fluorescence emission curve and refractive index of the solvent (water ~1.33) for sample and reference respectively.

8.2.6. Cell line and culture conditions

The cancer cells (A549 cell lines, human lung fibroblast) and normal cells (H9c2 cell line, rat heart myocardium) were cultured in an enriched cell culture medium of DMEM supplemented with 10 % fatal bovine serum (FBS), 100 units/mL of antibiotic penicillin G sodium and 100 μg/mL of streptomycin sulfate at temperature of 37 °C in the prevalence of 5 % carbon dioxide (CO_2) and 95 % relative humidity (RH). Following trypsinization, the cells were seeded at required density according to the respective experiments to allow them to re-equilibrate a day before the start of the experiment.

8.2.7. Cytotoxicity assay

The toxicity of the aqueous dispersion of as-prepared MoS_2 sample in presence of Hg^{2+} ions towards A549 and H9c2 cells were determined by using 3-[4,5-dimethylthiazol-2-yl]-2,5 diphenyl tetrazolium bromide (MTT) assay method [21].

A549 and H9c2 cells were seeded at a density of 1×10^6 cells per well. Then, different concentrations (viz. μg/mL 0, 8.69, 12.5, 19.23 etc. in the cellular medium) of MoS_2 aqueous solution were added to the cell medium and incubated for 2 hrs. After 2 hrs of incubation, aqueous solution of $HgCl_2$ was added to the culture medium (the final concentration of $HgCl_2$ in the cellular medium was ~47.62 nM) and incubated for 1 hr. The MTT stock solution of concentration 5 mg/mL was diluted in a ratio of 1 : 10 in 1 × PBS (phosphate buffer saline) buffer. After total 3 hrs of incubation, the culture medium was replaced with 40 μL of the diluted MTT solution. The cells were then incubated for another 3 hrs in 95 % RH and 5 % CO_2 at 37 °C. After 3 hrs, the MTT solution was discarded from each well and 50 μL of extraction buffer (80 % isopropanol, 20 % Triton X-100 and 12 (N) HCl) was added to each well. Finally, the formation of formazol crystal colour was monitored by measuring the absorbance at 570 nm by using a microplate reader (BioTek, USA).

8.2.8. Protocol of normal and cancer cell imaging

For cellular imaging via fluorescence microscopy method, H9c2 and A549 cells were seeded at a density of 1×10^9 cells in the 35 mm dish with a clean cover slip and incubated for 24 hrs in 37 °C, 5 % CO_2 and 95 % RH. After reaching 60–70 % confluency, the cells were treated with aqueous dispersion of MoS_2 sample and incubated for 2 hrs. After incubation, the cells were treated with $HgCl_2$ aqueous solution and incubated for an additional 1 hr. Following the incubations, the cells were washed with PBS and fixed with 4 % paraformaldehyde (PFA) for 10 min. After fixation, the cells were washed again with PBS and the cover slips were mounted with mounting media. Fluorescence microscopy studies were carried out with a Leica DM2000 (Germany) fluorescence microscope across different fields (using excitation and emission wavelengths of ~405 nm and ~455 nm respectively) under 40X magnification. Quantification analysis were performed using the ImageJ software.

8.2.9. Computational details

The geometry optimizations and related theoretical calculations were executed using ab-initio first principal DFT study by QE package [37]. Computationally convenient projector augmented wave (PAW) type pseudopotentials were used in the calculations. In this approach of computational iteration, the valence electrons include the $[Kr]4d^55S^1$ of Mo atom and $[Ne]3S^23P^4$ of S atom. Also, for more accuracy of the

exchange–correlation energy, generalized gradient approximation (GGA) shaped by Perdew–Burke–Ernzerhof (PBE) have been used in the calculation [38]. Plane wave basis set with kinetic energy cut off for wave functions is 50 Ry and charge density potential cut off is 450 Ry. The atomic positions and cell parameters were fully relaxed by self-consistent loop with an energy convergence of 10^{-6} eV. 16 × 16 × 1 Monkhorst–Pack *k*-mesh values were used for the self-consistent calculations and more dense 48 × 48 × 1 *k*-mesh values were used for non-self-consistent calculations of band structures and density of states of monolayer MoS_2. Further, 50 × 50 × 50 × 50 *k*-points mesh along the path M-Γ-K-M in the irreducible Brillouin zone were taken to obtain the band structure with a fine mesh points. The real and imaginary part of dielectric constants of the optimized structures are analysed to study the optical properties. In case of monolayer and bilayer MoS_2, a vacuum space of 15 Å and 25 Å respectively along Z-axis were used to isolate the neighbouring layers by preventing from any interaction among them. The geometry of the pristine structure as well as all the Hg adsorbed structures of MoS_2 are fully optimized.

8.3. Results and discussions

8.3.1. Characterizations of as-synthesized MoS2 nanoflakes

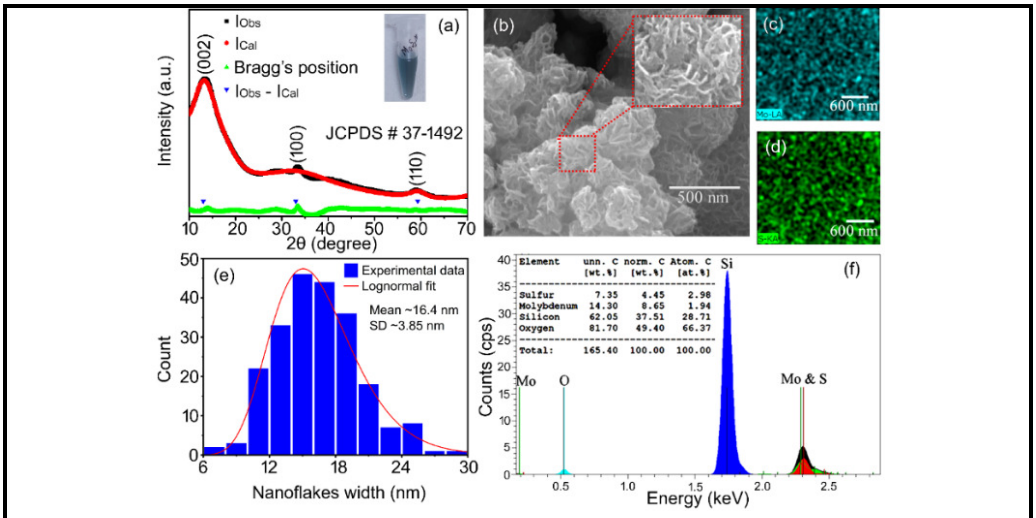

Figure 8.2. (a) X-ray diffractogram and (b) FESEM image of as-synthesized MoS_2. Elemental mappings of (c) Mo-La and (d) S-Ka. (e) Lognormal width distribution of MoS_2 nanoflakes as obtained from (b). (f) EDX spectrum of as-synthesized MoS_2 nanoflakes. Inset of (a) shows vial containing aqueous dispersion of MoS_2 nanoflakes.

The structural, morphological and optical characterizations of as-synthesized MoS_2 sample have been performed by XRD, FESEM, AFM, HRTEM, UV-vis absorption, fluorescence emission and Raman spectroscopic techniques respectively. The XRD spectrum of MoS_2 sample is shown in Figure 8.2a which confirms the formation of hexagonal crystal structure of MoS_2 prepared from the sodium salt of Mo and L-Cys (which acts as a rich source of S). Inset of Figure 8.2a shows a typical image of vial containing aqueous dispersion of as-synthesized MoS_2 sample under ambient light. The XRD data of the nanostructured MoS_2 has been analysed using rietveld refinement package and shows three distinct diffraction peaks with Bragg angles of 2θ ~14.0º, ~33.4º, and ~58.9º which were indexed to the (002), (100), and (110) crystal planes respectively. This XRD pattern is also consistent with the database of JCPDS (card #37-1492) and thereby confirms the presence of hexagonal phase of nanostructured MoS_2 having lattice parameters of a, b ~3.12 (1) Å, and c ~12.34 (4) Å [39,40]. As no other diffraction peaks were observed, the XRD results therefore confirm the purity and hexagonal phase of MoS_2 nanostructures. The strong intensity of the peak at 2θ ~14.0º reveals the high concentration of NSs which were mostly stacked with each other [39].

Figure 8.2b represents the FESEM micrographs of MoS_2 sample at ambient condition. From these figures we observe that as-prepared MoS_2 samples were basically composed of large number of flower-shaped nanoflakes due to staking of individual NSs. Similar type of flower-shaped nanoflake structure of MoS_2 have been explored by other researchers [41]. The FESEM method was also used to capture the elemental mapping which was completely coupled with the energy dispersive X-ray (EDX) spectroscopy setup and is shown in Figure 8.2c,d,f in order understand the quality of the growth of these nanostructures. The elemental mapping and EDX spectrum reveal the uniform distribution of Mo and S atoms and the purity of the synthesized nanostructured compound [42]. The average width of the MoS_2 was estimated from the

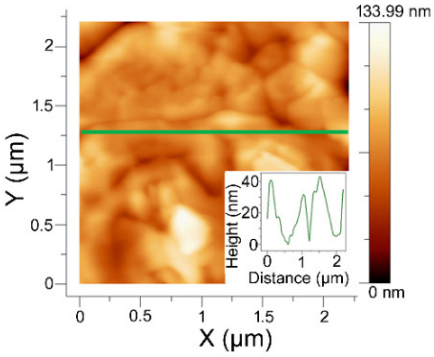

Figure 8.3. Topographic AFM image and roughness profile of MoS_2 nanoflakes along the green line.

lognormal width distribution as shown in Figure 8.2e-and is found to be ~16.4 nm with a standard deviation (SD) of ~3.85 nm. The topographical micrograph (in tapping mode) as acquired by AFM is shown in Figure 8.3. The AFM image shows the aggregated structure of MoS_2 sample with the average r.m.s. roughness of ~46.4 nm which may involve ~3 single layer of NSs.

To have a deeper insight about the microstructure of as-synthesized MoS_2 sample, TEM studies were also performed and is shown in Figure 8.4. The TEM micrographs of MoS_2 sample (Figure 8.4a, b) reveal the wrinkled morphology created by NSs which were seem to be stacked through weakly van der Wall interactions with one another to form nanoflakes like structure [41]. We have also obtained the selected area electron diffraction (SAED) pattern of MoS_2 sample via TEM technique as shown in Figure 8.4c. The SAED image shows hazy and broad diffraction rings which reveal low crystallization order of the as-synthesized MoS_2 nanoflakes sample [43]. This result is consistent with the broad (002) peak observed in XRD spectrum of MoS_2 nanostructured sample as shown in Figure 8.2a. The inter-layer spacing or d-spacing corresponding to (002) plane of MoS_2 lattice was found to be ~0.63 nm as estimated and averaged over 10 lattice fringes obtained by HRTEM (Figure 8.4d) and is the representation of the formation of MoS_2 NSs.

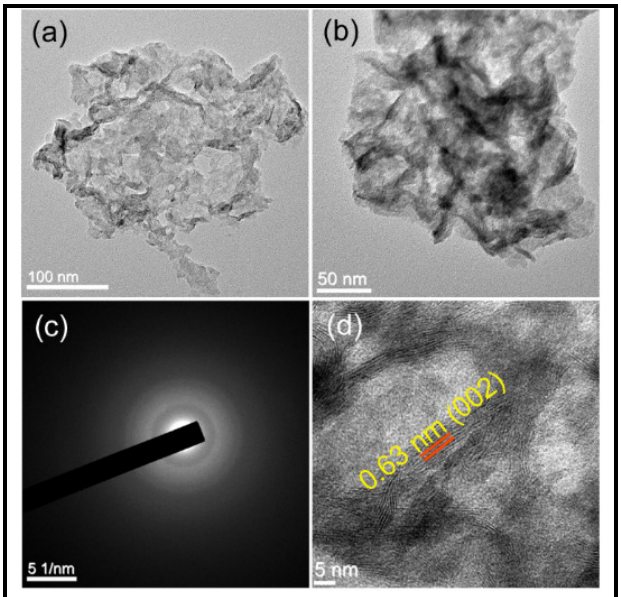

Figure 8.4. (a)-(b) TEM micrographs, (c) SAED pattern and (d) HRTEM micrograph of as-synthesized MoS_2 sample.

The optical absorption properties of as-synthesized MoS_2 nanoflakes aqueous colloidal solution (concentration of 1 mg/mL) were characterized by using UV-vis absorption spectroscopy as shown in Figure 8.5a. The well-defined absorption bands observed at ~306 nm and ~358 nm are attributed to the interband transitions between the occupied d_z^2 orbital and unoccupied d_{xy}, d_{yz}, d_{zx}, and $d_{x^2-y^2}$ orbitals in

hydrothermally synthesized nanostructured MoS_2 sample [44,45]. Moreover, the band gap energy (E_g) of MoS_2 sample was determined by using Tauc plot (inset of Figure 8.5a) near the band edge of allowed transition in the UV-vis absorption spectrum. As we did not observe any higher wavelength absorption peak, we may anticipate the presence of MoS_2 bilayers, trilayers or any higher number of layer stacking of MoS_2 to constitute the observed nanoflake like structure in the studied aqueous medium. Also, the stability of the aqueous dispersion of MoS_2 sample was examined by measuring the

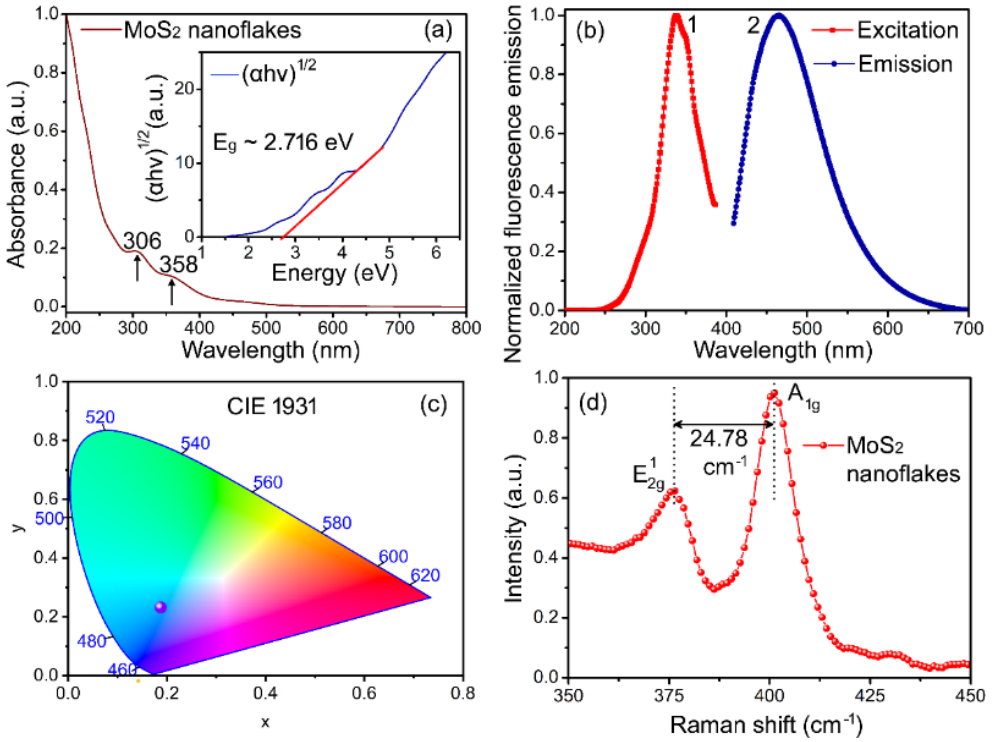

Figure 8.5. (a) UV-vis absorption, (b) steady state fluorescence excitation (curve 1) and emission (curve 2), (c) CIE 1931 color space coordinate and (d) Raman spectrum of synthesized MoS_2 nanoflakes aqueous dispersion. Inset of (a) shows the Tauc plot for indirect optical bandgap of MoS_2 nanoflakes sample.

ζ potential which was found to be -1.04 mV (Figure 8.6). Because, the stability of the MoS_2 nanoflakes in the aqueous medium is generally governed by strong electrostatic repulsion between NSs [46].

Therefore, the observed low value of ζ potential in our experiment corresponds to the staking of several MoS_2 NSs to eventually form nanoflakes like structures and their aggregations in aqueous medium. The flake like structures are already evidenced

from the FESEM image as shown in Figure 8.2b. The synthesized MoS_2 nanoflakes might have possessed indirect optical E_g [47]. In general, for the indirect band gap materials, the value of E_g is estimated using the eqn. (8.4) [45]

$$(\alpha h\nu)^{1/2} = A(h\nu - E_g) \ldots\ldots\ldots\ldots\ldots\ldots\ldots (8.4)$$

where α, h, and ν are the coefficient of absorbance, Plank's constant and frequency of incident light respectively. A is a proportionality constant. The value of E_g was obtained from the intercept between X-axis and the extrapolation of tangent to the linear part of $(\alpha h\nu)^{1/2}$ vs energy ($h\nu$) plot (inset of Figure 8.5a). The intrinsic indirect band gap of MoS_2 nanoflakes was calculated as ~2.716 eV. This result indicates that the formation of electron (e^-) and hole (h^+) pairs in MoS_2 was possible. Some researcher also reported this type of indirect band gap of MoS_2 nanoflakes [29].

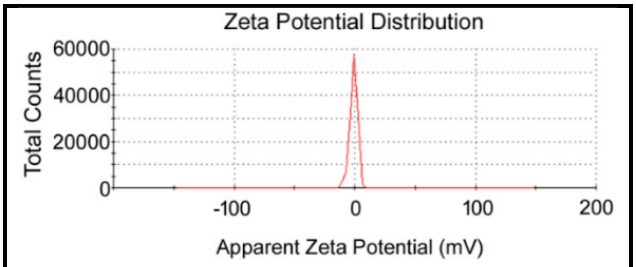

Figure 8.6. Zeta potential spectrum of aqueous dispersion of as-synthesized MoS_2 nanoflakes at an ambient condition.

Different light emitting properties of synthesized MoS_2 nanoflakes were investigated by the steady state fluorescence emission spectroscopic study. Figure 8.5b shows the normalized steady state fluorescence excitation (curve 1) and emission (curve 2) spectra of MoS_2 nanoflakes aqueous dispersion respectively. The strong emission peak observed at ~465 nm when excited at 400 nm suggesting the successful synthesis of fluorescent MoS_2 nanostructured sample. This observed strong fluorescence emission property of the synthesized MoS_2 nanoflakes is basically due to the direct allowed excitonic transitions after photoexcitation [48]. The obtained full width at half maximum (FWHM) (~115 nm, from curve 2) are comparable with that of organic fluorophore but the single emission peak in the excitation spectrum (curve 1) confirms the purity of the as-synthesized MoS_2 nanoflakes [49]. Also the stacking of few layers of MoS_2 (which in turn increased the indirect E_g) facilitates the enhancement of fluorescence emission due to much higher rate of inter-band relaxation [48]. It is important to mention that this unique optical behavior of few-layer MoS_2 is basically originated from the unusual electronic structure of d-orbital of Mo atoms, which construct the valance and conduction bands. The d- orbitals, which are strongly

localized at the site of Mo-atoms, construct the conduction band at the K-point of the Brillouin zone [50]. But, due to the middle position of Mo-atoms in the unit cell of S-Mo-S, these d-orbitals had very low interlayer coupling. However, the indirect bandgap (E_g) near the Γ-point is created by the linear combination of the atomic orbitals (LCAO) of Mo-atoms (d-orbitals) and S-atoms (antibonding p_z-orbitals) [50] Also, this E_g is very sensitive to the layer thickness. The fascinated fluorescence peak of MoS_2 located at ~465 nm (~2.67 eV) in the fluorescence spectrum is originated from the excitonic recombination of the electron (hole) trapped by the uncompensated -ve (or +ve) charge at the dangling bond [18]. The strong fluorescence emission of MoS_2 nanoflakes sample is further correlated with the QY. The UV-vis absorption and fluorescence emission spectra of MoS_2 nanoflakes aqueous solutions and quinine sulfate ($C_{20}H_{26}N_2O_6S$) (as a reference fluorophore) as shown in Figure 8.7 were used to estimate the QY of MoS_2 by using eqn. (8.3) and was found to be ~0.0891. We have also calculated the values of colour coordinates of MoS_2 sample in aqueous medium using 1931 Commission Internationale d'Eclairage (CIE) diagram [51] as shown in Figure 8.5c from the

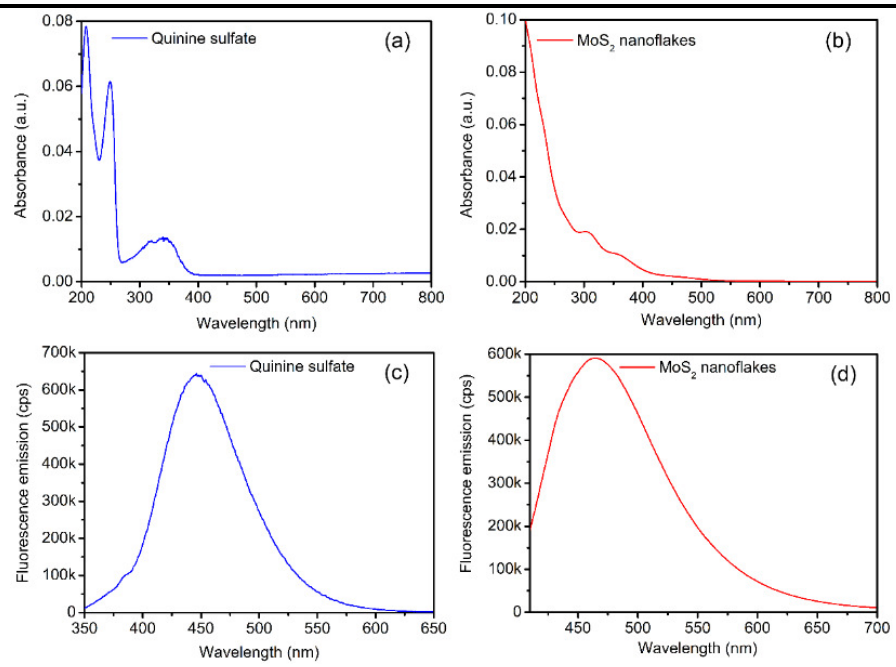

Figure 8.7. UV-vis absorption spectra of (a) Quinine sulfate and (b) MoS_2 nanoflakes. Fluorescence emission spectra of (c) Quinine sulfate and (d) MoS_2 nanoflakes. The excitation wavelengths were 340 nm and 400 nm for quinine sulfate aqueous solution and MoS_2 nanoflakes aqueous dispersion respectively.

observed steady state fluorescence emission and are found to be (x = 0.18766, y = 0.23144) respectively. The values of these parameters have an implication for designing any real life device applications of MoS_2 using their unique fluorescence characteristics. These parameters reveal the distinct identification of the bright blue fluorescence emission of MoS_2 in the colour space enabling their suitability for different sensing and imaging applications.

The layer-type of stacked MoS_2 was investigated by Raman spectroscopic measurements. In this measurement, an excitation laser source of wavelength of 532 nm was used to excite the layered MoS_2 sample and the corresponding Raman spectrum was recorded as presented in Figure 8.5d. The two characteristic peaks of MoS_2 nanoflakes appeared at ~376.48 cm^{-1} and ~401.26 cm^{-1} are attributed to the in-plane vibration of Mo–S bonds (E_{2g}^1) mode and out-of-plane vibration of S-atoms (A_{1g}) mode respectively [52] (Figure 8.5d). These obtained modes of vibration are different from that of the bulk MoS_2 (E_{2g}^1 ~382 cm^{-1} and A_{1g} ~408 cm^{-1} respectively) as reported by various researchers [48,52]. According to the literatures, the peak positions of both E_{2g}^1 mode and A_{1g} mode vary sensitively with the layers of MoS_2 [52]. Especially, with decrease in layer number, the out-of-plane vibrations shifts to higher wavenumber due to weaker van der Waals forces which mostly affect the A_{1g} mode, while in-plane vibration (E_{2g}^1 mode) shifts towards lower wavenumber because of the decrease in dielectric screening of the long-range electrostatic interactions [53]. The difference in wavenumber between E_{2g}^1 mode and A_{1g} mode (Δ ~24.78 cm^{-1}) confirms that the synthesized MoS_2 nanoflakes were formed by staking of few layers (possibly >3) of MoS_2 lamellae [18].

8.3.2. Fluorometric sensing of Hg^{2+} ion by as-synthesized MoS_2 nanoflakes in aqueous medium.

8.3.2.1. Mechanism of Hg^{2+} sensing

MoS_2 nanoflakes can bind with various metal ions via weak van der Wall and electrostatic attraction or covalent bonding interactions in the basal planes of the NSs in aqueous medium [17,18,54]. The optical and electronic properties of such 2D layered materials were drastically changed after interaction with metal ions [54]. In the present work, the initial UV-vis absorption and steady fluorescence spectroscopic results of

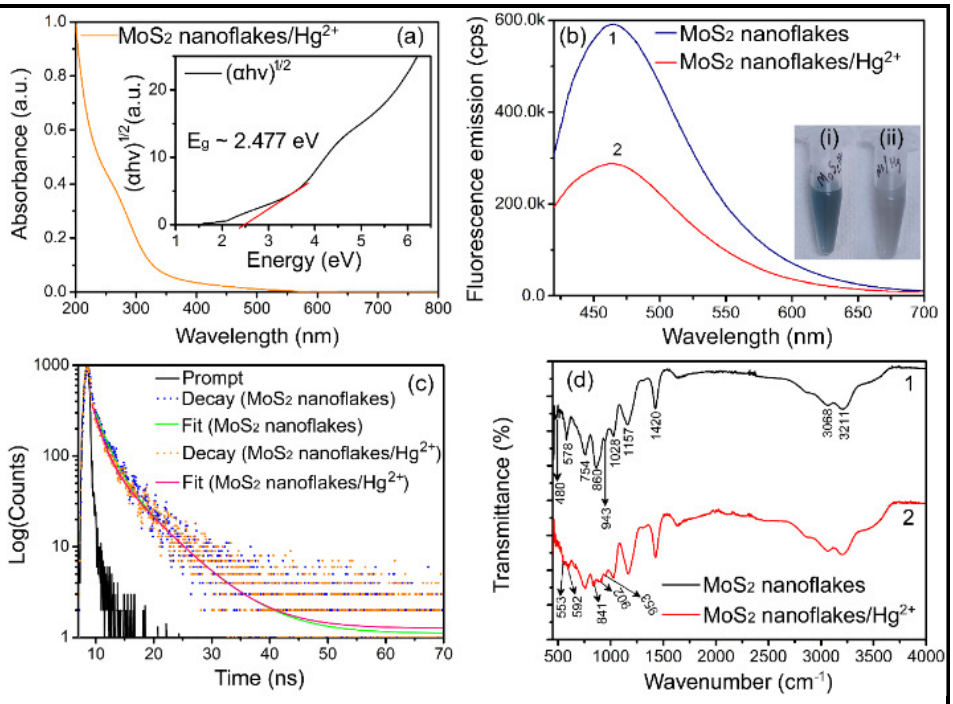

Figure 8.8. (a) UV-vis absorption spectrum of MoS_2 nanoflakes/Hg^{2+} mixed aqueous solution. (b) Fluorescence emission spectra of (1) MoS_2 nanoflakes aqueous dispersion and (2) MoS_2 nanoflakes/Hg^{2+} mixed aqueous solution. (c) TCSPC spectra of MoS_2 nanoflakes aqueous dispersion in absence and presence of Hg^{2+} ion. (d) ATR-FTIR spectra of (1) MoS_2 nanoflakes and (2) mixture of MoS_2 nanoflakes/Hg^{2+}. Insets of (a) and (b) show the Tauc plot for MoS_2/Hg^{2+} mixed solution and the coulometric change of fluorescent MoS_2 nanoflakes aqueous dispersion before (i) and after (ii) addition of Hg^{2+}.

MoS_2 and MoS_2/Hg^{2+} give an indication about the specific interactions of as-synthesized MoS_2 nanoflakes with Hg^{2+} ions in aqueous medium and its possible application of Hg^{2+} ion sensing both in aqueous solution and biological cells through the unique fluorescence emission properties of MoS_2 nanoflakes. Other analytical techniques such as ATR-FTIR spectroscopy, time-resolved fluorescence emission spectroscopy, CV etc. also provide the qualitative insights about the interactions of Hg^{2+} ion with the as-prepared MoS_2 sample.

The UV-vis absorption spectrum of MoS_2/Hg^{2+} mixed aqueous solution is shown in Figure 8.8a. It is observed that, the absorption bands of pure MoS_2 sample at

~306 nm and ~358 nm (as shown in Figure 8.5a) are now disappeared for the mixed solution. The strong affinity between S atom and Hg^{2+} ions in the mixed solution via covalent bonding interactions is most probably responsible for this observed changes of absorption properties of MoS_2 [54]. Also, the value of the optical E_g of MoS_2 after interaction with Hg^{2+} ions in aqueous solution is changed to ~2.477 eV as calculated from the UV-vis absorption spectroscopic data (inset of Figure 8.8a) and eqn. (8.4). More precisely, the adsorption of Hg^{2+} ions onto 2D MoS_2 via chemical interaction should involve strong forces due to sharing or exchange of valance electrons between S atoms Hg ions [55]. However, there should not be any significant interactions between the sorbed ions [56] in the basal plane of the NSs. On the other hand, the steady state fluorescence emission spectroscopic study of MoS_2 in absence and presence of Hg^{2+} ions show interesting results as shown in Figure 8.8b to elucidate the interaction of Hg^{2+} ion with MoS_2 nanoflakes in aqueous solution. From this figure it is observed that the fluorescence intensity of MoS_2 aqueous dispersion (concentration of 1 mg/mL) is significantly quenched after addition of $HgCl_2$ (concentration of ~566.3 nM) into MoS_2 aqueous solution when compared to that of pure MoS_2 aqueous dispersion. According to S. Mouri et al. [57] and Y. Y. Li et al. [58], fluorescent 2D MoS_2 behaves as an n-type semiconductor and the quenching or enhancement of fluorescence emission was mainly occurred due to the rearrangement of electron density between the NSs and the guest atom or molecule. In general, the fluorescence quenching is occurred when total electron density of host (NSs) is increased. In this work, Hg–S type of bonding was probably formed via covalent interactions between Hg^{2+} and S atom of MoS_2 [54]. Due to this reason, electron concentration of the host might have increased which is manifested in the fluorescence spectrum of $MoS_2/HgCl_2$ mixed aqueous solution. Also, most interestingly, the colour of MoS_2 aqueous dispersion (concentration of 1 mg/mL) was changed from bluish-green (inset of Figure 8.8b) to flaxen or pale yellowish-gray after addition of Hg^{2+} ions (concentration of ~566.3 nM) at ambient condition. This change in colour of the mixed solution is a direct visual evidence of some specific interaction of MoS_2 with Hg^{2+} ions in the aqueous medium.

In order to have further insights about the fluorescence quenching of MoS_2 by Hg^{2+} ions and their possible interactions, the fluorescence lifetime values of MoS_2 nanoflakes in absence and presence of Hg^{2+} ion in aqueous solution were estimated by time-resolved fluorescence emission spectroscopy based on the TCSPC method and is

shown in Figure 8.8c. The fluorescence decay data were fitted with two exponentials (eqn. (1) and eqn. (2)) and the estimated τ_{av} values and the corresponding normalised pre-exponential coefficients (α_1 and α_2) are summarized in Table 1. The as-synthesized MoS_2 nanoflakes in aqueous dispersion shows a long fluorescence lifetime of ~2.970 ns which is consistent with the data available in the literature, where the typical lifetimes are observed in the range from ~1.5 ns to ~5.9 ns [59]. The highest amplitude (~79.6 %) component of fluorescence lifetime (i.e., ~1.996 ns) is possibly attributed to the band edge fluorescence whereas the smallest amplitude (~20.4 %) corresponding to the higher fluorescence lifetime component (i.e., ~6.759 ns) may be assigned to the

Table 8.1. Time-resolved fluorescence decay parameters as obtained from the fitted data of MoS_2 nanoflakes and MoS_2 nanoflakes/Hg^{2+} mixed solutions. Corresponding fluorescence emission was monitored at 465 nm.

Sample name	Number of exponentials	λ_{ex} (nm)	τ_1 (ns)	α_1	τ_2 (ns)	α_2	τ_{av} (ns)	χ^2
MoS_2 nanoflakes	2	370	1.996	0.796	6.759	0.204	2.970	1.085
MoS_2 nanoflakes/Hg^{2+}	2	370	1.521	0.773	6.419	0.227	2.532	1.057

λ_{ex} = excitation wavelength, χ^2 = fitting parameter, close to 1 means a good fit.

defect states of 2D MoS_2 nanostructures [59,60]. Moreover, after addition of Hg^{2+} ion (~566.3 nM) to the MoS_2 aqueous dispersion, the value of τ_{av} decreased to ~2.532 ns. This decrease in the τ_{av} of MoS_2 in presence of Hg^{2+} gives a clear indication of the possibility of viable interactions between Hg^{2+} ions and MoS_2 resulting the decrease in both the band edge and defect state fluorescence emission of nanostructured MoS_2. It is therefore evident that the intrinsic fluorescence property of the as-synthesized MoS_2 is also highly sensitive to Hg^{2+} ion in aqueous medium and this observation elucidate the possibility of their application towards Hg^{2+} ions sensing in different medium.

FTIR spectroscopy is another excellent approach to probe the interactions between atoms in different microenvironment through the change in characteristics of molecular bond vibration. Figure 8.8d shows the FTIR spectra (in ATR mode) of MoS_2 nanoflakes in absence and presence of Hg^{2+} ions. The IR spectrum of as-prepared pure

MoS_2 nanoflakes sample (curve 1) shows transmittance peaks at around 480 cm^{-1}, 578 cm^{-1}, 754 cm^{-1}, 860 cm^{-1}, 943 cm^{-1}, 1028 cm^{-1}, 1157 cm^{-1}, 1420 cm^{-1}, 1630 cm^{-1}, 3068 cm^{-1}, and 3211 cm^{-1}. The IR bands observed at ~480 cm^{-1} and 578 cm^{-1} correspond to the Mo–S vibration of MoS_2 [61]. The bands observed at ~754 cm^{-1}, ~943 cm^{-1} are due to the stretching vibrations of Mo-O indicating the presence of molybdenum oxide (MoO_2) on the MoS_2 sample [62,63]. Additional bands observed at ~1028 cm^{-1}, 1157 $cm^{-1}$and 1420 cm^{-1} were originated due to sulfureted function groups S–O, O=S=O and O-S-O respectively and these results reveals that some S containing functional groups or structures might have present on the surface of MoS_2 NSs.[58] The IR peaks centred at around 1638 cm^{-1}, 3068 cm^{-1} and ~3211 cm^{-1} are attributed to the stretching vibrations of O–H moiety [64] of the adsorbed water molecule in the interlayer region of MoS_2 [65]. The presence of hydrophilic group (–OH) also facilitate good dispersibility of the as-synthesized MoS_2 nanoflakes in aqueous medium. Most interestingly, after interaction with Hg^{2+} (Figure 8.8d, curve 2) in aqueous solution, the vibrational bands at ~578 cm^{-1} and ~860 cm^{-1} of MoS_2 are shifted to ~592 cm^{-1} and ~841 cm^{-1} respectively with much reduced intensity. Additionally, the new IR bands with peaks centered at ~553 cm^{-1}, ~564 cm^{-1}, ~667 cm^{-1} and ~902 cm^{-1} are also emerged for MoS_2/Hg^{2+} mixed sample. Therefore, the observed changes in FTIR results give an indication of the covalent interaction of Hg^{2+} ions with MoS_2 nanoflakes.

To have a further understanding of the interaction of MoS_2 nanoflakes with Hg^{2+} ion in the aqueous medium, CV study was performed in the inert argon gas environment. Figure 8.9 shows CV curves of MoS_2 and $MoS_2/HgCl_2$ mixed solution recorded at the scan rate of 100 mVs^{-1} in the potential range from -1 to +1 V using glassy carbon, platinum (Pt) and Ag/AgCl as the working electrode, counter electrode and reference electrode

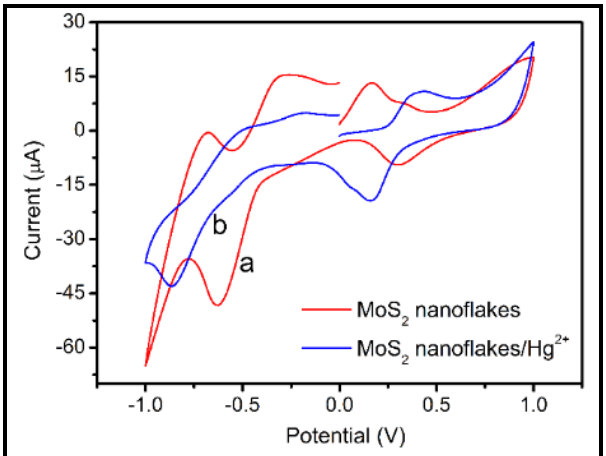

Figure 8.9. Cyclic voltammograms of MoS_2 nanoflakes in absence (a) and presence (b) Hg^{2+} ion in 0.1 M ammonium hexafluorophosphate (NH_4PF_6) aqueous solution at a scan rate of 100 mVs^{-1}.

respectively. From this figure it is observed that, when the potential was scanned positively (anodically), MoS_2 sample shows an appreciable anodic peak current of +13.4 μA at potential of +0.167 V. In fact, in the electrolytic medium MoS_2 had net negative charge due to the presence of S^{2-} group in MoS_2 and with increasing potential S^{2-} can donate two electrons to the solution medium and become S^0 thereby causing electrochemical oxidation of MoS_2 at potential at +0.167 V. When the potential was swiped from +1 V and scanned negatively (catholically), two strong reduction peaks were observed at +0.30 V and -0.63 V respectively. During this scan the oxidized S^0 atom in MoS_2 started to accept two electrons from the medium resulting the reduction of MoS_2 by creating S^{2-} anion. The electrochemically induced oxidation and reduction are also controlled by the diffusion kinetics of MoS_2 species around the electrodes [66] during the charge transfer process in the aqueous medium. On the other hand, MoS_2/Hg^{2+} mixed sample shows somewhat different voltammogram having changes in oxidation and reduction potentials compared to that of pure MoS_2. The corresponding oxidation peak is observed at +0.41 V and two reduction peaks are at +0.16 V and -0.86 V respectively. It is important to note that when we add Hg^{2+} ions into solution of MoS_2, strong electrostatic interaction between Hg^{2+} and S^{2-} group of MoS_2 was occurred resulting the attachment of Hg ions in the basal plane of MoS_2 NSs. But as S^{2-} is a natural reducer, it can share two electrons to the adsorbed Hg^{2+} ions in MoS_2 NSs to create Hg^0 (neutral). Therefore, it is presumed that the Hg and S atoms might not be separated from each other, rather S and Hg atoms are coordinated via covalent bonds. When the potential was applied both anodically and cathodically between the electrodes in the mixed solution, the oxidation and reduction potentials shifted to higher and lower values respectively compared to that of pure MoS_2. Additionally, the area under the curve for pure MoS_2 voltammogram is larger compared to that of for MoS_2/Hg^{2+} mixed solution. This observation implies that, the effective interaction between the electrolyte ion and the electrode was greatly reduced due to the association of Hg^{2+} ions with MoS_2 species in the solution. Therefore, the results obtained by CV study gives a clear indication of interaction of Hg^{2+} ion with MoS_2 nanoflakes in the aqueous solution.

8.3.2.2. Selectivity and sensitivity of the Hg^{2+} ion sensing

Steady state fluorescence emission spectroscopic measurements were further performed to investigate the sensitivity and selectivity of the interaction between as-

synthesized 2D MoS_2 nanoflakes and Hg^{2+} among various other interfering metal ions in aqueous medium. Figure 8.10a represents the fluorescence emission spectra of MoS_2

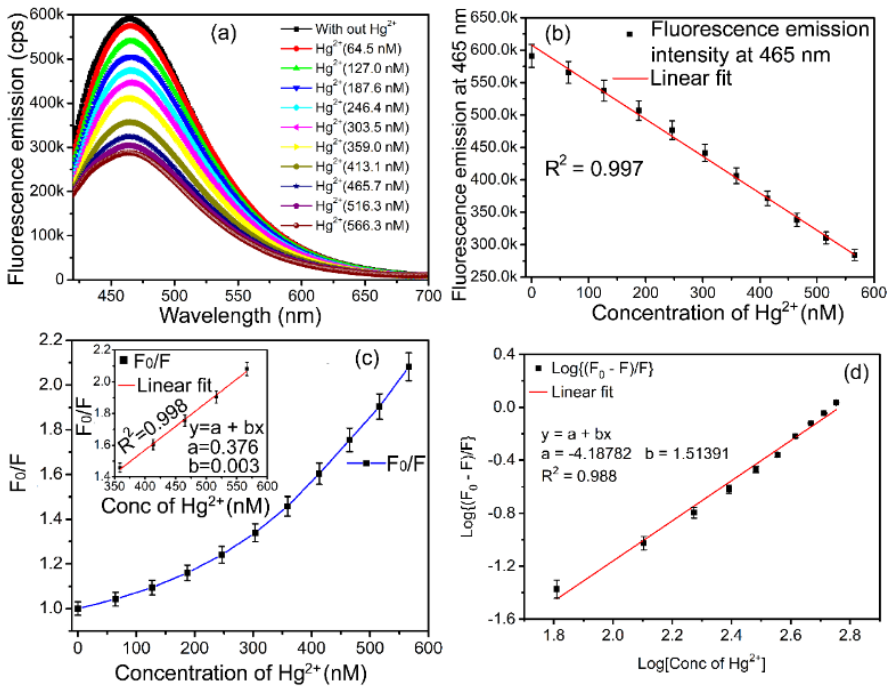

Figure 8.10. (a) Fluorescence emission spectra of MoS_2 nanoflakes for different concentrations of Hg^{2+} ion. (b) Plot of fluorescence emission intensity from MoS_2 vs. concentration of Hg^{2+}. (c) Stern-Volmer (SV) plot of MoS_2. (d) Plot of Log $\{(F_0-F)/F\}$ vs. Log [Conc of Hg^{2+}]. Inset of (c) shows the linear region of SV plot.

after successive titration with $HgCl_2$ aqueous solution in the concentration range from ~64.5 nM to ~566.3 nM in the mixed solution. The mixed solution was excited with at wavelength of 400 nm in the fluorescence emission measurement. The fluorescence intensity of the peak at wavelength of ~465 nm (~2.67 eV) was gradually quenched with the

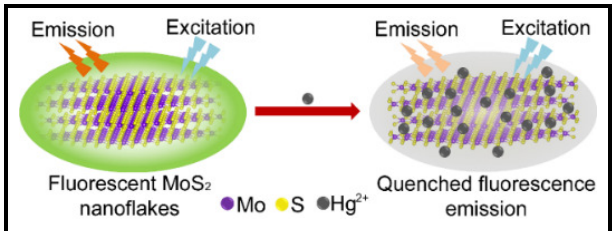

Figure 8.11. Schematic presentation of the interaction of fluorescent MoS_2 nanoflakes with Hg^{2+} in aqueous solution.

increase in concentration of Hg^{2+} in MoS_2 solution. The successive quenching of the fluorescence intensity observed at ~465 nm was found to be linear with increase in Hg^{2+}concentrations and a corresponding linear calibration eqn. can be written as F=607752–570 [Hg^{2+} (nM)] by linear fit of the emission data with a correlation coefficient of R^2 =0.997 as shown in Figure 8.10b. The mechanism of the fluorescence quenching is shown schematically in Figure 8.11.

The fluorescence quenching efficiency (E) was calculated by using eqn. (8.5) [67]

$$E = 1 - \frac{F}{F_0} \dots\dots\dots\dots (8.5)$$

where F and F_0 are the fluorescence emission intensities of MoS_2 aqueous solution in presence and absence of Hg^{2+} respectively. The value of E was estimated as ~0.52 by considering the fluorescence spectrum of pure MoS_2 (1 mg/mL) and MoS_2/Hg^{2+} mixed solution with Hg^{2+} concentration of ~566.3 nM. The value of the association constant or apparent binding constant (K_b) to a binding site and the number of binding sites (n) in the MoS_2/Hg^{2+} mixed aqueous solution have been determined from the quenched fluorescence emission intensities of MoS_2 nanoflakes in presence of Hg^{2+} by using eqn. (8.6) [68]

$$\mathrm{Log}\left\{\frac{\mathrm{F_0 - F}}{\mathrm{F}}\right\} = \mathrm{LogK_b} + \mathrm{nLog[M]} \dots\dots\dots\dots (8.6)$$

where [M] is the concentration of quencher (Hg^{2+}). The values of K_b and n were calculated from the intercept and slope of the plot as shown in Figure 8.10d and were found to be 15.41 × 10^3 M^{-1} and 1.514 respectively with a correlation coefficient of R^2 = 0.988. The change in Gibbs free energy (ΔG) for the interaction between MoS_2 and Hg^{2+} at room temperature (25ºC) was obtained using the Gibbs–Helmholtz relation [68] $\Delta G = -RTlnK_b$, where R is the universal gas constant and T is the temperature in K. The calculated value of ΔG was −23.895 $kJmol^{-1}$. The high negative value of ΔG indicates that the interaction between 2D MoS_2 and Hg^{2+} in the aqueous medium was spontaneous. Also, the quenching of fluorescence emission of MoS_2 by Hg^{2+} can be described by the well-known Stern–Volmer (SV) eqn. (8.7) [68]

$$\frac{F_0}{F} = 1 + K_{SV}[M] \dots\dots\dots\dots\dots\dots\dots\dots\dots\dots (8.7)$$

where K_{SV} is the SV quenching constant. Figure 8.10c shows the SV plot for the MoS_2/Hg^{2+} mixed system. The deviation from linearity of the SV plot might be due to the mixture of static and dynamic quenching [68]. Considering the slope of the straight-

line region of the F_0/F vs $[M]$ plot (i.e., at higher concentrations of Hg^{2+}) as shown in the inset of Figure 8.10c with correlation coefficient of $R^2 = 0.997$, the value of K_{SV} is calculated as 3.0×10^6 M^{-1}. The fluorescence quenching rate constant (K_q) and K_{SV} are also related by the relation [68] $K_q = K_{SV}/\tau$, where τ is the fluorescence lifetime of pure MoS_2 nanoflakes (i.e., ~2.970 ns). The value of K_q has been calculated as 1.01×10^6 $M^{-1}s^{-1}$ from this fluorometric titration. The high values of both K_{SV} and K_q confirm the efficient quenching of fluorescence of MoS_2 by Hg^{2+} in the aqueous medium. All the above calculated photophysical parameters are summarized in Table 8.2.

Table 8.2. Binding constant (K_b), binding sites (n), Gibbs free energy (ΔG), Stern–Volmer constant (K_{SV}), and quenching rate constant (K_q) for the MoS_2 nanoflakes/Hg^{2+} mixed system in the aqueous medium. R^2 is the corresponding correlation coefficient.

K_b (in M^{-1})	n	R^2	ΔG (in kJmol^{-1})	K_{SV} (in M^{-1})	K_q (in $M^{-1}s^{-1}$)	R^2
15.41×10^3	1.514	0.988	-23.895	3.0×10^6	1.01×10^6	0.997

To compare the sensitivity of the interaction of MoS_2 nanoflakes towards Hg^{2+} in aqueous medium, the limit of detection (LoD) and limit of quantitation (LoQ) of the sensing probe for Hg^{2+} ions have been determined from the linear SV plot (inset of Figure 8.7C) on the basis of 3σ method [69] using the eqn. (8.8) and eqn. (8.9) respectively.

$$LoD = \frac{3.3\sigma}{K_{SV}} \quad \ldots\ldots\ldots\ldots\ldots\ldots\ldots\ldots\ldots\ldots (8.8)$$

$$LoQ = \frac{10\sigma}{K_{SV}} \quad \ldots\ldots\ldots\ldots\ldots\ldots\ldots\ldots\ldots\ldots\ldots (8.9)$$

where σ is the residual standard deviation (error) of a regression line. The value of σ was calculated as 8.72308×10^{-5}. The values of LoD and LoQ were estimated as ~0.09 nM and ~0.3 nM respectively. The calculated LoD value indicates that the as-synthesized MoS_2 nanoflakes was highly sensitive towards Hg^{2+} as reflected in the spectrofluorometric measurement. The linear range of detection and LoD for Hg^{2+} ion sensing using MoS_2-based system via ratiometric approach of fluorescence emission as obtained in this present study are compared to the previously reported data available in the literature and are summarized in Table 8.3.

Table 8.3. Comparisons of linear range and limit of detection (LoD) of the analytic methods for the sensing of Hg^{2+} using 2D MoS_2-based system.

Probe	Detection principle	Linear range	LoD	Ref.
MoS_2/AlGaN/GaN	[a]HEMT	(0.1 – 100) ppb	0.011 ppb	[6]
[b]MoS_2 NSs/DNA/CD	Fluorometric assay	(0 – 10) nM	1.02 nM	[12]
MoS_2 NSs/DNA/silicon	Fluorometric assay	(0 – 1000) nM	0.86 nM	[13]
[c]MoS_2/GCE	[d]SWASV	0.1 nM – 0.2 nM	0.001 nM	[14]
[e]N-MoS_2 NSs	Fluorometric assay	(0.4 – 10) µM	28.0 nM	[17]
[f]B-MoS_2 QDs	Fluorometric assay	(0.005 – 41)	1.8 nmol/L	[22]
[g]ssDNA-MoS_2/ITO	Square wave voltammetry	10 fM – 10 nM	10 fM	[23]
Superstructure MoS_2 NSs	[h]SPR	1 pM – 1 µM	1.0 pM	[51]
MoS_2 nanoflakes	Fluorometric titration	(0.06 – 0.5) µM	0.09 nM	**This work**

[a]HEMT: High electron mobility transition; [b]MoS_2 NSs/DNA/CD: MoS_2 NSs/DNA/carbon dots; [c]MoS_2/GCE: MoS_2/Glassy carbon electrode; [d]SWASV: Square wave anodic stripping voltammetry; [e]N-MoS_2 NSs: N-doped MoS_2 NSs; [f]B-MoS_2 QDs: Boronic acid functionalized MoS_2 QDs; [g]ssDNA-MoS_2/ITO: MoS_2 NSs functionalized with single-stranded deoxyribonucleic acid (ssDNA) on ITO electrode; [h]SPR: Surface plasmon resonance

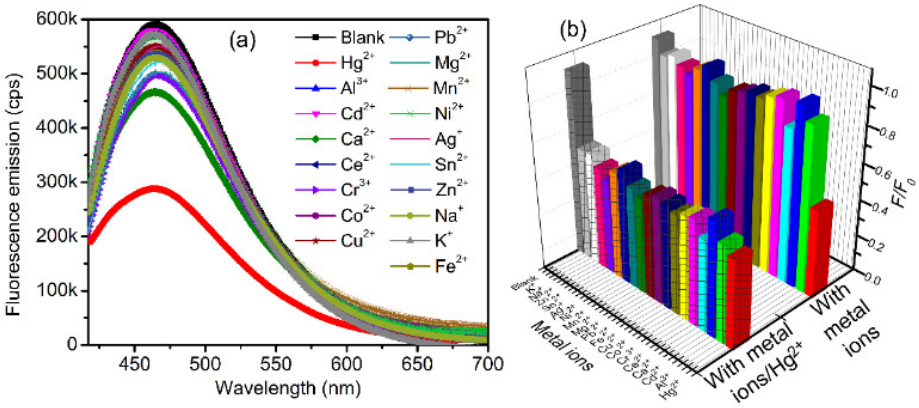

Figure 8.12. (a) Fluorescence emission spectra as obtained from aqueous dispersion of MoS_2 nanoflakes in presence of different metal ions. (b) Selectivity study of the sensor towards various metal ions.

To confirm the selectivity of the interaction of as-synthesized MoS_2 nanoflakes towards Hg^{2+} ion, the spectrofluorometric titration was also performed for other common and interfering metal ions such as Al^{3+}, Cd^{2+}, Ca^{2+}, Ce^{2+}, Cr^{3+}, Co^{2+}, Cu^{2+}, Fe^{2+}, Pb^{2+}, Mg^{2+}, Mn^{2+}, Ni^{2+}, Ag^{+}, Sn^{2+}, Zn^{2+}, Na^{+}, K^{+} etc. with the same fixed concentration (i.e., ~566.3 nM) as was considered for Hg^{2+} ion. The steady state fluorescence emission spectra of MoS_2 nanoflakes in presence of individual metal ions are shown in Figure 8.12a. Figure 8.12b shows 3D plot of the ratio-metric fluorescence response (F/F_0) of MoS_2 towards various metal ions including Hg^{2+} along with their mixed solution of Hg^{2+} and different metal ions taking separately. The quenching of fluorescence intensity of MoS_2 solution due to Hg^{2+} was much pronounced when compared to the other interfering metal ions as is clearly distinguished in from Figure 8.12b. Also this significant quenching of fluorescence due to Hg^{2+} ions was accompanied with a distinct colour change of MoS_2 solution from bluish-green to pale yellowish-gray after addition of Hg^{2+} ion (inset of Figure 8.8b). From these observations, it is confirmed that other relevant metal ions could not elicit remarkable reduction of fluorescence emission intensity of MoS_2 solution and no appreciable change in solution colour in the studied concentration range of those metal ions when compared to that for Hg^{2+} suggesting an excellent selectivity of the probe towards Hg^{2+} ion among a wide range of interfering metal ions in aqueous medium.

8.3.3. DFT study

The change in the spectroscopic properties due to the interaction of MoS_2 with Hg atom has been correlated with the theoretical results of band structure and DOS of MoS_2 monolayer and bilayer obtained via DFT approach using QE software package. 2D structure of MoS_2 has a layer of Mo atoms in between the two layers of S atoms. According to the experimental and theoretical studies of various researchers, this type of 2D material has an excellent efficiency for Hg adsorption [70,71]. Here, all the calculations have been performed on MoS_2 and Hg-adsorbed MoS_2 using the unit cell configurations as shown in Figure 8.13a, e, i and m. The band structure of pristine MoS_2 monolayer as shown in Figure 8.13b is direct in nature [71,72]. The minima of the conduction band (CB) and the maxima of the valence band (VB) lie at the same point in between the K and M points of the Brillouin zone. The corresponding bandgap was found to be ~1.64 eV as calculated from the DOS spectrum (Figure 8.13c) and is more or less consistent with the available theoretical and experimental results reported

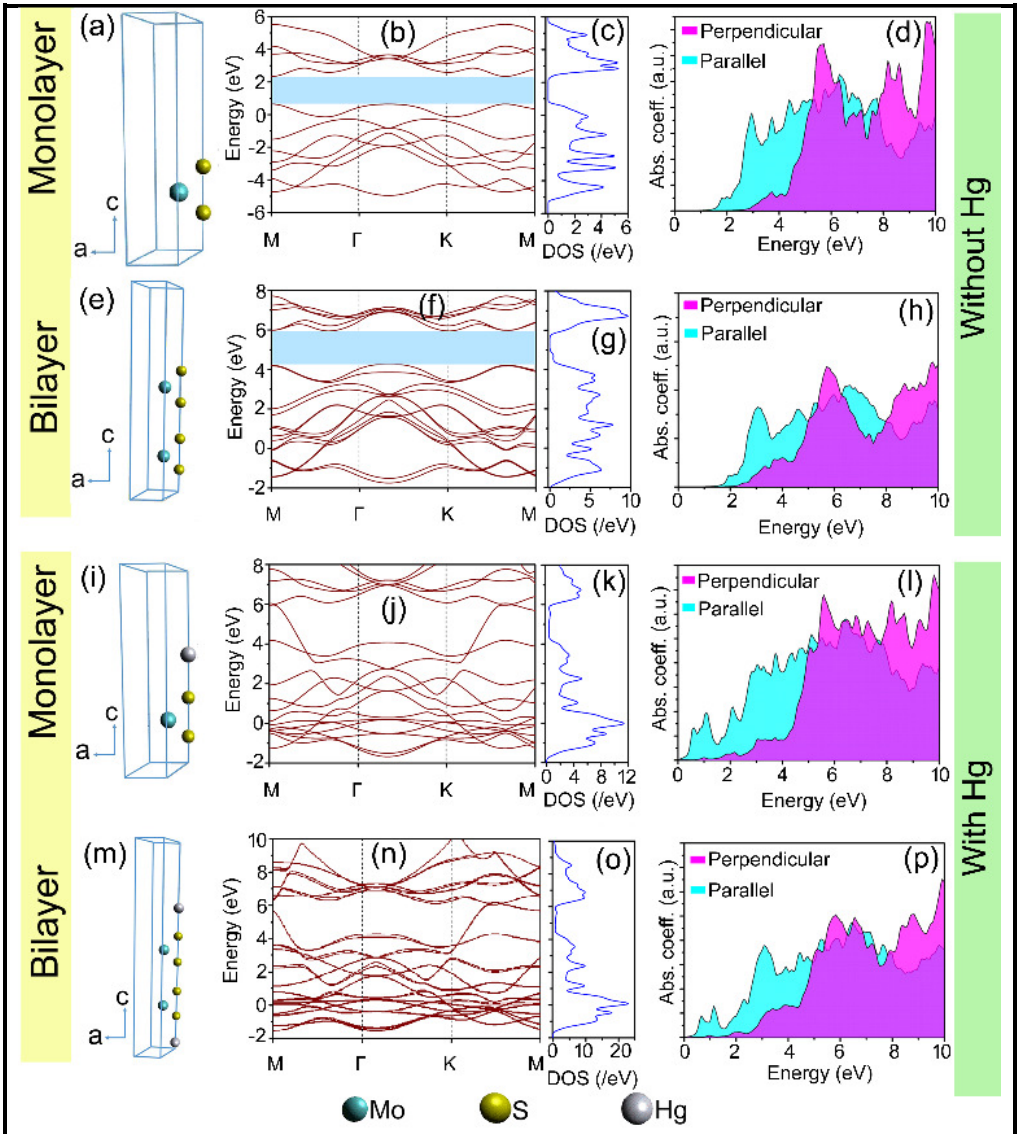

Figure 8.13. (a) Optimized unit cell of monolayer MoS_2. (b), (c) and (d) band structure, DOS and absorption coefficient of monolayer MoS_2 respectively. (e) Optimized unit cell of bilayer MoS_2. (f), (g) & (h) band structure, DOS and absorption coefficient of bilayer MoS_2 respectively. (i) Hg adsorbed optimized unit cell of monolayer MoS_2. (j), (k) and (l) band structure, DOS and absorption coefficient of Hg adsorbed monolayer MoS_2 respectively. (m) Hg adsorbed optimized unit cell of bilayer MoS_2. (n), (o) & (p) band structure, DOS and absorption coefficient of bilayer MoS_2 respectively.

elsewhere [72]. However, from Figure 8.13j it is observed that, after adsorption of Hg atom in the NSs, there was a drastic reduction of the band gap. Also the electron densities at CB and VB of MoS_2 monolayer are increased due to interaction Hg atom as shown in Figure 8.13k. As mentioned earlier that the increase in electron density may correspond to the quenching of fluorescence, [57,58] theoretically predicted change in electron density therefore suggests the experimentally observed fluorescence quenching of MoS_2 sample due to their interaction with Hg^{2+} species in the basal plane of MoS_2.

On the other hand, in case of bilayer MoS_2, the maxima of the VB lie in the region between the Γ and K points in Brilluion zone (Figure 8.13f). This clearly reveals a transition from the direct bandgap material to indirect bandgap material due to staking of MoS_2 layers [71]. For bilayer MoS_2, the bandgap is obtained from the band structure (Figure 8.13f) and the electronic DOS spectrum (Figure 8.13g) and was found to be ~1.62 eV which is less compared to that of pristine monolayer MoS_2 (Figure 8.13b). However, similar to Hg-adsorbed monolayer MoS_2 (Figure 8.13j), the band gap of bilayer MoS_2 (Figure 8.13n) was also drastically reduced due to interaction with Hg atom resulting an increase in total electron density as predicted from Figure 8.13o. This reduction of band gap of MoS_2 due to Hg adsorption and also contributed with experimental results. As in our experiment, MoS_2 nanoflakes were composed of several stacked layer of NSs, so, from the results obtained by DFT analysis it is anticipated that the increase in the concentration of electron density of MoS_2 nanostructured sample after interaction with Hg^{2+} ions was responsible for the observed fluorescence quenching of MoS_2. We have also calculated the absorption coefficients of MoS_2 (both mono and bilayer) (Figure 8.13d,h) and Hg-adsorbed MoS_2 (Figure 8.13l,p) along the horizontal and vertical direction of the unit cells. It is clearly observed that in presence of Hg, both parallel and perpendicular components of absorption coefficients have been shifted to the lower energy side which is clearly correlated with the reduced band gap of MoS_2 due to their interaction with Hg ion or atom.

8.3.4. Detection of Hg^{2+} ion in biological cell

Elemental metals and metal ions are essential compounds for biological system to maintain their biofunctionality such as blood osmotic pressure, catalytic activity of many enzymes, blood brain barrier etc. [73]. However, various heavy metals such as Cd, Pb, Hg, Co, As, etc. can cause adverse health effect even with very minimal exposer

[74]. Most of these heavy metals are naturally found in the environment, cosmetics and food products, wastage of batteries etc. [75]. Among the various heavy metals, animal exposer to Hg is a major concern of global scientific community due to its high toxicity as considered by WHO [1]. Noticeably, the higher emission from various sources such as vehicle emissions, industrial pollutants etc. causes the increase in the amount of Hg in the environment. Although, the Hg^0 from the inhaled Hg vapour shows significant

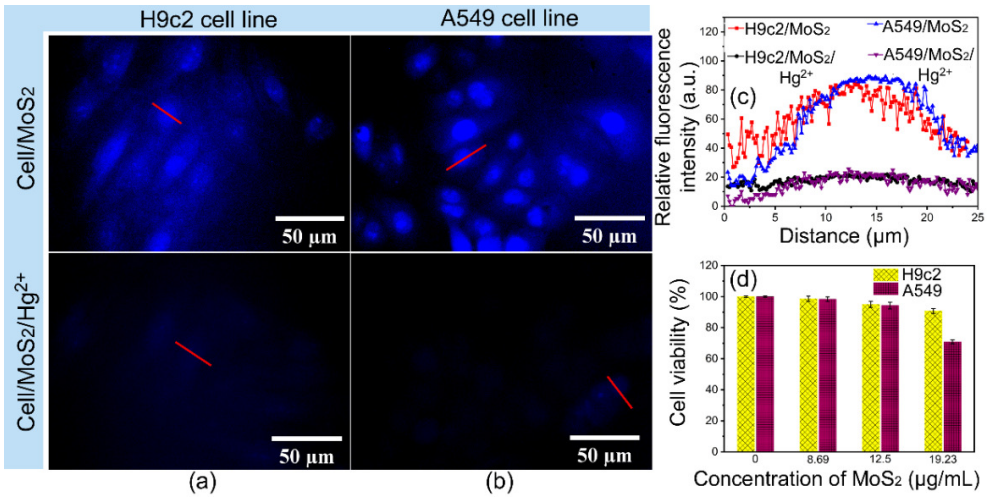

Figure 8.14. Fluorescence microscopic images of (a) normal myocardium cells (H9c2 cell line) and (b) cancerous lung fibroblast cell (A549 cell line) after treated with MoS_2 nanoflakes (top images) and MoS_2 nanoflakes/Hg^{2+} mixed solution (bottom images). (c) Relative fluorescence intensity profiles obtained from images as shown in (a) and (b) along the line (red colour). (d) Cell viability study for 3 hrs of incubation as obtained by MTT assay method.

bioavailability, they can be easily oxidised to Hg^{2+} ion that can be accumulated in the intracellular medium. It is also important to mention that the divalent mercury cations (i.e., Hg^{2+}) may induce genetic alternation that lead to cancer in human body [76]. J. Tong et al. [77] reported that exposer of both the organic (MeHgCl) and inorganic ($HgCl_2$) form of Hg with human neural cells (SK-N-SH cell line) causes 50% cell death for concentrations of 1.2 ± 0.22 $\mu molL^{-1}$ and 6.4 ± 0.36 $\mu molL^{-1}$ respectively. Therefore, the detection of Hg in the intracellular medium is of utmost important for both fundamental and biomedical interest.

In this present work we have also used as-synthesized highly fluorescent 2D MoS_2 nanoflakes to detect Hg^{2+} ion in both normal (H9c2 cell line) and cancer (A549 cell line) cells. Figure 8.14a,b (top images) show the fluorescence microscopic images of heart myocardium cell (H9c2) and lung fibroblast cancer cell (A549) after treated with MoS_2 aqueous dispersion (200 μL) using an optical excitation source of wavelength of 405 nm whereas, the bottom images represent the same cells after treated with MoS_2 and Hg^{2+} ion. It is observed from the figures that, the fluorescent MoS_2 nanoflakes samples successfully entered into both the normal and cancer cells as strong localized blue emission is observed from their intracellular regions. It is clearly seen that the MoS_2 are distributed throughout the cytoplasmic region including the nucleus of both the cells. The relative fluorescence intensity profile (Figure 8.14c) as obtained from both the microscopic images along the indicated line sections (red colour) are very similar. However, the most interesting observation is that the fluorescence images of both the cells after treated with MoS_2 solution (200 μL) and subsequently $HgCl_2$ (100 μL) (bottom images of Figure 8.14a,b) show significant reduction of brightness and contrast due to quenching of fluorescence of MoS_2 in the treated cells. The change in intensity profile along a particular line section (red line) of the microscopic images of cells before and after exposer with MoS_2 and MoS_2/Hg^{2+} samples are shown in Figure 8.14c. From these observations, it is evident that MoS_2 nanoflakes had strong interaction with Hg^{2+} ions within the cells, which is manifested as the reduced intensity of blue fluorescence spots in the microscopic cellular images. Therefore, this study confirms that, as-prepared MoS_2 nanoflakes sample successfully recognise the presence of Hg^{2+} ions in biological cells. It is worthy to mention that, in-vitro, the cellular uptake of MoS_2 nanoflakes should primarily depend on the altered diffusion and sedimentation velocities of individual nanoflakes in the culture medium [78]. However, the overall process of internalization of MoS_2 nanoflakes within the cell involves a complex mechanism. As the plasma membrane of mammalian contains negatively charged domains, they are generally impermeable to most of the negatively charged inorganic nanomaterials. So, the sub-cellular localization or translocation of the as-synthesized MoS_2 nanoflakes might have occurred through some endocytic pathways which are energy dependent [79-81]. Additionally, the uptake and intracellular trafficking of such nanomaterials may depend upon the compatible surface chemistry, shape and size of the nanomaterials as already reported in the literature [81].

The proper biocompatibility of the as-synthesized highly fluorescent MoS_2 nanoflakes is an important factor on the cell viability during the fluorescence-based cellular microscopic imaging as presented in this work. More precisely, it is of prime importance to assess the nanotoxicity of MoS_2 sample while their interaction with the biological cells. So, in this study to know the cell viability due to the interaction with MoS_2 in presence of Hg^{2+} ion, different concentrations (viz. µg/mL: 0, ~8.69, ~12.5, ~19.23 etc. in the cellular medium) of MoS_2 aqueous dispersion were added to the culture medium of both normal (H9c2 cell line) and cancer (A549 cell line) cells separately and were incubated for 2 hrs. The concentration of $HgCl_2$ solution in the cellular medium was ~47.62 nM. After the incubation period, the cellular viability was examined by using MTT assay method which is already described in the experimental section. Figure 8.14d shows the cell viability results (in percentage) for different concentrations of MoS_2 solutions as used in both H9c2 and A549 cell lines studies. From this figure, it is clearly observed that, normal myocardium cell shows no significant toxicity in the studied concentration range of MoS_2. Whereas, the human lung fibroblast cancer cells exhibited some extent of toxicity (cell viability ~70.9 %) only at the higher concentration of MoS_2 (i.e., ~19.23 µg/mL in the cellular medium). But, most interestingly, the concentration of MoS_2 (~8.69 µg/mL in the cellular medium) used for the detection of Hg^{2+} ions in cells via fluorescence imaging method did not show any significant drop of cell viability. Present study therefore reveals that the as-prepared MoS_2 nanoflakes are very safe at an optimal concentration (i.e., ~8.69 µg/mL in the cellular medium) to detect the presence of Hg^{2+} ion in both the normal and cancer cells with negligible cytotoxicity after an incubation period of 1 hr thereby assuring their acceptability for future biomedical applications.

8.4. Conclusions

In conclusion, the present work envisages the application of bio-inspired hydrothermally synthesized MoS_2 nanoflakes for detection of heavy metal ion namely, Hg^{2+} in aqueous solution as well as in normal and cancer cells (H9c2 and A549 cell lines) via fluorometric approach. XRD analysis confirms that as-synthesized MoS_2 sample was pure and had hexagonal lattice structure. The strong XRD peak observed at ~14^o corresponds the presence high concentration of NSs which were mostly stacked with one another. The stacking between large number of MoS_2 layers facilitates the

formation of flower shaped nanoflakes in the aqueous medium as evidenced from FESEM and TEM images. The average width of a nanoflake was found to be ~16.4 nm as estimated from the lognormal distribution using FESEM image of MoS_2 sample. The aggregation of MoS_2 NSs is also confirmed by AFM study and shows r.m.s surface roughness of ~46.4 nm. The SAED pattern of MoS_2 nanoflakes exhibits low crystallization order which is consistent with the broad XRD peaks. The low negative zeta potential of MoS_2 aqueous solution definitely corresponds to the stacking of several NSs to form nanflakes like structure. Raman spectroscopic results further supports the stacking of few layers of MoS_2 lamellae. The most interesting observation of this present work is the drastic fluorescence quenching of MoS_2 in aqueous medium after addition of Hg^{2+} ions, which is possibly due to the covalent interaction between Hg^{2+} and S atom of MoS_2 in the aqueous medium. This interaction might have increased the total electron density of MoS_2 nanostructured sample and is also correlated the theoretical results obtained DFT study. The reduction in fluorescence lifetime of MoS_2 as obtained by time-resolved fluorescence studies is consistent with the observed fluorescence quenching. SV plot analysis reveals both static and dynamic quenching of MoS_2 in presence of Hg^{2+} in in aqueous medium. FTIR and Cyclic voltammetry studies further support the interaction of Hg^{2+} ion with MoS_2 nanoflakes. The interaction of MoS_2 with Hg^{2+} ions is highly selective compared with all other interfering metal ions present in the same aqueous medium. Also the selective fluorescence quenching of MoS_2 is highly sensitive to the concentration of Hg^{2+} ions in the mixed aqueous solution. The LoD and LoQ are found to be ~0.09 nM and ~0.3 nM respectively as estimated from the linear plot of ratiomatric fluorescence response of MoS_2 due to Hg^{2+} ions. The ratiometric approach of analysing fluorescence quenching for the detection of such metal ions using MoS_2 is definitely advantageous as this method automatically discarded the perturbation of any external influences during the fluorometric measurement. The unique fluorescence quenching of MoS_2 has been utilized to successfully recognize the presence of Hg^{2+} ions in intracellur medium of both normal and cancer cells as studied by fluorescence imaging microscopic study. As-synthesized MoS_2 nanoflakes did not show any significant cellular toxicity in the studied concentration of MoS_2 for cellular investigation as confirmed by MTT assay method. Therefore, this present study reveals an efficient and facile approach of detecting toxic

metal ion namely Hg in biological cells through the unique change of fluorescence properties of such nanostructured MoS_2.

References

[1] Mercury and Health. World Health Organization (WHO) (2017). https://www.who.int/news-room/fact-sheets/detail/mercury-and-health/

[2] H. Kozlowski, P. Kolkowska, J. Watly, K. Krzywoszynska, S. Potocki, *Curr. Med. Chem.*, 21 (2014) 3721–3740.

[3] Y. Zhang, T. Yan, L. Yan, X. Guo, L. Cui, Q. Wei, B. Du, *J. Mol. Liq.*, 198 (2014) 381–387.

[4] S. Rathnakumar, S. Bhaskar, A. Rai, D. V. V. Saikumar, N. S. V. Kambhampati, V. Sivaramakrishnan, S. S. Ramamurthy, *ACS Appl. Nano Mater.*, 4 (8) (2021) 8066–8080.

[5] M. Saqib, S. Bashir, H. Li, S. S. Wang, Y. Jin, *Anal. Chem.*, 91 (2019) 3070–3077.

[6] A. Nigam, N. Goel, T. N. Bhat, T. Md. Rahman, S. B. Dolmanan, Q. Qiao, S. Tripathy, M. Kumar, *Sens. Actuators B Chem.*, 309 (2020) 127832.

[7] S. Kender, K. Bogus, G. K. Pedersen, K. Dybkjær, T. A. Mather, E. Mariani, A. Ridgwell, J. B. Riding, T. Wagner, S. P. Hesselbo, M. J. Leng, *Nat. Commun.*, 12 (2021) 5186.

[8] J. George, R. E. Masto, L. C. Ram, T. B. Das, T. K. Rout, M. Mohan, *Arch. Environ. Contam. Toxicol.*, 68 (3) (2015) 451–461.

[9] R. Kahhat, E. Parodi, G. L. Gallegos, C. Mesta, I. V. Rowe, *Sci. Total Environ.*, 662 (2019) 940–951.

[10] K. Jaglal, *Water Environ. Res.*, 92 (10) (2020) 1826–1832.

[11] J. V. Burda, J. Sponer, J. Leszczynski, P. Hobza, *J. Phys. Chem. B*, 101 (1997) 9670–9677.

[12] K. Srinivasan, K. Subramanian, K. Murugan, K. Dinakaran, *Analyst*, 141 (2016) 6344–6352.

[13] K. Srinivasan, K. Subramanian, K. Murugan, G. Benelli, K. Dinakaran, *Environ. Sci. Pollut. Res.*, 25 (2018) 10567–10576.

[14] R. Aswathi, K. Y. Sandhya, *J. Mater. Chem. A*, 6 (2018) 14602–14613.

[15] A. Garg, S. Basu, N.P. Shetti, K.R. Reddy, *J. Environ. Chem. Eng.*, 9 (2021) 106408.

[16] S. Thurakkal, D. Feldstein, R. P. Causín, E. Malic, X. Zhang, *Adv. Mater.*, 33 (3) (2021) 2005254.

[17] J. Liu, X. Li, X. Gong, T. Qing, P. Zhang, B. Feng, *Nano*, 13 (5) (2018) 1850057.

[18] S. Dolai, P. Maiti, A. Ghorai, R. Bhunia, P. K. Paul, D. Ghosh, *ACS Appl. Mater. Interfaces*, 13 (2021) 438−448.

[19] H. Chen, Q. Wu, Y. Wang, Q. Zhao, X. Ai, Y. Shena, X. Zou, *Chem. Commun.*, 58 (2022) 7730–7740.

[20] E. Singh, P. Singh, K. S. Kim, G. Y. Yeom, H. S. Nalwa, *ACS Appl. Mater. Interfaces*, 11 (2019) 11061−11105.

[21] K. Kasirajan, M. Karunakaran, M. Balaji, P. Nithya, P. Boomi, M. Sundrarajan, S. Balamurugan, *J. Mol. Liq.*, 323 (2021) 114631.

[22] X. Guo, J. Huang, Y. Wei, Q. Zeng, L. Wang, *J. Hazard. Mater.*, 381 (2020) 120969.

[23] C. Pal, T. T. Suzuki, S. Majumder, *Chem. Phys. Lett.*, 784 (2021) 139115.

[24] Y. Yan, B. Y. Xia, X. Ge, Z. Liu, J. Y. Wang, X. Wang, *ACS Appl. Mater. Interfaces*, 5 (2013) 12794−12798.

[25] A. Sinha, Dhanjai, B. Tan, Y. Huang, H. Zhao, X. Dang, J. Chen, R. Jain, *Trends Anal. Chem.*, 102 (2018) 75–90.

[26] A. Nigam, N. Goel, T.N. Bhat, T. Md. Rahman, S. B. Dolmanan, Q. Qiao, S. Tripathy, M. Kumar, *Sens. Actuators B Chem.*, 309 (2020) 127832.

[27] A. Amalraj, R. Pavadai, S. Subramanian, P. Perumal, *Appl. Surf. Sci.*, 602 (2022) 154222.

[28] F. F. Martín, M.V. Llopis, J. C. C. Rodríguez, A. L. Martínez, A. S. Cabezuelo, M. T. F. Arguelles, J. M. C. Fernández, *Appl. Sci.*, 11 (2021) 7849.

[29] Y. Wang, J. Z. Ou, S. Balendhran, A. F. Chrimes, M. Mortazavi, D. D. Yao, M. R. Field, K. Latham, V. Bansal, J. R. Friend, S. Zhuiykov, N. V. Medhekar, M. S. Strano, K. K. Zadeh, *ACS Nano*, 7 (11) (2013) 10083–10093.

[30] Y. Wang, E. D. Gaspera, B. J. Carey, P. Atkin, K. J. Berean, R. M. Clark, I. S. Cole, Z. Q. Xu, Y. Zhang, Q. Bao, J. Z. Ou, T. Daeneke, K. K. Zadeh, *Nanoscale*, 8 (2016) 12258–12266.

[31] K. Chang, W. Chen, *ACS Nano*, 5 (2011) 4720.

[32] C. Sweet, A. Pramanik, S. Jones, P. C. Ray, *ACS Omega*, 2 (2017) 1826−1835.

[33] D. Ghosh, N. Chattopadhyay, *OPJ*, 3 (2013) 18–26.

[34] P. Maiti, T. Singha, U. Chakraborty, S. Dutta Roy, P. Karmakar, B. Dey, S. A. Hussain, S. Paul, P. K. Paul, *Mater. Chem. Phys.*, 234 (2019) 158–167.

[35] A. Hazra, P. Ghosh, P. Roy, *Spectrochim. Acta A Mol. Biomol. Spectrosc.*, 271 (2022) 120905.

[36] M. Tang, X. Liu, N. Zhang, J. Pang, Y. Zou, F. Chai, H. Wu, L. Chen, *Anal. Methods*, 11 (2019) 5214–5221.

[37] P. Giannozzi, S. Baroni, N. Bonini, M. Calandra, R. Car, C. Cavazzoni, D. Ceresoli, G.L. Chiarotti, M. Cococcioni, I. Dabo, A.D. Corso, S.D. Gironcoli, S. Fabris, G. Fratesi, R. Gebauer, U. Gerstmann, C. Gougoussis, A. Kokalj, M. Lazzeri, L. Martin-Samos, N. Marzari, F. Mauri, R. Mazzarello, S. Paolini, A. Pasquarello, L. Paulatto, C. Sbraccia, S. Scandolo, G. Sclauzero, A.P. Seitsonen, A. Smogunov, P. Umari, R.M. Wentzcovitch, *J. Phys. Condens. Mat.*, 21 (2009) 395502.

[38] J. P. Perdew, K. Burke, M. Ernzerhof, *Phys. Rev. Lett.*, 77 (1996) 3865.

[39] S. Chen, N. Shi, M. Huang, X. Tan, X. Yan, A. Wang, Y. Huang, R. Ji, D. Zhou, Y.G. Zhu, A. A. Keller, J. L.G. Torresdey, J. C. White, L. Zhao, *ACS Nano*, 15 (10) (2021) 16344–16356.

[40] M. Mulu, D. R. Devi, N. Belachew, K. Basavaiah, *RSC Adv.*, 11 (2021) 24536–24542.

[41] M. Barzegar, M. Berahman, A. I. Zad, *Beilstein J. Nanotechnol.*, 9 (2018) 608–615.

[42] R. Gusain, N. Kumar, F. Opoku, P. P. Govender, S. Shina Ray, *ACS Appl. Nano Mater.*, 4 (2021) 4721−4734.

[43] L. Yang, A. Mukhopadhyay, Y. Jiao, J. Hamel, M. Benamara, Y. Xing, H. Zhu, *J. Mater. Chem. A*, 5 (2017) 25359–25367.

[44] G. Eda, H. Yamaguchi, D. Voiry, T. Fujita, M. Chen, M. Chhowalla, *Nano Lett.*, 11 (2011) 5111–5116.

[45] S. R. Tulsani, A. K. Rath, D. J. Late, *Nanoscale Adv.*, 1 (2019) 1387–1394.

[46] A. Gupta, S. Vasudevan, *J. Phys. Chem. C*, 122 (2018) 19243−19250.

[47] A. Steinhoff, J. H. Kim, F. Jahnke, M. Rösner, D. S. Kim, C. Lee, G. H. Han, M. S. Jeong, T. O. Wehling, C. Gies, *Nano Lett.*, 15 (10) (2015) 6841–6847.

[48] A. Splendiani, L. Sun, Y. Zhang, T. Li, J. Kim, C. Y. Chim, G. Galli, F. Wang, *Nano Lett.*, 10 (2010) 1271–1275.

[49] Q. Li, T. Y. Luo, M. Zhou, H. Abroshan, J. Huang, H. J. Kim, N. J. Rosi, Z. Shao, R. Jin, *ACS Nano*, 10 (9) (2016) 8385–8393.

[50] D. Y. Qiu, F. H. Jornada, S. G. Louie, *Phys. Rev. B*, 93 (2016) 235435.

[51] S. Karmakar, S. Pramanik, A. K. Kole, U. Chatterjee, P. Kumbhakar, *J. Hazard. Mater.*, 424 (2022) 127702.

[52] C. Mutalik, G. Okoro, H. L. Chou, I. H. Lin, S. Yougbaré, C. C. Chang, T. R. Kuo, *ACS Sustainable Chem. Eng.*, 10 (27) (2022) 8949–8957.

[53] S. Xiao, P. Xiao, X. Zhang, D. Yan, X. Gu, F. Qin, Z. Ni, Z. J. Han, K. K. Ostrikov, *Sci. Rep.*, 6 (2016) 19945.

[54] F. Jia, Q. Wang, J. Wu, Y. Li, S. Song, *ACS Sustainable Chem. Eng.*, 5 (2017) 7410−7419.

[55] T. Xue, K. Qi, C. Hu, *Sens. Actuators B Chem.*, 284 (2019) 589–594.

[56] Y. S. Ho, G. Mckay, *Wat. Res.*, 34 (3) (2000) 735–742.

[57] S. Mouri, Y. Miyauchi, K. Matsuda, *Nano Lett.*, 13 (12) (2013) 5944−5948.

[58] Y. Y. Li, Z. M. Qi, M. Liu, Y. Y. Wang, X. R. Cheng, G. B. Zhang, L. S. Sheng, *Nanoscale*, 6 (2014) 15248−15254.

[59] A. Portone, L. Romano, V. Fasano, R. D. Corato, A. Camposeo, F. Fabbri, F. Cardarelli, D. Pisignano, L. Persano, *Nanoscale*, 10 (2018) 21748.

[60] P. Sharma, M. Singh Mehata, *Mater. Res. Bull.*, 131 (2020) 110978.

[61] Y. Wang, J. Hu, Q. Zhuang, Y. Ni, *ACS Sustainable Chem. Eng.*, 4 (2016) 2535−2541.

[62] C. Liu, S. Zeng, B. Yang, F. Jia, S. Song, *J. Mol. Liq.*, 296 (2019) 111987.

[63] R. Pirarath, P. Shivashanmugam, A. Syed, A. M. Elgorban, S. Anandan, M. Ashokkumar, *Front. Enviorn. Sci. Eng.*, 15 (1) (2021) 15.

[64] F. Ru, P. Du, X. Lu, *Anal. Chim. Acta.*, 105 (2020) 139–146.

[65] S. S. Karade, D. P. Dubal, B. R. Sankapal, *RSC Adv.*, 6 (2016) 39159–39165.

[66] X. Hu, Y. Li, G. Zeng, J. Jia, H. Zhan, Z. Wen, *ACS Nano*, 12 (2) (2018) 1592–1602.

[67] P. Maiti, T. Singha, U. Chakraborty, S. Dutta Roy, P. Karmakar, B. Dey, S. A. Hussain, S. Paul, P. K. Paul, *Mater. Chem. Phys.*, 234 (2019) 158–167.

[68] P. Maiti, U. Saren, U. Chakraborty, T. Singha, S. Paul, P. K. Paul, *ACS Omega*, 7 (2022) 29013−29026.

[69] M. P. Szmyt, B. Buszewski, R. G. Kopciuch, *Mater. Chem. Phys.*, 242 (2020) 122484.

[70] H. Zhao, G. Yang, X. Gao, C. H. Pang, S. W. Kingman, T. Wu, Environ. *Sci. Technol.*, 50 (2) (2016) 1056–1064.

[71] M. Chhowalla, H. S. Shin, G. Eda, L. J. Li, K. P. Loh, H. Zhang, *Nature Chem.*, 5 (2013) 263–275.

[72] X. Deng, X. Liang, S. P. Ng, C. M. L. Wu, *Appl. Surf. Sci.*, 484 (2019) 1244–1252.

[73] C. Marchetti, *ISRN Toxicol.*, (2013) 184364, http://dx.doi.org/10.1155/2013/184360.

[74] A. Nersesyan, M. Kundi, M. Waldherr, T. Setayesh, M. Mišík, G. Wultsch, M. Filipic, G. R. M. Barcelos, S. Knasmueller, *Res. Rev. Mutat. Res.*, 770 (2016) 119–139.

[75] H. Ali, E. Khan, I. Ilahi, *J. Chem.*, (2019) 6730305, https://doi.org/10.1155/2019/6730305.

[76] M. E. C. López, G. L. Macêdo, S. I. D. Pereira, G. P. F. Arrifano, D. L. W. P. Diniz, J. L. M. Nascimento, A. M. Herculano, *Pharmcol. Res.*, 60 (2009) 212–220.

[77] J. Tong, Y. Wang, Y. Lu, *J. Environ. Sci.*, 41 (2016) 138–145.

[78] E. C. Cho, Q. Zhang, Y. Xia, *Nat. Nanotechnol.*, 6 (2011) 385–391.

[79] K. Cleal, L. He, P. D. Watson, A. T. Jones, *Curr. Pharm. Des.*, 19 (2013) 2878–2894.

[80] S. Mayor, R. Pagano, *Nat. Rev. Mol. Cell. Biol.*, 8 (2007) 603–612.

[81] S. Roy, K. A. Deo, K. A. Singh, H. P. Lee, A. Jaiswal, A. K. Gaharwar, *Adv. Drug. Deliv. Rev.*, 187 (2022) 14361.

****

CHAPTER ~ 9

Overall Conclusion and Future Plan of Research

This chapter gives the overall conclusion of the research presented in this thesis. My future plan of research is also highlighted.

CHAPTER~9

Overall conclusion and future plan of research

Throughout this thesis work, I have mainly studied the photophysical properties of biologically relevant cationic organic dyes namely Rhodamine B, acridine orange etc. and their interaction with noble metal nanoparticles such as, gold nanoparticles (Au NPs), silver nanoparticles (Ag NPs) in the aqueous environment. Efforts are also given to study the interaction of MoS_2 nanostructured material for ion sensing applications. The change in the spectroscopic results of dye/Au NPs mixed system in presence of bioanalyte namely L-Cysteine and D-Cysteine have been systematically studied. Our observations reveal that Au NPs drastically quenches the fluorescence of Rhodamine B dye in aqueous solution, but after addition of L-Cysteine to the dye/Au NPs assembly in the solution eventually restores the fluorescence signal and the recovery of this signal was very selective to L-Cysteine among all other relevant amino acids. Also, the selective fluorescence is accompanied with distinct colour change of the final solution only for L-Cysteine. The selective interaction of dye/Au NPs system is also tested with real human urine sample in presence of L-Cys thereby confirming this fluorescence based assay method is a viable approach for L-Cysteine detection and this study may contribute valuable database both for fundamental as wells as biomedical interest. Additionally, the ratio metric analysis of the fluorescence recovery ensures precise and accurate detection of target analytes due to automatic cancellation of external perturbation on the fluorometric assay experiments. Most interestingly the studied method is very simple and cost effective for selective and sensitive detection of L-Cys.

It is further observed that the interaction of thiol containing amino acid D-Cys with dye/Au NPs system is highly selective as confirmed by high fluorescence recovery of quenched fluorescence of RhB dye accompanied with a distinct colour change when compared to that due to L-Cys or any other relevant amino acids in aqueous solution as

well as in real bio-sample (urine). D-Cysteine is known to be as an important regulator of neurotransmitters and the overall neural cell dynamics in our physiological system. Under appropriate optimum condition, the proposed dye/nanoparticle mixed system may be considered as an efficient biosensing platform for the detection of D-Cysteine via spectrofluorometric method. Overall, these studies open up a new possibility for the development of sensing platform using novel metal NPs and organic dyes for various other bioanalyes or ionic species in aqueous solution as well as in real bio sample via proposed ratiometric fluorescence based technique.

Two dimensional layered nanostructured material namely molybdenum disulfide (MoS_2) nanoflakes has gained significant attention of the global scientific community due to their unique layer structure and efficient surface properties as well as tuneable optical properties and easy exfoliation in aqueous medium. In this thesis work, we synthesize MoS_2 nanoflakes using L-Cysteine by hydrothermal method and systematically investigated their application for detection of heavy metal ion namely Hg^{2+} in aqueous solution. The drastic fluorescence quenching of MoS2 occurred due to their interaction with Hg2+ in aqueous solution compared to all other relevant metal ions. The reduction of fluorescence intensity of MoS2 is found to highly sensitive to the concentration of Hg^{2+} ion in the solution thereby confirming the proposed fluorometric method as an efficient approach for Hg^{2+} ion detection in aqueous environment. Fluorescence imaging microscopic study also reveals the similar fluorescence quenching in real human cell containing Hg^{2+} ion. Also MTT assay confirm the cell viability our MoS_2 nanoflake sample for cellular study thereby assuring the biocompatibility of MoS_2 nanoflakes and is an effective for Hg^{2+} ion sensing for biomedical interest as well.

In another work I have studied the interaction of silver nanoparticles (Ag NPs) with cationic dye acridine orange (AO) in presence of biological macromolecule DNA by means of electronic spectroscopic technique. It was observed that Ag NPs significantly quench the fluorescence properties of dye molecules. Also presence of DNA in the mixed solution further quenches the emission. UV-vis absorption results reveal the binding of Ag NPs with DNA. However, addition of DNA dye did not significantly alter the fluorescence emission properties of AO dye.

Therefore, the study of the interaction and photophysical properties of various noble metal and metal-based nanostructures with organic, inorganic and biological

compounds in the aqueous medium becomes an emerging area of material science research due to their promising applications in the fields of sensing, nanobiotchnology especially for biomedical and environmental aspects.

In near future I want to extend my research to study the interaction behaviour between other noble metal and metal-based nanostructures such as copper nanoparticles, platinum nanoparticles, molybdenum disulfide quantum dots with some biologically relevant organic fluorescent dyes namely, cumarin, cyanine, etc. in presence of important biomolecules including hemoglobin, human serum albumin and some other proteins via spectrofluorometric method. It will be very interesting for me to determine the nature of binding and nature of protein deformation if any (change of the orientation of amino acids) in presence of noble metal and metal-based nanostructures. Special emphasis may be given to the fabrication of hybrid nanostructures for biomedical applications. Additionally, I have also planned to focus on some quantum-chemical calculations and theoretical simulations of organic dyes and noble metal nanoparticles, respectively. I am looking forward to carry out those interesting research in near future.

****

REPRINTS OF PUBLICATIONS

Materials Chemistry and Physics 234 (2019) 158–167

Contents lists available at ScienceDirect

Materials Chemistry and Physics

journal homepage: www.elsevier.com/locate/matchemphys

Selective and sensitive detection of L-Cysteine via fluorometric assay using gold nanoparticles and Rhodamine B in aqueous medium

Pradip Maiti [a,b], Tanmoy Singha [a], Utsav Chakraborty [a], Sannak Dutta Roy [a], Parimal Karmakar [c], Bapi Dey [d], Syed Arshad Hussain [d], Sharmistha Paul [b,**], Pabitra Kumar Paul [a,*]

[a] Department of Physics, Jadavpur University, Jadavpur, Kolkata, 700032, India
[b] West Bengal State Council of Science and Technology, Department of Higher Education, Science and Technology and Biotechnology, Vigyan Chetana Bhavan, Sector-I, Salt Lake, Kolkata, 700064, India
[c] Department of Life Science & Bio-technology, Jadavpur University, Jadavpur, Kolkata, 700032, India
[d] Department of Physics, Tripura University, Suryamaninagar, 799022, Tripura, India

HIGHLIGHTS

- Gold nanoparticles can sufficiently quench the fluorescence of Rhodamine B dye.
- L-Cysteine was detected selectively from fluorescence of dye/nanoparticle mixture.
- Selective fluorescence response was accompanied with an observable color change.
- The calibration curve for the assay of L-Cysteine was almost linear.
- Selective response of L-Cysteine in real human urine sample via fluorometric assay.

GRAPHICAL ABSTRACT

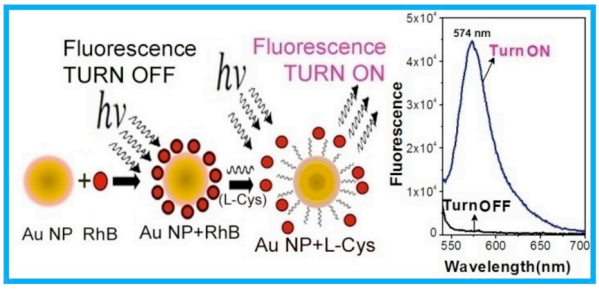

ARTICLE INFO

Keywords:
Gold nanoparticle
Rhodamine B
Amino acids
Colorimetric/fluorometric
L-cysteine
Urine

ABSTRACT

An assay method based on fluorometric and colorimetric change was developed for selective sensing of important thiol containing amino acid L-Cysteine (L-Cys) by using gold nanoparticles (Au NPs) and Rhodamine B (RhB) in aqueous environment. This fluorometric assay is basically relies on the competitive binding between RhB and Au NPs via electrostatic interaction as well as strong thiol(-SH)-Au NPs bonding via chemisorption. Citrate stabilized Au NPs (diameter ~27 nm) was synthesized by soft chemical method and characterized by UV–Vis absorption spectroscopy and Transmission electron microscopic (TEM) techniques. The change in non-radiative energy transfer between RhB and Au NPs are responsible for the observed drastic fluorescence quenching of RhB via FRET process. The recovery of fluorescence from the assay solution of RhB/Au NPs after addition of L-Cys was found linear over the concentration range 0.01 μM–1000 μM with experimental limit of detection (LOD) of 0.01 μM. The selective interaction of L-Cys with the mixed solution of RhB/Au NPs was reflected by the color change from wine to bluish-black of the final solution. The proposed fluorometric assay method accompanied with the observed colorimetric change could successfully differentiate other interfering amino acids including thiol (-SH) containing compounds namely L-Methionine, L-Homocysteine and antioxidant glutathione with the high degree of accuracy. Also the LOD is comparable to the concentration of L-Cys present in the blood plasma.

* Corresponding author.
** Corresponding author.
E-mail addresses: sharmistha.paul@gov.in (S. Paul), pkpaul@phys.jdvu.ac.in (P.K. Paul).

https://doi.org/10.1016/j.matchemphys.2019.06.001
Received 26 February 2019; Received in revised form 30 May 2019; Accepted 3 June 2019
Available online 4 June 2019
0254-0584/

The proposed sensing mechanism is also confirmed with pure human urine sample to detect the response of L-Cys in the urine. Therefore, this fluorometric assay technique for detection of L-Cys has great potential with the diagnostic impact for biomedical interest.

1. Introduction

The thiol containing amino acid L-Cys generally found in human plasma is well known as the building block of proteins and is involved in verity of important biological processes [1]. Normally a small amount of L-Cys is present in human body in the form of N-acetyl-L-cysteine (NAC) commonly known as L-Cys and is naturally derived from the amino acids serine and methionine [2]. It is widely used in pharmaceutical industry as medicine to treat different type of physiological complications [3–6]. The body prepares the important antioxidant from NAC by converting it firstly into L-Cys and then into glutathione [7]. Antioxidants such as or ascorbic acid (vitamin C) fight against the free radicals in our body and reduce oxidative stress before damage of the vital molecules. For healthy adults about 4.1 mg/kg/day of L-Cys is required as recommend by Joint FAO/WHO/UNO expert consultation [8]. Although L-Cys has a number of health benefits, the elevated amounts of such amino acid may cause neurotoxicity [9], promotes urinary stone formation [10] *etc.* and it can also be regarded as the biological marker for various diseases [11–13]. Therefore, it is of utmost importance to detect the concentration of L-Cys by a highly sensitive, selective and convenient method with high degree of accuracy in order to prevent its adverse effects in our health.

Various analytical methods such as immunoassay, electrochemistry, chromatography *etc.* are recently being explored for the detection of L-Cys and are performed in conjugation with liquid chromatography, fluorimetry, colorimetry, differential pulse voltammetry and spectrofluorimetry *etc.* [14–19]. But immunoassay and chromatography required expensive biological reagents and complicated instrumentations. Also the electrochemical methods show relatively low selectivity to L-Cys. Some methods utilize the fluorometric detection after direct labeling of suitable fluorescent probe with target bio-analyst. However direct labeling sometimes causes structural alternation of the biological species resulting erroneous information. Also these detection methods directly utilizing the absolute fluorescence intensity sometimes may include unwanted noise due to environmental perturbation in the measurement. In recent times the colorimetric methods are attracted great attention but are still limited because of their lack of effectiveness at very low concentration. Therefore, it is of crucial importance to design the appropriate sensing platform for the detection of L-Cys both selectively and quantitatively with high degree of accuracy in the physiological range. In this direction, the method based on the fluorometric assay may offer great advantages for the detection of L-Cys as they enable a direct and level free detection in an aqueous environment even at very low concentration. Also the ratio-metric fluorescence recovery from the fully quenched state of any suitable fluorescent probe in presence of the analyst biomolecule ensures the elimination of any external perturbation involved in the measurements.

Metal nanoparticles are attracted considerable attention for their excellent ability to modulate the spectroscopic properties of various interesting cationic organic dyes in the aqueous environment [20,21]. The ground and excited state electronic properties of such dye molecules adsorbed onto the surface of gold or silver nanoparticles show significant physical and physicochemical behavior which sometimes enable their use in many biomolecular recognition processes [22]. The reduction of excited state fluorescence life time down to several hundreds of picoseconds has been attributed to energy or electron transfer processes [23,24] from excited dye molecules to these nanoparticles. The resonant coupling between the oscillatory electric dipole of plasmonic electrons and the dipole of excited dye molecules may be a possible reason for ultra-fast energy transfer [25]. These interesting photophysical processes of small organic dyes assembled on to the novel nanoparticle's surfaces are sometimes very sensitive to the specific guest-host geometry in a particular environment, which allows their possible application in the field of biosensors [26]. On the other hand, these nanoparticles may aggregate in solution while interacting with many biological molecules namely protein, enzyme, amino acids *etc.* [27] resulting substantial effect on the surface plasmonic band under optical irradiation.

In this present report we address a highly sensitive and selective method for detection of L-Cys via fluorescence turn-off and turn-on mechanism based on the interaction of RhB and Au NPs in aqueous media. The cationic dye RhB belongs to xanthene family of organic dyes and has high fluorescence quantum yield (0.71) in water with good photo-stability [28,29]. The fluorescence emission of RhB was turned on from its initial quenched state and was recovered (approximately 68 fold) after addition of L-Cys to RhB/Au NPs mixed solution at a concentration range between 0.01 μM and 1000 μM. Most interestingly this fluorometric method was accompanied with a significant and noticeable color changes of the final solution and is therefore a direct visual evidence for selective determination of L-Cys over all other associated amino acids in the aqueous medium.

2. Experimental

2.1. Materials

The amino acid of our interest i.e., L-Cys ($C_3H_7NO_2$, M.W: 121.15 $gmol^{-1}$) along with all other essential and non-essential amino acids used in this present work, RhB ($C_{28}H_{31}ClN_2O_3$, M.W: 479.02 $gmol^{-1}$), chlorauric acid ($HAuCl_4$, $3H_2O$, M.W: 339.79 $gmol^{-1}$), glutathione (M.W: 307.32 $gmol^{-1}$), ascorbic acid ($C_6H_8O_6$, M.W: 176.12 $gmol^{-1}$), uric acid ($C_5H_4N_4O_3$, M.W:168.11 $gmol^{-1}$) were purchased from Sigma Aldrich chemical company, USA and used without further purification. The purity of RhB was checked via spectroscopic method prior to use in the experiment. Trisodium citrate ($Na_3C_6H_5O_7$, M.W: 258.06 $gmol^{-1}$), sodium chloride (NaCl, M.W: 58.44 $gmol^{-1}$), potassium chloride (KCl, M.W: 74.5513 $gmol^{-1}$) were purchased from Merck Chemical Company, Germany. All the glasswares were cleaned with freshly prepared aqua-regia solution (3:1 mixture of hydrochloric acid (HCl) and nitric acid HNO_3) followed by subsequent rinsing with triple distilled deionized Milli-Q water (resistivity 18.2 MΩ cm, pH~7, collected from Synergy integrated with an Elix®-Advantage set-up, Millipore SAS, France) and then were autoclaved for 24 h before use. Aqueous solutions of the chemicals were also prepared with the same triple distilled Milli-Q water.

2.2. Synthesis of Au NPs

Au NPs were synthesized by citrate reduction method as described elsewhere [30]. In a typical procedure, 50 ml aqueous solution of $HAuCl_4$, $3H_2O$ (concentration of 0.25 M) was heated to boiling and 1.2 ml of $Na_3C_6H_5O_7$ (1%) was added into the solution under vigorous stirring for preparing gold nanocolloidal solution. Within a time of 70 s, the boiling solution turned faintly to blue color and after 120 s the blue color changed to deep red. The solution was then set aside to cool down at room temperature. The final concentration of the gold nanocolloidal solution became 0.1 mM at pH ~7.

2.3. Characterizations techniques

The UV–Vis absorption spectra of the samples were recorded in the wavelength range of 200–800 nm by a double beam UV–Vis absorption

spectrophotometer (UV-1800, Shimadzu, Japan) after proper baseline correction for the solvent background. Steady state fluorescence spectra of the samples were recorded in the range of wavelength 545–700 nm by using a Horiba Spectrofluorometer (Fluoromax-4C, Horiba Scientific Incorporated, USA). An excitation light source of wavelength 530 nm emerged through a slit having width of 2 nm was used for all the steady state fluorescence emission measurements. Both the absorption and emission spectra were collected from the sample solution in quartz cell (Kozima, Japan) of 1.0 cm path length at room temperature (25 °C). The hydrodynamic nanoparticle size distribution and the effective surface Zeta potential (ζ) of the as-synthesized Au NPs were obtained by a Zetasizer (Zetasizer Nano ZS, Malvern Instruments Ltd, UK) via dynamic light scattering method (DLS) at an ambient condition. High resolution TEM study of the Au NPs was carried out on a Transmission Electron Microscope (TEM) operated at 200 kV (JEM-2010 TEM, JEOL Ltd., Japan). For TEM study, the sample solutions were incubated for 15 min and then a small drop was spread onto the carbon coated copper microgrid (PELCO® 300 Mesh Grids, Ted Pella Inc. USA) and subsequently dried at room temperature. Time resolved fluorescence emission measurements were acquired by using time-correlated single photon counting (TCSPC) method (Fluorolog, Horiba Jobin Yvon, USA) to obtain the excited state fluorescence lifetime of the samples. In this method, the sample solutions were excited at 510 nm by using a picoseconds pulsed diode laser. The fluorescence decay data were collected over 200 channels which were calibrated on a non-linear time scale with increasing time according to an arithmetic progression with a Hamamatsu photomultiplier tube (R928P). The raw decay data as obtained were analyzed using IBH DAS6 software.

2.4. Method of fluorometric assay experiments

A 2 mL of 0.1 mM Au NPs solution was incubated at room temperature (25 °C) for 5 min with the 2 mL of 0.1 μM RhB (probe molecules) solution so that the assay could be formed. Freshly prepared L-Cys solution of different concentration (1 mM - 0.01 μM) was added (200 μL) separately with the assay and kept for 3 min and subsequently the fluorescence spectra were recorded. For the colorimetric study, freshly prepared different amino acids, glutathione, uric acid, ascorbic acid and different neurotransmitters (K^+ and Na^+) stock solutions of concentration 0.1 mM were added with the assay and the color change was observed instantly. For confirmation of selectivity of the assay, mixture of freshly prepared mixed individual solutions of L-Cys and different amino acids, glutathione, uric acid, ascorbic acid and neurotransmitters (in 1:1 vol ratio, concentration of 0.1 mM each) were added to the RhB/Au NPs solution and fluorescence emission was measured after 3 min for each mixed solutions.

3. Results and discussion

3.1. Characterization of synthesized Au NPs

Fig. 1A shows the UV–Vis absorption spectrum of the citrate-stabilized Au NPs in aqueous colloidal solution and shows distinct absorption band with its maximum at around 528 nm along with two weak humps at 251 nm and 356 nm. The former is due to the strong characteristic surface plasmon resonance (SPR) while the other two are due to the intra-band electronic transitions of gold and can be related with the traces of such bands as similarly reported for silver nanoparticles by some researchers [31,32]. The well resolved and sharp SPR maximum band is basically due to both longitudinal and transverse SPR

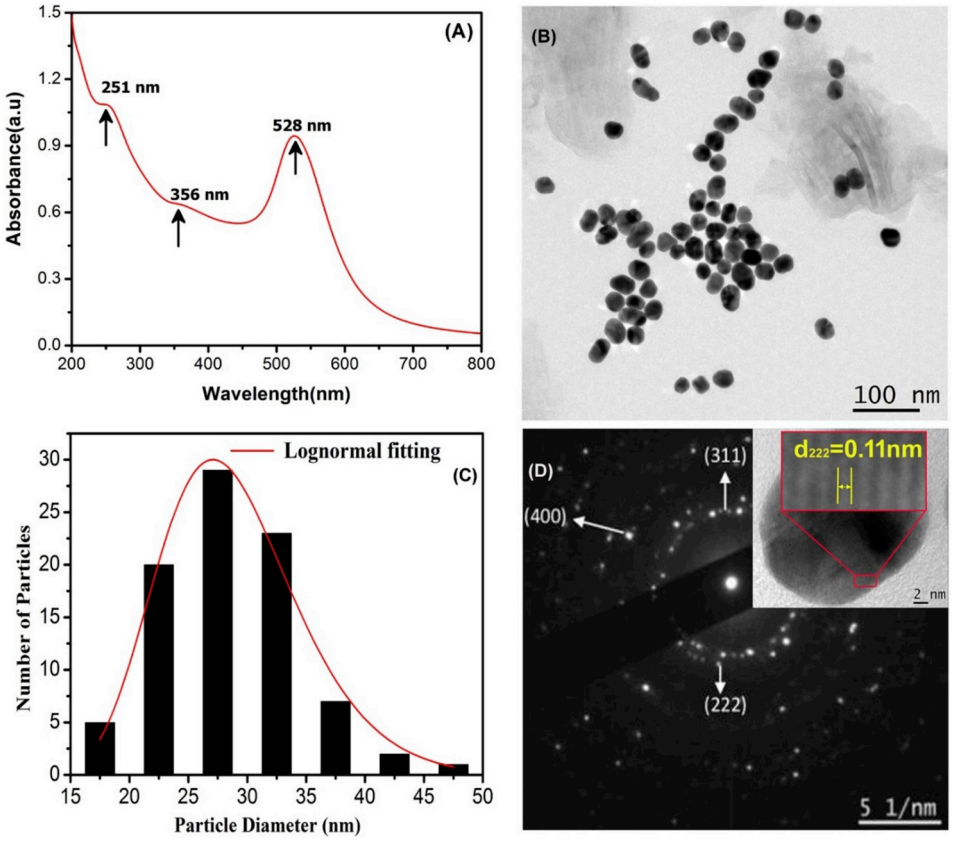

Fig. 1. (A) UV–Vis absorption spectrum of Au NPs in aqueous colloidal solution (concentration of 0.1 mM). (B) TEM micrograph of as-synthesized mono-dispersed Au NPs desiccated at room temperature, (C) Lognormal fitting of the particle size distribution, (D) SAED pattern with the Miller-indices of Au NPs. Inset of (D) shows the HR TEM micrograph with crystal spacing.

equivalently, which reveals a sign of the formation of spherical Au NPs. The molar extinction coefficient of Au NPs (with maximum SPR observed at 528 nm) was calculated as $540 \times 10^7\ M^{-1}cm^{-1}$ [33].

The DLS study (Fig. S1, supplementary information) revels that the average hydrodynamic size of Au NPs was about 53.78 nm. To have further knowledge about the homogeneity of NPs distributions the surface zeta potential (ζ) was measured (Fig. S2) and was found to be −30.1 mV at room temperature and solution pH ~7. These results suggest that Au NPs could overcome the van der Waals attraction through the strong electrostatic repulsion between the negatively-charged citrate coronas around the NPs surface in aqueous medium and therefore Au NPs remained effectively stabilized prior to their use in the experiment [34].

However, to have a more precise and clear understanding of the size and morphology of Au NPs, TEM study was performed. Fig. 1B shows that Au NPs were mono-dispersed with nearly spherical in shape and the average particle diameter was ~27.5 nm as calculated from the size distribution curve (Fig. 1C). The selected area electron diffraction (SAED) (Fig. 1D) reveals the good crystalline nature of Au NPs. The rings as seen in SAED pattern were indexed and corresponds to the electron diffractions originated from (311), (222), (400) *etc.* planes of FCC gold crystal. The interplaner spacing as calculated (Fig. 1D) was about 0.11 nm corresponding to the lattice plane (222). The High resolution-TEM micrograph was also shown in the inset of Fig. 1D. The energy dispersive X-ray spectrum (EDS) curve (Fig. S3) shows the nucleation of Au NPs without any impurities and the presence of large number of Au NPs in its colloidal solution used for the experiment.

3.2. UV–Vis absorption spectroscopic study

The cationic dye RhB is a well-known laser dye from the xanthene family of organic dyes and its molecular structure is shown as the inset of Fig. 2A. The UV–Vis absorption spectrum of pure RhB solution (concentration of 6 μM) as shown in Fig. 2A (curve 3) exhibits a strong absorption band at around 554 nm which is attributed to the characteristic π-π* transition of dye monomer units and a very weak band observed at around 520 nm is assigned to the dimeric states of RhB molecules due to the n-π* transition [29]. In aqueous solution at low concentration (i.e. 6 μM) RhB dimmers are in equilibrium with the monomers and their mean numbers should remain constant at a particular concentration [29]. However, in our work, the concentration of RhB solution was about 0.1 μM for the detection of L-Cys. So it was presumed that most of the RhB molecules might exist as monomer units in the studied aqueous solution because of their very low concentration. RhB/Au NPs mixed solution (1:1 vol ratio) (Fig. 2A, curve 2) showed that the main characteristic absorption band position (554 nm) of RhB was almost unaltered but with decreased intensity along with an increase in absorbance of dimeric band (520 nm) compared to that of pure RhB. This change in the absorption spectrum of RhB in presence of Au NPs was possibly due to their adsorption on to the nanoparticles surface. More precisely this aggregation effects were manifested as the close packing of RhB dye molecules around the Au NPs surface and this eventually induced enhanced dye-dye intermolecular interaction. Some authors [20–22] also reported this type of aggregations of other xanthene family dyes on the Au NPs surface via strong electrostatic interaction. In fact, addition of Au NPs to the aqueous solution of RhB certainly changed the micro-environment around the electronic states of the dye molecules and this might have altered their electric transition dipole-moment. The interaction of molecular dipoles of RhB with the plasmonic field produced by Au NPs eventually affected the excitation energies of the individual dye molecules resulting decrease in absorbance of dye monomeric band at 554 nm.

The closer association of dye molecules on the Au NPs surface additionally induced the aggregations of NPs in the mixed sample which was also observed from TEM analysis (Fig. 2B). It is clearly observed that different size of dye/Au composite systems were formed in the mixed ensembles which have been correlated with the observed UV–Vis results. The DLS measurement shows that the hydrodynamic diameter of the NPs increases after addition of RhB and the negative charges on the surface of citrate stabilized Au NPs were reduced as evidenced from Fig. S4 and Fig. S5 respectively.

3.3. Sensing of L-Cys based on fluorometric assay

In this work we systematically design a highly sensitive sensing platform for the quantitative as well as selective recognition of L-Cys using fluorometric assay of RhB/Au NPs in the aqueous medium. The sensing of L-Cys via fluorometric assay mechanism is schematically shown in Fig. 3. The fluorescence emission spectra of RhB/Au NPs mixed aqueous solution (1:1 vol ratio) in absence (curve a) and presence (curve b) of L-Cys (concentration of 100 μM) was shown in Fig. 4A. It is observed that RhB/Au NPs mixed aqueous solution had negligibly small value of emission intensity because of efficient fluorescence resonance energy transfer (FRET) from excited dye molecules to the Au NPs surface as well as also the decrease in radiative rate constant of individual RhB molecules adsorbed on NPs surface. The energy transfer from donor RhB to acceptor Au NPs is mainly due to FRET process which is clearly

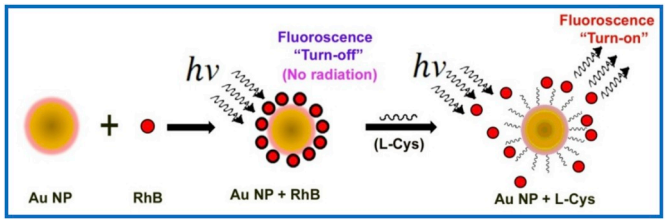

Fig. 3. Mechanism of detection of L-Cys using fluorometric assay.

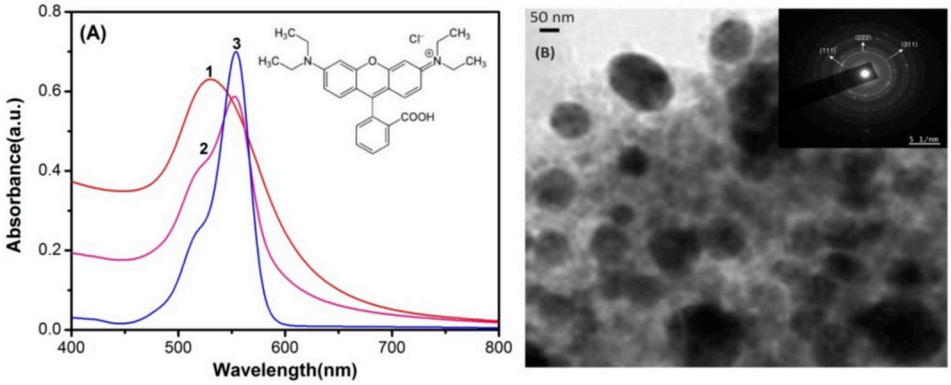

Fig. 2. (A) UV–Vis absorption spectra of (1) aqueous colloidal dispersion of Au NPs (0.1 mM), (2) mixed aqueous solution of RhB (6 μM) and Au nanocolloidal solution (0.1 mM), (3) aqueous solution of pure RhB (6 μM). Inset shows the molecular structure of RhB dye. (B) TEM micrograph of RhB mixed Au NPs showing the aggregation of Au NPs. Inset shows the corresponding SAED pattern which suggests that the crystallinity of the Au NPs was not lost due to the adsorption RhB molecules onto their surface.

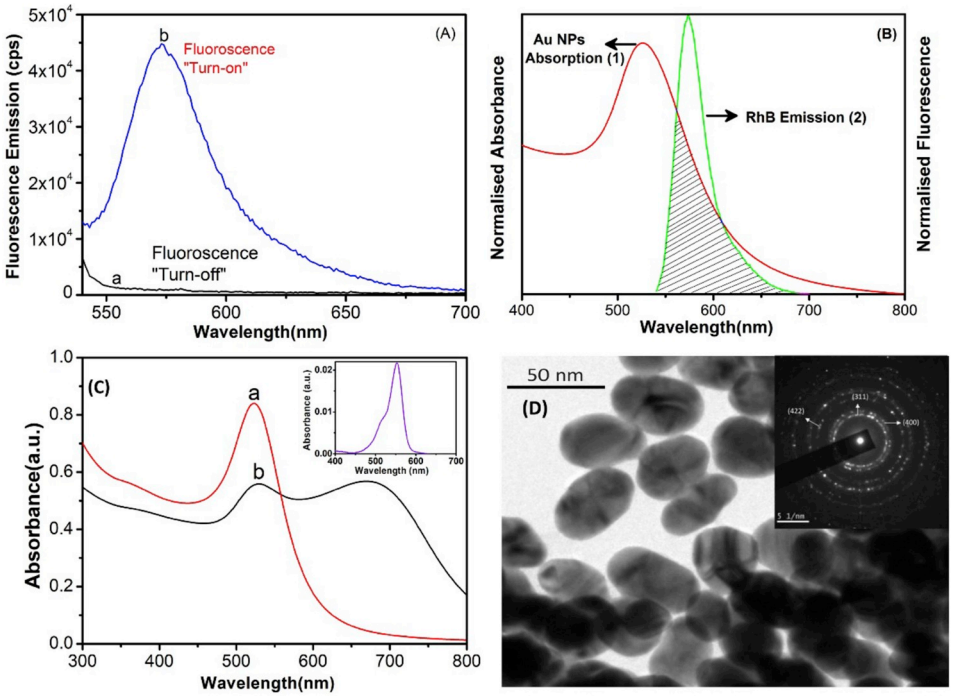

Fig. 4. (A) Fluorescence emission spectrum from the assay of RhB/Au NPs in absence (curve a) and presence (curve b) of L-Cys, (B) Overlapping between normalized emission spectrum of RhB (curve 2) and absorption spectrum of Au NPs (curve 1), (C) UV–Vis absorption spectra of RhB/Au NPs mixed solution (0.1 mM & 0.1 μM in 1:1 vol ratio) in absence (curve a) and presence (curve b) of L-Cys. Inset shows the UV–Vis absorption spectrum of RhB (0.1 μM) in presence of L-Cys (0.1 mM), (D) TEM micrograph of RhB/Au NPs/L-Cys mixed sample. Inset shows the corresponding SAED pattern.

perceived from the large overlap between the emission of RhB and absorbance of Au NPs as shown in Fig. 4B. However, most interestingly after addition of L-Cys solution to the RhB/Au NPs mixed solution the fluorescence emission at around 574 nm was found to emerge with much increased intensity from its quenched state as shown in Fig. 4A (curve b). This observation clearly suggests that the emission of RhB molecules which were adsorbed onto the Au NPs surface before addition of L-Cys was recovered to a great extent and was possibly due to a strong interaction between L-Cys and Au NPs through the thiol moiety (-SH) [35]. Due to this strong affinity of thiol to Au NPs, the L-Cys molecules were strongly bound to NPs resulting the escape of RhB molecules away from NPs surface. Because the attachment of RhB molecules with Au NPs were due to electrostatic interaction whereas L-Cys tend to attach with Au NPs by Au–S bond via chemisorptions which is relatively much stronger. As a result, the electrostatic charge distribution around the NPs surface was disrupted causing the release of RhB molecules from Au NPs surface resulting the decrease of fluorescence quenching via nonradiative energy transfer. Thus addition of L-Cys eventually restored the fluorescence band intensity of RhB at around 574 nm. However, the control experiment (Fig. S6) (i.e. fluorescence emission of RhB/L-Cys mixed aqueous solution without Au NPs) reveals a negligible effect of L-Cys on the emission profile of RhB molecules in the studied aqueous medium as the unaltered emission band position and no such significant rise and fall of emission intensity with increase or decrease of L-Cys concentration. But the slight decrease in emission intensity of RhB after addition of L-Cys solution of different concentrations might only be due to the dilution of the RhB concentration in the mixed solution and not due to any interaction in their ground or excited electronic states.

The aggregation of Au NPs was further evidenced from UV–Vis absorption spectroscopy as shown in Fig. 4C. It was observed that an additional SPR band appeared at around 670 nm after addition of L-Cys [35] and intensity of the main SPR band at around 528 nm was sufficiently reduced compared to that in case of RhB/Au NPs mixed aqueous solution (Fig. 2A, Curve 2). So the emergence of the new SPR band of RhB/Au NPs mixture in presence of L-Cys corresponded possible aggregation of Au NPs and have already been reported by A. Mocanu et al. [36].

In order to support the above results as obtained from fluorometric assay method, TEM study (Fig. 4D) was also performed for the RhB/Au NPs/L-Cys mixed solution at the same ambient condition. We already observed that the dye molecules were adsorbed on the Au NPs surface resulting some aggregation of Au NPs and the distribution became inhomogeneous (Fig. 2B). However, from Fig. 4D it is clearly observed that after addition of L-Cys in RhB/Au NPs mixed aqueous solution, the distribution of NPs became more homogeneous but the average size of the particle increased to about 40 nm. This increased size distribution of Au NPs was basically due to some aggregation of individual NPs in the relatively higher viscous medium after addition of L-Cys. However, the crystallinity of Au NPs after addition of L-Cys possibly was not altered as distinct diffraction rings was observed from SAED images (Inset of Fig. 4D). DLS study as shown in Fig. S7 further reveals the increase in the hydrodynamic particle size distribution (~67.84 nm) of Au NPs in presence of RhB and L-Cys compared to pure Au NPs (~53.78 nm). Also the Zeta potential (ZP) (ζ) as measured for RhB/Au NPs/L-Cys mixed solution was found to be −13.0 mV (Fig. S8) which is much lower than that of pure Au NPs (−30.1 mV) as well as RhB/Au NPs mixture (−20 mV). The reduced ZP of Au NPs in RhB/Au NPs/L-Cys mixture eventually favored further aggregation of NPs. More precisely the addition of L-Cys to the RhB/Au NPs mixed aqueous solution might have displaced the negatively charged citrate around NPs surfaces resulting the decrease in negative ZP of Au NPs. This in turn also favored the aggregation of Au NPs in aqueous medium [35].

3.3.1. *Sensitivity of the proposed method*

In the present work, we have also studied the quantitative detection of L-Cys via fluorometric assay of RhB/Au NPs assembly in the same aqueous environment. Fig. 5 demonstrates the fluorescence spectra of RhB/Au NPs mixed aqueous solution in presence of various L-Cys concentrations viz. 0.01 μM, 0.1 μM, 1.0 μM, 10 μM, 100 μM and 1000 μM. From Fig. 5, we immediately see that the fluorescence emission band of RhB at 574 nm was recovered and their intensity increased systemically with increase in L-Cys concentration. Also the increase in fluorescence recovery efficiency with the concentration of L-Cys was almost linear (Inset of Fig. 5). The systematic recovery of fluorescence from RhB/Au NPs mixed solution in presence of L-Cys was highly sensitive with the change in the concentration of L-Cys. Therefore, this fluorometric assay

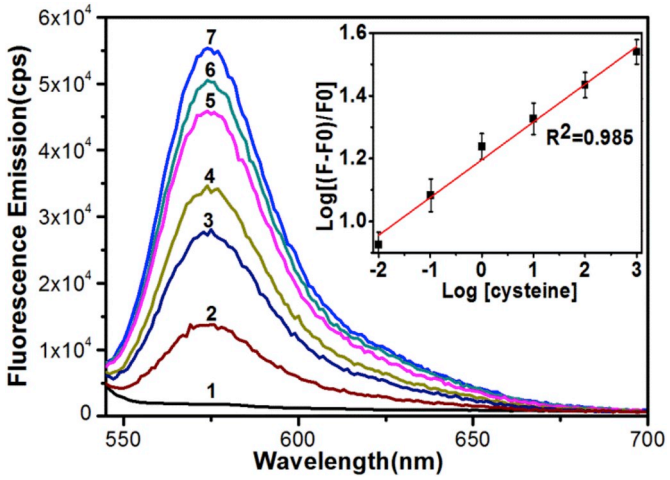

Fig. 5. Fluorescence recovery from assay of RhB/Au NPs in presence of L-Cys of various concentration viz. 0.01 μM (2), 0.1 μM (3), 1.0 μM (4), 10 μM (5), 100 μM (6) and 1000 μM (7). The spectrum (1) represents fluorescence emission of RhB/Au NPs mixed solution. Inset shows the plot of Log[fluorescence recovery efficiency] versus Log [L-Cys concentration].

in aqueous medium may be a suitable and efficient sensing platform for quantitative detection of amino acid L-Cys. The increased number of L-Cys molecules with increase in their concentration in RhB/Au NPs mixed solution definitely segregates more number of dye molecules from the surface of Au NPs and this has been manifested as the systematic linear increase in the fluorescence emission intensity. In fact, the initial quenched fluorescence emission of RhB due to Au NPs via FRET process was gradually decreased as the concentration of L-Cys was increased. A very good linear relationship between the fluorescence recovery efficiency (at 574 nm) and the concentration of L-Cys can be used to calibrate the proposed method of L-Cys detection in the concentration range of 0.01 μM–0.1 mM as obtained from the inset of Fig. 5. The calibration equation (eqn. (1)) for this approach can be written as

$$\mathrm{Log}[(F - F_0)/F_0] = \mathrm{Log}\,[C] + \text{ constant} \quad (1)$$

where C is the concentration of L-Cys which was added into RhB/Au NPs mixed solution during the fluorometric assay experiments.

The linear fitted plot as shown in inset of Fig. 5 is almost passed through the initial point of the calibration curve and hence the limit of detection (LOD) may be approximately considered as 0.01 μM. The sensibility or the LOD of the proposed L-Cys detection method can be comparable with the results reported in the literature as cited in Table 1. Furthermore, the present technique utilizes the ratiometric fluorescence response of the fluorescent probe (RhB). Hence the effect of any impurity or external perturbation on the fluorescence was automatically discarded during the calibration of the proposed assay. Also the range of detection in the present method is comparable to the concentration of L-Cys present in the blood plasma [37] (near about micromolar), which suggests that our detection technique will have great potential with the diagnostic impact for biomedical interest.

Table 1
Comparison with other reported methods for detection of L-Cys.

Probe	Detection principle	Range (in μM)	LOD (μM)	References
TCEP & CMQT[a]	HPLC-UV	20–300	0.5	[14]
Fluorescein–modified gold nanoparticles	Fluorescence	0.8–4.1	0.1	[15]
Ficin	Colorimetry	0.05–14	0.02	[16]
Poly(p-coumaric acid)/MWNT/GCE[b]	Differential pulse voltammetry	7.5–1000	1.1	[17]
Cu^{2+} -caclein	Fluorimetry	0.3–12	0.04	[18]
Tl(III)[c]	Spectrofluorimetry	0.1–5.5	0.1	[19]
Rhodamine B Coated Au NPs	Fluorometric assay	0.01–100	0.01	**This work**

[a] TCEP - tris(2-carboxyethyl)phosphine hydrochloride, CMQT - 2-Chloro-1-thylquinolinium tetrafluoroborate.

[b] MWNT/GCE - multi-walled carbon nanotubes modified glassy carbon electrode.

[c] Tl(III) - Thallium(III).

3.3.2. Selectivity of the proposed method

In the practical purposes a good biosensor should selectively responds to a particular biological analyte which is to be sensed at a given time otherwise the sensing process will be failed to give the desired output. To evaluate the selectivity of the proposed method towards L-Cys, the interference of various other twenty amino acids such as L-Aspartate (L-Asp), L-Histidine (L-His), L-Methionine (L-Met), L-Serine (L-Ser), L-Tryptofan (L-Try), L-Alanine (L-Ala), L-Arginine (L-Arg), L-Glycine (L-Gly), L-Isolevcine (L-Iso), L-Proline (L-Pro), L-Threonine (L-Thr), L-Valine (L-Val), L-Asparagine (L-Aspa), L-Glutamic Acid (L-Glu), L-Glutamine (L-Glut), L-Phenylalanine (L-Phe), L-Leucine (L-Leu), L-Tyrosine (L-Tyr) L-Lysine (L-Lys) and L-Homocysteine (L-HomoCys) and antioxidant glutathione (GSH) were tested via the same fluorometric assay method in aqueous medium. Apart from these amino acids, the interactions of other relevant biosamples such as uric acid and ascorbic acid and some neurotransmitters (K^+ and Na^+) are also examined with the proposed assay method.

3.3.3. Colorimetric response of the assay

The most interesting observation was that just after addition of equal amounts of various amino acids including L-Cys separately to the RhB/Au NPs mixed aqueous solution the color of the final solution became nearly bluish-black (as shown in Fig. 6) only in case of L-Cys and could be clearly visualized with the naked eye. The concentrations of aqueous solutions of all the amino acids, other biosamples and neurotransmitters were same (0.1 mM) for these colorimetric observations. This was the initial visual evidence that L-Cys could selectively bind to Au NPs thereby changing the color of the final solution. It is already evident from Fig. 4C (Curve b) that the addition of L-Cys to RhB/Au NPs mixed aqueous solution causes the emergence of the new absorption band of Au NPs at around 670 nm which implies a very fast and strong interaction between L-Cys and Au NPs in presence of probe RhB in the ground electronic states resulting the change of color of RhB/Au NPs mixed solution from wine to bluish-black.

Fig. 7 shows the change in fluorescence recovery efficiency as a function of various amino acids including L-Cys as well as glutathione, uric acid, ascorbic acid and some neurotransmitters like Na^+, K^+ *etc.* and

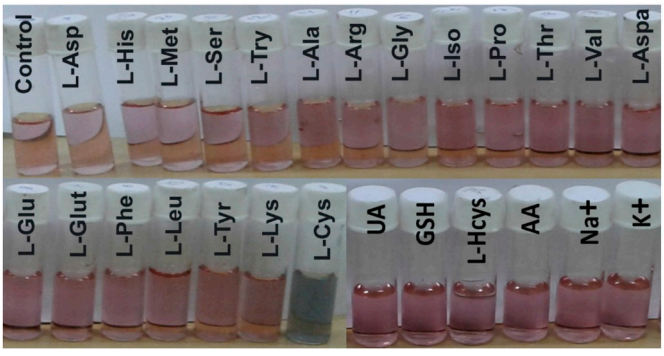

Fig. 6. Digital photographs of RhB/Au NPs mixed solution before (Control) and after adding of all twenty amino acids, glutathione, uric acid, ascorbic acid and neurotransmitters. Images reveal a direct visual evidence for the color change (from wine to bluish black) only for L-Cys solution in the mixed ensemble. (For interpretation of the references to color in this figure legend, the reader is referred to the Web version of this article.)

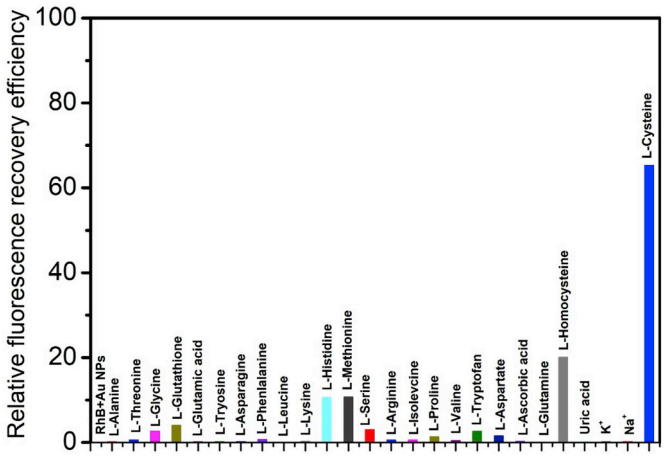

Fig. 7. Relative fluorescence recovery efficiency of the assay of RhB/Au NPs at 574 nm upon addition of L-Cys and other amino acids, glutathione, uric acid, ascorbic acid and neurotransmitters.

the corresponding emission spectra are shown in Fig. S9. From this plot it is clearly observed that the fluorescence recovery efficiency of RhB/Au NPs system in presence of L-Cys was significantly maximum compared to the rest of the amino acids although the concentration of all the amino acids remained same. The all other amino acids showed almost negligible effect on the quenched state of RhB adsorbed onto Au NPs surface resulting no noticeable change in fluorescence intensity of the dye molecules. Additionally, there was no significant enhancement of fluorescence recovery efficiency while using the other amino acids of concentration of at least 100 times higher than that of pure L-Cys (Figure not shown). However, only other three essential amino acids namely L-Histidine, L-Methionine and L-Homocysteine showed slightly greater fluorescence recovery efficiency but still very less compared to the L-Cys. The slight difference of the fluorescence recovery efficiency in presence of L-Histidine and L-Methionine as shown in Fig. 7 might be due to the electrostatic interaction of $-NH_2^+$ with the negatively charged Au NPs and very minimal interaction through the less accessible intra-bond S-atom resulting a slight decrease in overall fluorescence quenching via FRET between excited RhB molecules and Au NPs during photo excitation [38]. It is also relevant to mention here that it was unlikely for Au NPs to self-assemble with these two amino acids via covalent combination through S–Au bonds in the same aqueous environment as compared to L-Cys [39]. However, for L-Cys, the thiol moiety (-SH) is the head group and more exposed to aqueous environment causing greater extent of interaction with Au NPs. Although L-Homocysteine is a homologue of the amino acid L-Cys but differing with additional methylene bridge, it still shows almost 1/3 less fluorescence recovery efficiency compared to L-Cys while considering same molar concentrations for both the amino acids during the assay experiments. Additionally, the concentration of L-Homocysteine used was 0.1 mM which is much higher compared to its presence in real blood plasma. So it is excepted that in real biosample it would leave negligible effect in the detection of L-Cys by the proposed method.

In this work it is therefore highly important to study the relative fluorescence recovery efficiency of RhB/Au NPs system when exposed to L-Cys in presence of other interfering essential and non-essential amino acids. This is because of the fact that the physiological plasma medium contains other amino acids as well along with L-Cys. So, the fluorescence recovery efficiency study of RhB/Au NPs mixed aqueous solution was carried out in presence of L-Cys mixed with other amino acids (0.1 mM) and is shown in Fig. 8. The corresponding emission spectra are also shown in Fig. S10. Interestingly it has been observed that the fluorescence recovery efficiency from RhB/Au NPs mixed solution in presence of L-Cys mixed with various other amino acids was nearly equal or close

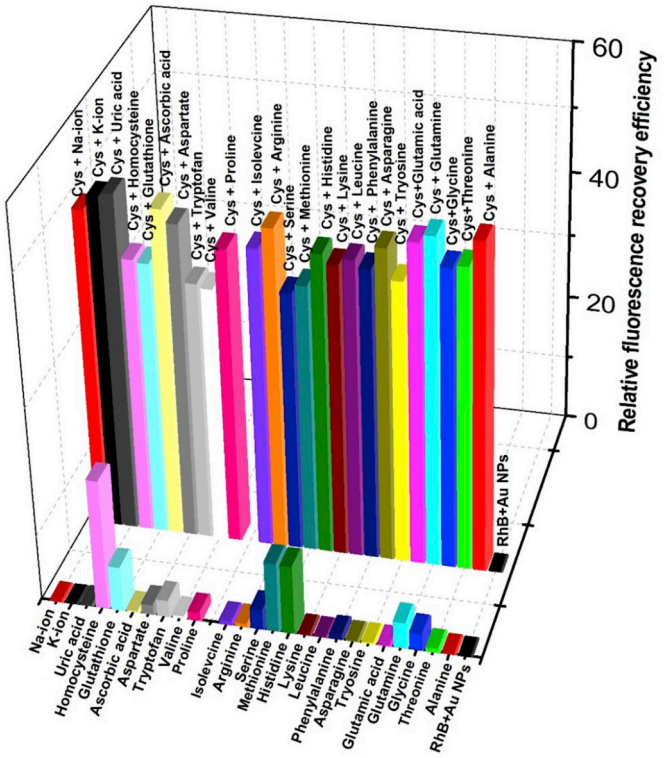

Fig. 8. The plot of relative fluorescence recovery efficiency (at 574 nm) from the assay of RhB/Au NPs when exposed to the aqueous solution of L-Cys (0.1 mM) mixed with other amino acids (0.1 mM), glutathione (0.1 mM), uric acid (0.1 mM), ascorbic acid (0.1 mM) and neurotransmitters (0.1 mM). Figure also represents the relative fluorescence recovery efficiency of the assay when added separately with other amino acids (0.1 mM), glutathione (0.1 mM), uric acid (0.1 mM), ascorbic acid (0.1 mM) and neurotransmitters (0.1 mM).

to that obtained with pure L-Cys only. These results suggest that in the presence of L-Cys, approximately 20-fold enhancement of the fluorescence recovery efficiency was obtained when compared to that in presence of other amino acids without L-Cys in the mixture. From this study it can also be concluded that the presence of more freely assessable –S atoms in L-Cys compared to that in case of all other amino acids, L-Cys binds to Au NPs surface via S–Au bonding competitively and selectively in faster way resulting the displacement of RhB molecules from Au NPs surface. Consequently, the fluorescence quenching due to FRET between RhB and Au NPs was reduced. This is why fluorescence intensity became much higher when L-Cys was present with other amino acids in aqueous medium. Therefore, the proposed technique may be an efficient sensing platform for highly selective determination of amino acid L-Cys in aqueous medium.

3.3.4. *Real bio-sample analysis by using the fluorometric assay*

The proposed fluorescence based sensing mechanism for detection of L-Cys is also tested with real biosample in the present work. The L-Cys may present in both human blood plasma and urine. In our experiments we have used normal urine sample which was provided by our laboratory volunteer research student (male) having no renal complications. These experiments were performed with extra precaution to avoid any type of contamination or direct human contact with the urine sample. It is already known that [40] the excess amount of free L-Cys in urine causes the disease Cystinuria which leads to the formation of L-Cys stones in the renal system. The same assay condition was maintained while doing the real sample analysis. The fluorescence recovery efficiencies were measured from the RhB/Au NPs system in presence of pure human urine, L-Cys and other amino acid mixed urine and are shown in Fig. 9. The corresponding fluorescence emission spectra are shown in

Fig. S11. From Fig. 9 it is observed that, the assay experiment with just pure urine sample shows nearly 35% fluorescence recovery whereas addition of L-Cys (0.1 mM, 200 μL) to the urine shows enhancement of fluorescence recovery efficiency up to 62%. The normal level of L-Cys in human urine is about 0.13 mmol/day [41] and any excess amount of L-Cys in the urine is therefore manifested as several health issues. Therefore, the initial fluorescence recovery with pure urine sample is basically due to usual presence of L-Cys in the urine. However, the increase of fluorescence recovery efficiency after addition L-Cys in the urine is a confirmation of selective detection of L-Cys because presence of all other amino acid did not show any significant rise in fluorescence recovery efficiency as observed from Fig. 9. Thus the present mechanism may be a suitable method for the determination of L-Cys in the human urine sample in order to diagnose the disease Cystinuria.

3.4. Time resolved fluorescence emission spectroscopic study

The time resolved fluorescence emission spectroscopy is a useful and powerful method to know the excited state life time of fluorophore and the nature of quenching whether it is dynamic or static. In this study, the time resolved fluorescence emission of RhB aqueous solution (0.1 μM) was measured by using Time correlated single photon counting (TCSPC) method in absence and presence of Au NPs and L-Cys respectively using an excitation laser source of wavelength of 510 nm and the corresponding fluorescence emission was monitored at 574 nm. The fluorescence decay plots as obtained were fitted by two exponential functions according to eqn. (2) and are shown in Fig. 10. The average lifetimes of the samples were calculated according to eqn. (3) [23] and are summarized in Table 2.

$$I(t) = \alpha_1 e^{-t/\tau_1} + \alpha_2 e^{-t/\tau_2} \quad (2)$$

$$\tau_{av} = \frac{\sum_i \alpha_i \tau_i^2}{\sum_i \alpha_i \tau_i} \quad (3)$$

where α_1, α_2 are the normalized pre-exponential factors of the molecules with lifetime τ_1 and τ_2 respectively. τ_{av} is the average fluorescence life time. The average fluorescence life time of pure RhB was calculated as 1.384 ns [29] but it was decreased to 1.225 ns after the addition of Au NPs (0.1 mM). This decrease in fluorescence lifetime might be related to the reduced excited state energy of RhB molecules due to their adsorption onto Au NPs surface in solution as well as the non-radiative energy transfer from RhB to Au NPs and some extent of dye aggregation. The relationship between the intensity of fluorescence emission and the life time of fluorophore may be given as in eqn. (4) [36].

$$\tau_{obs} = \frac{1}{K_{obs}} = \frac{1}{K_r + K_{nr} + K_{et}} \quad (4)$$

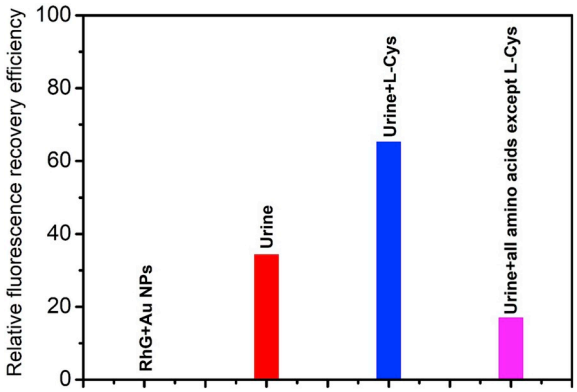

Fig. 9. Real biosample analysis by using the fluorometric assay with pure human urine and amino acids.

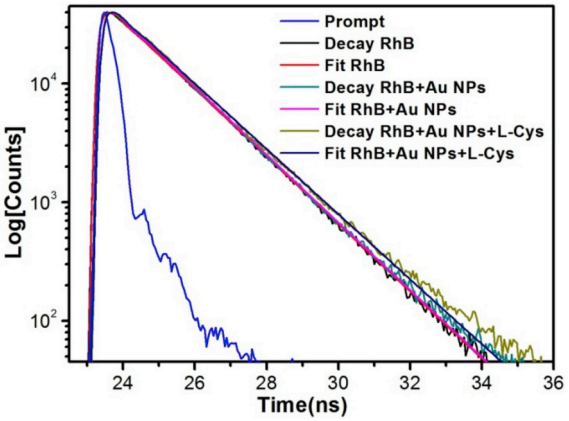

Fig. 10. Fluorescence decay plots of pure RhB aqueous solution and of RhB/Au NPs mixed solution in absence and presence of L-Cys.

That is the observed lifetime τ_{obs} is the inverse of the observed decay rates, radiative decay rate K_r, non-radiative decay rate K_{nr} and the rate of energy transfer K_{et}. For a particular organic dye in specific environment, both the radiative and non-radiative decay rates are normally considered as constant. From the steady state measurement, it was already observed that the decrease in radiative rate of RhB upon adsorption on to Au NPs was only 20% to the overall fluorescence quenching. Thus the rate of energy transfer K_{et} is the major contributor to the decreased fluorescence lifetime of the fluorophore in presence of Au NPs which played the dominant role in fluorescence quenching. However, the most interesting observation was that when L-Cys solution was added to the RhB/Au NPs mixed solution the average fluorescence lifetime of RhB molecules was again enhanced significantly to 1.342 ns which is almost close to that of pure dye molecules. More precisely the reversal of the fluorescence lifetime of RhB after addition of L-Cys is basically attributed to the availability of free RhB molecules in the surrounding aqueous medium of Au NPs/L-Cys conjugated systems. Therefore, this result also supports the fluorescence recovery of RhB molecules from their quenched state in the surface of Au NPs when exposed to L-Cys solution. The very small difference in the average lifetime in this case as compared to that of pure RhB may be due to the different microenvironment of the surrounding medium of dye molecules after addition of L-Cys because the dielectric properties of the medium might have changed [42]. This may slightly affect the decay path of the excited RhB molecules.

4. Conclusion

We have successfully developed a sensing platform for selective and quantitative detection of important bio-thiol namely L-Cys via fluorometric assay of RhB and Au NPs in aqueous medium as well as in real biosample (human urine). The LOD for L-Cys was found to be 0.01 μM in our experimental range of concentration. The initial fluorescence quenching of RhB in presence of Au NPs without L-Cys in the mixture was possibly dominated by FRET mechanism which depends upon the relative distance between dye and nanoparticles. As the decrease in the radiative rate of RhB/Au NPs complex systems contributed only 20% of the overall fluorescence quenching, which also suggests that the excited state energy transfer was dominant factor for the drastic fluorescence quenching. The selective fluorescence response of RhB/Au NPs complex molecular assemblies in presence of L-Cys in the mixture was also accompanied with a color change from wine to bluish-black which was not observed for all other amino acids including other thiol containing compounds, namely L-Methionine, L-Homocysteine, glutathione in the same aqueous environment. Additionally, the other relevant biosamples such as uric acid, ascorbic acid, neurotransmitters have shown negligible interference over the selective determination of L-Cys. However,

Table 2
Fluorescence life time parameters as obtained from the fitted data of pure RhB and RhB/Au NPs mixed solution in absence and presence of L-Cys. Corresponding fluorescence emission was monitored at 574 nm.

Sample name	Number of Exponential	λ_{ex}(nm)	τ_1(ns)	α_1	τ_2(ns)	α_2	τ_{av}(ns)	χ^2
RhB	2	510	0.066	0.375	1.522	0.156	1.384	1.276
RhB/Au NPs	2	510	0.037	1.311	1.517	0.129	1.225	1.156
RhB/Au NPs/L-Cys	2	510	0.048	0.788	1.577	0.132	1.342	1.279

λ_{ex} = Excitation wavelength.

the assay with real biosample shows about 35% fluorescence recovery occurred from the mixture. This is basically due to the usual presence of L-Cys in normal urine. In aqueous solution the thiol moiety in L-Cys formed strong bonding with the citrate caped Au NPs and might have displaced RhB molecules from the surface of Au resulting the aggregation of individual NPs as confirmed by UV–Vis absorption spectroscopy. The TEM study confirmed that our synthesized Au NPs was nearly spherical with average diameter of 27.5 nm. DLS and Zeta potential studies revealed the homogeneity of Au NPs distribution in aqueous solution and did not aggregate prior to their use in the experiments. Fluorescence lifetime of RhB adsorbed onto Au NPs surface was reduced compared to that of pure RhB in aqueous solution as confirmed by TCSPC study. Addition of L-Cys in the mixture restored the fluorescence lifetime of pure RhB resulting the decrease of fluorescence quenching via FRET. Therefore, the present study may be proposed as an efficient sensing platform for selective and highly sensitive detection of L-Cys via fluorometric assay mechanism using Au NPs and RhB.

Acknowledgements

Authors P. Maiti and P. K. Paul are grateful to West Bengal State Council of Science and Technology (WBSCST), Govt. of West Bengal for financial assistance (Project Ref. No. 493/WBSCST/F/0545/15(Pt–I) to perform this work. P. K. Paul also thankful to SERB, DST, Govt. of India for financial assistance through project Ref. No. SB/EMEQ-142/2014. Authors are grateful to CSS of Indian Association for the Cultivation of Science, Kolkata for providing HR TEM facility used in this work. S. A Hussain is also thankful to SERB, DST, Govt. of India for financial support through project Ref. No. EMR/2014/000234.

Appendix A. Supplementary data

Supplementary data to this article can be found online at https://doi.org/10.1016/j.matchemphys.2019.06.001.

References

[1] E.G. Schulz, H.R. Schirmer, Principles of Protein Structure, first ed., Springer, New York, 1978.
[2] W. Wang, O. Rusin, X. Xu, K.K. Kim, O.J. Escobedo, O.S. Fakayode, A.K. Fletcher, M. Lowry, M.C. Schowalter, M.C. Lawrence, R.F. Fronczek, M.I. Warner, M. R. Strongin, Detection of homocysteine and cysteine, J. Am. Chem. Soc. 127 (2005) 15949–15958.
[3] K.J. Nicholson, J. Connelly, C.J. Lindon, E. Holmes, Metabonomics: a platform for studying drug toxicity and gene function, Nat. Rev. Drug Discov. 1 (2002) 153–161.
[4] K.R. Atkuri, J.J. Mantovani, L.A. Herzenberg, L.A. Herzenberg, N-Acetylcysteine-a safe antidote for cysteine/glutathione deficiency, Curr. Opin. Pharmacol. 7 (2007) 355–359.
[5] S.K. Biswas, I. Rahman, Environmental toxicity, redox signaling and lung inflammation: the role of glutathione, Mol. Asp. Med. 30 (1–2) (2009) 60–76.
[6] R.V. Kondratov, O. Vykhovanets, A.A. Kondratova, M.P. Antoch, Antioxidant N-acetyl-l-cysteine ameliorates symptoms of premature aging associated with the deficiency of the circadian protein BMAL1, Aging 1 (12) (2009) 979–987.
[7] V.I. Lushchak, Glutathione homeostasis and functions: potential targets for medical interventions, J. Amino Acids 2012 (2011) 1–26.
[8] World Health Organization, Food and Agriculture Organization of the United Nations, United Nations University, Protein and Amino Acid Requirements in Human Nutrition, WHO, 2002. http://www.who.int/iris/handle/10665/43411.
[9] R. Janáky, V. Varga, A. Hermann, P. Saransaari, S.S. Oja, Mechanisms of L-cysteine neurotoxicity, Neurochem. Res. 25 (9–10) (2000) 1397–1405.
[10] J.D. Rimer, Z. An, Z. Zhu, M.H. Lee, D.S. Goldfarb, J.A. Wesson, M.D. Ward, Crystal growth inhibitors for the prevention of l-cystine kidney stones through molecular design, Science 330 (6002) (2010) 337–341.
[11] B. Halliwel, Reactive Oxygen species in living systems: source, biochemistry, and role in human disease, Am. J. Med. 91 (1991) 14–22.
[12] J.T. Jarrett, The biosynthesis of thiol- and thioether-containing cofactors and secondary metabolites catalyzed by radicals-adenosylmethionine enzymes, J. Biol. Chem. 290 (2015) 3972–3979.
[13] E. Mukwevho, Z. Ferreira, A. Ayeleso, Potential role of sulfur-containing antioxidant systems in highly oxidative environments, Molecules 19 (2014) 19376–19389.
[14] R. Glowacki, J. Stachniuk, K. Borowczyk, A simple HPLC-UV method for simultaneous determination of cysteine and cysteinylglycine in biological fluids, Acta Chromatogr. 28 (2016) 333–346.
[15] M. Bouri, R. Salghi, A. Rios, M. Zougagh, Fluorescence determination of L-cysteine in wound dressings by fluoroscein coated gold nanoparticles, Anal. Lett. 49 (2016) 1221–1232.
[16] Z. Huang, Y. Yang, Y. Long, H. Zheng, A colorimetric method for cysteine determination based on the peroxidase-like activity of ficin, Anal. Methods 10 (2018) 2676–2680.
[17] G. Ziyatdinova, E. Kozlova, H. Budnikov, Selective electrochemical sensor based on the electropolymerized pcoumaric acid for the direct determination of L-cysteine, Electrochim. Acta 270 (2018) 369–377.
[18] L. Chang, T. Wu, F. Chen, Determination of L-cysteine base on the reversion of fluorescence quenching of calcein by copper(II) ion, Microchim Acta 177 (2012) 295–300.
[19] A.A. Ensafi, B. Rezaei, S. Nouroozi, Flow injection spectrofluorometric determination of cystine and cysteine, J. Braz. Chem. Soc. 20 (2009) 288–293.
[20] N. Narband, M. Uppal, C.W. Dunnill, G. Hyett, M. Wilson, I.P. Parkin, The interaction between gold nanoparticles and cationic and anionic dyes: enhanced uv-visible absorption, Phys. Chem. Chem. Phys. 11 (2009) 10513–10518.
[21] N. Kometani, M. Tsubonishi, T. Fujita, K. Asami, Y. Yonezawa, Preparation and optical absorption spectra of dye-coated Au, Ag, and Au/Ag colloidal nanoparticles in aqueous solutions and in alternate assemblies, Langmuir 17 (2001) 578–580.
[22] M.C. Daniel, D. Astruc, Gold nanoparticles: assembly, supramolecular chemistry, quantum-size-related properties, and applications toward biology, catalysis, and nanotechnology, Chem. Rev. 104 (2004) 293–346.
[23] J.R. Lakowicz, Principles of Fluorescence Spectroscopy, third ed., Plenum Press, New York, 1983.
[24] D. Gust, T.A. Moore, A.L. Moore, Molecular mimicry of photosynthetic energy and electron transfer, Acc. Chem. Res. 26 (1993) 198–205.
[25] F. Tam, G.P. Goodrich, B.R. Johnson, N.J. Halas, Plasmonic enhancement of molecular fluorescence, Nano Lett. 7 (2007) 496–501.
[26] P.C. Ray, Size and shape dependent second order nonlinear optical properties of nanomaterials and their application in biological and chemical sensing, Chem. Rev. 110 (9) (2010) 5332–5365.
[27] R.A. Sperling, W.J. Parak, Surface modification, functionalization and bioconjugation of colloidal inorganic nanoparticles, Philos. Trans. Royal Soc. A 368 (2010) 1333–1383.
[28] T. Karstens, K. Kobs, Rhodamine B and rhodamine 101 as reference substances for fluorescence quantum yield measurements, J. Phys. Chem. 84 (14) (1980) 1871–1872.
[29] N.K.M.N. Srinivas, S.V. Rao, D.N. Rao, Saturable and reverse saturable absorption of rhodamine b in methanol and water, J. Opt. Soc. Am. B 20 (12) (2003) 2470–2479.
[30] G. Frens, Controlled nucleation for the regulation of the particle size in monodisperse gold suspensions, Nat. Phys. 241 (1973) 20–22.
[31] X.C. Ma, Y. Dai, L. Yu, B.B. Huang, Energy transfer in plasmonic photocatalytic composites, Light Sci. Appl. 5 (2016) 16017–16029.
[32] S.D. Roy, M. Ghosh, J. Chowdhury, Adsorptive parameters and influence of hot geometries on the SER(R)S spectra of methylene blue molecules adsorbed on gold nanocolloidal particles, J. Raman Spectrosc. 46 (2015) 451–461.
[33] N.R. Jana, L. Gearheart, C.J. Murphy, Seeding growth for size control of 5-40 nm diameter gold nanoparticles, Langmuir 17 (2001) 6782–6786.
[34] W. Zhao, M.A. Brook, Y. Li, Design of gold nanoparticle-based colorimetric biosensing assays, Chembiochem 9 (2008) 2363–2371.
[35] F. Chai, C. Wang, T. Wang, Z. Ma, Z. Su, L-cysteine functionalized gold nanoparticles for the colorimetric detection of hg^{2+} induced by ultraviolet light, Nanotechnology 21 (2010) 25501–25506.
[36] A. Mocanu, I. Cernica, G. Tomoaia, L.D. Bobos, O. Horovitz, M.T. Cotisel, Self-assembly characteristics of gold nanoparticles in the presence of cysteine, Colloid. Surf. Physicochem. Eng. Asp. 338 (2009) 93–101.

[37] J.W. Olney, C. Zorumski, M.T. Price, J. Labruyere, L-cysteine, a bicarbonate sensitive endogenous excitotoxin, Science 248 (1990) 596–599.
[38] R. Cao, B. Li, A simple and sensitive method for visual detection of heparin using positively-charged gold nanoparticles as colorimetric probes, Chem. Commun. 47 (2011) 2865–2867.
[39] M. Bahram, E. Mohammadzadeh, Green synthesis of gold nanoparticles with willow tree bark extract: a sensitive colourimetric sensor for cysteine detection, Anal. Methods 6 (2014) 6916–6924.
[40] E. Kaniowska, G. Chwatko, R. Głowacki, P. Kubalczyk, E. Bald, Urinary excretion measurement of cysteine and homocysteine in the form of their S-pyridinium derivatives by high-performance liquid chromatography with ultraviolet detection, J. Chromatogr. A 798 (1998) 27–35.
[41] C.S. Biyani, J.J. Cartledge, Cystinuria-diagnosis and management, EAU-EBU Update Ser. 4 (2006) 175–183.
[42] H. Chen, S.S. Ahsan, M.E.B.S. Berrios, H.D. Abrun, W.W. Webb, Mechanisms of quenching of alexa fluorophores by natural amino acids, J. Am. Chem. Soc. 132 (2010) 7244–7245.

ACS OMEGA

http://pubs.acs.org/journal/acsodf

Article

Comparative and Selective Interaction of Amino Acid D-Cysteine with Colloidal Gold Nanoparticles in the Presence of a Fluorescent Probe in Aqueous Medium

Pradip Maiti, Ujjal Saren, Utsav Chakraborty, Tanmoy Singha, Sharmistha Paul, and Pabitra Kumar Paul*

Cite This: *ACS Omega* 2022, 7, 29013−29026

Read Online

ACCESS | Metrics & More | Article Recommendations | Supporting Information

ABSTRACT: In this communication, we report the comparative and selective interaction of amino acid D-cysteine (D-Cys) with citrate caped gold nanoparticles (Au NPs) in the presence of a fluorescent dye, rhodamine B (RhB), in aqueous solution. Au NPs of size 27.5 nm could almost fully quench the steady-state fluorescence emission of RhB at their optimum concentrations in the mixed solution. The interactions of D-Cys, L-Cys, all other relevant D- and L-amino acids, neurotransmitters, and other relevant biological compounds with the Au NPs/RhB mixed solution have been explored by monitoring the fluorescence recovery efficiencies from the almost fully quenched state of RhB fluorescence via a simple steady-state spectrofluorometric method. The higher fluorescence recovery for the interaction of D-Cys with the Au NPs/RhB mixed system is accompanied by a distinct color change (red-wine to bluish-black) of the assay medium after the reaction compared to that of all other interfering compounds considered in this work. The sensitivity of this fluorometric response lies in a broad linear range of concentrations of D-Cys and the limit of detection (LOD) is found to be 4.2 nM, which is low compared to many other methods available in the literature. The different degrees of interaction of D-Cys and L-Cys with the Au NPs/RhB mixed sample have been further explored by circular dichroism (CD) spectroscopy and Fourier transform infrared (FTIR) spectroscopy. The selective interaction of D-Cys with the proposed Au NPs/RhB mixed system is also found to be correlated with interparticle cross-linking and aggregations of nanoparticles by the analysis of ζ potential and dynamic light scattering (DLS) study, transmission electron microscopy (TEM), atomic force microscopy (AFM), UV−vis absorption spectroscopy etc. The proposed interaction mechanism is further studied with a normal human urine sample to elucidate that the optimized combination of Au NPs and RhB may be realized as an efficient platform for detection of the amino acid D-Cys in a real biosample via a simple fluorometric approach.

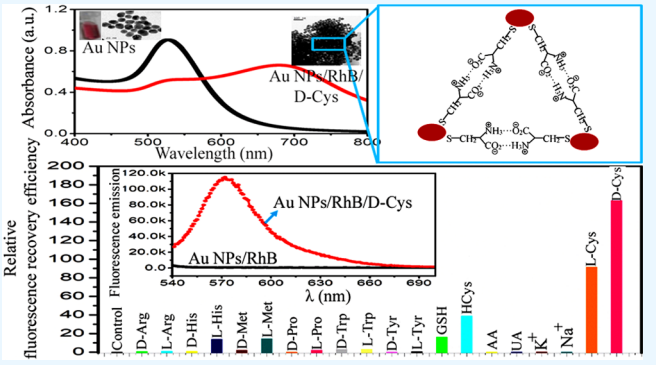

1. INTRODUCTION

The fundamental part of antibodies, signaling molecules, enzymes, hormones, receptors, and protein structures present in all living organisms is amino acids. They also act as biochemical rulers in the neurotransmission.[1,2] All of the amino acids present in the nature exist mainly in two forms: dextrorotatory (D) and levorotatory (L) enantiomers. On the basis of the protein-creating efficiency, there are in total 20 amino acids that have been reported. Previously, it was presumed that only L-amino acids were necessary in mammals, including humans, in the formation of components for proteins and peptides. However, various sensitive and selective analytical approaches developed for detecting chiral amino acids[3,4] suggested that diverse D-amino acids are also present in mammalian tissues. Different studies have been performed to explore the physiological functions of D-amino acids. The physiological and the biochemical activities of different D-amino acids such as D-cysteine (D-Cys), D-aspartate (D-Asp), D-alanine (D-Alan), D-serine (D-Ser) etc. in our nerve cells, skin, arterial walls, bones, other tissues, and body fluids, including amniotic fluid, urine, blood plasma, cerebrospinal fluid (CSF), saliva etc., have been systematically studied by various researchers in the last several years.[5,6]

The semi-essential, proteinogenic amino acid cysteine ($C_3H_7NO_2S$) (abbreviated as Cys) contains thiol (−SH), amine ($-NH_2$), and carboxylic (−COOH) functional groups.

Received: May 2, 2022
Accepted: August 1, 2022
Published: August 12, 2022

The −SH moiety mainly takes part in the nucleophilic enzymatic reactions.[7] Also, the −SH group plays an important structural role in the formation of many proteins by creating the disulfide derivative of Cys.[8] D-Cys creates hydrogen sulfide (H_2S) and decreases the disulfide bonds present in the receptors.[8] This may act synergistically and increase the responsiveness of neurotransmitters specifically to a particular activity. The deviant activity of receptors causes diseases in the central nervous system (CNS) such as amyotrophic lateral sclerosis, Alzheimer's disease, schizophrenia etc.[9,10] In the endocrine gland, H_2S prevents discharge of insulin due to glucose generation by the pernicious β cells.[11] Tong et al. showed that the biofilm formation of *Streptococcus mutans* and *Streptococcus sanguinis* on the surface of teeth could be controlled by free D-Cys.[12]

In recent times, the study of the interactions of various proteins and amino acids with nanoparticles (NPs) has attracted great attention in the field of nano-biotechnology.[13] Among the various amino acids, D-Cys is also responsible for the growth of various diseases and disorders in the human body. Thus, the selective and quantitative recognition of D-Cys is very important for the diagnosis and treatments of various diseases. D-Cys can interact and be functionalized with several interesting metal nanoparticles (NPs)[13,14] because NPs possess significant adsorption capabilities due to their large surface area to volume ratio.[15] Sometimes this type of biomolecules can bind with such NPs via selective covalent interactions.[16] Among the various metal-based NPs,[17,18] noble metal NPs such as gold nanoparticles (Au NPs) show significant prospects regarding their potential in various fields of biomedical applications such as drug delivery,[19] biomolecular sensing[20−22] etc. The high extinction coefficient of Au NPs in the visible region renders them as an efficient platform for signaling molecular recognition processes through their color change.[21] The small sizes of these metal NPs with a large surface curvature facilitate their binding with various organic dyes, proteins[16,18] etc. The degree of structural perturbation of the protein molecules due to their interaction with NPs varies for different protein species.[23] As the amino acids are the basic structural units of protein molecules, the study of the interaction of amino acids with Au NPs via a simple spectrofluorometric technique is of particular importance. The −SH-containing amino acid D-Cys is recognized as an important regulator of neurotransmitters and the overall neural cell dynamics in our physiological system. Therefore, a comparative study of the interaction of various forms of Cys and their chiral discrimination while interacting with Au NPs is important for both fundamental and biomedical interests.

In the present study, we have addressed the interaction or reactivities of D-Cys and L-Cys as well as all other relevant amino acids, neurotransmitters etc. with citrate caped Au NPs in the presence of a fluorescent probe, namely rhodamine B (RhB), in aqueous medium. RhB is a cationic organic dye with a high fluorescence quantum yield and has been used as an interesting signaling agent for various biomolecular recognition events.[24,25] The fluorescence emission of the RhB dye is almost fully quenched by the colloidal solution of Au NPs and the mechanism of the quenching has been described in detail in this work. The fully quenched fluorescence emission of this dye due to Au NPs in the aqueous solution is recovered via selective interaction with the amino acid D-Cys through SH−Au bond formation and aggregation of Au NPs. This interaction is also reflected as a distinct color change of the assay medium from red-wine to bluish-black, which is different from the interaction with L-Cys or any other interfering compounds studied in this work. The ratio-metric determination of the fluorescence recovery efficiency[26,27] in the presence of various analytes in the assay medium automatically eliminates the perturbation from any external influences during the assay. However, there are few recent reports on the detection of D-Cys based on various methods such as SRM-chromatography, colorimetric, ultra-high-performance liquid chromatography (UHPLC)-URMS-chromatography, electrokinetic chromatography etc.[28−32] However, the proposed fluorometric method, which is free from any direct leveling, offers great advantages for the detection of D-Cys, especially up to the nanomolar level. The aggregations of the Au NPs/RhB system in the presence of both the −SH-containing amino acids, D- and L-Cys, have been visualized by transmission electron microscopy (TEM) and atomic force microscopic (AFM) studies and are correlated with the observed Fourier transform infrared (FTIR), UV−vis absorption, and steady-state fluorescence spectroscopic results. The different extents of interaction of D-Cys and L-Cys with the proposed Au NPs/RhB mixed system in aqueous medium are also distinguished by the chiral properties using the circular dichroism (CD) spectroscopic technique. Au NPs and the RhB-based fluorescence turn-on sensing platform are also tested with normal human (male) urine as a real biosample to realize the same selective response of the D-Cys present in urine.

2. EXPERIMENTAL SECTION

2.1. Materials. All of the chemicals used in this work were of analytical grade and were used as obtained without further purification. Gold(III) chloride acid trihydrate ($HAuCl_4 \cdot 3H_2O$, MW: 393.83 g mol^{-1}), RhB ($C_{28}H_{31}ClN_2O_3$, MW: 479.02 g mol^{-1}), D-Cys ($C_3H_7NO_2S$, MW: 121.15 g mol^{-1}), and other D- and L-amino acids, ascorbic acid (AA) ($C_6H_8O_6$, MW: 176.12 g mol^{-1}), uric acid (UA) ($C_5H_4N_4O_3$, MW: 168.11 g mol^{-1}), glutathione (GSH) ($C_{10}H_{17}N_3O_6S$, MW: 307.33 g mol^{-1}), and homocysteine ($C_4H_9NO_2S$, MW: 138.18 g mol^{-1}) (Hcys), were purchased from Sigma-Aldrich Chemical Company. Trisodium citrate ($Na_3C_6H_5O_7$, MW: 258.06 g mol^{-1}), sodium chloride (NaCl, MW: 58.44 g mol^{-1}), and potassium chloride (KCl, MW: 74.5513 g mol^{-1}) were purchased from Merck Chemical Company, Germany. All of the glasswares were cleaned with freshly prepared aqua regia (mixture of HCl and HNO_3 in 3:1 ratio) followed by subsequent rinsing with triple distilled deionized Milli-Q water (resistivity 18.2 MΩ cm, pH ∼ 7 at 25 °C, collected from Synergy integrated with an Elix Advantage setup; make: Millipore SAS, France) and then were autoclaved for 24 h before use. Aqueous solutions of the samples were also prepared with the same triple distilled deionized Milli-Q water.

2.2. Synthesis of Au NPs. The well-documented Frens' soft chemical reduction method has been used to obtain monodispersed gold nanocolloids with the desired particle size distribution.[21,33] In brief, an aliquot of a 50 mL aqueous solution of $HAuCl_4 \cdot 3H_2O$ (0.25 M) was heated to boil and 1.2 mL of $Na_3C_6H_5O_7$ (1%) was added into the solution under vigorous stirring for the formation of gold nanocolloids. In about 100 s, the boiling solution turned faintly blue. After 120 s, the blue color changed to deep red, which indicates the formation of the spherical Au NPs. The synthesized nanocolloidal solution was set aside to cool down to room temperature and stored at 4 °C for future use. The final

https://doi.org/10.1021/acsomega.2c02725
ACS Omega 2022, 7, 29013−29026

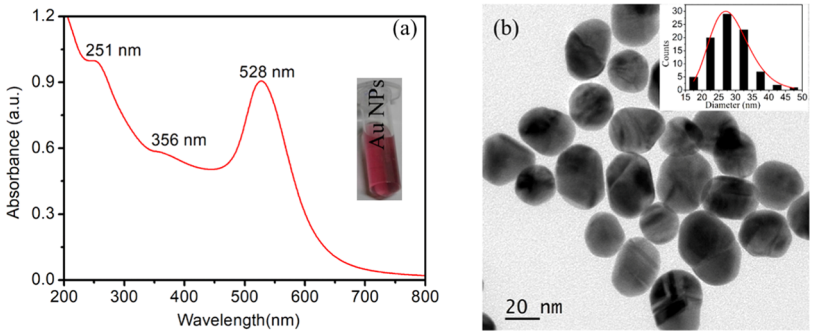

Figure 1. (a) UV−vis absorption spectrum of Au NPs' colloidal dispersion (0.1 mM) and (b) TEM micrograph of the as-synthesized Au NPs. The insets of (a) and (b) show the digital micrographs of the vial containing as-synthesized Au NPs' dispersion and lognormal fitting of the NPs' size distribution curve, respectively.

concentration of the aqueous gold nanocolloidal solution was 0.1 mM at pH ∼ 7 in ambient temperature.

2.3. Characterization Techniques. High-resolution transmission electron microscopy (HRTEM) measurements, energy-dispersive spectroscopy (EDS) images, and selected area electron diffraction (SAED) patterns of the Au NPs were collected using a field emission transmission electron microscope (JEM-2010 TEM, JEOL Ltd., Japan) operated at an accelerating voltage of 200 kV. For the HRTEM study, the sample solutions were incubated for 15 min and then a small drop from each solution was spread onto the carbon-coated copper microgrid (PELCO 300 Mesh Grids, Ted Pella Inc.) and subsequently dried at room temperature (25 °C). The hydrodynamic nanoparticle size and the effective surface ζ potential of the as-synthesized Au NPs were obtained by a Zetasizer (Zetasizer Nano ZS, Malvern Instruments Ltd., U.K.) via the dynamic light scattering (DLS) method at ambient condition. The UV−vis absorption spectra of the samples were obtained in the wavelength range of 200−800 nm by a double-beam UV−vis absorption spectrophotometer (UV-1800, Shimadzu, Japan) after proper baseline correction for the solvent background. The steady-state fluorescence emission spectra of the sample solutions were recorded using a spectrofluorometer (Fluoromax-4C, Horiba Instruments Incorporated, USA) under the following conditions: excitation and emission monochromator slit widths of 2 nm each, excitation wavelength of 530 nm, emission wavelength range of 540−700 nm, and experimental temperature of 25 °C. Fluorescence-grade quartz cuvettes (path length 1.0 cm, Kozima, Japan) were used in all of the absorption and fluorescence emission measurements. CD spectroscopic measurements were carried out using a JASCO J-815 CD spectrometer (JASCO International Co., Ltd., Japan). The surface morphology and roughness measurement of the samples were performed using a commercially available atomic force microscope (AFM) (NaioAFM, Nanosurf, Germany) in tapping mode in a humidity-controlled environment. For AFM analysis, the freshly prepared Au NPs aqueous colloidal dispersion and a mixture of Au NPs/RhB in the presence of D-Cys and L-Cys, respectively, were deposited onto smooth glass substrates. FTIR spectra of the samples were recorded using a FTIR spectrometer (model: Spectrum Two, make: Perkin Elmer Inc.) in attenuated total reflection (ATR) mode at ambient temperature. The pH of the aqueous solutions was measured using a digital pH meter (FiveEasy Plus, Mettler Toledo, Germany).

2.4. Sample Preparation for the Spectrofluorometric Measurements. The Au NPs/RhB mixed solution was prepared by adding 2 mL of freshly prepared Au NPs of concentration 0.1 mM into 2 mL of freshly prepared RhB of concentration 0.1 μM at ambient condition. Thus, the final concentrations of the Au NPs and RhB in the total 4 mL mixed solution were 0.05 mM and 0.05 μM, respectively. The pH of the RhB aqueous solution was 7.0 and remained approximately constant through the whole analysis. Then, a freshly prepared 200 μL aqueous solution of each concentration of D-Cys (concentration range from 1000 μM to 1 nM) was added to the Au NPs/RhB mixed ensemble separately and incubated for 3 min at room temperature (25 °C). Also, the D-Cys aqueous solution was prepared by using ultrapure triple distilled Milli-Q water at pH 7.0. The final concentrations of D-Cys in all of the Au NPs/RhB/D-Cys mixed solutions were in the range 0.0476 nM to 47.6 μM. After the incubation period of 3 min, colorimetric images, the UV−vis absorption, and steady-state fluorescence emission spectra of the Au NPs/RhB/D-Cys complex were recorded immediately. Also, aqueous solutions (fixed concentration of 0.1 mM) of other relevant D- and L-amino acids such as D-arginine (D-Arg), L-arginine (L-Arg), D-histidine (D-His), L-histidine (L-His), D-methionine (D-Met), L-methionine (L-Met), D-proline (D-Pro), L-proline (L-Pro), D-tryptophan (D-Trp), L-tryptophan (L-Trp), D-tyosine (D-Tyr), L-tyosine (L-Tyr), L-cysteine (L-Cys), and other −SH-containing compounds like glutathione (GSH) and homocysteine (Hcys) as well as some different biomolecules such as ascorbic acid (AA), uric acid (UA), and neurotransmitters (Na^+ and K^+) were prepared in the same ambient condition. A 200 μL aqueous solution of each compound was added separately to the Au NPs/RhB mixed solution and incubated for 5 min at ambient condition prior to the spectrofluorometric measurements. The 5 min incubation time used for other analytes except D-Cys was just to confirm whether these other compounds have any effect on the proposed interaction even after a longer time of incubation compared to that of D-Cys.

3. RESULTS AND DISCUSSION

3.1. Characterization of the Au NPs. The UV−vis absorption spectroscopic data were recorded to explore the optical absorption properties of the as-synthesized citrate-stabilized colloidal aqueous dispersion of Au NPs and are shown in Figure 1a. The figure shows a distinct absorption band with its maximum at around 528 nm due to the strong characteristic surface plasmon resonance (SPR) of the Au NPs. Also, there are two weak humps observed at 251 and 356 nm,

https://doi.org/10.1021/acsomega.2c02725
ACS Omega 2022, 7, 29013−29026

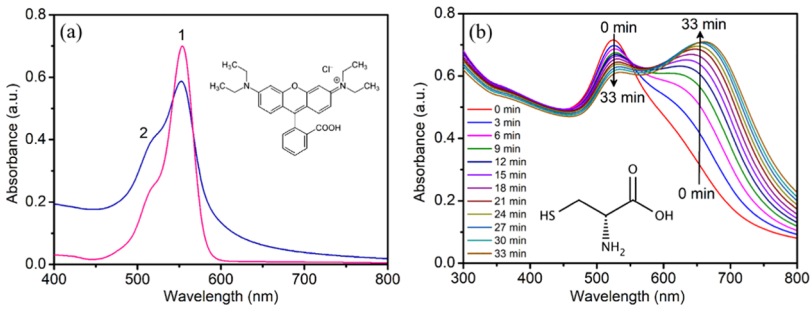

Figure 2. UV−vis absorption spectra of (a) pure RhB aqueous solution (0.1 μM) (curve 1), Au NPs/RhB mixed solution (the concentrations of Au NPs and RhB are 0.05 mM and 0.05 μM in the mixed solution, respectively) (curve 2) and (b) mixed solution of Au NPs and D-Cys (the concentrations of Au NPs and D-Cys are 0.09 mM and 6.25 μM in the mixed solution, respectively) recorded at different intervals of time. The insets of (a) and (b) show the molecular structure of RhB and D-Cys, respectively.

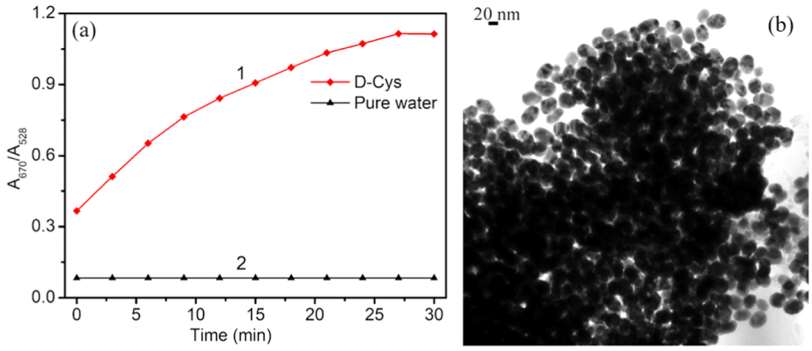

Figure 3. (a) Ratio of the absorbance at 670−528 nm of Au NPs after addition of D-Cys (curve 1) and pure water (200 μL) (curve 2). (b) TEM micrograph of as-synthesized Au NPs after incubation with D-Cys for 15 min at room temperature.

which are mainly attributed to the intraband electronic transitions of gold.[34] The sharp and well-resolved SPR maximum band is originated basically due to both the longitudinal and transverse SPR equivalently, which is an indication of the formation of spherical Au NPs.[35]

The average hydrodynamic diameter of the colloidal Au NPs as obtained from the DLS study was about 48.04 nm (as shown in Figure S1a in the Supporting Information). The surface ζ potential of the Au NPs was found to be −30.1 mV (as shown in Figure S1b in the Supporting Information). The high negative ζ potential reveals the homogeneity and stability of the NPs in the aqueous colloidal dispersion. On the other hand, the TEM micrograph as shown in Figure 1b gives the visual evidence that Au NPs were monodispersed with nearly spherical shape and the average particle diameter was ∼27.5 nm, as is evidenced from the lognormal fitting of the particles' size distribution curve (the inset of Figure 1b obtained from Figure S2a in the Supporting Information). The good crystalline nature of the Au NPs was shown by the SAED pattern (as shown in Figure S2b in the Supporting Information). The rings as shown in SAED were indexed as (311), (222), and (400) and correspond to the electron diffractions originated from the planes of the face-centered cubic (FCC) gold crystal.[36] The interplanar spacing of the as-synthesized FCC Au NPs was 0.11 nm for the (222) plane as calculated from the HRTEM micrograph (as shown in Figure S2c in the Supporting Information). The EDS spectrum (as shown in Figure S2d in the Supporting Information) reveals that the nucleation of Au NPs occurred without any impurities and confirms the presence of a large number of NPs in its aqueous colloidal dispersion.

3.2. UV−Vis Absorption Spectroscopic Study.

The UV−vis absorption spectroscopic measurements were carried out by adding D-Cys and other D- and L-amino acids, neurotransmitters, AA, UA, including other −SH-containing compounds such as Met, HCys, GSH etc., to the mixed solution of Au NPs and RhB (aqueous mixture of Au NPs (0.1 mM) and RhB (0.1 μM) in 1:1 volume ratio). Figure 2a shows the UV−vis absorption spectra of pure RhB (0.1 μM) (curve 1) along with the mixture of RhB and Au NPs in aqueous solution (curve 2). The concentrations of Au NPs and RhB in the mixed solution were 0.05 mM and 0.05 μM, respectively. The inset of Figure 2a shows the molecular structure of the laser dye RhB. The UV−vis absorption spectrum of pure RhB exhibits a strong absorption band at around 554 nm, which is attributed to the $\pi-\pi^*$ transition of the dye monomer unit, and a weak hump is observed at around 520 nm, which is originated from the n−π^* transition due to the presence of dimeric units.[24] The UV−vis absorption results of the mixed solution further reveal that the monomeric absorption peak of RhB remains unaltered but with decreased intensity, whereas the dimeric band intensity (520 nm) increases. This variation of the absorption intensity may possibly be due to the closure association of the RhB molecules adsorbed onto the NPs' surface. As RhB is a cationic dye and citrate caped Au NPs have a large negative surface ζ potential, the strong electrostatic interaction between Au NPs and RhB is mainly responsible for the adsorption of the dye molecules on the NPs' surface, resulting in the change in the absorption behavior of the dye molecules in their aqueous mixed solution. The number of dye molecules (N_{dye}) linked with each Au NP is determined using the relation[37] (eq 1)

https://doi.org/10.1021/acsomega.2c02725
ACS Omega 2022, 7, 29013−29026

$$N_{dye} = \frac{n_{Au}}{\{[\text{Au NPs}]/[\text{RhB}]\}} \quad (1)$$

where n_{Au} is the number of gold atoms in each NP. The number of gold atoms per NP (n_{Au}) is calculated by using the expression[37,38] $n_{Au} = (\pi/6)(59\ \text{nm}^{-3})(d_{av})3$, where d_{av} is the mean diameter of the Au NPs. Thus, in this case, an Au NP of average diameter 27.5 nm is composed of 642 138 gold atoms. In the mixed solution of Au NPs (0.1 mM) and RhB (0.1 μM), 642 dye molecules are adsorbed on each Au NP surface.

On the other hand, the UV−vis absorption spectrum of RhB in the presence of D-Cys as shown in Figure S3a in the Supporting Information reveals that there is no appreciable effect of D-Cys on the absorption behavior of RhB in the mixed solution of RhB and D-Cys. The concentration of RhB was kept fixed for all of these mixed solutions, which were prepared using RhB and the Au NPs solution in 1:1 volume ratio. The UV−vis absorption spectra of the Au NPs (concentration of 0.1 mM) recorded at different intervals of time after addition of the aqueous solution of D-Cys (concentration of 0.1 mM) are shown in Figure 2b. The respective concentrations of Au NPs and D-Cys in the mixed solution were 0.09 mM and 6.25 μM. The inset of Figure 2b shows the molecular structure of D-Cys. The additional band of Au NPs observed at around 670 nm is originated due to the strong interaction of D-Cys with the citrate caped Au NPs in the mixed aqueous solution. The absorbance of the main SPR band at around 528 nm gradually decreases and the new band at 670 nm systematically increases with the incubation time for the mixed solution. The absorbance ratio (A_{670}/A_{528}) of the Au NPs colloidal dispersion, as shown in Figure 3a, increases with the incubation time in the presence of D-Cys. This is possibly due to the strong cooperative metal ion-ligand interactions.[39] Because of this interaction, the citrate layer on the nanoparticles' surface may be displaced and the interparticle separations of the NPs are possibly reduced due to the subsequent cross-linking through the amino groups of D-Cys. As a consequence, the increased dipole−dipole interactions and the coupling between neighboring plasmons eventually induced the formation of aggregates or clusters[39,40] of Au NPs. This aggregation is manifested as the emergence of the additional band at around 670 nm in the UV−vis absorption spectra.[41,42] In order to have direct visual evidence for the formation of aggregates or clusters of NPs, TEM analysis was also performed. Figure 3b shows the TEM image of the Au NPs/RhB/D-Cys mixed sample and clearly shows very dense and aggregated domains of the NPs when compared to the TEM image of pure Au NPs as shown in Figure 1b. This aggregation eventually induces enhanced dye−dye intermolecular interaction in the mixed solution of Au NPs and RhB. As a result, the RhB molecules might have altered electric transition dipole moments in the microenvironment of Au NPs.[43]

3.3. Interaction of D-Cys with the Au NPs/RhB Mixed Solution. To understand the interaction of D-Cys with the Au NPs/RhB mixed ensemble in aqueous medium and the related photophysical properties, steady-state fluorescence emission measurements were performed. It is observed from Figure S3c in the Supporting Information that the steady-state fluorescence emission intensity of the peak at around 574 nm of RhB in the Au NPs/RhB mixed aqueous solution (1:1 volume ratio) is almost quenched for an Au NP concentration of 0.05 mM in the mixed solution at ambient condition. It is important to mention that the electrostatic interaction between the dye molecules and the negatively charged citrate layer on the Au NPs or any formation of H bonds does not change the electronic transition dipole moment of the xanthene moiety of the RhB molecules[44] as there is no shift of the emission band (574 nm) of dye molecules after photoexcitation of the Au NPs/RhB mixed ensemble in the absence or presence of D-Cys. Therefore, the effect of direct molecule on nanoparticle interaction may be excluded from the initial fluorescence quenching of RhB molecules in the presence of Au NPs. Additionally, the possibility of dynamic collisional quenching of fluorescence may be less due to the existence of a strong electrostatic interaction between the RhB molecules and negatively charged citrate caped Au NPs in the studied aqueous medium. Interestingly, there is a sufficient spectral overlap between the absorption spectrum of Au NPs and fluorescence emission spectrum of RhB as shown in Figure S3b in the Supporting Information. So, the observed quenching of fluorescence emission (574 nm band) of RhB in the Au NPs/RhB mixed solution is mostly due to the efficient nonradiative energy migration through the resonance energy transfer (RET) process (as shown in Figure S3b,c in the Supporting Information) using the dipole−dipole resonance interaction between the excited RhB dye (donor) molecules and Au NP surface (acceptor), as well as the decrease in the radiative rate constant of individual RhB molecules when they are adsorbed onto the NPs' surface.[21,43] This resonance energy transfer process is a distance-dependent phenomenon and therefore the concentration of the Au NPs (acceptor) plays a significant role in controlling the relative distance between the donor and acceptor sites in the mixed solution. The RET efficiency (E) is calculated using the expression[44,45] (eq 2)

$$E = 1 - \frac{F}{F_0} \quad (2)$$

where F_0 and F are the fluorescence emission intensity of RhB in the absence and presence of Au NPs, respectively. The value of energy transfer efficiency (E) is estimated as 0.9989, considering the fluorescence spectrum of Au NPs/RhB with concentrations of RhB and Au NPs as 0.05 μM and 0.05 mM in the mixed solution, respectively. The value of the binding constant (K_b) to a binding site and the number of binding sites (n) per RhB molecule in the Au NPs/RhB mixed aqueous solution are determined from the fluorescence quenching data of RhB in the presence of Au NPs by using the following eq 3[46]

$$\text{Log}\left\{\frac{F_0 - F)}{F}\right\} = \text{Log}\, K_b + n\ \text{Log}[\text{Q}] \quad (3)$$

where [Q] is the corresponding quencher (Au NPs) concentration. The values of K_b and n are calculated from the intercept and slope of the plot as shown in Figure S3c,d in the Supporting Information and are found to be 2.202×10^3 M^{-1} and 0.376, respectively. The change in Gibbs free energy (ΔG) for the interaction between RhB and Au NPs at room temperature (25 °C) is obtained using the Gibbs−Helmholtz relation[46] $\Delta G = -RT \ln K_b$, where R is the universal gas constant and T is the temperature. The calculated value of ΔG is −19.07 kJ mol^{-1}. The negative ΔG value indicates that the interaction between RhB and Au NPs is spontaneous. Also, the quenching of the fluorescence emission of RhB by Au NPs is further described by the well-known Stern−Volmer equation (eq 4)[47]

https://doi.org/10.1021/acsomega.2c02725
ACS Omega 2022, 7, 29013−29026

Table 1. Binding Constant (K_b), Binding Sites (n), Gibbs Free Energy (ΔG), Stern–Volmer Constant (K_{SV}), and Quenching Rate Constant (K_q) for the Au NPs/RhB Mixed Aqueous Solution[a]

K_b (M^{-1})	n	R^2	ΔG (kJ mol^{-1})	K_{SV} (M^{-1})	R^2	K_q (M^{-1} s^{-1})
2.202×10^3	0.376	0.9924	−19.07	8.174×10^6	0.9924	5.906×10^{15}

[a] R^2 is the corresponding correlation coefficient.

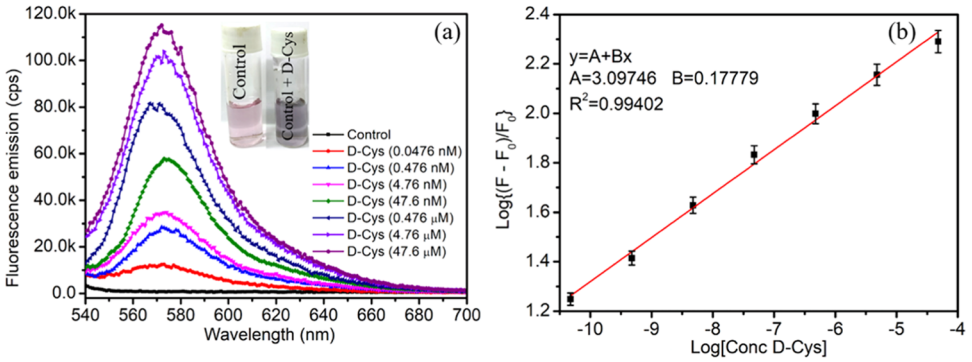

Figure 4. (a) Recovery of fluorescence emission from the Au NPs/RhB mixed solution when added with D-Cys of various concentrations (0.0476 nM to 46.7 μM in the mixed solution). The concentrations of Au NPs and RhB in their mixed solution used here are 0.05 mM and 0.05 μM, respectively. (b) Linear dynamic plot of the fluorescence recovery efficiency of the Au NPs/RhB mixed solution for various concentrations of D-Cys. The inset of (a) shows the digital micrographs of the vial containing the Au NPs/RhB mixed solution before (control) and after incubation for 3 min with D-Cys. The excitation wavelength was 530 nm.

$$\frac{F_0}{F} = 1 + K_{SV}[Q] \quad (4)$$

where K_{SV} is the Stern–Volmer quenching constant. The deviation from linearity of the Stern–Volmer plot at higher quencher concentration implies that the fluorescence quenching of the RhB dye is a mixture of static and dynamic (diffusion) quenching.[48] Considering the slope of the straight-line region of the F_0/F vs [Q] plot (i.e., at lower concentrations of Au NPs) as shown in Figure S3c,e in the Supporting Information, the value of K_{SV} is calculated as 8.174×10^6 M^{-1}. The bimolecular fluorescence quenching rate constant (K_q) and K_{SV} are related by the relation[49] $K_q = K_{SV}/\tau_0$, where τ_0 is the fluorescence emission lifetime of pure RhB (1.384 ns).[21] The value of K_q is calculated as 5.906×10^{15} M^{-1} s^{-1} for this fluorometric titration experiment. The high values of both K_{SV} and K_q substantiate the efficient quenching of RhB (donor) fluorescence by gold nanoparticles in the aqueous medium. All of the above calculated photophysical parameters are summarized in Table 1.

However, interestingly, after addition of D-Cys to the mixed solution of Au NPs and RhB, the original fluorescence emission (574 nm) of dye molecules is recovered from their quenched state as shown in Figure 4a. The concentrations of RhB and Au NPs for the assay experiments were optimized in such a way that there is an almost complete quenching of the fluorescence emission of RhB in the Au NPs/RhB mixed system before addition of the D-Cys solution when excited with light of wavelength 530 nm and recovery of fluorescence signal in the presence of D-Cys at ambient condition. This "turn-off" and "turn-on" mechanism of fluorescence emission due to the presence of D-Cys in the assay medium is schematically shown in Figure 5. For the assay experiments, the concentrations of RhB and Au NPs in their aqueous mixture were fixed at 0.05 μM and 0.05 mM, respectively. These selected concentrations of RhB and Au NPs in their aqueous solution at ambient condition may be considered as an optimized condition for the fluorescence recovery from the mixed ensemble when exposed

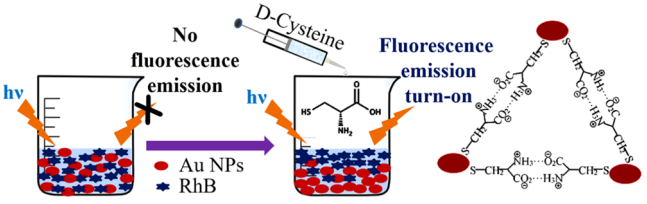

Figure 5. Schematic presentation of the proposed fluorescence "off–on" mechanism and chemical coordination between the D-Cys molecules and citrate caped Au NPs.

to D-Cys in aqueous medium. Here we have studied the recovery of fluorescence emission from the Au NPs/RhB mixed solution in the absence (control) and presence of various concentrations of D-Cys. Also, there is a distinct color change of the mixed final solution from red-wine (control) to bluish-black (after addition of D-Cys) as shown in the inset of Figure 4a. From the fluorescence emission of RhB in the presence of different concentrations of D-Cys (viz. 0.06 nM to 62.5 μM in the mixed solution) as shown in Figure S3f in the Supporting Information, it is further confirmed that there is no significant effect of D-Cys on the fluorescence emission properties of RhB in aqueous solution as the emission spectra of the RhB/D-Cys mixed solution for all concentrations of D-Cys are almost unaltered. Therefore, RhB dye has been considered as a good and efficient fluorescent probe for recognition of the amino acid D-Cys in aqueous medium via a simple spectrofluorometric method in the present work.

It is known that at neutral or under near-physiological pH, citrate caped Au NPs possess three carboxylated ($-COO^-$) groups,[50] whereas the D-Cys molecule has $-SH$, $-COO^-$ groups, and the amino group (NH_3^+) in the same aqueous environment. The citrate layer surrounding the Au NPs in aqueous dispersion gives an overall strong negative surface potential as is already confirmed by the ζ potential study (as shown in Figure S1b in the Supporting Information). It is already reported elsewhere that at neutral pH (7.0) cysteine is

https://doi.org/10.1021/acsomega.2c02725
ACS Omega 2022, 7, 29013−29026

Table 2. Comparisons of the Analytic Methods for the Determination of D-Cysteine

probe/systems	detection principle	range (in μM)	LOD (in nM)	ref
4-fluoro-7-nitrobenzofurazan	SRM-chromatogram	0−300		28
Ag NPs-embedded nanopaper	colorimetric		4880	29
NCS-OTPP[a]	UHPLC-HRMS-chromatograms	0.098−1000	19.20	30
polar ionic elution[b]	chiral UHPLC-MS	0.413−4.13	165.08	31
L-carnitine methyl ester bis	electrokinetic chromatography	10−150	1100	32
Au NPs/RhB mixed system	colorimetric and fluorometric assay	0.001−100	4.2	this work

[a](*R*)-(5-(3-Isothiocyanatopyrrolidin-1-yl)-5-oxopentyl)triphenylphosphonium. [b]MeOH/MeCN/H_2O 49/49/2 v/v/v.

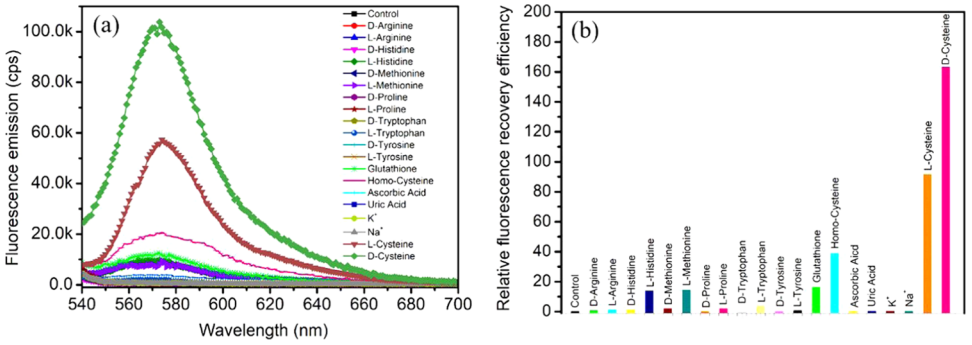

Figure 6. (a) Recovery of fluorescence emission from the Au NPs/RhB mixed solution (concentrations of Au NPs and RhB in their mixed solution are 0.05 mM and 0.05 μM, respectively) in the presence of all of the relevant analytes used in this work. The concentrations of all of the analytes are 47.6 μM in the Au NPs/RhB mixed solution. (b) Relative fluorescence recovery efficiency (at 574 nm) of the Au NPs/RhB mixed solution due to each analyte as calculated from the corresponding emission intensities. Excitation wavelength was 530 nm.

neutral,[51] due to which there will be very less possibility of citrate caped Au NPs having direct interaction with D-Cys through its $-NH_2$ group via electrostatic attraction.[42] However, due to the strong affinity of the −SH moiety of D-Cys towards the Au NPs' surface, they try to encapsulate[41] Au NPs by thiolate−Au bond formation via chemisorption,[39] which eventually displaces the original citrate layer of Au NPs. As a consequence, the RhB molecules that were adsorbed onto the citrate caped nanoparticles' surface by electrostatic interaction[52] now become free in the surrounding environment. This is why the intrinsic fluorescence emission of RhB with peak centered at 574 nm is retrieved after photoexcitation. However, the displacement of the citrate layer of Au NPs should depend upon various factors like the concentration of D-Cys molecules in the assay medium, overall charge distribution, surface potential around the nanoparticle surface, temperature etc. Immediately after the reaction of D-Cys with Au NPs/RhB systems, the presence of amino acid molecules in the encapsulating shell of nanoparticles starts to induce cross-linking (as shown schematically in Figure 5 between the neighboring encapsulated Au NPs) in the mixed solution, resulting in the formation of Au NP aggregates or clusters, which causes a color change of the mixed solution from red-wine to bluish-black[53,54] after the reaction. The aggregation of Au NPs in the presence of D-Cys is already evidenced by the UV−vis absorption (Figure 2b) and TEM study (Figure 3b) as discussed earlier. From the above discussion, it is clear that the fluorescence emission band intensity at 574 nm of the mixed solution of Au NPs and RhB is recovered after addition of D-Cys and this fluorescence recovery is most probably due to the availability of free RhB molecules in the mixed ensemble. Overall, due to the interaction of D-Cys with the Au NPs/RhB system in solution, the relative distance between the dye molecules and Au NPs might have increased, resulting in the decrease of fluorescence quenching via nonradiative energy transfer pathways.

3.4. Sensitivity of the Interaction of the Au NPs/RhB Mixed Ensemble towards D-Cys. In this work, it is important to understand the sensitivity of the interaction of D-Cys with Au NPs/RhB mixed aqueous solution. It is observed that under the optimized experimental condition, the fluorescence emission intensity obtained from the Au NPs/RhB/D-Cys mixed solution increases almost linearly with the increase in concentrations of D-Cys. The relative fluorescence recovery efficiency is defined by $[(F - F_0)/F_0]$ and is given by the following linear equation (eq 5)[52]

$$\mathrm{Log}\left[\frac{(F - F_0)}{F_0}\right] = \mathrm{Log}[\mathrm{C}] + A \quad (5)$$

where C is the concentration of D-Cys and A is an arbitrary constant. The relative fluorescence recovery efficiency and the concentration of D-Cys follow the linear equation $y = 3.09746 + 0.17779[\mathrm{C}]$ with a correlation coefficient (R^2) of 0.99402 as shown in Figure 4b, and the concentration range of 0.004 nM to 47.6 μM in the Au NPs/RhB mixed ensemble. Thus, this method of recovery of fluorescence emission shows very high sensitivity to a broad linear range of concentrations of D-Cys. To compare the sensitivity of Au NPs/RhB towards D-Cys, the limit of detection (LOD) has been determined by the 3σ method[55] using the expression LOD = $(k \times \mathrm{SD})/S$, where S is the slope of the recovered fluorescence emission from the Au NPs/RhB vs concentration of D-Cys (in M) plot (see the Supporting Information for the detailed calculations). The LOD value of D-Cys (as shown in Figure S7a,b,c in the Supporting Information) is found to be 4.2 nM. This LOD value indicates that the proposed Au NPs/RhB mixed ensemble is highly sensitive towards D-Cys for spectrofluorometric measurement. The linear range and LOD of D-Cys

https://doi.org/10.1021/acsomega.2c02725
ACS Omega 2022, 7, 29013−29026

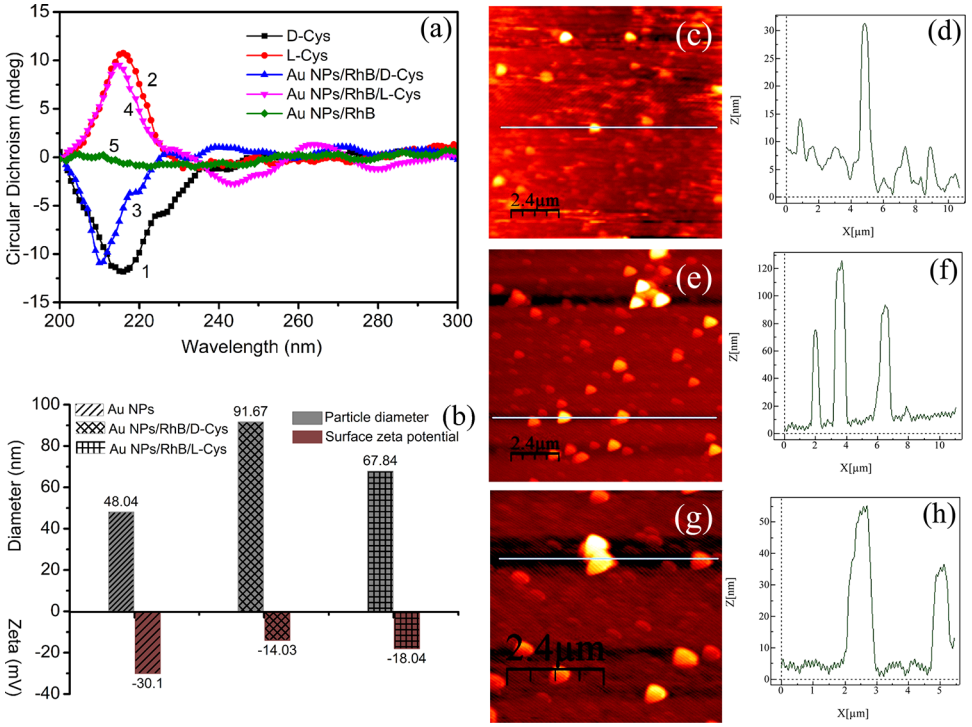

Figure 7. (a) CD spectra of the aqueous solution of pure D-Cys (curve 1, 1 mM), pure L-Cys (curve 2, 1 mM), mixed solution of Au NPs/RhB/D-Cys (curve 3), Au NPs/RhB/L-Cys (curve 4), and Au NPs/RhB (curve 5). (b) Column plot of the hydrodynamic diameter and surface ζ potential of the NPs as obtained from Au NPs/RhB/D-Cys and Au NPs/RhB/L-Cys mixed solutions (c–h). AFM topographic micrographs and surface roughness plot of (c, d) as-synthesized Au NPs, (e, f) Au NPs/RhB/D-Cys mixed system, and (g, h) Au NPs/RhB/L-Cys (g, h) mixed systems deposited on a smooth glass substrate. The RMS surface roughness has been measured along the chosen lines as shown in the figures.

determination as previously reported in the different studies have been compared with the present work and summarized in Table 2.

3.5. Selectivity Study of the Proposed Bio-Nano Interactions. The selectivity of the interaction of the Au NPs/RhB mixed solution towards D-Cys in the presence of other relevant interfering analytes such as AA, UA, neurotransmitters, other D- and L-amino acids including D-Arg, L-Arg, D-His, L-His, D-Met, L-Met, D-Pro, L-Pro, D-Trp, L-Trp, D-Tyr, L-Tyr, L-Cys, −SH-containing compounds like GSH and Hcys etc. is tested under the same optimized experimental conditions of the Au NPs/RhB mixed solution and the corresponding fluorescence emission spectra are illustrated in Figure 6a. The chemical structures of all of the interfering compounds are shown in Figure S4 in the Supporting Information. From Figure 6a it is observed that the fluorescence emission intensities of the Au NPs/RhB mixed solution in the presence of D-Cys and L-Cys are significantly high compared to those for other interfering compounds, although the concentrations of all of the analytes were the same in these spectrofluorometric measurements. However, when the Au NPs/RhB mixed solution is added with D-Cys, the final solution turns red-wine to bluish-black in color, which is different when mixed with L-Cys solution separately, as shown in Figure S5 in the Supporting Information. The relative fluorescence recovery efficiency $[(F - F_0)/F_0]$ as shown in Figure 6b becomes remarkably high for D-Cys compared to that for all other relevant interfering species or elements. From the above observations it is clear that the interaction of the Au NPs/RhB mixed ensembles with D-Cys in aqueous medium is selective due to the high fluorescence recovery as well as distinct color change of the Au NPs/RhB mixed solution when compared to the interactions with L-Cys and all other D- and L-amino acids, physiologically relevant interfering elements etc. as studied in this experiment. It is important to mention that the difference between fluorescence recovery efficiencies for D-Cys and L-Cys might be attributed to the different chiralities in the molecular structure of these amino acids, as is evidenced from the CD spectra shown in Figure 7a. The high selectivity of the interaction of the Au NPs/RhB mixed solution with D-Cys may be attributed to the change in structural configuration of the amino acid D-Cys, which is manifested as the observed change in the peak position of the CD spectrum. This is because any change in the configuration of the functional group (−SH) while interacting with the Au NPs/RhB mixed ensemble in aqueous medium possibly disrupts the chiral properties in the structure of D-Cys. As a result, there is a blue shift of the peak position at 210 nm in the CD spectrum as shown in Figure 7a. On the other hand, when L-Cys is added to the Au NPs/RhB mixed solution, the peak position observed at 216 nm in the CD spectrum is not altered except for a slight reduction of intensity. These observations clearly indicate that the chiral properties of L-Cys were possibly less affected while interacting with the Au NPs/RhB mixed ensemble compared to those of D-Cys. From the DLS study, as shown in Figures 7b, S8a, and S9a, it is observed that the particle size of Au NPs increases in the presence of both D- and L-Cys. However, for D-Cys, the increase in hydrodynamic particle diameter is higher (91.67 nm) compared to that of L-Cys (67.84 nm). This observation implies the possibility of a high degree of aggregation of Au NPs while interacting with D-Cys when compared to that due to L-Cys. As mentioned earlier, amino acids basically displace the citrate layer of the Au NPs during interaction and induce interparticle cross-linking, which favors

https://doi.org/10.1021/acsomega.2c02725
ACS Omega 2022, 7, 29013−29026

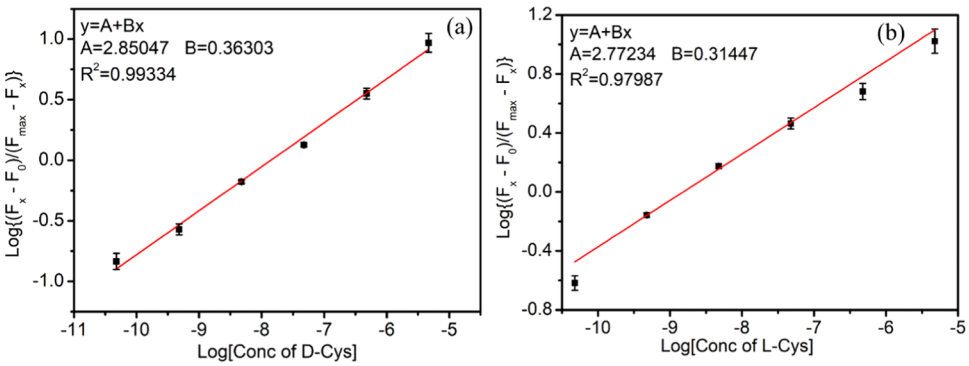

Figure 8. Plot of (a) Log{$(F_x - F_0)/(F_{max} - F_x)$} vs Log[concentration of D-Cys] and (b) Log{$(F_x - F_0)/(F_{max} - F_x)$} vs Log[concentration of L-Cys] to determine the binding constants of the Au NPs/RhB system with D-Cys and L-Cys, respectively.

rapid aggregation of Au NPs. However, the rate or extent of interparticle cross-linking is possibly higher for D-Cys than for L-Cys. Additionally, the less negative ζ potential (Figures 7b, S8b, and S9b) of the Au NPs/RhB mixed solution containing D-Cys (−14.03 mV) compared to that with L-Cys (−18.04 mV) confirms the higher aggregation of NPs in the case of D-Cys.[56] To have a better understanding and direct visual evidence of the formation of aggregates or clusters, AFM topographical imaging is performed in a tapping mode. Figure 7c−h shows the AFM topographical image and surface roughness plot of the drop-casted film deposited onto smooth glass substrates from the Au NPs/RhB mixed solution in the presence of D-Cys and L-Cys, respectively. For all of these measurements, Au NPs/RhB mixed solutions were prepared in 1:1 volume ratio and their concentrations in the mixed solution were 0.05 mM and 0.05 μM, respectively. These images show that D-Cys facilitates a higher extent of aggregation or formation of clusters of Au NPs in the mixed solution. The root-mean-square (RMS) surface roughness of the Au NPs/RhB film is estimated as 4.4 nm, whereas for L-Cys and D-Cys it becomes 7.25 and 18.92 nm, respectively. That is, the surface roughness of the film having D-Cys is much higher compared to that of L-Cys. Our AFM analysis revels that D-Cys induces a much greater degree of nanoparticle aggregation. Also, the hydrogen bond between the neighboring D-Cys molecules in the aqueous solution is highly affected by the steric hindrance due to the presence of Au NPs. The high extent of aggregation of NPs in the aqueous mixture of Au NPs/RhB facilitated higher fluorescence recovery from the quenched state due to the release of more number of RhB dye molecules from the Au surface.

Interestingly, our proposed Au NPs/RhB mixed platform does not show any significant or appreciable fluorescence recovery by other aminothiols such as Hcys and GSH in the same aqueous medium as studied in this work. In case of Hcys and GSH, we observe a slight recovery of fluorescence emission from the Au NPs/RhB matrix in aqueous medium. Although Hcys is a homologue of the amino acid Cys, it differs with an additional methylene bridge in its molecular structure. It is also known that[57] nearly at physiological pH, Hcys contains one amino group ($-NH_3^+$), one $-COO^-$ group, and one −SH group in aqueous medium, whereas citrate caped Au NPs possess three $-COO^-$ groups in the same aqueous medium. Therefore, the direct electrostatic binding between Hcys and Au NPs is minimal. Due to the presence of the −SH group in Hcys, there will be still some interaction via thiolate−Au bond formation, but the rate of displacing the citrate layer on which the cationic RhB molecules are bound might be limited due to the difference in the orientation of the amino acid groups or in the interfacial free energies when compared to D-Cys or L-Cys in the studied aqueous environment.[41] As a consequence, the fluorescence emission recovery from the Au NPs/RhB mixed ensemble is less compared to D-Cys and L-Cys. On the other hand, GSH has two −COOH groups associated with glutamic acid and glycine residues and three amino groups ($-NH_3^+$) in three amino acids, and one sulfur atom present in the Cys residue. It is expected that at intermediate or higher pH the disassociation of −COOH groups may hinder[58] the binding of GSH with Au nanocolloids via the α amine group. This results in a very little cross-linking between the −SH group and Au colloids. As we have studied the binding interactions at neutral pH (7.0), less interaction between Au and GSH results in lower fluorescence recovery in the Au NPs/RhB aqueous medium. Additionally, the GSH molecule is relatively bulky in size compared to cysteine or Hcys, and therefore, the interfacial reactivity may be less probable due to energetic consideration. However, literature revels that the amino acid Trp can selectively bind with Au NPs.[59] In the present work, we did not find any significant fluorescence recovery from the Au NPs/RhB mixed solution in the presence of D- and L-Trp. This is possibly due to the formation of the nonfluorescent Trp−RhB complex.[60]

The binding constant, sometimes referred to as the association constant (K_a), of the Au NPs/RhB system with D-Cys and L-Cys in the aqueous medium has been determined using the Benesi−Hildebrand equation (eq 6)[61,62]

$$\frac{1}{(F_x - F_0)} = \frac{1}{(F_{max} - F_0)} + \frac{1}{K_a[M](F_{max} - F_0)} \quad (6)$$

where F_o, F_x, and F_{max} are the fluorescence emission intensities obtained from the mixture of Au NPs/RhB in the absence of D-Cys (or L-Cys), with an intermediate concentration of D-Cys (or L-Cys) and the concentration of D-Cys (or L-Cys) at saturation level, and [M] is the concentration of D-Cys (or L-Cys). The magnitude of the binding constant (K_a) gives an indication about the strength of interaction between the guest and host for their complexation in a medium and is related to the change in Gibbs free energy[46] ($\Delta G = -RT \ln K_a$) for the process. The values of K_a have been obtained from the intercept of the plot of Log{$(F_x - F_0)/(F_{max} - F_x)$} vs Log[M] as shown in Figure 8 for both D-Cys and L-Cys, and are summarized in Table 3. These values confirm that both D-Cys and L-Cys can bind to the Au NPs/RhB system in aqueous solution. But, in the case of D-Cys, this interaction is stronger

https://doi.org/10.1021/acsomega.2c02725
ACS Omega 2022, 7, 29013−29026

Table 3. Binding Constant (K_a) and Gibbs Free Energy (ΔG) for D-Cys and L-Cys with the Au NPs/RhB Mixed Systems in Aqueous Solution[a]

chiral amino acids	K_a (M^{-1})	R^2	ΔG (kJ mol^{-1})
D-Cys	708.712	0.9933	−16.261
L-Cys	592.025	0.9798	−15.816

[a] R^2 is the corresponding correlation coefficient.

than that for L-Cys. Therefore, due to the strong binding interaction between D-Cys and citrate caped Au NPs in aqueous medium, the fluorescence recovery efficiency is much higher compared to L-Cys. The values of the Gibbs free energy ΔG and binding constant K_a for Au NPs/RhB/D-Cys and Au NPs/RhB/L-Cys complexes have been calculated from the steady-state fluorescence emission spectra and are summarized in Table 3. The negative ΔG indicates that the interactions of both D-Cys and L-Cys with the Au NPs/RhB system are spontaneous. However, the higher negative value of ΔG reveals the faster rate of interaction in the case of D-Cys with the assay medium compared to that for L-Cys.

For further investigation on the selectivity and interaction mechanism of Au NPs/RhB with D- and L-Cys, FTIR spectroscopic measurements in ATR mode were performed and are shown in Figure 9. The FTIR spectra of pure D-Cys and L-Cys (curve 1 in (a) and (b), respectively) are very similar and show IR bands with peaks centered at 3166, 1582, and 1390 cm^{-1}, which are attributed to the stretching of $-NH_3^+$ and the asymmetric and symmetric stretching of the $-COO^-$ functional groups of Cys molecules, respectively. In addition, Cys molecules have a weak IR vibrational band near 2550 cm^{-1}, which is originated due to the characteristic stretching vibration of the S−H bond (thiol group). Other vibrational bands are observed at 2968 cm^{-1} (CH_2 stretching, asymmetric), 2078 cm^{-1} (NH_3 bending, asymmetric), 1522 cm^{-1} (N−H bending), 1340 cm^{-1} (NH_3 bending, symmetric), 1294 cm^{-1} (CH_2 wagging), 1195 cm^{-1} (CH_2 twisting), 1130 cm^{-1} (SO_2 stretching), 1062 cm^{-1} (NH_3 rocking), 941 cm^{-1} (S−H bending), 866 cm^{-1} (N−O stretching), 635 cm^{-1} (COOH bending), 536 cm^{-1} (COOH rocking) etc. These results are consistent with the FTIR spectra of amino acids reported elsewhere.[63−65] Interestingly, for the Au NPs/RhB/D-Cys system, the IR bands corresponding to the stretching of $-NH_3^+$ and $-COO^-$ groups of D-Cys are almost absent, possibly due to their cross-linking with other cysteine molecules attached to the neighboring Au NPs. However, for the Au NPs/RhB/L-Cys system, the bands of these stretching vibrations are also abruptly reduced compared to pure L-Cys but the peaks are still visible. These observations may reveal that the interparticle cross-linking is much stronger in the case of D-Cys in the assay medium, resulting in a rapid and greater extent of nanoparticle aggregations, which is reflected in the different color change of the final solution. This may also be due to the change in their dipole moments when binding with a high electron density of the metal surface. But the most significant observation is that the S−H stretching vibration band (2550 cm^{-1}) totally disappears for D-Cys after interacting with the Au NPs/RhB mixed system in aqueous medium (Figure 9a curve 3). This indicates that S−H bonds are cleaved in the presence of the metal NPs, which further indicates the strong binding interaction of D-Cys with Au NPs. On the other hand, the S−H stretching vibration band is not totally absent for L-Cys when interacted with the Au NPs/RhB system but it appears as a weak band near 2550 cm^{-1} as shown in Figure 9b (curve 3). Therefore, it is clear that the interaction of D-Cys with the Au NPs/RhB mixed system is stronger compared to that of L-Cys in the studied aqueous medium. Additionally, the FTIR spectra of the Au NPs/RhB mixed system (curve 2 in Figure 9a,b, respectively) confirm that there is no such significant effect of RhB molecules on the interaction of D-Cys or L-Cys molecules with Au NPs in the assay medium.

3.6. Real Biosample Analysis. The proposed nano-bio interaction is also studied in the presence of normal human urine. The normal urine sample was collected from a healthy laboratory volunteer (male researcher) having no renal complications. In this investigation with the normal urine sample, we maintained the same optimized concentrations of RhB and Au NPs in their mixed solution as discussed earlier, and took extra precautions to avoid any direct contact or any type of contamination with the urine sample. D-Cys may present in both urine and blood plasma. It is already known that diseases like cystinuria leading to the formation of kidney and renal system stone occur due to the free presence of Cys in the urine.[66,67] The fluorescence emission spectra of the mixed solution of Au NPs/RhB (control) in the presence of normal urine (200 μL), mixture of normal urine (200 μL) and D-Cys (0.1 mM, 200 μL), and mixture of normal urine (200 μL) and all other analytes (0.1 mM) used in the present work except D-Cys are shown in Figure S10 in the Supporting Information. The concentrations of D-Cys and all other analytes in the final assay medium containing urine were 2.38 μM, respectively. The corresponding fluorescence recovery efficiency is shown in Figure 10. From this figure it is clear that, the normal urine shows fluorescence recovery efficiency of 42% but mixture of normal urine and D-Cys shows fluorescence recovery efficiency of 73%. Therefore, the usual presence of Cys in the normal

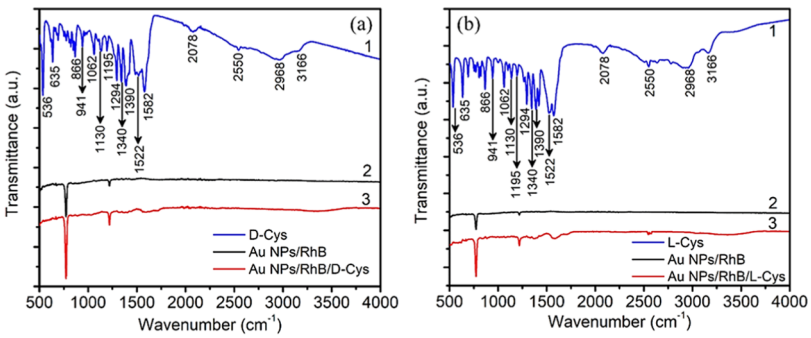

Figure 9. ATR-FTIR spectra of (a) D-Cys (b) and L-Cys in the absence and presence of Au NPs/RhB, respectively.

https://doi.org/10.1021/acsomega.2c02725
ACS Omega 2022, 7, 29013−29026

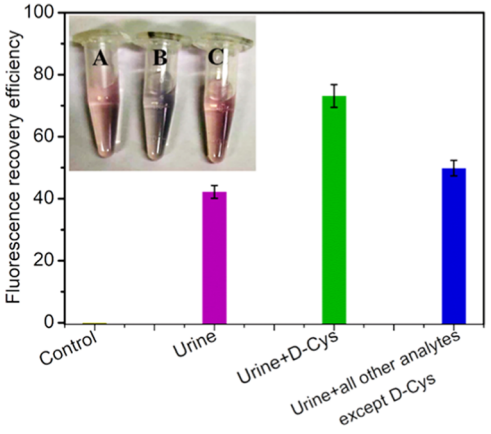

Figure 10. Plot of the fluorescence recovery efficiencies for the Au NPs/RhB mixed solution in the presence of normal human urine and all other analytes relevant to the present work. The inset shows the digital photograph of vials containing the Au NPs/RhB mixed solution with (A) urine, (B) mixture of urine and D-Cys, and (C) mixed solution of urine and all other analytes except D-Cys. The photograph and fluorescence emission spectra are taken after 3 min of incubation for all of these mixed solutions.

urine gives the initial fluorescence recovery from Au NPs/RhB system. It is also observed that when all other D and L-amino acids along with the other relevant interfering compounds as considered are mixed with the proposed assay matrix, the fluorescence recovery efficiency is slightly higher than that due to pure normal urine. This may be due to the presence of L-Cys as was added with all other interfering compounds. Additionally, there is also a distinct color change (from red-wine to bluish-black) of the assay solution after addition of D-Cys compared to all other analytes including L-Cys as shown in the inset of Figure 10. This study confirms the proposed nano-bio interaction is manifested as the selective binding of D-Cys with Au NPs/RhB in in human urine as well. Therefore, the proposed Au NPs/RhB system in aqueous medium under the appropriate and optimized condition may be used as an efficient platform for rapid detection of D-Cys in human urine in a ratio-metric approach to diagnose various renal complications.

4. CONCLUSIONS

In conclusion, we demonstrate a simple fluorometric method to explore the comparative and selective interaction of the amino acid D-Cys among various other D- and L-amino acids, neurotransmitters, relevant biological compounds etc., with citrate caped gold nanoparticles (27.5 nm) in the presence of the fluorescent dye RhB. Au NPs are found to almost fully quench the fluorescence emission of RhB dye in the optimized concentrations of both Au NPs and RhB via a nonradiative energy transfer pathway from the excited RhB molecules to Au NPs in aqueous solution at neutral pH. This quenched fluorescence is selectively recovered with high efficiency after addition of D-Cys to the Au NPs/RhB mixed solution and there was a distinct color change of the assay medium after reaction with D-Cys when compared to the effect of other interfering compounds studied in this work. The degree of aggregation of Au NPs is greater due to the interaction with D-Cys compared to L-Cys due to strong thiolate–Au bond formation via chemisorption and possibly greater interparticle cross-linking compared to that due to L-Cys and in aqueous solution. The higher value of binding constant and higher negative value of Gibbs free energy for D-Cys interacting with the Au NPs/RhB mixed system compared to those for L-Cys as estimated from the fluorescence recovery results confirm the stronger interaction of D-Cys with the nanoparticle system in the studied aqueous medium. The difference in aggregations of D-Cys and L-Cys while interacting with Au NPs/RhB mixed systems in solution is correlated with the ζ potential results and chiral properties of the amino acids, as evidenced by the ζ potential study and CD spectroscopic characterization, respectively. The ATR-FTIR study further distinguishes the difference of interactions of both D-Cys and L-Cys with the assay matrix through the change in vibrational signatures of the S–H bond as well as other relevant functional groups and is consistent with the observations by the other analytical methods used in this present work. The interaction of D-Cys with the proposed nanoparticle-based platform is highly sensitive and lies in the broad linear range of concentration of 1 nM to 100 μM. The LOD for D-Cys is found to be 4.2 nM, which is lower compared to many available detection methods cited in the literature. The normal human urine sample when mixed with the assay matrix (Au NPs/RhB) and D-Cys exhibits a higher fluorescence recovery and distinct color change (red-wine to bluish-black) of the assay medium after reaction compared to that for L-Cys or all other interfering compounds as studied. Therefore, the proposed bio-nano interaction may be realized as an efficient approach for the selective recognition of the amino acid D-Cys in the aqueous environment.

■ ASSOCIATED CONTENT

Supporting Information

The Supporting Information is available free of charge at https://pubs.acs.org/doi/10.1021/acsomega.2c02725.

DLS and ζ potential spectra of Au NPs; TEM micrograph of Au NPs for lognormal fitting of particle size distribution plot; SAED pattern for crystalline nature of Au NPs; HRTEM micrograph to calculate lattice spacing; EDS spectrum for the identification of Au peaks; UV–vis spectra of RhB and RhB/D-Cys; spectral overlap between UV–vis absorption spectrum of Au NPs and fluorescence emission spectrum of RhB for RET; fluorescence emission quenching of pure RhB in presence of different concentration of Au NPs; Log$\{(F_0 - F)/F\}$ vs Log[Conc of Au NPs] plot to obtained binding constant (K_b) and number of binding sites (n) of Au NPS/RhB mixed ensembles; Stern–Volmer plot to determine the Stern–Volmer constant (K_{SV}) of RhB in Au NPs/RhB complex; fluorescence emission spectra of RhB and mixture of RhB/D-Cys; chemical structure of amino acids and biomolecules for selectivity study; colorimetric response from mixed solution of Au NPs/RhB, Au NPs/RhB/D-Cys and Au NPs/RhB/L-Cys; recovery of fluorescence emission from Au NPs/RhB mixed solution in presence of different concentrations of L-Cys; determination of limit of detection (LOD) of Au NPs/RhB towards D-Cys by 3σ method; DLS and ζ potential spectra Au NPs/RhB/D-Cys and Au NPs/RhB/L-Cys; real bio-sample analysis—fluorescence emission spectra of Au NPs/RhB in presence of normal human urine, mixture of urine and D-Cys, mixture of urine and all other relevant analytes except D-Cys (PDF)

https://doi.org/10.1021/acsomega.2c02725
ACS Omega 2022, 7, 29013–29026

AUTHOR INFORMATION

Corresponding Author

Pabitra Kumar Paul − *Department of Physics, Jadavpur University, Kolkata 700032, India;* orcid.org/0000-0002-3490-525X; Phone: +91-9477631142; Email: pabitra_tu@yahoo.co.in, pabitrak.pal@jadavpuruniversity.in; Fax: 91-33-24138917

Authors

Pradip Maiti − *Department of Physics, Jadavpur University, Kolkata 700032, India;* orcid.org/0000-0001-6879-591X

Ujjal Saren − *Department of Physics, Jadavpur University, Kolkata 700032, India;* orcid.org/0000-0003-2949-9987

Utsav Chakraborty − *Department of Physics, Jadavpur University, Kolkata 700032, India;* orcid.org/0000-0003-1528-0335

Tanmoy Singha − *Department of Physics, Jadavpur University, Kolkata 700032, India;* orcid.org/0000-0002-4683-6204

Sharmistha Paul − *West Bengal State Council of Science and Technology, Department of Science and Technology and Biotechnology, Kolkata 700064, India*

Complete contact information is available at: https://pubs.acs.org/10.1021/acsomega.2c02725

Notes

The authors declare no competing financial interest.

ACKNOWLEDGMENTS

P.M. wishes to thank Jadavpur University and Rashtriya Uchchatar Shiksha Abhiyan (RUSA) 2.0 (ref no. R-11/604/19) for providing excellent infrastructural and financial support to perform the experimental studies. P.M., S.P., and P.K.P. are also grateful to the West Bengal State Council of Science and Technology (WBSCST), Govt. of West Bengal for financial assistance (ref no. 493/WBSCST/F/0545/15(Pt-I)) to perform this work. P.K.P. is also thankful to SERB DST, Govt. of India for finanical assistance through the project (ref no. SB/EMEQ-142/2014). The authors are grateful to CSS of the Indian Association for the Cultivation of Science, Kolkata for providing the HRTEM and CD measurements facility used in this work. The authors are also grateful to Prof. Partha Roy of the Department of Chemistry at Jadavpur University for providing access to the ATR-FTIR measurements in this study.

REFERENCES

(1) Widlak, W. *Molecular Biology Not Only for Bioinformaticians*; Springer, 1998.

(2) Kessel, A.; Ben-Tal, N. *Introduction to Proteins Structure, Function, and Motion*, 2nd ed.; CRC Press, 2018.

(3) Kimura, R.; Tsujimura, H.; Tsuchiya, M.; Soga, S.; Ota, N.; Tanaka, A.; Kim, H. Development of a cognitive function marker based on D-amino acid proportions using new chiral tandem LC-MS/MS systems. *Sci. Rep.* **2020**, *10*, No. 804.

(4) Carenzi, G.; Sacchi, S.; Abbondi, M.; Pollegioni, L. Direct chromatographic methods for enantioresolution of amino acids: recent developments. *Amino Acids* **2020**, *52*, 849−862.

(5) Liu, J.; Fu, B.; Zhang, Z. Ionic Current Rectification Triggered PhotoelectrochemicalChiral Sensing Platform for Recognition of Amino Acid Enantiomers on Self-StandingNanochannel Array. *Anal. Chem.* **2020**, *92*, 8670−8674.

(6) Karakawa, S.; Shimbo, K.; Yamada, N.; Mizukoshi, T.; Miyano, H.; Mita, M.; Lindner, W.; Hamase, K. Simultaneous analysis of d-alanine, d-aspartic acid, and d-serine using chiral high-performance liquid chromatography-tandem mass spectrometry and its application to the rat plasma and tissues. *J. Pharm. Biomed. Anal.* **2015**, *115*, 123−129.

(7) Liu, D.; Lv, Y.; Chen, M.; Cheng, D.; Song, Z.; Yuan, L.; Zhang, X. A long wavelength emission two-photon fluorescent probe for highly selective detection of cysteine in living cells and an inflamed mouse model. *J. Mater. Chem. B* **2019**, *7*, 3970−3975.

(8) Winther, J. R.; Thorpe, C. Quantification of thiols and disulfides. *Biochim. Biophys. Acta, Gen. Subj.* **2014**, *1840*, 838−846.

(9) Chen, X.; Hu, Y.; Cao, Z.; Liu, Q.; Cheng, Y. Cerebrospinal Fluid Inflammatory Cytokine Aberrations in Alzheimer's Disease, Parkinson's Disease and Amyotrophic Lateral Sclerosis: A Systematic Review and Meta-Analysis. *Front. Immunol.* **2018**, *9*, No. 2122.

(10) Kjældgaard, A.-L.; Pilely, K.; Olsen, K. S.; Pedersen, S. W.; Lauritsen, A. O.; Moller, K.; Garred, P. Amyotrophic lateral sclerosis: The complement and inflammatory hypothesis. *Mol. Immunol.* **2018**, *102*, 14−25.

(11) Pichette, J.; Gagnon, J. Implications of Hydrogen Sulfide in Glucose Regulation: How H_2S Can Alter Glucose Homeostasis through Metabolic Hormones. *Oxid. Med. Cell. Longevity* **2016**, *2016*, No. 3285074.

(12) Tong, Z.; Ni, L.; Ling, J. Antibacterial peptide nisin: A potential role in the inhibition of oral pathogenic bacteria. *Peptides* **2014**, *60*, 32−40.

(13) Zhang, M.; Ye, B. C. Colorimetric Chiral Recognition of Enantiomers Using the Nucleotide-Capped Silver Nanoparticles. *Anal. Chem.* **2011**, *83*, 1504−1509.

(14) Rodríguez-Zamora, P.; Angeles, B. S.; Buendía, F.; Silis, C. C.; Fabila, J.; Díaz, J. B.; Díaz, L. M. F.; Borbón, L. O. P.; Díaz, G.; Garzón, I. L. Revisiting the conformational adsorption of L- and D-cysteine on Au nanoparticles by Raman spectroscopy. *J. Raman Spectrosc.* **2020**, *51*, 243−255.

(15) Klein, J. Probing the interactions of proteins and nanoparticles. *Proc. Natl. Acad. Sci. U.S.A.* **2007**, *104*, 2029−2030.

(16) Lei, J.; Ju, H. Signal amplification using functional nanomaterials for biosensing. *Chem. Soc. Rev.* **2012**, *41*, 2122−2134.

(17) Zhu, J.; Shen, J.; Hu, B.; Yang, L.; Jiang, C. Chromaticity Evolutionary Detection of Food Contaminant Semicarbazide through an Upconversion Luminescence-Based Nanosensor. *Anal. Chem.* **2022**, *94*, 1126−1134.

(18) Goas, M. L.; Saber, J.; Bolívar, S. G.; Rabanel, J. M.; Awogni, J. M.; Boffito, D. C.; Banquy, X. (In)stability of ligands at the surface of inorganic nanoparticles: A forgotten question in nanomedicine? *Nano Today* **2022**, *45*, No. 101516.

(19) Li, J.; Liu, J.; Chen, C. Remote Control and Modulation of Cellular Events by Plasmonic Gold Nanoparticles: Implications and Opportunities for Biomedical Applications. *ACS Nano* **2017**, *11*, 2403−2409.

(20) Maduraiveeran, G.; Sasidharan, M.; Ganesan, V. Electrochemical sensor and biosensor platforms based on advanced nanomaterials for biological and biomedical applications. *Biosens. Bioelectron.* **2018**, *103*, 113−129.

(21) Maiti, P.; Singha, T.; Chakraborty, U.; Roy, S. D.; Karmakar, P.; Dey, B.; Hussain, S. A.; Paul, S.; Paul, P. K. Selective and sensitive detection of L-Cysteine via fluorometric assay using gold nanoparticles and Rhodamine B in aqueous medium. *Mater. Chem. Phys.* **2019**, *234*, 158−167.

(22) Dizman, H. M.; Kazancioglu, E. O.; Shigemune, T.; Takahara, S.; Arsu, N. High sensitivity colorimetric determination of L-cysteine using gold nanoparticles functionalized graphene oxide prepared by photochemical reduction method. *Spectrochim. Acta, Part A* **2022**, *264*, No. 120294.

(23) Shemetov, A. A.; Nabiev, I.; Sukhanova, A. Molecular Interaction of Proteins and Peptides with Nanoparticles. *ACS Nano* **2012**, *6*, 4585−4602.

(24) Bigdeli, A.; Ghasemi, F.; Moayed, S. A.; Shahrajabian, M.; Kashani, N. F.; Jafarinejad, S.; Nejad, M. A. F.; Nezhad, M. R. H. Ratiometric fluorescent nanoprobes for visual detection: Design

https://doi.org/10.1021/acsomega.2c02725
ACS Omega 2022, 7, 29013−29026

principles and recent advances - A review. *Anal. Chim. Acta* **2019**, *1079*, 30−58.
(25) Yang, X. F.; Guo, X. Q.; Zhao, Y. B. Development of a novel rhodamine-type fluorescent probe to determine peroxynitrite. *Talanta* **2002**, *57*, 883.
(26) Han, S.; Yang, L.; Wen, Z.; Chu, S.; Wang, M.; Wang, Z.; Jiang, C. A dual-response ratiometric fluorescent sensor by europium-doped CdTe quantum dots for visual and colorimetric detection of tetracycline. *J. Hazard. Mater.* **2020**, *398*, No. 122894.
(27) Yang, F.; Lin, D.; Pan, L.; Zhu, J.; Shen, J.; Yang, L.; Jiang, C. Portable Smartphone Platform Based on a Single Dual-Emissive Ratiometric Fluorescent Probe for Visual Detection of Isopropanol in Exhaled Breath. *Anal. Chem.* **2021**, *93*, 14506−14513.
(28) Ferré, S.; Ruiz, V. G.; Zangari, J.; Girel, S.; Martinou, J. C.; Sardella, R.; Rudaz, S. Separation and determination of cysteine enantiomers in plasma after derivatization with 4-fluoro-7-nitro-benzofurazan. *J. Pharm. Biomed. Anal.* **2022**, *209*, No. 114539.
(29) Zor, E. Silver nanoparticles-embedded nanopaper as a colorimetric chiral sensing platform. *Talanta* **2018**, *184*, 149−155.
(30) Ma, Q.; Qi, C.; Li, X. L.; Shi, Q.; Xu, C. Y.; Jin, T.; Min, J. Z. Simultaneous Determination of DL-cysteine, DL-homocysteine, and glutathione in saliva and urine by UHPLC-Q-Orbitrap HRMS: Application to studies of oxidative stress. *J. Pharm. Biomed. Anal.* **2021**, *196*, No. 113939.
(31) Pucciarini, L.; González-Ruiz, V.; Zangari, J.; Martinou, J. C.; Natalini, B.; Sardella, R.; Rudaz, S. Development and validation of a chiral UHPLC-MS method for the analysis of cysteine enantiomers in biological samples. *J. Pharm. Biomed. Anal.* **2020**, *177*, No. 112841.
(32) Greño, M.; Marina, M. L.; Puyana, M. C. Use of single and dual systems of γ- cyclodextrin or γ -cyclodextrin/L-Carnitine derived ionic liquid for the enantiomeric determination of cysteine by electrokinetic chromatography. A comparative study. *Microchem. J.* **2021**, *169*, No. 106596.
(33) Frens, G. Controlled Nucleation for the Regulation of the Particle Size in Monodisperse Gold Suspensions. *Nat. Phys. Sci.* **1973**, *241*, 20.
(34) Dutta Roy, S.; Ghosh, M.; Chowdhury, J. Adsorptive parameters and influence of hot geometries on the SER(R) S spectra of methylene blue molecules adsorbed on gold nanocolloidal particles. *J. Raman Spectrosc.* **2015**, *46*, 451−461.
(35) Jones, M. R.; Osberg, K. D.; Macfarlane, R. J.; Langille, M. R.; Mirkin, C. A. Templated Techniques for the Synthesis and Assembly of Plasmonic Nanostructures. *Chem. Rev.* **2011**, *111*, 3736−3827.
(36) Zhang, J.; Zhao, B.; Meng, L.; Wu, H.; Wang, X.; Li, C. Controlled synthesis of gold nanospheres and single crystals in hydrogel. *J. Nanopart. Res.* **2007**, *9*, 1167−1171.
(37) Chandrasekharan, N.; Kamat, P. V.; Hu, J.; Jones, G., II Dye-Capped Gold Nanoclusters: Photoinduced Morphological Changes in Gold/Rhodamine 6G Nanoassemblies. *J. Phys. Chem. B* **2000**, *104*, 11103−11109.
(38) Acres, R. G.; Feyer, V.; Tsud, N.; Carlino, E.; Prince, K. C. Mechanisms of Aggregation of Cysteine Functionalized Gold Nanoparticles. *J. Phys. Chem. C* **2014**, *118*, 10481−10487.
(39) Wang, T.; Hu, X.; Dong, S. The fragmentation of gold nanoparticles induced by small biomolecules. *Chem. Commun.* **2008**, 4625−4627.
(40) Wu, H. P.; Huang, C. C.; Cheng, T. L.; Tseng, W. L. Sodium hydroxide as pretreatment and fluorosurfactant-capped gold nanoparticles as sensor for the highly selective detection of cysteine. *Talanta* **2008**, *76*, 347−352.
(41) Zhang, F. X.; Han, L.; Israel, L. B.; Daras, J. G.; Maye, M. M.; Ly, N. K.; Zhong, C. J. Colorimetric detection of thiol-containing amino acids using gold nanoparticles. *Analyst* **2002**, *127*, 462−465.
(42) Li, L.; Li, B. Sensitive and selective detection of cysteine using gold nanoparticles as colorimetric probes. *Analyst* **2009**, *134*, 1361−1365.
(43) Alarcos, N.; Cohen, B.; Ziolek, M.; Douhal, A. Photochemistry and Photophysics in Silica-Based Materials: Ultrafast and Single Molecule Spectroscopy Observation. *Chem. Rev.* **2017**, *117*, 13639−13720.
(44) Tira, D. S.; Focsan, M.; Ulinici, S.; Maniu, D.; Astilean, S. Rhodamine B-Coated Gold Nanoparticles as Effective "Turn-on" Fluorescent Sensors for Detection of Zinc II Ions in Water. *Spectrosc. Lett.* **2014**, *47*, 153−159.
(45) Chu, S.; Wang, H.; Ling, X.; Yu, S.; Yang, L.; Jiang, C. A Portable Smartphone Platform Using a Ratiometric Fluorescent Paper Strip for Visual Quantitative Sensing. *ACS Appl. Mater. Interfaces* **2020**, *12*, 12962−12971.
(46) Manjubaashini, N.; Kesavan, M. P.; Rajesh, J.; Thangadurai, T. D. Multispectroscopic and bioimaging approach for the interaction of rhodamine 6G capped gold nanoparticles with bovine serum albumin. *J. Photochem. Photobiol., B* **2018**, *183*, 374−384.
(47) Chandrakar, V.; Tapadia, K.; Gupta, S. K. Greener approach for gold nanoparticles synthesis from fruit peel extract of Manilkara zapota: a fluorometric assay for determination of thiourea. *Inorg. Nano-Met. Chem.* **2022**, 1−9.
(48) Prusti, B.; Chakravarty, M. An electron-rich small AIEgen as a solid platform for the selective and ultrasensitive on-site visual detection of TNT in the solid, solution and vapor states. *Analyst* **2020**, *145*, 1687−1694.
(49) Prasanth, S.; D Raj, R.; Vineeshkumar, T. V.; Thomas, R. K.; Sudarsanakumar, C. Exploring the interaction of L-cysteine capped CuS nanoparticles with bovine serum albumin (BSA): a spectroscopic study. *RSC Adv.* **2016**, *6*, 58288.
(50) Lim, I.-I. S.; Ip, W.; Crew, E.; Njoki, P. N.; Mott, D.; Zhong, C. J.; Pan, Y.; Zhou, S. Homocysteine-Mediated Reactivity and Assembly of Gold Nanoparticles. *Langmuir* **2007**, *23*, 826−833.
(51) Saroha, B.; Kumar, A.; Maurya, R. R.; Lal, M.; Kumar, S.; Rajor, H. K.; Bahadur, I.; Negi, D. S. Adsorption of cysteine on metal (II) octacynaomolybdate(IV) at different pH values: Surface complexes characterization by FT-IR, SEM with EDXA, CHNS and Langmuir isotherm analysis. *J. Mol. Liq.* **2022**, *349*, No. 118197.
(52) Hung, S. H.; Lee, J. Y.; Hu, C. C.; Chiu, T. C. Gold-nanoparticle-based fluorescent "turn-on" sensor for selective and sensitive detection of dimethoate. *Food Chem.* **2018**, *260*, 61−65.
(53) Link, S.; Sayed, M. A. E. Shape and size dependence of radiative, non-radiative and photothermal properties of gold nanocrystals. *Int. Rev. Phys. Chem.* **2000**, *19*, 409−453.
(54) Blatchford, C. G.; Campbell, J. R.; Creighto, J. A. Plasma Resonance − Enhanced Raman Scattering by Adsorbates on Gold colloids: the effects of aggregation. *Surf. Sci.* **1982**, *120*, 435−455.
(55) Wang, H.; Yang, L.; Chu, S.; Liu, B.; Zhang, Q.; Zou, L.; Yu, S.; Jiang, C. Semiquantitative Visual Detection of Lead Ions with a Smartphone via a Colorimetric Paper-Based Analytical Device. *Anal. Chem.* **2019**, *91*, 9292−9299.
(56) Jokerst, J. V.; Lobovkina, T.; Zare, R. N.; Gambhir, S. S. Nanoparticle PEGylation for imaging and therapy. *Nanomedicine* **2011**, *6*, 715−728.
(57) Lim, I.-I. S.; Mott, D.; Ip, W.; Njoki, P. N.; Pan, Y.; Zhou, S.; Zhong, C. J. Interparticle Interactions in Glutathione Mediated Assembly of Gold Nanoparticles. *Langmuir* **2008**, *24*, 8857−8863.
(58) Basu, S.; Pal, P. Glutathione-Induced Aggregation of Gold Nanoparticles: Electromagnetic Interactions in a Closely Packed Assembly. *J. Nanosci. Nanotechnol.* **2007**, *7*, 1904−1910.
(59) Zhang, L.; Xu, C.; Liu, C.; Li, B. Visual chiral recognition of tryptophan enantiomers using unmodified gold nanoparticles as colorimetric probes. *Anal. Chim. Acta* **2014**, *809*, 123−127.
(60) Feng, Y.; Liu, W.; Prieto, R. M.; Chen, X. D. Dye-protein interactions between Rhodamine B and whey proteins that affect the photoproperties of the dye. *J. Photochem. Photobiol., A* **2021**, *408*, No. 113092.
(61) Yuvaraj, P.; Ajantha, J.; Karuppusamy, M.; Easwaramoorthi, S.; Rao, J. R. Hydrogen Bond-Assisted Colorimetric Picomolar Level Detection of Hg^{2+} Ions in 100% Aqueous Solution. *ACS Sustainable Chem. Eng.* **2021**, *9*, 10309−10317.

https://doi.org/10.1021/acsomega.2c02725
ACS Omega 2022, 7, 29013−29026

(62) Benesi, H. A.; Hildebrand, J. H. A Spectrophotometric Investigation of the Interaction of Iodine with Aromatic Hydrocarbons. *J. Am. Chem. Soc.* **1949**, *71*, 2703−2707.
(63) Lodhi, M. S.; Khan, M. T.; Aftab, S.; Samra, Z. Q.; Wang, H.; Wei, D. Q. A novel formulation of theranostic nanomedicine for targeting drug delivery to gastrointestinal tract cancer. *Cancer Nanotechnol.* **2021**, *12*, No. 26.
(64) Andal, V.; Bhuvaneswari, G. Silver oxide nano-colloid based selective colorimetric sensor for the recognition of cystine in aqueous solution. *Mater. Res. Innovations* **2020**, *24*, 202−209.
(65) Pawlukojć, A.; Leciejewicz, J.; Ramirez-Cuesta, A. J.; Nowicka-Scheibe, J. L-Cysteine: Neutron spectroscopy, Raman, IR and ab initio study. *Spectrochim. Acta, Part A* **2005**, *61*, 2474−2481.
(66) Shtukenberg, A. G.; Hu, J.; Sahota, A.; Kahr, B.; Ward, M. D. Disrupting Crystal Growth through Molecular Recognition: Designer Therapies for Kidney Stone Prevention. *Acc. Chem. Res.* **2022**, *55*, 516−525.
(67) Claes, D. J.; Jackson, E. Cystinuria: mechanisms and management. *Pediatr. Nephrol.* **2012**, *27*, 2031−2038.

https://doi.org/10.1021/acsomega.2c02725
ACS Omega 2022, 7, 29013−29026